QUANTUM INFORMATION PROCESSING IN NANOSTRUCTURES

John-Henry Reina Estupiñán

A thesis submitted for the degree of
Doctor of Philosophy at the University of Oxford

Lincoln College
University of Oxford
Hilary Term 2002

ABSTRACT

Quantum information processing in nanostructures

JOHN-HENRY REINA ESTUPIÑÁN
Lincoln College, Oxford
D.Phil. thesis, Hilary 2002

Since information has been regarded as a physical entity, the field of quantum information theory has blossomed. This brings novel applications, such as quantum computation. This field has attracted the attention of numerous reasearchers with backgrounds ranging from computer science, mathematics and engineering, to the physical sciences. Thus, we now have an interdisciplinary field where great efforts are being made in order to build devices that should allow for the processing of information at a quantum level, and also in the understanding of the complex structure of some physical processes at a more basic level. This thesis is devoted to the theoretical study of structures at the nanometer-scale, "nanostructures," through physical processes that mainly involve the solid-state and quantum optics, in order to propose reliable schemes for the processing of quantum information. Initially, the main results of quantum information theory and quantum computation are briefly reviewed. Next, the state-of-the-art of quantum dots technology is described. In so doing, the theoretical background and the practicalities required for this thesis are introduced. A discussion of the current quantum hardware used for quantum information processing is given. In particular, the solid-state proposals to date are emphasised.

A detailed prescription is given, using an optically-driven coupled quantum dot system, to reliably prepare and manipulate exciton maximally entangled Bell and Greenberger-Horne-Zeilinger (GHZ) states. Manipulation of the strength and duration of selective light-pulses needed for producing these highly entangled states provides us with crucial elements for the processing of solid-state based quantum information. The all-optical generation of states of the so-called Bell basis for a system of two quantum dots (QDs) is exploited for performing the quantum teleportation of the excitonic state of a dot in an array of three coupled QDs. Theoretical predictions suggest that several hundred single quantum bit rotations and controlled-NOT gates could be performed before decoherence of the excitonic states takes place. In addition, the exciton coherent dynamics of a coupled QD system confined within a semiconductor single mode microcavity is reported. It is shown that this system enables the control of exciton entanglement by varying the coupling strength between the optically-driven dot system and the microcavity. The exciton entanglement shows collapses and revivals for suitable amplitudes of the incident radiation field and dot-cavity coupling strengths. The results given here could offer a new approach for the control of decoherence mechanisms arising from entangled "artificial molecules."

In addition to these ultrafast coherent optical control proposals, an approach for reliable implementation of quantum logic gates and long decoherence times in a QD system based on nuclear magnetic resonance (NMR) is given, where the nuclear resonance is controlled by the ground state "magic number" transitions of few-electron QDs in an external magnetic field.

The dynamical evolution of quantum registers of arbitrary length in the presence of environmentally-induced decoherence effects is studied in detail. The cases of quantum bits (qubits) coupling individually to different environments ("independent decoherence"), and qubits interacting collectively with the same reservoir ("collective decoherence") are analysed in order to find explicit decoherence functions for any number of qubits. The decay of the coherences of the register is shown to strongly depend on the input states: this sensitivity is a characteristic of *both* types of coupling (collective and independent) and not only of the collective coupling, as has been reported previously. A non-trivial behaviour—"recoherence"—is found in the decay of the off-diagonal elements of the reduced density matrix in the specific situation of independent decoherence. The results lead to the identification of decoherence-free states in the collective decoherence limit. These states belong to subspaces of the system's Hilbert space that do not become entangled with the environment, making them ideal elements for the engineering of "noiseless" quantum codes. The relations between decoherence of the quantum register and computational complexity based on the new dynamical results obtained for the register density matrix are also discussed.

This thesis concludes by summarising and pointing out future directions, and in particular, by discussing some biological resonant energy transfer processes that may be useful for the processing of information at a quantum level.

A La Vigía

Raíces sin tiempo

AGRADECIMIENTOS

Son muchas las situaciones y muchas las personas con las cuales me siento en deuda hacia la culminación de este camino. Espero poder agradecer a todos aquellos que de una u otra forma han hecho de este proceso un invaluable proyecto de vida.

Primero que todo debo agradecer a la Agencia Colombiana para el Fomento de la Ciencia y la Tecnología, COLCIENCIAS, por el apoyo financiero que permitió el desarrollo de mi investigación aquí en Oxford.

Gracias a mi supervisor, Dr. Neil F. Johnson, por las estimulantes discusiones durante la realización de esta investigación doctoral. Gracias Neil por el apoyo y la confianza depositadas en el proyecto.

Gracias al Dr. Luis Quiroga, co-autor de algunos de los artículos publicados en esta tesis, por el oportuno intercambio de ideas y discusiones. Gracias Luis por estar allí en los momentos en que necesité de una mano.

Gracias al Laboratorio Clarendon, Departamento de Física, Universidad de Oxford, por el acceso a sus excelentes instalaciones. Un especial agradecimiento al Dr. Simon C. Benjamin por el apoyo y por las interesantes discusiones relacionadas con diferentes aspectos del procesamiento de información a nivel cuántico. Gracias a Brian Burns por el excelente soporte técnico e intercambio musical! A Janet Andrews por su siempre oportuna y efectiva ayuda.

Un agradecimiento muy especial a mi querido amigo Don Gerardo "El Chicanero" Hechenblaikner por todos los momentos compartidos aqui en Oxford y en Lienz. Gerald, todos los triunfos y fracasos han sido mejor recibidos gracias a vuestra sincera y desinteresada amistad. Gracias por ayudarme a mantener la cordura.

La dedicación y tenacidad de Rakesh Roshan han sido inspiradoras. Gracias Rakesh por tu amistad, ejemplo y por los excelentes currys compartidos a través de estos años. Gracias a Andrea Jiménez por los cafes y por las distracciones a veces necesarias!

Gracias al glorioso "Lincoln College MCR Football Club—IX LCMCRFC" por todos los gratos momentos. Aunque los estados de ebriedad de muchos de ustedes, además de algunos otros pequeños detalles técnicos!, facilitaron algunas de las amplias derrotas sufridas los Sábados por la mañana, debo admitir que en general siempre pasamos un buen tiempo juntos. Alain Forclaz, Andy Boyle, Gav Maggs, Mario Edmundo, Mark Dillingham, Dave Rhodes y Matt Southward: gracias por los buenos tiempos, en especial aquellos de invierno. Foklá, gracias por ayudar a mantener mi sanidad después de aquellas noches en Bar Med, en especial cuando de ir a Court Place Gardens, rio abajo, se trataba! Gracias a Alexis Heeb por los tiempos compartidos.

Un agradecimiento muy especial va para Maurizio Tinnirello, Allan Garrick y Elaine Sar. Vuestra sincera amistad y apoyo han hecho de mis dias en Oxford una experiencia mas amigable y enriquecedora. Allan, gracias por las inolvidables noches de jazz en el 'Cricketers' y el 'Spin'. Maurizio, gracias por la persistencia y por la necesidad de querer crear un mundo mejor. También gracias por los buenos partidos de tennis.

Gracias a Juan Carlos Granada, influyente y motivante persona en mi vida. Gracias Juan Carlos por todo el apoyo y soporte previos al inicio de mi ciclo en Oxford. Gracias a Walter Emir Garcés por el optimismo y entusiasmo permanentemente transmitidos.

Gracias a la familia Steers por todo el apoyo vital brindado durante estos años. Gracias a Peter, Andrea, Jon y Matt. Muchas gracias a Bill y Betty Corcoran, asi como también a Tim y May por acogerme como parte de su familia.

El mas profundo agradecimiento para mi familia Vigieña. Gracias a mi mamá, Nicolas y mis hermanos y hermanas, asi como también a Helena, Maritza, Arleth, Billy, Maria José y William por todo el amor y el apoyo de siempre.

Por último, pero no menos, quiero agradecer a mi esposa. No puedo poner en palabras el agradecimiento tan inmenso que tengo para contigo. Gracias por todo tu invaluable apoyo, por ayudar a hacerme sentir como en casa, por hacerme querer ser un mejor hombre y por compartir los dones de tu vida.

ACKNOWLEDGEMENTS

There have been many situations and many people whom I would like to acknowledge, for their kindness and support throughout this part of my life. I hope to be able to acknowledge all of the people who, in one form or another, have made this process an invaluable and unforgettable part of my life.

First, I would like to say thank you to the Colombian Agency for Science and Technology, COLCIENCIAS, for the financial support which enabled me to conduct the research which forms this thesis here at Oxford University.

Thanks to my supervisor, Dr. Neil F. Johnson, for the stimulating discussions during the development of the ideas in this thesis. Thank you Neil for the support and confidence you gave to me throughout this project.

Thank you to Professor Luis Quiroga, co-author of several of the papers presented in this thesis. Thank you for the opportune exchange of ideas, and for the fruitful discussions. Thank you also for being there when I needed someone's helping hand.

Thank you to the Clarendon Laboratory, Department of Physics, Oxford University, for access to the excellent facilities. Thanks also to Dr. Simon C. Benjamin, for the support and for the interesting discussions of different aspects of quantum information processing. Thanks to Brian Burns for the support you provided, both computer-wise and music-wise! Also, thanks to Janet Andrews, for your continual opportune and effective help.

A special acknowledgement goes to my dear friend, Don Gerardo "El Chicanero" Hechenblaikner, for all of the special times we shared in Oxford and in Lienz. Gerald, thanks to your sincere and selfless friendship, all of the triumphs and defeats have been easier to bear. Thank you for helping me to keep my sanity!

The dedication and tenacity of Rakesh Roshan has been inspirational. Thank you Rakesh, for your friendship, for your example, and also for all of the excellent currys we shared through the years. Thanks also to Andrea Jiménez for all the coffees, and the sometimes necessary distractions.

Thanks to the glorious "Lincoln College MCR Football Club—IX LCMCRFC" for all of the memorable moments. Despite the drunken state of some of you, plus all of those little technical faults!, both of which contributed to some of the biggest defeats suffered by Saturday morning football in Oxford, I must admit that we had a great time together. Alain Forclaz, Andy Boyle, Gav Maggs, Mario Edmundo, Mark Dillingham, Dave Rhodes and Matt Southward: thank you for the good times, especially in winter! Fokla, thank you for helping me to keep my health, after some of those nights in Bar Med, especially that time you sent me down the river back to Court Place Gardens! Thanks also to Alexis Heeb, for all the times we shared together.

A very special acknowledgement goes to Maurizio Tinnirello, Allan Garrick and Elaine Sar. Your sincere friendship and support have made my days in Oxford much more friendly and enriched. Allan, thank you for those unforgettable nights in the 'Spin' and the 'Cricketers'. Maurizio, many thanks for your persistence, and for your continual reminders of the necessity of building a better world. Also, thanks a lot for those great tennis matches.

Thank you to Juan Carlos Granada, an influential and motivational person in my life. Thank you Juan Carlos, for your support and for your input to the initiation of my time in Oxford. Thanks also to Walter Emir Garces, for the optimism and enthusiasm that you always transmit.

Thank you to the Steers family for all the vital support you have given over these years. Thanks to Peter, Andrea, Jon and Matt. Many thanks to Bill and Betty Corcoran, and also Tim and May. Thanks to all of you for making me feel like part of your family.

The deepest acknowledgement to my Vigieña family. Thanks to my Mum, Nicolas, my brothers and sisters, and also to Helena, Maritza, Arleth, Billy, Maria José and William for all your continuing love and support.

Finally, but of course not least, I would like to acknowledge my immense gratitude to my wife. It is impossible to put words to this, but thank you for all of your invaluable support, for helping me to feel at home, for making me want to be a better man and for sharing with me the many gifts of your life.

Contents

1 Introduction 1

2 Background material: From quantum information to quantum technology 7

2.1 Fundamentals of quantum information and quantum computing 7
  2.1.1 From binary digits to universal quantum computation 7
  2.1.2 Quantum computation by geometric means 16
  2.1.3 Quantum entanglement: a communication resource 18
  2.1.4 Quantum algorithms and quantum games 23
  2.1.5 Quantum decoherence and quantum error correction 27
  2.1.6 Physical qubits 33
2.2 Quantum dots 36
  2.2.1 Background to fabrication and involved physical processes 37
  2.2.2 Experimental state-of-the-art: quantum wave function engineering and quantum light emitters 39
  2.2.3 Kohn theorem and properties of an interacting system 42
  2.2.4 Solid state qubits 42
2.3 Discussion 43

3 Quantum entanglement of artificial molecules 45

3.1 Generation of maximally entangled states in optically-driven quantum dots 46
  3.1.1 Wave function and unitary evolution 46
  3.1.2 Coupling of $N = 2$ QDs and generation of Bell states 48
  3.1.3 Coupling of $N = 3$ QDs and generation of GHZ states 50
3.2 Results and discussion 53
3.3 Pseudo-spin operators and the density matrix 58
  3.3.1 Bell states 59
  3.3.2 GHZ states 61
3.4 Quantum information processing with coupled QDs 62
3.5 Concluding remarks 65

4 Quantum teleportation in a solid state system 67
- 4.1 The quantum teleportation protocol . . . 67
- 4.2 Teleportation as a quantum circuit . . . 69
- 4.3 Physical implementation in a quantum dot system . . . 74

5 Spintronics: a solid state NMR-based quantum switch 79
- 5.1 Preliminaries . . . 79
- 5.2 The nanostructure switch . . . 80
- 5.3 Nuclear spin-electron spin effective coupling: tuning the resonance frequency ω_{NMR} . . . 85
- 5.4 Far infrared radiation and nuclear qubit control . . . 88
- 5.5 Discussion . . . 92

6 The art of noise: decoherence of quantum registers 95
- 6.1 Independent versus collective decoherence . . . 97
- 6.2 Dimensionality of the field and decoherence rates for few-qubit systems . 102
  - 6.2.1 Single qubit case . . . 102
  - 6.2.2 $L = 2$ qubit register . . . 103
- 6.3 Discussion . . . 115
- 6.4 Relevance to a model quantum dot Hamiltonian . . . 117
- 6.5 Decoherence effects on the generation of QD exciton entangled states . . . 118

7 Conclusions and perspectives 122
- 7.1 Summary . . . 122
- 7.2 Future directions . . . 124

A Collapsing and reviving QD entanglement in a microcavity 129
- A.1 Model and results . . . 129
- A.2 The QD-microcavity wave function & Bell state generation . . . 134

B n-dimensional Hilbert space of exciton entanglement 139

C Single-qubit decoherence 143

D Time evolution and the reduced density matrix 148
- D.1 The time evolution operator $U_I(t)$ . . . 148
- D.2 The reduced density matrix of a L-qubit register . . . 149

List of Figures

2.1 A quantum network containing 4 gates. From left to right, the QR state $|\Psi\rangle$ experiences the action of the following quantum logic gates: i) Hadamard (H), ii) phase shift $[P(\varphi)]$, iii) Controlled-U (U), and iv) controlled-NOT (CNOT or XOR). The network produces the final state "output" $|\Psi'\rangle \equiv XOR_{23}U_{12}P(\varphi)_1H_1\,|\Psi\rangle$. In this operational notation, the subscripts denote the qubits to be addressed, and in any 2-qubit gate U_{ij}, i, and j denote the control and target bits respectively. Note that the first two unitary transformations are single qubit gates while the remaining ones are two qubit gates. 10

2.2 Schematic of a quantum dot array. The dots of the figure are formed in a wetting layer, sandwiched between two GaAs layers. Barrier layers of AlGaAs and gold electric contacts complete the structure. The figure is adapted from Ref. [58]. . 37

2.3 Schematic of a nanoprobing (scanning near-field optical probing) system used to measure the near-field luminescence properties of quantum dots at low temperatures. This near-field probe can scan, dot-by-dot, the optical properties of an entire ensemble of dots. The figure is adapted from Ref. [64]. 40

2.4 Intensity (a) auto- and (b) cross-correlation functions between photons due to the recombination of *e-h* pairs. (a) *Monochromatic* photons: X^0 line auto-correlation function $g^{(2)}_{11}(\tau)$ (as a function of cw excitation power): this gives the probability of finding the QD occupied with a single exciton at time τ after the emission of the previous X^0 photon. (b) *Multicolor* photons: intensity cross-correlation between the emitted photons from the nX^S line and the photons from the X^0 line for increasing cw excitation power. In both plots, thick (thin) solid lines correspond to measured (calculated) values. The figure is adapted from Ref. [79]. 41

3.1 Schematic of the optical setup for the $N = 2$ QDs system. The identical QDs, containing no net charge, are radiated with long-wavelength classical light of central frequency ω, $\xi(t) = Ae^{-i\omega t}$. Formation of single excitons within the individual QDs and their inter-dot hopping in the presence of the Förster interaction are illustrated schematically. The bandgap ϵ as well as the conduction band (CB) and the valence band (VB) of the system are also sketched. 46

3.2 Schematic of the energy levels for our 2 QDs system in (a) the absence ($W = 0$), and (b) the presence ($W \neq 0$) of the interdot interaction, when there is no external light applied to the system. If the QDs are sufficiently close to each other, external laser pulses can induce a resonant energy transfer process and hence an exciton can hop between dots. Here, the triplet subspace $J = 1$ is considered as the only one optically active. The states $|J, M_i\rangle$ on the left are the associated kets of the $\{|M_i\rangle\}$ basis. 49

3.3 Energy diagram for the 3 QD system in the absence of external light, for (a) $W = 0$, and (b) $W \neq 0$ interdot interaction. The depicted energy levels are associated with the $J = 3/2$ subspace states of the $\{|M_i\rangle\}$ basis, whose kets are shown in the left-handside of diagram. 51

3.4 Generation of the Bell State $|\phi^+\rangle = \frac{1}{\sqrt{2}}(|00\rangle + |11\rangle)$. The τ_{BELL}-pulses shown here correspond to the implementation of a Hadamard transform followed by a quantum CNOT gate: $\text{CNOT}_{12}H_1$. $W = 0.1$, $\varphi = 0$, and (a) $A = \frac{1}{25}$, (b) $A = \frac{1}{50}$, (c) $A = 10^{-2}$, and (d) $A = 10^{-3}$. $|\Psi(t)\rangle$ denotes the total wavefunction of the system at time t, in both laboratory (solid curves) and rotating frames (dashed curves). The energy is in units of the band gap ϵ, and $|\Psi_0\rangle = |0\rangle$. 54

3.5 Generation of the Bell state $|\phi^+\rangle$. $A = 10^{-3}$, $\varphi = 0$, and (a) $W = 0.1$, (b) $W = 0.05$, and (c) $W = 10^{-2}$. 55

3.6 Generation of the GHZ state $\frac{1}{\sqrt{2}}(|000\rangle + |111\rangle)$. $W = 0.1$, $\varphi = 0$, and (a) $A = \frac{1}{25}$, (b) $A = \frac{1}{50}$, (c) $A = 10^{-2}$, and (d) $A = 10^{-3}$. The τ_{GHZ}-pulses given here are equivalent to the realisation of the entangling network $\text{CNOT}_{13}\text{CNOT}_{12}H_1$. 57

3.7 (a) Population of the vacuum state ρ_{00} and biexciton state ρ_{22} in two coupled QDs, as a function of time. (b) Time-evolution of overlap with maximally entangled Bell state. $\epsilon = 1$, $W = \epsilon/10$, $A = W/5$, and $\varphi = \pi/2$. Blue (thin solid) line shows exact numerical result in the laboratory frame. Red (thick solid) line in (b) represents the exact numerical solution in the rotating frame. Pink (dashed) line shows approximate analytical result. (c) Time-evolution of overlap with maximally entangled GHZ states $|\Psi_{\text{GHZ}}(\pi/2)\rangle$, and (d) $|\Psi_{\text{GHZ}}(\pi/2)\rangle_2$, under the action of a rectangular pulse of light at resonance. $\epsilon = 1$, $W = \epsilon/10$, and $A = 2W/5$. Red (solid) line represents exact numerical solution. Blue (dashed) line shows approximate analytical result. 60

3.8 Measurement of exciton interference fringes for single-dot photoluminescence emission intensity as a function of relative pulse delay and the power density $P_1 = 0.067$ μJ cm^{-2}/pulse. Plots (e) and (f) show Rabi-like oscillations due to quantum interference of a two-level (exciton) system for the coarse delay shown in (b) 30 ps, and (c) 0 ps, respectively. The two excitonic levels are the ground state $|0\rangle$, with energy $E_0 = 1.67243$ eV, and the excited excitonic state $|1\rangle$, with $E_1 = 1.6926$ eV ($\Delta E = 20.2$ meV). The figure is adapted from Ref. [65]. 64

4.1 Schematics of the quantum teleportation process. For simplicity the kets notation for the quantum states associated with the 3-particle system has been omitted (see text). 68

4.2 Circuit schemes to teleport an unknown quantum state from Alice to Bob using an arrangement of (a) 3, (b) 4 and (c) n qubits (coupled quantum dots). The methods employ (a) Bell, (b) GHZ, and (c) Schrödinger's cat states respectively. In (c) $|\Psi_{\text{CAT}}\rangle \equiv |\Psi_{\text{CAT}}\rangle_{2,n-1}$. 72

4.3 Practical implementation of teleportation using optically-driven coupled quantum dots. (a) Initial state of the system. (b) Intermediate step: radiating the system with the pulse $\xi(t)$. (c) Bell basis measurement and the quantum state of the system at the dashed line in Fig. 4.2(a). (d) Final state. Typical values for GaAs-based dots are diameter $d_1 = 20$ nm, thickness $d_2 = 5$ nm and separation $d_3 \leq 20$ nm (these dimensions and separation depend on the kind of materials employed, see text). 75

4.4 Generation of (a) the Bell State $|\Psi_{\text{BELL}}(0)\rangle$ and (b) the GHZ state $|\Psi_{\text{GHZ}}(0)\rangle$. These pulses correspond to the realisation of the Hadamard gate followed by one CNOT gate and two CNOT gates respectively [see Figs. 4.2(a) and 4.2(b)]. In units of the band gap $\epsilon = 2.8$ eV, $W = 0.1$, $A = \frac{1}{25}$. $|\psi(0)\rangle = |0\rangle$. Here $|\psi(t)\rangle$ denotes the total wavefunction of the system in the laboratory frame at time t. 77

5.1 Schematics of the model quantum dot. A nuclear impurity of spin-half is placed at the centre of a quasi-2D dot (spin-zero). The dot is in the presence of an external static magnetic field B and laterally confined by the parabolic potential $m^*\omega_0^2 r^2/2$. 81

5.2 Energy of the ground state (in units of the confinement energy $\hbar\omega_0$) of a two-electron QD for vanishing Landé factor $g^* = 0$ (i.e., the Zeeman spin splitting has been ignored) as a function of the ratio of cyclotron and oscillator frequency ω_c/ω_0. (a) without and (b), (c), (d) considering the interaction between electrons. The electron repulsion strength $\beta =$ (b) 0.5, (c) 1.0, (d) 3.0. As the magnetic field increases, the interaction between electrons undergoes a sequence of different ground states, and alternating sequence of singlet and triplet states $(m, S) = (0,0), (-1,1), (-2,0), (-3,1), (-4,0), \ldots$. The magnetic field strengths at which these transitions occur are indicated by the dashed lines. 83

5.3 Energy of the ground state (in units of the confinement energy $\hbar\omega_0$) of a two-electron system in the presence of Zeeman spin splitting ($g^* = -0.44$) as a function of ω_c/ω_0. The electron repulsion strength $\alpha/l_0^2 = 3.0\,\hbar\omega_0$. As the magnetic field strength increases, the singlet ground states are suppressed and we are left with only triplet-triplet transitions. In this case the (m, S) sequence is given by $(0,0), (-1,1), (-2,0), (-3,1), (-5,1), (-7,1), (-9,1), \ldots$ 84

5.4 Variation of the electron spin-nucleus spin effective coupling Δ_m as a function of ω_c/ω_0. The centre-of-mass motion remains in its ground state. The electron repulsion strength $\beta = 3.0$. The two-electron ground state undergoes transitions in the relative angular momentum m. The sequence, in terms of $|m|$ and the total electron spin S, is given by $(|m|, S) = (0,0), (1,1), (3,1), (5,1), \ldots$ The triplet state component $S_z = -1$. 87

5.5 Variation of the electron spin-nucleus spin effective coupling Δ_m for electron repulsion strengths (a) $\beta = 1.0$, and (b) $\beta = 0.5$. The $(|m|, S)$ sequence is given by $(0,0), (1,1), (3,1), (5,1), \ldots$ $S_z = -1$. Here, and in Fig. 5.4, the values $m^* = 0.2m_0$, and $g^* = 2.0$, which are appropriate for silicon conduction band electrons, have been used. 88

5.6 Relative variation of the effective nuclear magnetic resonance frequency of the carbon impurity nucleus, $\Delta\omega_{\rm NMR} = (\omega_{\rm NMR} - \omega_{\rm NMR,0})/\omega_{\rm NMR,0}$, as a function of ω_c/ω_0. The electron repulsion parameter $\beta = 3.0$. Solid line corresponds to centre-of-mass in the ground state. Dashed line corresponds to centre-of-mass in the first excited state after absorption of IR light. For the nuclear qubit (carbon impurity) we have considered the g-factor $g_{_N} = -0.55477$. 89

5.7 Schematic of the double QD system. Each QD contains 2 electrons. (a) Configuration 1, vertically arranged QDs with the nuclear impurity qubits and the electrons in dots j and $j+1$. The *inter-dot* correlation for electrons $(j+1, 2)$, and $(j, 1)$ is illustrated. Note that the separation between electrons in different dots is given in terms of the distances $|\boldsymbol{r}_{i+1,\nu} - \boldsymbol{r}_{i,\delta}|$ and d. The distance d does not correspond with the real scale of the system (see text). (c) Configuration 2, in-plane QDs: schematic of the *inter-dot* correlation for electrons $(j+1, 2)$, and $(j, 1)$. In this case, all of the dots are confined to the $z = 0$ plane. 91

5.8 Scaling up Configuration 2: The K dots of the system are confined to the $z = 0$ plane. Within the entire ensemble of dots, the B-field is able to address the QDs both locally and globally. 92

6.1 Two-qubit "independent decoherence" due to the coupling to a reservoir of the Ohmic type ($d = 1$) as a function of time t and the transit time t_s, for the input states associated with $\Gamma_1^+(t,T)$ ($i_a \neq j_a$, $i_b \neq j_b$). Here, $c_1 = 0.25$, and (i) $\theta = 10^{-3}$, (ii) 10^0, and (iii) 10^2. $\Gamma_i^\pm(t,T)$, with $i = 1, 3$ are defined in the text. . 106

6.2 Two-qubit "independent decoherence" caused by the coupling to an 'Ohmic environment' as a function of times t and t_s, for the input states associated with $\Gamma_1^-(t,T)$ ($i_a \neq j_a$, $i_b \neq j_b$). $c_1 = 0.25$, and (i) $\theta = 10^{-3}$, (ii) 10^0, and (iii) 10^2. . . 107

6.3 Two qubit "independent decoherence" due to the super-Ohmic environment $d = 3$ [Eq. (6.27)], as a function of times t and t_s, for the input states associated with $\Gamma_3^+(t,T)$. $c_3 = 0.25$, and (i) $\theta = 10^{-3}$, (ii) 10^0, and (iii) 10^2. 109

6.4 Two-qubit "independent decoherence" due to the super-Ohmic environment $d = 3$ as a function of times t and t_s for the input states associated with $\Gamma_3^-(t,T)$. $c_3 = 0.25$, and (i) $\theta = 10^{-3}$, (ii) 10^0, and (iii) 10^2. 110

6.5 Two-qubit "independent decoherence". $d = 3$, coupling strength $c_3 = 0.01$, and (i), (iii) $\theta = 10^{-3}$, and (ii), (iv) $\theta = 10^2$. 112

6.6 Two-qubit "collective decoherence" for (i) $d = 1$ 'Ohmic environment' [Eq. (6.31)], and (ii) $d = 3$ 'super-Ohmic environment' [Eq. (6.33)], as a function of time and the temperature $\theta \equiv \omega_{_T}/\omega_c$. $c_1 = c_3 = 0.25$, and $i_a \neq j_a$, and $i_b \neq j_b$. $\Gamma_{_d}^+(t,T)$ ($d = 1, 3$) is defined using Eqs. (27) and (28). 114

6.7 Relevance of the Förster interaction in the entanglement generation process (zero decoherence limit). Thick (red) lines represent the Bell-state overlap, $A = 0.1$: solid, Forster term included; dotted, Forster term not included. Thin (blue) lines represent the GHZ-state overlap, $A = 0.2$; same meaning as for solid and dotted lines. 119

6.8 Maximally entangled exciton states generation in the presence of phase decoherence: (a) $\langle O_{\text{BELL}}(t)\rangle$ for $A = 0.1$, red (dashed) line and $A = 0.4$, blue (solid) line. (b) $\langle O_{\text{GHZ}}(t)\rangle$ for $A = 0.2$, red (dotted) line and $A = 0.4$, blue (solid) line. In plots (a) and (b) Γ is kept fixed: $\Gamma = 0.001$. In figures (c) and (d) $A = 0.4$ is kept fixed whereas Γ is varied: $\Gamma = 0.001$, red (short dashed) line, $\Gamma = 0.01$, blue (solid) line and $\Gamma = 0.1$, green (long dashed) line. These curves correspond to (c) $\langle O_{\text{BELL}}(t)\rangle$ and (d) $\langle O_{\text{GHZ}}(t)\rangle$. 121

7.1 (a) Measured excitation transfer times in the photosynthetic unit (PSU) of purple bacteria. The pigments of the LH1 (32 BChls in a ring of radius $r \sim 59$ Å) complex absorb at 875 nm, while the LH2 complexes contain two types of BChls which absorb at 850 nm (16 BChls, $r \sim 23$ Å) and 800 nm (8 BChls, $r \sim 28$ Å), which are labelled B850 and B800. Carotenoids are shown as 'curled strings.' Typical distances between B800 and B850 are of the order of 20 Å. (b) Schematic of the energy levels of the electronic excitations in the PSU of BChl-a containing purple bacteria. The funneling of the excitation energy towards the photosynthetic reaction centre (RC) is shown. Dashed (solid) lines represent intracomplex (intercomplex) energy transfer. LH-I is found in all purple bacteria; LH-II exists in most species. The additional complex LH-III appears in certain species only. P, and B stand for RC accessory pigments. The figure is adapted from Refs. [70, 71]. 126

A.1 Overlap $O(t) = \text{Tr}\{\rho(t)\rho_{\text{BELL}}\}$ of Bell state as a function of time. The driving classical field coupling factor is kept fixed at $g_l = 0.1$, while $g_c =$ (a) 0.001, (b) 0.01, (c) 0.02, and (d) 0.08. In all of the plots, energies are measured in units of $V = 1$. The given results correspond to the resonance condition $\omega_x = \omega_c = \omega = 10$.131

A.2 Overlap $O(t)$ of the Bell state as a function of time for driving field amplitudes $g_l =$ (a) 0.01, (b) 0.1, (c) 0.2, (d) 0.5. The QD-cavity coupling is kept fixed at $g_c = 0.02$. 132

A.3 Collapses and revivals of the Bell state as a function of time in the rotating frame. The driving field amplitude $g_l = 1.2$, and the QD-cavity coupling $g_c = 0.25$. . . 133

C.1 (i) Decoherence of a single qubit for an "Ohmic environment" as a function of t (in units of ω_c). The contributions arising from the separate integration of thermal ($\exp[-\Gamma_T(t)]$) and vacuum ($\exp[-\Gamma_V(t)]$) fluctuations are shown as dotted curves. $c_1 = 0.25$, (a) $\theta \equiv \omega_T/\omega_c = 1$, (b) 10^{-2}, (c) 10^{-5}. If ω_c is the Debye cutoff, $\theta \approx 10^{-2}\ T$ (see text): the decoherence shown corresponds to $T = 100$ K, $T = 1$ K, and $T = 1$ mK, respectively. (ii) Coherence decay for (a) $\theta = 10^{-5}$, (b) 10^{-2}, (c) 10^{2}. $c_1 = 0.25$. Here, time is given in units of the thermal frequency $\omega_T \equiv k_B T/\hbar$. 145

C.2 Decoherence of a single qubit for (i) $d = 1$, and (ii) $d = 3$, as a function of time (in units of the cut-off ω_c) and the temperature parameter $\theta \equiv \omega_T/\omega_c$. $c_1 = c_3 = 0.25$. If ω_c is the Debye cut-off, the range of coherence decay goes from a few mK up to (a) 10^4 K [plot (i)] and (b) 1.5×10^3 K [plot (ii)]. 146

List of Tables

2.1 Characteristic 'gating,' and dephasing time scales for comparing different physical systems currently used as qubits. The figure of merit $\mathcal{M}$ gives an estimation of the number of qubit operations that could be realised on a qubit register before it decoheres. 36

6.1 Characteristic times for two-qubit independent decoherence $\tau^{\pm}_{dec}$ for $(d = 1)$-dimensional density of states of the field. Different temperature, transit time, and coupling strength values are considered. $i_a \neq j_a$, $i_b \neq j_b$ (see text). 105
6.2 Characteristic times for two qubit independent decoherence $\tau^{\pm}_{dec}$ for $(d = 3)$-dimensional density of states of field. $i_a \neq j_a$, $i_b \neq j_b$. 111

C.1 Single-qubit decoherence times for different temperatures, and coupling strength c_i $(i = 1, 3)$; for $d = 1$ (Ohmic), and $d = 3$ (super-Ohmic) dimensional density of states of the field. 144

Chapter 1

Introduction

The ways in which quantum theory can tell us about nature have been the subject of long periods of debate throughout its history since its foundation, a century ago [1, 2, 3]. Some of the very same issues that revealed most of the 'difficulties' [4, 5] of this theory have come to be of great practical use for technological purposes in the emerging field of quantum information processing (QIP) [6]. In 1935, Einstein, Podolsky, and Rosen (EPR) [4], and Schrödinger [5] pointed out that one such aspect of quantum theory is the phenomenon of *entanglement*. By means of predictions associated with an entangled (EPR-pair) state, EPR argued that quantum mechanics is an 'incomplete' physical theory because of the violation of "local realism," a description of the world where the physical properties of spatially separated subsystems of a composite system are characterised by an 'independent' and 'objective reality.' This was the subject of many fundamental discussions concerning the basic structure of quantum theory. This conflict had to wait for almost 30 years for its resolution, when Bell reported, in his celebrated 1964 paper [7], that this local realism leads to constraints on the predictions of spin correlations (Bell's inequalities), which can be *violated* by quantum theory for a system in the singlet (Bell) state $|\uparrow\rangle|\downarrow\rangle - |\downarrow\rangle|\uparrow\rangle$, being $|\uparrow\rangle$ ($|\downarrow\rangle$) a particle's spin "up" ("down") state along a given axis [2]. After this breakthrough, several experiments [8, 9] were performed in support of Bell's findings. This feature—*nonlocality*—reveals quantum entanglement at its best, an outstanding phenomenon of quantum physics. As we shall see below, quantum entanglement has led to several important practical applications for QIP, where it has been recognised as a valuable resource for communication at both classical and quantum levels.

After these theoretical developments, there was a further long period until we arrived to the point which settled the foundations of the field of quantum information processing. It was realised that quantum mechanical principles are not just exotic theoretical statements but fundamental for a new technology of practical information processing [6]. This is based on the ideas of Feynman [10] and Benioff [11] presented in 1982, and a few years later, in 1985, by Deutsch [12]. These findings have developed in concrete practical applications: quantum computation [6, 10, 11, 12], quantum cryptography [13], quantum teleportation [14], quantum dense coding [15], and quantum games [16, 17, 18], all of which represent exciting new arenas in which to exploit such intrinsic quantum mechanical correlations.

The discovery of algorithms for which a computer based on the principles of quantum mechanics [19, 20, 21, 22] should beat any modern digital computer has triggered intense research into realistic controllable quantum systems. Since the seminal idea of Feynman [10] and Benioff [11] in 1982, and the work of Deutsch in 1985 [12], both pure and applied research in the field of quantum information processing has blossomed. In 1994, Shor [21, 23, 24] opened the way to new fast quantum searching algorithms: he discovered that a quantum computer can factorize large integers. Two years later the proof that quantum error-correcting codes exist arrived [25, 26]. The main areas of research in this active field include ion traps [27, 28, 29], quantum electrodynamics cavities [30, 31, 32, 33, 34, 35], nuclear magnetic resonance [36, 37, 38, 39, 40, 41], optical lattices and Bose-Einstein condensation [42, 43, 44], Josephson junctions [45, 46, 47, 48], and quantum dots [49, 51, JHR1, 53, JHR2, 54, 55]. All of the above proposals have decoherence and operational errors as the main obstacles for their experimental realisation: these, as we shall see throughout this thesis, pose much stronger problems here than in conventional digital computers.

The main challenge we face in order to process information at a quantum level is to identify a physical system with an appropriate internal dynamic and corresponding external driving forces, which enables one to selectively manipulate quantum superpositions and entanglements. A fundamental requirement for the experimental realisation of such proposals is the successful generation of highly entangled quantum states. In particular, coherent evolution of two quantum bits (qubits) in an entangled state of the Bell type [7, 8] is relevant to both quantum cryptography and quantum teleportation. Maximally entangled states of three qubits, such as the so-called GHZ states [56], are not only of intrinsic interest but are also of great practical importance in such proposals. In this thesis, a novel approach for the generation of such n-qubit maximally entangled states is given.

Besides the capability to control and manipulate entanglement, a high level of isolation from the environment is required to reach a full unitary evolution. Quantum information processing will be a reality when optimal control of quantum coherence in noisy environments can be achieved. The various communities typically rely on different hardware methodologies. It is therefore extremely important to clarify the underlying physics and limits for each type of physical realisation of QIP systems.

Following this line of reasoning, this thesis presents several practical schemes for performing quantum information processing by using quantum dots [57, 58, 59], and gives a detailed analysis of the way in which decoherence may affect such processes. In Section 2.2.4 an outline of the main QIP solid-state proposals to date is provided. Next, the work presented in this thesis is outlined.

Chapter 2 is divided into two main parts. The first one, Section 2.1, is devoted to a short review of the field of quantum information and quantum computation. This aims to provide a unifying framework upon which the bulk of the results presented in this thesis can be fully understood from a QIP perspective. This starts with the basic definitions of bits, quantum registers, through to the universal gate (or set of gates) for building the universal quantum computer, from a quantum network model of computation. It is shown how two-qubit gates suffice for quantum computation and the power of the quantum circuit representation for *entangling* and *disentangling* quantum states is emphasised. This leads to the "no-cloning theorem," which leads us to many interesting applications, such as quantum cryptography. Also briefly reviewed is the recently formulated and alternative approach to performing quantum computation by using only geometric means: holonomic or geometric quantum computation. Following this, quantum entanglement is highlighted, particularly its usefulness as a communication resource, in order to describe some of its most celebrated practical applications to date: quantum teleportation, quantum cryptography, dense coding, and quantum data compression. Deutsch's concept of quantum parallelism is emphasized in order to gain insight into the potential for efficiently solving certain classically intractable algorithms. After this, a subject central to the field of QIP is introduced: the decoherence phenomenon. Possible ways to overcome it, in particular quantum error correction, are discussed. Section 2.1 ends by providing a description of the currently available hardware for the practical implementation of quantum computation: in particular, a discussion of the main physical quantum bits currently employed (or proposed) for such a purpose is given.

In contrast, in the second part of this chapter, Section 2.2, the practical side of QIP is discussed, in particular, the state-of-the-art experimental advances of quantum dot technology, which is the main domain for the practical nanostructure schemes proposed in this thesis. This is done by briefly presenting a framework of concepts behind nanometer-scale structures such as quantum wells, quantum wires, and quantum dots. In so doing, the necessary experimental techniques are introduced, such as far- and near-field optical spectroscopy, and coherent optical ultrafast spectroscopy. This allows a presentation of an important subject referred to as the "engineering of quantum wave functions." Here, eigenstates (or the state vectors) of a given quantum dot system can be addressed and manipulated *individually* at will [60, 61, 62]. This 'experimental breakthrough' is the main motivation for the proposals presented in Chapters 3 and 4 of this thesis. The background to Chapter 5 is given in Section 2.2.3, where the properties of an interacting (QD) system and Kohn's theorem are discussed. Section 2.2 is closed by reviewing the advantages of modern quantum technology and their relevance to QIP: the most representive solid-state qubit proposals for quantum computing to date are summarised. To summarise, Chapter 2 aims to give a tour through quantum information theory to quantum technology in order to establish a connection between the two and to introduce the necessary background to follow this thesis.

Chapter 3 gives a detailed prescription for producing an *all optical* generation and control of exciton[1] maximally entangled states in coupled QDs by using a state-of-the-art semiconductor setup [JHR1, 53]. Starting from suitably initialized states, it is shown that this optically-driven coupled QD system leads to reliable generation of highly entangled

---

[1] Excitons are electronic excitations which play a fundamental role in the optical properties of dielectric solids. They correspond to a bound state of one electron and one hole which can be created by light or can appear as a result of relaxation processes of free electrons and holes.

states of two and three quantum dots. In the physical implementation of the quantum entanglement scheme proposed here, recent experimental results involving coherent optical control of excitons in single quantum dots on the nanometer and femtosecond scales [60, 61, 62, 63, 64] are exploited. The amazing degree of control of the quantum states of these individual "artificial atoms" [61], due to the manipulation of the confined state wave function of a single dot, is an exciting and promising development. As one exciton can be trapped in the dot, this gives the direct possibility of using QDs as elements with quantum memory capacity in quantum computation operations, through a precise and controlled excitation of the system. As demonstrated in [61], it is possible to excite and probe *only* one individual QD within a broad distribution of dots, with the important result that the dephasing time is much longer in a single dot (a few tens of picoseconds) than in the bulk semiconductors ($<$ 1 ps) studied before. Hence, new experimental work means that much longer intrinsic coherence times are currently available, a fact of fundamental importance when looking towards the practical implementation of universal quantum logic gates (see Chapter 2) for quantum computation.

The development of quantum information theory has shown that quantum entanglement brings important *practical* applications. In 1993, Bennett and co-workers [14] demonstrated that quantum entanglement can indeed be used as a *resource* for the communication of quantum states via a celebrated process that they termed quantum teleportation. Here, an arbitrary unknown quantum state can be transmitted by using a pair of particles in a highly entangled state which is shared beforehand by the two communicating parties (sender and receiver). The protocol invokes the additional transmission of two classical bits of information and a final measurement in order to perform the process. This idea is explored further in Chapter 4 where it is shown that exciton maximally-entangled states can be used as the above-mentioned quantum resource and can hence provide a true solid-state teleportation protocol [JHR2]. This set-up exploits recent advances in the optical control of excitons in coupled quantum dots in order to teleport an excitonic state from one dot to another. It is shown that only two unitary transformations are needed to perform this process: a quantum controlled-NOT (CNOT) gate and a Hadamard gate (see Chapter 2 for definitions). The explicit laser pulses necessary to generate the source of entangled states are given, along with the corresponding quantum logic gates employed in the process. It is shown in Chapter 6 that the role of phonons, at low temperatures, does not necessarily amount to the loss of control over the exciton system due to destruction of coherence while performing the required unitary transformations.

In contrast to the above ultrafast coherent optical proposal for entanglement generation, Chapter 5 proposes a setup for the implementation of a solid-state NMR-based quantum switch for quantum logic, where typical decoherence times are in the miliseconds time scale [JHR3]. Here, the so-called "magic-number" (ground state) transitions in few-electron QDs containing a nuclear spin impurity can be used to implement single and two-qubit unitary transformations for conditional quantum dynamics. The basic setup consists of a nuclear spin-$\frac{1}{2}$ impurity placed at the centre of a 2 electrons QD in the presence of an external perpendicular magnetic field B. In such a system, the nuclear magnetic resonance is controlled by the ground state transitions that arise as the B-field is changed: it is shown that the hyperfine coupling between the electrons and the nucleus can be changed and hence provide a mechanism for tuning the nuclear resonance frequency. It is also shown that this nuclear qubit control can be accomplished by exciting the QD with infra-red (IR) radiation. This is because the electrons centre-of-mass (CM) motion absorbs IR radiation, hence affecting its associated CM wavefunction which in turns allows for externally controlling the nucleus-electron effective coupling (the electrons relative motion remains unaffected in accordance with Kohn's theorem). Decoherence effects in systems of spin $\frac{1}{2}$ nuclei are expected to be minimal as nuclear spins are weakly coupled to their environment. Therefore, such spin systems are natural qubits for quantum information processing since they offer both long decoherence and long relaxation times.

In Chapter 6, the dynamical evolution of a quantum register of arbitrary length coupled to an environment of arbitrary coherence length is predicted within a general model of decoherence [JHR5]. The situations of quantum bits (qubits) coupling individually to different environments ("independent decoherence") and qubits interacting collectively with the same reservoir ("collective decoherence") are studied. In both cases, explicit decoherence functions are derived for any number of qubits. It is found that the decay of the coherences of the register strongly depend on the input states: it is shown that this sensitivity is a characteristic of *both* types of coupling (collective and independent) and not only of the collective coupling, as has been reported previously. A non-trivial behaviour—"recoherence"—is found in the decay of the off-diagonal elements of the reduced density matrix in the specific situation of independent decoherence. The results lead to the identification of decoherence-free states in the collective decoherence limit. These states belong to subspaces of the system's Hilbert space that do not get entangled with the environment, making them ideal elements for the engineering of "noiseless" quantum codes. The relations between decoherence of the quantum register and computational complexity are also discussed, based on the new dynamical results obtained for the register density matrix. In the last section of this chapter [JHR4], the above formalism is applied in order to analyse the effects of decoherence on the optical generation of the exciton maximally entangled states reported in Chapter 3.

In Appendix A, the exciton coherent dynamics of an optically driven coupled quantum dot system confined within a semiconductor microcavity [JHR6] is reported. It is shown that coupling of this QD system to a single mode microcavity enables the control of exciton entanglement by varying the coupling strength between the dot system and the microcavity. The exciton entanglement shows collapses and revivals for suitable amplitudes of incident radiation field and dot-cavity coupling strengths. The results given here can be viewed as an alternative approach for the control of decoherence mechanisms arising from entangled artificial molecules.

Concluding remarks and future directions are given in Chapter 7. In particular, the possibility of exploiting highly efficient and ultrafast biological processes exhibited by some molecules due to Förster's resonant energy transfer (FRET) [69, 70, 71, 72, 74] and Dexter [73] processes in order to perform information processing tasks at a quantum level are considered.

Chapter 2

Background material: From quantum information to quantum technology

This Chapter aims to give a basic review of the main results concerning the processing of information at a quantum level and also to present the background to the theoretical models of the physical realisations proposed in this thesis. It is not intended to provide a historical review of the development of classical information theory and computer science, and the way they were linked to fundamental aspects of quantum physics to give birth to the field of quantum information theory. Instead, the background and the necessary concepts of quantum computing and quantum information are presented to further establish the link with the solid-state implementations presented in this thesis.

2.1 Fundamentals of quantum information and quantum computing

For the purpose of the QD-based implementations proposed in this thesis, the network model of computation is adopted. Here one can imagine a quantum computer (QC) as a physical device that takes an initial state (input) into some final state (output) via a set of quantum networks that evolves in a unitary fashion. Next, the methods to build such networks are presented.

2.1.1 From binary digits to universal quantum computation

Bits and quantum registers: A binary digit, or *bit*, is the basic unit of information in classical communication and information theory. This has only two possible states: 0 and 1 in the binary system generally used in digital computers (in a proper electromechanical device, this basis can be represented by an "on-off," or "open-closed," or "go-no go" states). The relevance of this base–2 representation to computer technology arises from the reliable compact manner in which data can be digitally stored. For example, the year 2002 (decimal system) can be written in binary system as 11111010010. At first glance, this number appears to be more compact in base–10 than in its binary equivalent; however, a physical representation of a four digit number in base 10 requires 10^4 states, while its binary representation 'only' requires $2^{11} = 2048$ states: it is clear that the binary system appears to be the most convenient one for the storage and processing of the information. Therefore, we shall hereafter assume that information is stored in registers in a binary form[1].

In contrast to the binary digit, or classical bit, the elementary unit for the processing of quantum information is the quantum bit or *qubit*, a term coined by Schumacher [81]. In this case the Boolean states 0 and 1 are represented by a pair of normalised and orthogonal quantum states labelled as $\{|0\rangle, |1\rangle\}$ [81]. These states form a 'computational basis', that we shall name the $\mathcal{B}_1$-basis, so that any other state of the qubit can be written as a linear superposition $\alpha|0\rangle + \beta|1\rangle$, with $|\alpha|^2 + |\beta|^2 = 1$, $\alpha, \beta \in \mathbf{C}$. Typical examples of qubits are nuclei with spin 1/2, two-level atoms, polarised photons, etc.

A *quantum register* (QR) of size n, is a quantum system of n qubits with a 2^n dimensional Hilbert space, and hence with 2^n mutually orthogonal quantum states available, which can be written compactly as $\{|j\rangle\}$, where j is an n-bit binary number ($j = 2^{n-1}j_{n-1} + 2^{n-2}j_{n-2} + \cdots + 2^1 j_1 + 2^0 j_0$, $j_m \in \{0, 1\}$), and $|j\rangle$ denotes the tensor product $|j_{n-1}\rangle \otimes |j_{n-2}\rangle \cdots |j_1\rangle \otimes |j_0\rangle$, or $|j_{n-1}j_{n-2}\cdots j_1 j_0\rangle$ for short. Though a qubit is a prescribed two-state system, it is fundamentally different from a classical bit. A given quantum physical system that serves for the storage, processing, and readout of a computational process by using a qubit has to deal with a microscopic system that is to be "switched *on* or *off*" by appropriately manipulating its interaction with an external driving source, bearing in mind its interaction with the other qubits of the system and also with the surrounding environment. This has an additional ingredient: the dynamics of a qubit is ruled by the principles of quantum physics. This means that while a binary string of n classical bits can store *only* one number at a given time, say

$$\underbrace{1}_{j_{n-1}}\underbrace{0}_{j_{n-2}}\underbrace{0}_{j_{n-3}}\cdots\underbrace{0}_{j_1}\underbrace{0}_{j_0}\,, \tag{2.1}$$

an n-quantum register can store a superposition of all of the 2^n mutually orthogonal quantum states $\{|j\rangle\}$ simultaneously: this is the computational power of quantum interference, which led to the so-called quantum parallelism (see below). To see this, we need to prepare the register in such a way that each qubit is in the superposition state $(|0\rangle + |1\rangle)/\sqrt{2}$. Hence we are left with a quantum register in the state

$$\frac{1}{\sqrt{2}}(|0\rangle + |1\rangle)_{j_{n-1}} \otimes \frac{1}{\sqrt{2}}(|0\rangle + |1\rangle)_{j_{n-2}} \otimes \cdots \otimes \frac{1}{\sqrt{2}}(|0\rangle + |1\rangle)_{j_0}\,, \tag{2.2}$$

---

[1] A binary string can be represented in any base b as: $c_n b^n + c_{n-1}b^{n-1} + \cdots + c_1 b^1 + c_0 b^0$, where c_i are 'place-value' coefficients. Usually, the number representing this expansion is written as $c_n c_{n-1} \cdots c_2 c_1 c_0$ (base b). For example, in the decimal system, the number 2002 is the compact way of writing $2 \times 10^3 + 0 \times 10^2 + 0 \times 10^1 + 2 \times 10^0$. Its binary equivalent is 11111010010, i.e., $1 \times 2^{10} + 1 \times 2^9 + 1 \times 2^8 + 1 \times 2^7 + 1 \times 2^6 + 0 \times 2^5 + 1 \times 2^4 + 0 \times 2^3 + 0 \times 2^2 + 1 \times 2^1 + 0 \times 2^0$, while for the Mayans (vigesimal number system) this should read 502.

which in binary notation is the sum of 2^n quantum states $|j\rangle$

$$\sum_{j\in\{0,1\}^n} |j\rangle = |00\cdots 00\rangle + |00\cdots 01\rangle + |00\cdots 10\rangle + \cdots + |100\cdots 00\rangle + \cdots + |11\cdots 10\rangle + |11\cdots 11\rangle \,, \tag{2.3}$$

where the normalisation factor $2^{-n/2}$ has been omitted. Eq. (2.3) can be written in base-10 as

$$\frac{1}{\sqrt{2^n}}\Big\{ |0\rangle + |1\rangle + |2\rangle + |3\rangle + \cdots + \overbrace{|2^{n-1}\rangle} + \cdots + |2^n - 1\rangle \Big\} \equiv \frac{1}{\sqrt{2^n}} \sum_{m=0}^{2^n-1} |m\rangle \ , \tag{2.4}$$

where the overbraced state is the quantum representation (in decimal notation) of the binary string represented by Eq. (2.1). Hence, it is clear that due to the quantum superposition principle, a quantum computer can, in principle, be prepared in a superposition of (and as we shall see below, can process) 2^n states in a given n-QR at once. Here, there is an important issue to be highlighted: a qubit is an extremely fragile physical system and its reliability to store and process information at will is going to be limited by the interactions that it might have with the environment that surrounds it—the problem of noise at a quantum level. This QR-environment coupling, known as *decoherence*, produces an undesirable effect over the register: it makes superpositions such as $|0\rangle + |1\rangle$ lose their phase, and therefore their ability to interfere reliably, which results in the destruction of the quantum computation. This can also be viewed as a loss of the unitarity of the quantum evolution of the QR, an essential requirement for quantum computation to occur. This fundamental point shall be returned to later: Chapter 6 is devoted to the study of the way in which quantum registers decohere and some possible ways to overcome it.

Quantum logic and the universal quantum computer: Building blocks of a quantum computer are now introduced. As in the case of the processing of classical information in digital computers, logic gates and networks for the processing of quantum information [83] are introduced. A *quantum logic gate* is a device that performs a prescribed unitary operation on selected qubits in a definite time t and a *quantum network* is a device built of quantum logic gates whose computational steps are synchronised in time [83]. Such quantum networks are to be represented by a circuit notation that accounts for the action of the logic gates. Here, a qubit is represented by a horizontal line—"wire"— that evolves in time from left to right, and single and two qubit gates are represented respectively by a prescribed symbol on one wire, and by symbols on two wires connected by a vertical line. The qubit associated with the filled dot is usually called the "control" (or source), and the other one is called the "target." An example is shown in the following network of *size* 4 (Fig. 2.1):

It turns out that *any* possible unitary transformation to be performed by a quantum computer can be simulated by an appropriate combination of the set of quantum logic gates shown in Fig. 2.1, i.e., by performing arbitrary single qubit rotations and 2-qubit XOR (or U) gates. Thus, the sets of gates $\{P(\varphi), H, \text{XOR}\}$, and $\{P(\varphi), H, U\}$ are universal for quantum computation: *all logic gates* to be performed on a given quantum register

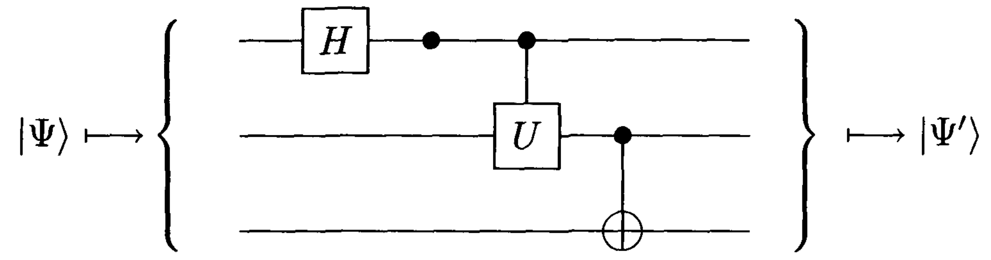

Figure 2.1: A quantum network containing 4 gates. From left to right, the QR state $|\Psi\rangle$ experiences the action of the following quantum logic gates: i) Hadamard (H), ii) phase shift $[P(\varphi)]$, iii) Controlled-U (U), and iv) controlled-NOT (CNOT or XOR). The network produces the final state "output" $|\Psi'\rangle \equiv XOR_{23}U_{12}P(\varphi)_1H_1\,|\Psi\rangle$. In this operational notation, the subscripts denote the qubits to be addressed, and in any 2-qubit gate U_{ij}, i, and j denote the control and target bits respectively. Note that the first two unitary transformations are single qubit gates while the remaining ones are two qubit gates.

can be constructed by composing the gates of either of these sets. These are the so-called *universal quantum logic gates* [83, 84, 85, 86, 87]. A quantum system capable of realising and manipulating at will a given set of universal quantum gates is said to perform *universal quantum computation.* Such a machine is the so-called universal quantum computer, a concept first introduced by Deutsch in 1985 [12, 84].

The main result to be emphasized here is that *2-qubit gates are sufficient for quantum computation.* As can be imagined, there are many combinations of gates that can be built to perform elementary 'quantum arithmetical operations' such as binary addition and multiplication. However, it is not the purpose of this section to describe in detail such quantum networks. Many basic constructions can be found in Refs. [88, 89]. We are now ready to define the building blocks from which one can assemble a circuit that can evaluate any *arbitrary* Boolean function:

1. The *phase-shift gate* $P(\varphi)$ is a single qubit gate that performs the unitary operation $P(\varphi)(|m\rangle) \mapsto e^{im\varphi}\,|m\rangle$, where $m \in \{0,1\}$, or $P(\varphi) \equiv |0\rangle\langle 0| + e^{i\varphi}\,|1\rangle\langle 1|$.

2. The *Hadamard gate* H is also a single qubit gate that performs the unitary operation known as the Hadamard transform $H(|m\rangle) \mapsto \frac{1}{\sqrt{2}}[(-1)^m\,|m\rangle + |1-m\rangle]$, or $H \equiv \frac{1}{\sqrt{2}}[(|0\rangle + |1\rangle)\langle 0| + (|0\rangle - |1\rangle)\langle 1|]$. These gates are schematically represented in the language of quantum circuits as shown in Fig. 2.1. It is easy to show that by combining the set of transformations $\{P(\varphi), H\}$, any single qubit rotation can be generated. Hence, the Hadamard and the phase shift gates suffice to perform any unitary transformation on a single qubit.[2] Other relevant single qubit gates are the identity $I \equiv |0\rangle\langle 0| + |1\rangle\langle 1|$; the quantum NOT gate, which in analogy with

---

[2] To see this, compose the network $P(\varphi+\pi/2)\,H\,P(2\theta)\,H\,|m\rangle$, $m \in \{0,1\}$. This gives the most general rotation of a single qubit:

$$V(\theta,\varphi) \equiv e^{i\theta}\begin{pmatrix} \cos\theta & e^{i\varphi}\sin\theta \\ \sin\theta & e^{i\varphi}\cos\theta \end{pmatrix}. \tag{2.5}$$

the classical NOT gate transforms $|0\rangle$ to $|1\rangle$ and vice versa: NOT $\equiv |0\rangle\langle 1| + |1\rangle\langle 0|$; and the V-gate $V \equiv P(\pi/2)$.

3. The *controlled-U* gate is a two-qubit gate that performs the operation $|0\rangle\langle 0| \otimes I + |1\rangle\langle 1| \otimes U$, where U is some prescribed single-qubit unitary transformation. This gate leaves the target qubit unchanged or applies the U gate depending on whether the control qubit is $|0\rangle$ or $|1\rangle$: $|0\rangle|m\rangle \mapsto |0\rangle(I|m\rangle)$, and $|1\rangle|m\rangle \mapsto |1\rangle(U|m\rangle)$. The network representation corresponding to this gate is shown in Fig. 2.1. This 2-qubit gate comprises a general family of quantum gates, each of them, together with $P(\varphi)$, and H, being universal for quantum computation.

4. The *controlled*-NOT (CNOT or XOR) gate is an important example of a U gate[3]: it flips the target bit if the control bit is in the state $|1\rangle$ and acts trivially otherwise. This action can be formally written as: CNOT$(|j\rangle|m\rangle) \mapsto |j\rangle|j \oplus m\rangle$, where $j, m \in \{0, 1\}$, and $\oplus$ denotes addition modulo 2 or XOR operation. This is why the symbol $\oplus$ is schematically used to represent such a gate, as seen in Fig. 2.1.

The CNOT gate is usually termed as a *measurement gate* due to the fact that it maps $|m\rangle_1|0\rangle_2 \mapsto |m\rangle_1|m\rangle_2$, i.e., if the purpose is to measure the final state of 'qubit 1,' then a measurement of the output state of 'qubit 2' reveals the answer. The advantage of this procedure over a direct measurement of qubit 1 is that it is a "non-demolition" measurement: the original quantum state of qubit 1 remains the same after the measurement. However, this is only valid if the qubit 1 is originally in one of the two states of the computational basis $\mathcal{B}_1 \equiv \{|0\rangle, |1\rangle\}$: if $|m\rangle_1$ is initially in a superposition of the states of this basis, then the state is "collapsed" by the measurement. This is because it is impossible to build a universal quantum "cloning machine" $|\Psi\rangle|0\rangle \mapsto |\Psi\rangle|\Psi\rangle$, with $|\Psi\rangle$ being the arbitrary superposition state $|\Psi\rangle = \alpha|0\rangle + \beta|1\rangle$, $\alpha, \beta \neq 0$ (this important result is known as the *no-cloning theorem*[4]) [90]. In fact, if we 'run' the CNOT$_{12}$ gate over the initial state $|\Psi\rangle_1|0\rangle_2$, we transform $(\alpha|0\rangle + \beta|1\rangle)|0\rangle \mapsto \alpha|00\rangle + \beta|11\rangle$. This output state is known as an *entangled state* because it cannot be written as a direct product of quantum states

---

[3] Another common two-qubit gate is the controlled phase shift gate $B(\varphi)$, which performs the unitary transformation: $|m\rangle|n\rangle \mapsto e^{imn\varphi}|m\rangle|n\rangle$, $m, n \in \mathcal{B}_1$. In the language of networks, this gate is represented as

$|\Psi\rangle_{1,2} \mapsto \{$ 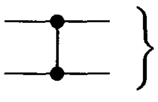 $\} \mapsto |\Psi'\rangle_{1,2}$.

[4] This result leads to interesting applications such as quantum cryptography (see Subs. 2.1.3). To prove the "no-cloning theorem" it suffices to note that, in order to generate a copy of an arbitrary quantum state $|\Psi\rangle$, we should be able to realise a unitary transformation U that produces the evolution $U(|\Psi\rangle|0\rangle) = |\Psi\rangle|\Psi\rangle$. Consider the state $|\Psi'\rangle$ such that $|\Psi'\rangle \neq |\Psi\rangle$. Hence, $U(|\Psi'\rangle|0\rangle) = |\Psi'\rangle|\Psi'\rangle$. Next, we make $|\Phi\rangle = (|\Psi\rangle + |\Psi'\rangle)/\sqrt{2}$, obtaining $U(|\Phi\rangle|0\rangle) = (|\Psi\rangle|\Psi\rangle + |\Psi'\rangle|\Psi'\rangle)/\sqrt{2} \neq |\Phi\rangle|\Phi\rangle$, which fails the cloning operation since U must not depend on any chosen $|\Phi\rangle$ [90]. From this we can state that unless we know beforehand the state of a qubit (which is to be represented by classical information), it is impossible to generate copies of a quantum state faithfully.

for the two qubit register, i.e., $\alpha\,|00\rangle + \beta\,|11\rangle \neq |\Psi_1\rangle \otimes |\Psi_2\rangle$. Hence, a measurement of the output of qubit 2 should collapse the state of qubit 1. This is to be contrasted with the case of single qubit gates, where the input and the output of a general n-QR can always be expressed as a *product* or *separable state* $|\Psi_1\rangle \otimes |\Psi_2\rangle \otimes \cdots \otimes |\Psi_n\rangle$, for arbitrary superpositions $|\Psi_i\rangle$.

The fact that the CNOT gate takes superpositions of the control qubit into entanglement of the corresponding output qubits is an outstanding property. In addition to this, the CNOT gate is a *reversible* gate: from its output we can reconstruct its input. It suffices to repeat the same gate, i.e., $\text{CNOT}_{1,2}(\text{CNOT}_{1,2}(|\Psi_1\rangle\,|\Psi_2\rangle)) \equiv |\Psi_1\rangle\,|\Psi_2\rangle$. Thus, the CNOT can be used to perform *reversible computation.* As we shall see below, *quantum entanglement* is at the very heart of any quantum computational process and also a fundamental ingredient of most of the 'spooky' technological applications that quantum information brings as a byproduct. This is why the subject of quantum entanglement is further explored in this thesis, particularly looking at physical implementations in the solid state.

For illustrative purposes, let us go back to the network presented in Fig. 2.1. By making $U \equiv \text{CNOT}$, we are left with the *entangling* quantum network $\widehat{N}_{\text{GHZ}} \equiv \text{CNOT}_{23}\text{CNOT}_{12}$ $P(\varphi)_1 H_1$, which in the most elementary case performs the transformation

$$\widehat{N}_{\text{GHZ}}(|\Psi\rangle \equiv |000\rangle) \longmapsto |\Psi'\rangle \equiv \tfrac{1}{\sqrt{2}}(|000\rangle + \mathrm{e}^{i\varphi}\,|111\rangle)\ , \tag{2.6}$$

thus producing a highly entangled state of three qubits known as the *maximally* entangled Greenberger-Horne-Zeilinger state [56]. In Fig. 2.1, the action of the first single qubit gates H, and $P(\varphi)$ is to rotate and to 'phase-shift' the state $|0\rangle_1$ into $\frac{1}{\sqrt{2}}(|0\rangle_1 + \mathrm{e}^{i\varphi}\,|1\rangle_1)$ while the other qubits remain unaffected. As expected at this stage, the 3-QR state is still a separable state. Next, we enter the CNOT_{12} gate. Since its control qubit is in a superposition state, it is clear that this gate will entangle the qubits 1 and 2 of the register. Indeed, after this XOR gate operation we are left with the state $\frac{1}{\sqrt{2}}(|00\rangle + \mathrm{e}^{i\varphi}\,|11\rangle) \otimes |0\rangle$, the product state of the maximally entangled (Bell or EPR) state of two qubits $|\Psi_{\text{BELL}}\rangle$ [7, 4], and the qubit state $|0\rangle$. The last action of the network leaves the quantum register in the output GHZ state $|\Psi_{\text{GHZ}}\rangle \equiv |\Psi'\rangle$ of Eq. (2.6). The subject of quantum entanglement and the issue of how to quantify the degree of entanglement of a given entangled state is addressed in the Subsection 2.1.3.

In the physical implementations to be described in some of the subsequent chapters of this thesis, the universal set of gates $\{P(\varphi), H, \text{CNOT}\}$ shall be referred to. The logic gates $P(\varphi)$, and H, can be written in the $\mathcal{B}_1$-basis, and the CNOT gate in the computational basis of two-qubits $\mathcal{B}_2 \equiv \{|00\rangle\,, |01\rangle\,, |10\rangle\,, |11\rangle\}$ as follows:

$$P(\varphi) \equiv \begin{pmatrix} 1 & 0 \\ 0 & \mathrm{e}^{i\varphi} \end{pmatrix}, \quad H \equiv \tfrac{1}{\sqrt{2}} \begin{pmatrix} 1 & 1 \\ 1 & -1 \end{pmatrix}, \quad \text{CNOT} \equiv \begin{pmatrix} 1 & 0 & 0 & 0 \\ 0 & 1 & 0 & 0 \\ 0 & 0 & 0 & 1 \\ 0 & 0 & 1 & 0 \end{pmatrix}. \tag{2.7}$$

Another fundamental logic gate, whose classical version is universal for *reversible computation*, is the "*controlled-controlled*-NOT" (c^2-NOT) gate or Toffoli gate [91]; a 3-qubit gate that maps $|a\rangle\,|b\rangle\,|c\rangle \mapsto |a\rangle\,|b\rangle\,|c \oplus (a \wedge b)\rangle$. Hence, the third qubit experiences a flip or a NOT operation if and only if the control qubits $|a\rangle$, and $|b\rangle$ are in the state $|1\rangle$. By contrast, if the third qubit is prepared in the state $|0\rangle$ then this gate computes the AND of the first two qubits: $|a\rangle\,|b\rangle\,|0\rangle \mapsto |a\rangle\,|b\rangle\,|a \wedge b\rangle$. In addition, if we prepare $|a\rangle = |1\rangle$, then the c^2-NOT gate becomes a CNOT gate with $|b\rangle$, and $|c\rangle$ as inputs. This means that the Toffoli gate is capable of generating operations such as NOT, AND, and CNOT in such a way that all the information about the input is 'preserved'[5]. Thus, the Toffoli gate provides us with a complete operator set: any gate can be generated with just a c^2-NOT gate, thus giving the logical connectives for performing quantum arithmetic and the evaluation of functions in general.

Quantum parallelism: The fact that a quantum system is capable of performing a computation was first pointed out by Feynman [10] and Benioff [11] in 1982. However, it was Deutsch [12], in 1985, who made this idea more concrete by establishing that a quantum computer can perform the best of its computational potential by realising a process that he termed "quantum parallelism." By doing this, it is easy to see that a quantum computer can perform certain computational tasks much faster than any classical digital computer. This observation turns out to be the first quantum algorithm, known as the Deutsch-Josza algorithm [19], where physical principles such as quantum interference and quantum entanglement were made evident as a powerful computational resource.

To see why this is so, suppose we are given a device "*oracle*" that computes the Boolean function $f\,:\; x \in \{0,1\} \mapsto f(x) \in \{0,1\}$ in a single step. The problem is to determine whether $f(x)$ is *constant* (i.e., $f(0) = f(1)$), or *balanced* ($f(0) \neq f(1)$), with the minimum possible number of queries. It is clear that any attempt at solving this by using classical means invokes the oracle twice. In contrast, we note that with the help of a quantum strategy, a "quantum oracle $\mathcal{U}_f$" that performs the unitary transformation $\mathcal{U}_f\,:\; |x\rangle\,|y\rangle \longrightarrow |x\rangle\,|y \oplus f(x)\rangle$ in a single step, this problem is easily solved with only one query. Here $x, y \in \mathcal{B}_1$. Imagine a two wire network that is given with the input $|\Psi_0\rangle = |0\rangle\,(|0\rangle - |1\rangle)/\sqrt{2}$. The following algorithm shows how to solve this (Deutsch's)

---

[5] The Toffoli gate is schematically represented as

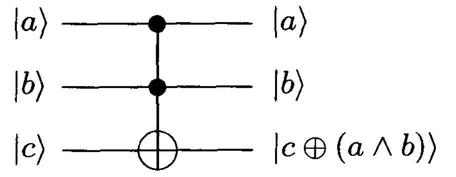

where the filled dots indicate the control qubits while the target qubit, denoted by $\oplus$, is negated if and only if the control bits are in the state $|1\rangle\,|1\rangle$. The action of this gate can be written operationally as c^2-NOT$_{ijk}$, where i, j (k) stand for the control (target) qubits. The Toffoli gate can be built from the controlled-V (C-V), CNOT, and Hadamard gates as follows: $c^2\text{-NOT}_{123} \equiv H_3 V_{13} \text{CNOT}_{12} V^{\dagger}_{23} \text{CNOT}_{12} V_{23} H_3$, where C-$V^{\dagger} \equiv$ C-V^{-1}. Similarly, the CNOT gate can be constructed by applying a simple network of H, and C-V gates as follows: $\text{CNOT}_{12} \equiv H_2 V_{12} V_{12} H_2$. There are, of course, plenty of quantum networks that can be built to represent the above-mentioned gates, but there is a main concern when building such networks: it is desirable and almost necessary to minimise the number of gates required to perform a given quantum computational task.

problem efficiently:

1. Apply the Hadamard transform to the first qubit:
$$H : |\Psi_0\rangle \to |\Psi_1\rangle\,, \quad |\Psi_1\rangle \equiv \tfrac{1}{2}(|0\rangle + |1\rangle)(|0\rangle - |1\rangle)\,. \tag{2.8}$$
2. Send the 2-qubit state $|\Psi_1\rangle$ through the quantum oracle. This gives you the result
$$\mathcal{U}_f : |\Psi_1\rangle \to \tfrac{1}{2}[(-1)^{f(0)}\,|0\rangle + (-1)^{f(1)}\,|1\rangle](|0\rangle - |1\rangle) \equiv |\Psi_2\rangle\,. \tag{2.9}$$
Note that the generic action of this function evaluator $\mathcal{U}_f$ over a state of the type $|x\rangle\,(|0\rangle - |1\rangle)$ gives the output $(-1)^{f(x)}\,|x\rangle\,(|0\rangle - |1\rangle)$.
3. Apply H to the first qubit of $|\Psi_2\rangle$. Then perform a measurement in the $\mathcal{B}_1$-basis of qubit 1 final output. The result of this measurement reveals the answer to our problem.

Note that the state of qubit 1 in Eq. (2.9) can be written as

$$(-1)^{f(0)}\,|0\rangle + (-1)^{f(1)}\,|1\rangle = \begin{cases} \pm(|0\rangle + |1\rangle) & \text{if } f \text{ is constant} \\ \pm(|0\rangle - |1\rangle) & \text{if } f \text{ is balanced}\,. \end{cases} \tag{2.10}$$

Hence, after step 3 of this protocol, we shall always find qubit 1 in the state $|0\rangle$ if the function is constant and $|1\rangle$ is the function is balanced. Also note that qubit 2 remains in the same state throughout this protocol. Thus, by using quantum superpositions instead of classical evaluations, we have solved this problem with just one query (throughout the whole process we have assumed a coherent evolution of the qubit states). The power of quantum parallelism becomes even more evident when we try to solve the same problem but for large registers, i.e., when $x \in \{0,1\}^n$. This will be discussed later in Sec. 2.1.4. Thus, Deutsch pointed out one of the most outstanding properties of a quantum computer and paved the way for the development of the field of quantum information processing.

So far, we have been concerned only with the formal framework that allows an introduction of all the elements required to perform universal quantum computation. However, nothing has been said about concrete physical implementations that may lead to a practical demonstration of the quantum logic gates introduced above. This point shall be returned to later, to briefly describe the experimental hardware currently used for a few qubit quantum computation and possible future prospects. As you may imagine, the extremely fragile nature of the quantum states used as qubits means that the requirements necessary for any hardware useful for quantum computation are rather stringent. The dynamics of the qubit physical evolution on a quantum computer is ruled by the laws of quantum physics. Thus, we should expect any unitary transformation or quantum gate U (e.g., the matrix operator $U \equiv \textsc{cnot}$ given in Eq. (2.7)) to be represented by an operator $U(t)$

$$U(t) = \mathcal{T}\exp\Big(-\frac{i}{\hbar}\int \mathcal{H}(t)dt\Big)\,, \tag{2.11}$$

such that $U(t) \equiv U$. Here, $\mathcal{T}$ denotes time-ordering, and $\mathcal{H}$ is the Hamiltonian that describes the physical system used to represent the qubits. Thus, the dynamic action of a quantum gate can be viewed in terms of the time evolution of the unitary matrix $U(t)$ which, according to the quantum mechanical Schrödinger's equation, connects the initial wavefunction coefficients to the final ones: mapping on the qubit basis states uniquely specifies the dynamics of an *arbitrary* initial quantum state. Hence, it should be possible to identify a Hamiltonian $\mathcal{H}$, acting over a definite time t, that produces the desired U-gate. This is the main idea behind any intended physical implementation of quantum computation. In practice, there are different quantum hardwares that exploit different types of Hamiltonians in order to implement such quantum logic gates.

Quantum hardware requirements: The building of hardware for a quantum computer implies the processing of quantum information in a *coherent* fashion (see Subs. 2.1.5). Regardless of the chosen technology, we need the feasibility to reliably perform the following experimentally :

1. Preparation and Storage: We must be able to *prepare* an n-quantum register in a definite state such as $|00\cdots 00\rangle$, and to *store* the information used while processing the quantum computation for a time long enough to perform an arbitrarily complex computational task[6].

2. Isolation: The quantum register must be well isolated from the environment, so that we can minimize the errors due to decoherence.

3. Measurement: We must be able to efficiently measure the QR states in the basis $\mathcal{B}_1$.

4. Unitary operations: We must be able to manipulate individual qubit states, and to have control over the interactions among qubits, so that we can perform universal quantum gates over any subset of gates of the quantum register.

5. Precision: We must be able to control the unitary evolution of the register in such a way that the gates are implemented with high precision.

Some aspects of this prescription shall be made more precise below, especially when discussing the subject of 'quantum errors' that need to be taken into account when performing practical quantum computation (see Sec. 2.1.5). The subject of quantum hardware practicalities will be returned to in Section 2.1.6, where different physical systems that may serve as quantum registers are explored.

Next, another way to realise quantum computation is discussed, the so-called *geometric* or *holonomic quantum computation* [95, 96].

---

[6] In practice, this time is bounded by *decoherence* of the register states (see Subs. 2.1.5).

2.1.2 Quantum computation by geometric means

It is interesting that there is an alternative way of performing quantum computations. This is built on the results of Berry [92, 93, 94], who showed that a quantum system under cyclic evolution acquires, besides the dynamic phase induced by the time evolution of the system, a *geometric phase*, the so-called Berry phase. It can be shown [95, 96, 97] that universal quantum gates can be implemented by purely geometric means, i.e., by using Abelian and non-Abelian geometric computations (holonomies) [92, 93, 94] rather than dynamic ones. The holonomies can be either Abelian phase factors (Berry phases) or general non-Abelian operations, depending on whether the eigenspace of the system's Hamiltonian is nondegenerate or degenerate. An interesting feature of the holonomic quantum computation is its potential robustness to certain types of computational errors, hence offering a natural way of performing *fault-tolerant* quantum computation. Let us formally establish the idea of a cyclic evolution to build the geometric phase and the non-Abelian Berry phase (non-adiabatic state evolution):

Cyclic evolution: The concept of a cyclic evolution is based on the adiabaticity [98] of the quantum state evolution of a given physical system, say the vector state $|\Psi\rangle$. In quantum mechanics, a basic goal is to calculate amplitudes, and then square them to obtain the probability of an event. Formally, in a Hilbert space $\mathbf{H}$, we have $|\langle\Psi|\Psi\rangle|^2 = 1$. However, this implies an ambiguity: there is no physical distinction between the two states $|\Psi\rangle$, and $\mathrm{e}^{i\varphi}|\Psi\rangle$. To fix this, the projective space $\mathbf{P}$ is introduced, in which vectors are grouped into equivalence classes such that we map $\mathbf{\Pi} : \mathbf{H} \longrightarrow \mathbf{P}$, where $|\Psi\rangle \mapsto [|\Psi\rangle] = \{|\Psi'\rangle : |\Psi'\rangle = r\mathrm{e}^{i\varphi}|\Psi\rangle\}$, for any $r > 0$ and real φ [97]. Hence, a cyclic evolution of the system's state $|\Psi\rangle$ translates into a closed curve $\mathbf{\Pi}(\mathcal{C}) \in \mathbf{P}$ covered in a period τ. In $\mathbf{H}$ the situation is rather different: at $t = \tau$, the path $\mathcal{C} \in \mathbf{H}$ followed by the initial state $|\Psi(0)\rangle$ no longer coincides with the final state $|\Psi(\tau)\rangle$ of the system: there is a phase difference of $\mathrm{e}^{i\varphi}$ between them. This phase can be determined by making the following (adiabatic) approximation: for each point $|\Psi(t)\rangle$ on $\mathcal{C}$, $t \in [0,\tau]$, we can choose a $|\Psi_\Pi(t)\rangle$ from $\mathbf{\Pi}(\Psi(t))$ in such a way that $|\Psi_\Pi(0)\rangle = |\Psi_\Pi(\tau)\rangle$. Hence we can write

$$|\Psi(t)\rangle = \mathrm{e}^{if(t)}\,|\Psi_\Pi(t)\rangle \ , \tag{2.12}$$

where the phase change of $|\Psi(0)\rangle$ is now given through the function $f(t)$: $\varphi = f(\tau) - f(0)$.

Calculating geometric and dynamic phases: Let us start by writing the system's Schrödinger equation

$$i\hbar\frac{\mathrm{d}}{\mathrm{d}t}\,|\Psi(t)\rangle = \mathcal{H}(t)\,|\Psi(t)\rangle \ , \tag{2.13}$$

where $\mathcal{H}(t)$ represents the system's Hamiltonian. From Eqs. (2.12), and (2.13) we obtain

$$\varphi = \int_0^\tau \mathrm{d}f(t) = -\frac{1}{\hbar}\int_0^\tau \langle\Psi(t)|\,\mathcal{H}\,|\Psi(t)\rangle\,\mathrm{d}t + i\int_0^\tau \langle\Psi_\Pi(t)|\,\tfrac{\mathrm{d}}{\mathrm{d}t}\,|\Psi_\Pi(t)\rangle\,\mathrm{d}t \ . \tag{2.14}$$

Hence, we end up with a total phase φ which is built of a *dynamic phase* δ that depends on the Hamiltonian $\mathcal{H}(t)$, and a *geometric phase* γ that depends only on the path $\mathcal{C}$, and is independent of the rate at which $|\Psi(t)\rangle$ completes $\mathcal{C}$, the Hamiltonian, or the choice of reference $\{|\Psi_\Pi\rangle\}$ [97]. These geometric and dynamic phases can be calculated as:

$$\begin{aligned} \gamma &= i\oint_{\mathcal{C}} \langle\Psi_\Pi|\,\mathrm{d}\,|\Psi_\Pi\rangle && (2.15) \\ \delta &= -\frac{1}{\hbar}\int_0^\tau \langle\Psi(t)|\,\mathcal{H}\,|\Psi(t)\rangle\,\mathrm{d}t\,. && (2.16) \end{aligned}$$

A particular case of the geometric phase γ is the Berry's phase [92], which occurs when the system's dynamics is performed under adiabatic conditions. This imposes restrictions over the rate at which $|\Psi(t)\rangle$ completes a given cyclic evolution. A fundamental characteristic of the Berry phase is that the energy eigenspace of the instantaneous Hamiltonians is non-degenerate along the path $\mathcal{C}$. As a model example, it can be shown, by using Eq. (2.15), that the Berry phase of a spin-half particle located in an external oscillating field gives the result

$$\gamma = -\pi(1-\cos\theta)\ , \qquad (2.17)$$

where θ is the angle between the Bloch vector and the z-axis [97]. As said, it is assumed that through the qubit cyclic evolution, the Hamiltonian parameters are changed adiabatically. The generalization of this result to any closed path gives $\gamma = \Omega/2$, where Ω is the solid angle enclosed by $\mathcal{C}$ on the Bloch sphere [92]. Thus, the Berry phase depends only on the area covered by the motion of the system, and is independent of the details of how this motion is executed.

The results explained above currently constitute a novel approach to quantum computation. Here, quantum gates can be built by using purely holonomies. A procedure to perform this is outlined in Ref. [97] for the case of a nuclear magnetic resonance (NMR) system via the use of the Abelian Berry phase. Recent experimental work has combined the above results to perform a first step towards geometric quantum computation [99]. The Abelian geometric phase has been used to experimentally demonstrate the controlled phase shift gate $B(\varphi)$ in an NMR system [99]. There is also another proposal for doing this via a Josephson junction system [100]. However, to be able to perform universal geometric quantum computation we need to combine this particular geometric gate (or any other 2-qubit entangling gate) with single qubit gates. The proposals of Refs. [99, 100] are restricted to Abelian holonomies only, which due to adiabatic conditions, have the disadvantage of being too slow if compared with typical dynamical time-scales, making it very difficult for any realistic realisation of quantum computation.

A leap has been taken towards the implementation of holonomic quantum computation. The adiabaticity difficulty has been overcome in two recent proposals [101, 102], by using non-Abelian holonomies to perform geometric quantum gates in a set of trapped ions [101], and in an NMR system [102]. The use of *non-adiabatic* state evolution implies two main differences from what was said for the Abelian Berry phase: i) After a time $t=\tau$, the state vector evolution is *non-cyclic*, and ii) The geometric phase Γ acquired over the period τ is different from the one found for the adiabatic evolution, $\Gamma \neq -\pi(1-\cos\theta) = \gamma$. Details concerning these new results, and the way they can be used to perform conditional quantum dynamics (e.g., the controlled phase shift gate) can be found in Refs. [101, 102]. It is worth noting that any scheme attempting to perform quantum computation using only geometric phases has to *eliminate the dynamic phase.* In NMR this can be done by using a refocussing technique known as spin-echo [97, 99].

Research in the subject of geometric quantum computation is in a very early stage. Further theoretical developments are expected, particularly those related to the robustness of the geometric QC to errors, and the way decoherence may affect the geometric phases during the quantum computation. So far, there has been an experimental demonstration of the 2-qubit gate $B(\varphi)$ in an NMR setup [99], and some other physical implementations are expected in the near future in different systems such as trapped ions, and solid state setups.

2.1.3 Quantum entanglement: a communication resource

Entanglement is a central concept in quantum information theory. In a system consisting of n quantum subsystems, it shows a form of correlations between such subsystems that cannot be understood or explained in any "classical" fashion because it points out exactly what distinguishes the quantum from the classical world. These correlations imply that each subsystem carries some knowledge, some degree of information, about the other parts. This degree of knowledge can be quantified, as is shown below. This section is restricted to the main elements and definitions that characterise the degree of entanglement of a given quantum system. This will be crucial for a more complete understanding of the results reported in Chapters 3 and 4. A detailed review of the current developments regarding the subject of entanglement can be found in Ref. [103].

Quantifying quantum entanglement: It is well known how to quantify entanglement in the case of a bipartite system (a system consisting of two subsystems, namely A and B) in a total pure state. For more than two subsystems, or mixed states, the situation is not so clear (for a survey of recent developments see, e.g., Ref. [103]). Next, the basic tools and definitions are given. Consider a bipartite system composed of subsystems A, and B. The state vector for this system is in the finite dimensional Hilbert space $\mathcal{H}_{AB} = \mathcal{H}_A \otimes \mathcal{H}_B$. This is to be referred to as an $n \otimes m$ system, where n and m are the dimensions of the spaces $\mathcal{H}_A$ and $\mathcal{H}_B$ respectively. A general *pure* state of the system can be written as

$$|\Psi\rangle_{AB} = \sum_{i,j} c_{ij}\, |i\rangle_A \otimes |j\rangle_B \ , \tag{2.18}$$

where $\{|i\rangle_A\}$, and $\{|j\rangle_B\}$ are a complete orthonormal basis set for each subsystem. Next, the Schmidt decomposition theorem is introduced.

Theorem: For any given pure state $|\Psi\rangle_{AB}$ it is always possible to find a complete set of orthonormal vectors $\{|n\rangle_A\}$, and $\{|\widetilde{n}\rangle_B\}$, in spaces $\mathcal{H}_A$ and $\mathcal{H}_B$ such that

$$|\Psi\rangle_{AB} = \sum_{n=1}^{k} \alpha_n\, |n\rangle_A \otimes |\widetilde{n}\rangle_B \ , \tag{2.19}$$

where the coefficients $\alpha_n > 0$, and $k \leq \dim \mathcal{H}_{AB}$. Eq. (2.19) is called the Schmidt decomposition of $|\Psi\rangle_{AB}$. Note that this decomposition contains only one index, in contrast to Eq. (2.18). The proof of this theorem is almost straightforward (see, e.g., Ref. [2]). Note: i) There is no Schmidt decomposition for a system of more than two subsystems. ii) A bipartite pure state is said to be *entangled* if at least two cofficients of the α_n's do not vanish (the number of non-vanishing coefficients is called the Schmidt number of $|\Psi\rangle_{AB}$)[7].

Degrees of entanglement: The entanglement of a given quantum state can be defined in terms of the concept of separability: if a given state does not satisfy the separability criterion, then the state is said to be entangled. However, it is not so easy to find a unique separability criterion that solves the problem of determining with certainty whether a given quantum state is entangled or not. In fact, this question has led to a very active field of research: manipulation of entanglement, where quantifying, concentrating and distilling entanglement, and using mixed-state entanglement as a resource for quantum communication are central subjects [103]. One separability criterion is based on the violation of Bell inequalities [105], where separable states are required to satisfy all Bell inequalities [105]. However, this is not a very strong criterion since there are some entangled states that also satisfy all standard Bell inequalities [106, 107, 108]. A stronger and more useful criterion is based on the concept of partial transposition of Peres [109], in which he noted that a separable state remains a positive operator if subjected to partial transposition. For a detailed discussion of these criteria, see, e.g., Ref. [103] and references therein. Regarding the contents of this thesis, it is necessary to introduce some definitions concerning the degree of entanglement of a given quantum system. It follows from the Schmidt theorem that for a bipartite system[8] (each subsystem having a two-dimensional Hilbert space)

$$|\Psi\rangle_{AB} = \alpha\,|0\rangle_A\,|0\rangle_B + \beta\,|1\rangle_A\,|1\rangle_B \ . \tag{2.21}$$

Suppose that any present phase is absorbed by the Schmidt vectors, such that we can define $\alpha,\, \beta \in \mathbf{R}$, with $|\alpha| \leq |\beta|$. Then, the following terminology will be used throughout this thesis:

Product state: A state is a product state if and only if $\alpha = 0$.

---

[7] In a bipartite system, subsystems A and B are described by *density operators* ρ_A and ρ_B. It turns out that these operators have the same non-vanishing eigenvalues: they are equal to the square of the Schmidt numbers. A state acting on Hilbert space $\mathcal{H}_{AB}$ is called *separable* [103] if it is of the form

$$\rho = \sum_{i=1}^{k} c_i \rho_i^A \otimes \rho_i^B \ , \tag{2.20}$$

for some k, where ρ_i^A and ρ_i^B are states on $\mathcal{H}_A$ and $\mathcal{H}_B$ respectively. If ρ is a *pure* state, i.e., $\rho = |\Psi_{AB}\rangle\langle\Psi_{AB}|$, then it is easy to see whether is entangled or not: indeed, it is separable if and only if $|\Psi\rangle_{AB} = |\Psi\rangle_A \otimes |\Psi\rangle_B$.

[8] For the physical implementations proposed in this thesis, this bipartite system is to be represented by a two-QD system, where its exciton states can be found, under certain prescribed initial conditions, in a maximally entangled state, as defined above.

Entangled state: A state is entangled if and only if $\alpha \neq 0$.

Maximally entangled state: A state is maximally entangled if and only if $|\alpha| = |\beta|$.

The most famous entangled states are the maximally entangled states $|\phi^{\pm}\rangle \equiv \frac{1}{\sqrt{2}}(|0\rangle\,|0\rangle \pm |1\rangle\,|1\rangle)$, and $|\psi^{\pm}\rangle \equiv \frac{1}{\sqrt{2}}(|0\rangle\,|1\rangle \pm |1\rangle\,|0\rangle)$. These four mutually orthogonal states are so important because they exhibit the strongest possible Bell-EPR correlations [2, 139], the reason they are known as the Bell-basis states. Also, as will be seen below, these states are crucial to many communication protocols. It was shown in Section 2.1.1 that these entangled states can be generated and manipulated in terms of universal quantum logic gates: suppose, for example, that a two qubit state is initialised in the state $|\Psi_0\rangle = |0\rangle\,|0\rangle$. Then, by applying the two successive quantum gates $\text{CNOT}_{12}H_1$ to $|\Psi_0\rangle$, the Bell state $|\phi^{+}\rangle$ is generated (the same sort of unitary transformations can be applied to n-qubit systems in order to generate, for example, "Schrödinger cat states"-like). In this thesis, a solid-state based setup for producing maximally entangled states of the Bell type will be provided (see Chapter 3). It is interesting that once $|\phi^{+}\rangle$ has been generated, the remaining states of the Bell basis can be also generated by applying *only single qubit gates* to it (the unitary transformations introduced in Section 2.1.1). Now that the basic definitions of entanglement have been introduced, the main practical applications of quantum entanglement as a *communication resource* are introduced.

Quantum teleportation: This is arguably the most striking application of quantum entanglement. Here, the quantum state $|\Psi\rangle$ of a system can be transmitted from one spatial location to another with neither physical transportation of the system itself nor previous knowledge of $|\Psi\rangle$. This apparently impossible task invokes only the use of a two-particle maximally entangled state (e.g., $|\phi^{+}\rangle$)— that has to be shared beforehand between the two parties that wish to transmit $|\Psi\rangle$— assisted by the communication of two classical bits of information. The details of the whole teleportation protocol, as originally given by Bennett *et al.* [14], will be explained in Chapter 4, where a practical application, the teleportation of the excitonic state of a QD system, is proposed. This is perhaps the most evident of the demonstrations of quantum entanglement as an information resource.

Dense coding: Classical information can be transmitted by means of a quantum channel, i.e., via the use of qubits. In principle, the task is very simple: if a sender, Alice, wants to transmit a classical binary string, say 0110, to a physically distant receiver Bob, via quantum means, she simply prepares the state $|0110\rangle$ and send it to Bob who can then extract the information by measuring the qubits in the $\mathcal{B}_1$-basis, therefore obtaining four bits of classical information, precisely the message sent by Alice. However, communicating one bit per qubit is obviously not the best thing that one can do with qubits. In fact, this way of sending classical bits is actually more expensive than sending them via a proper classical channel. It turns out, however, that the qubits offer an additional advantage over the classical bits: *one can communicate two classical bits by sending only one qubit.*

Once more, the trick relies on the possibility of generating entangled states: suppose Alice and Bob are given one particle each which has been previously prepared in the maximally entangled state $|\phi^+\rangle$. They don't know each other and have never interacted previously, before this entangled pair is given to them. Alice then can communicate to Bob two classical bits by sending him only one qubit. This is the so-called dense coding, an idea proposed by Bennett and Wiesner in 1992 [15]. This is based on the fact that the four Bell-basis states can be projected onto the computational basis to convey two classical bits of information. This can clearly be seen in terms of the unitarity of the studied quantum logic gates. First, after receiving the qubit that Alice has sent to Bob, he performs $\text{CNOT}_{12}(|\phi^+\rangle)$, hence generating the disentangled state $|\psi_1\rangle \equiv \frac{1}{\sqrt{2}}(|0\rangle + |1\rangle)\,|0\rangle$. Second, he realises the operation $H_1(|\psi_1\rangle)$, thus obtaining the state $|0\rangle_1\,|0\rangle_2$. From this output, qubit 1 is referred to as the *phase* bit (+ or −), and qubit two as to the *parity* bit (this tells whether the spins are aligned or anti-aligned: $|\phi\rangle$ or $|\psi\rangle$). Hence, a measurement of this output in the computational basis should give the result 00: Bob finishes with two classical bits of information. In the same way, by using any of the remaining states of the Bell-basis $|\phi^-\rangle$, $|\psi^+\rangle$, $|\psi^-\rangle$, Bob should obtain the following two classical bits output: 10, 01, and 11 respectively; thus, in any case, transmitting two classical bits per qubit. Note that this process can be seen as a way of performing *secure communication*: the qubit trasmitted by Alice will convey two classical bits of information only if the receiver has the other qubit of the *apriori* distributed entangled pair. This is an example of the information content of quantum entanglement and the way it can be exploited for classical communication.

Quantum key distribution: Suppose that Alice and Bob now need to communicate an extremely confidential message, such that the information is not to be deciphered by a dangerous eavesdropper "Miryam." This task can be accomplished with certainty only if Alice and Bob are allowed to share a private cryptographic *quantum key K*, a secret random bit string known only to them, in order to encode and protect the original message. The problem assumes that Alice and Bob have at their disposal a public classical channel, and a quantum channel that is insecure. Hence, the original problem of communicating a message has been converted into a cryptographic key exchange problem. This is often referred to in the literature as *quantum cryptography.*

As in the previous cases of entanglement-assisted communication, the key exchange can only be accomplished with certainty by means of quantum entanglement. It is to be added to this problem that Miryam is an efficient eavesdropper: she can interact with the quantum information carriers used by Alice and Bob, and she can also tap, without disturbing, any classical communication that Alice and Bob may transmit during the process of sharing the private key. The quantum key distribution schemes are based on the no-cloning theorem, since, in contrast to the situation of classical communication, the message sent from Alice to Bob cannot be tapped and faithfully copied by an eavesdropper. Any 'excess' of Miryam's eavesdropping should be easily detected by Alice and Bob, who can then abort the protocol and create a new key. Thus, any attempt by an eavesdropper to obtain relevant information about K and remain undetected should be negligible.

Let's see how to establish such a secured shared random key. Suppose that Alice and Bob share a supply of entangled (singlet) Bell states $|\psi^-\rangle$. Then, they perform the following protocol. Alice and Bob measure either σ_x or σ_z over each qubit they have[9]. Hence, each choice occurs with probability 1/2. Once these measurements are performed, the observables they measure are publicly announced, but the obtained outcomes are not revealed. If their qubits are measured along different axes, the outcomes are uncorrelated, hence Alice and Bob discard their results. In contrast, if their qubits are measured along the same axis, their results, though random, are perfectly correlated, thus establishing a shared random key. It is easy to check that this protocol is robust against Miryam attacks to the quantum information carriers, where she can try, for example, to entangle her qubits with those transmitted between Alice (A) and Bob (B) and then perform a measurement of her qubits (after knowing the results announced by Alice and Bob). The result is that Miryam (M) does not obtain any significant information from Alice's and Bob's and her own measurement results. Hence, the generated random key K is secure.

To see why this is so, suppose that Miryam has indeed attacked the quantum channel in order to extract information from that of Alice and Bob. The most general possible state that describes A, B, and the intervention of M can be written as

$$|\aleph\rangle_{ABM} = |00\rangle_{AB}\,|e_{00}\rangle_M + |01\rangle_{AB}\,|e_{01}\rangle_M + |10\rangle_{AB}\,|e_{10}\rangle_M + |11\rangle_{AB}\,|e_{11}\rangle_M \ , \tag{2.22}$$

where we can imagine the states e_{ij} as the states of a surrounding environment—Miryam (see Section 2.1.5). As $|\psi^-\rangle$ is an eigenstate of both $\sigma_x^A\sigma_x^B$, and $\sigma_z^A\sigma_z^B$ (eigenvalue -1), hence Alice and Bob can verify that effectively $\sigma_z^A\sigma_z^B = -1$ (the phase bit). Then, they must have

$$|\aleph\rangle_{ABM} = |01\rangle_{AB}\,|e_{01}\rangle_M + |10\rangle_{AB}\,|e_{10}\rangle_M \ , \tag{2.23}$$

and $\sigma_x^A\sigma_x^B = -1$ (the parity bit), which implies

$$|\aleph\rangle_{ABM} = \tfrac{1}{\sqrt{2}}(|01\rangle_{AB} - |10\rangle_{AB})\,|e\rangle_M \ . \tag{2.24}$$

Comparing Eqs. (2.22), (2.23), and (2.24), it is clear that Miryam's qubits must be unentangled from Alice's and Bob's if their pair (or any of the Bell-basis) is to be an eigenstate of $\sigma_i^A\sigma_i^B$, $i = x, z$. This means that despite Miryam's efforts, the shared key is safe: even her knowledge of quantum mechanics does not allow her to learn anything about the secret random key! In contrast, if Alice and Bob measure a part of the shared key and find that the results are not perfectly correlated, then Miryam may have been successful, in which case they have to abort this key and try to generate a new secure one. Once more, it is evident that the capability to successfully perform a quantum key distribution protocol relies on the generation and distribution at will of particles in a highly entangled pair [13]. Any state of the Bell-basis could serve for this purpose.

---

[9] Here, σ_i denote the Pauli matrices: $\sigma_x = \begin{pmatrix} 0 & 1 \\ 1 & 0 \end{pmatrix}$, $\sigma_z = \begin{pmatrix} 1 & 0 \\ 0 & -1 \end{pmatrix}$. These are single qubit transformations that can be used for phase shifting and flipping of the qubits of the Bell basis: i) Apply σ_z to qubit 1: $|\phi^+\rangle \leftrightarrow |\phi^-\rangle$, and $|\psi^+\rangle \leftrightarrow |\psi^-\rangle$. ii) Apply σ_x to qubit 1: $|\phi^+\rangle \leftrightarrow |\psi^+\rangle$, and $|\phi^-\rangle \leftrightarrow -|\psi^-\rangle$. The Bell-basis states can be characterized as the simultaneous eigenstates of the commuting observables $\sigma_x^A\sigma_x^B$, and $\sigma_z^A\sigma_z^B$, where the eigenvalue of $\sigma_x^A\sigma_x^B$ is the parity bit, and the eigenvalue of $\sigma_z^A\sigma_z^B$ is the phase bit. These operators can in principle be measured simultaneously.

This is not the only available quantum protocol. In fact, the so-called BB84 protocol of Brassard and Bennett [110] does not require the entangled pairs to be shared by Alice and Bob: here, Alice can prepare the pairs herself, from which she measures one qubit of each pair and sends the other qubit to Bob. Then Bob can measure and verify his results with Alice as explained above. This scheme is as secure as the former. The corresponding security proofs can be found in Refs. [111, 112]. The effects of the insecurity of the quantum channel can also affect the results of Alice's and Bob's measurement. However, it can be shown that the errors due to possible imperfections in the channel can be distinguished from the errors that occur because of Miryam's eavesdropping [111, 112]. Experimental demonstrations of quantum key distribution are far more advanced than any other QIP task. For an account of the main experimental achievements in this subject see, e.g., Refs. [113].

Quantum data compression: A qubit is a useful measure of quantum information content. Jozsa and Schumacher have shown that given a system of n qubits, it is possible to find a subspace of Hilbert space in which one can describe any state vector of the system, and that the dimension of this subspace is $2^{nS(\rho)}$, for $S(\rho) < 1$ [81, 114]. Hence, only $nS(\rho)$ qubits are required to represent the quantum information content, where $S(\rho)$ is the von Neumann entropy of the quantum source,

$$\begin{aligned} S(\rho) &= -\,\mathrm{Tr}\rho\log_2\rho\,, \\ \rho &= \sum_i p_i\,|\Psi_i\rangle\,\langle\Psi_i|\;. \end{aligned} \tag{2.25}$$

Here, ρ is the density matrix representing the system, $|\Psi_i\rangle$ are the states trasmitted by the source and p_i their probability of transmission. The von Neumann entropy is a measure of the minimum asymptotic number of qubits that are required to compress the initial state of a system that is to be faithfully transmitted and finally recovered by a decoder. As can be seen, $nS(\rho) < n$, hence the name quantum data compression.

This is to be compared with classical data compression, where redundant data can also be compressed and then faithfully decoded. The main difference between the two is that classical compression has allowed only orthogonal states, while *any* superposition of states is allowed quantum-mechanically. Hence, a general quantum compression that involves non-orthogonal states does not have any classical analogue. In fact, if the quantum states to be compressed and transmitted are non-orthogonal, the encoder cannot make a copy of them because of the no-cloning theorem. The snag here is that a practical implementation of these 'compressions' and 'decodings' is extremely demanding. As pointed out in Ref. [6](c), this is the ultimate compression allowed by the laws of physics.

2.1.4 Quantum algorithms and quantum games

Quantum algorithms: Deutsch's *quantum parallelism* is an outstanding property of a quantum computer. It points out that a quantum computer can perform certain computational tasks faster than any modern digital computer. This was rigorously stated in the 'Deutsch problem,' whose solution gave birth to the first quantum algorithm, the so-called Deutsch-Josza algorithm [19], where the interplay between interference effects and quantum entanglement gives rise to a celebrated speed up of the quantum computational process: this leads to an exponential gap between the complexity class of the quantum problem and the corresponding complexity class of the classical problem. In other words, the quantum parallelism leads to the solution of problems that are otherwise intractable by any classical means. After Deutsch's, other quantum algorithms have been discovered, the most remarkable one being Shor's algorithm for efficient factorisation of large numbers [21, 23]. This finding is arguably one of the main breakthroughs in the subject of quantum information theory of the past decade. It established a solution to a problem that, from the complexity point of view, was thought to be intractable, and brings practical uses as a byproduct, because it is exactly the same difficulty of factoring a large number that holds up modern schemes for public key cryptography, such as the RSA scheme [115]. Other relevant algorithms are those of Simon [20], and Grover's search algorithm [22]. A common element to all these algorithms is the use of the quantum parallelism property, where the linear superposition principle plays a remarkable role when extracting a 'global' information of a given function f. In this section we shall concentrate on a generalisation of Deutsch's algorithm [19, 24]. A detailed analysis of Shor's algorithm can be found in Ref. [23].

Generalised Deutsch's problem: Suppose we are given a device *oracle* that computes the Boolean function $f : x \in \{0,1\}^n \to f(x) \in \{0,1\}$ that takes any n-binary string x as input and produces a single bit $f(x) \in \mathcal{B}_1$ as output, in a single step. The problem assumes that the function f is either *constant* or *balanced* depending on whether the result of the 2^n possible evaluations gives the same output (0 or 1) or a situation where half of them are 0's and the other half 1's. The problem is to determine whether f is constant or balanced (we previously analysed the simplest case $n = 1$, where $f(0) = f(1)$ or $f(0) \neq f(1)$).

Before we give the solution to this problem, let us first analyse its complexity class: if we attempt to solve this problem with a classical computing device in the worst possible scenario, we shall have to call the oracle $2^{n-1} + 1$ times. Thus, the number of oracle queries grows exponentially with n. But there is a much cleverer way to solve this problem. In doing so, we start by replacing the classical oracle "f" with a quantum oracle $\mathcal{U}_f$ which performs the unitary transformation $\mathcal{U}_f : |x\rangle\,|a\rangle \to |x\rangle\,|a \oplus f(x)\rangle$ in a single step, where $|x\rangle$ is an n-qubit state (input) such as the one given in Eq. (2.3), and $|a\rangle$ is an ancilla single qubit state ($a \in \mathcal{B}_1$). Thus, the solution of Deutsch's problem is straightforward: Suppose the n-QR and the ancilla are initialised in the states $|x\rangle = |0\rangle^{\otimes n}$, and $|a\rangle = (|0\rangle - |1\rangle)/\sqrt{2}$. Next, perform the following protocol:

1. Apply the Hadamard transform H to $|x\rangle$. This leads to the state

$$|\Psi_1\rangle = \frac{1}{\sqrt{2^{n+1}}} \sum_{x\in\{0,1\}^n} |x\rangle\,(|0\rangle - |1\rangle)\ . \tag{2.26}$$

For the sake of clarity, the qubit $|x\rangle$ is explicitly given in Eq. (2.3).

2. Apply the quantum oracle to the quantum register: $\mathcal{U}_f(|\Psi_1\rangle)$. This yields
$$|\Psi_2\rangle = \frac{1}{\sqrt{2^{n+1}}} \sum_{x\in\{0,1\}^n} (-1)^{f(x)} |x\rangle (|0\rangle - |1\rangle) . \tag{2.27}$$
3. Next, perform a measurent to determine whether f is constant or balanced. This measurement can be realised as follows: Apply the Hadamard transform to all of the first n-qubits of the register given by Eq. (2.27). This yields[10]
$$|\Psi_3\rangle = \frac{1}{2^{n+\frac{1}{2}}} \sum_{x,y\in\{0,1\}^n} (-1)^{f(x)+(x\cdot y)} |y\rangle (|0\rangle - |1\rangle) . \tag{2.29}$$
This reduces the measurement problem to that of finding whether or not the first n qubits are in the state $|0\rangle$, thus solving Deutsch's problem.

To see why the third step solves the problem, note that the probability of finding the system's output $|\Psi_3\rangle$ in the initial state $|0\rangle \otimes |0\rangle \otimes \cdots \otimes |0\rangle \otimes |a\rangle$ is
$$\frac{1}{2^{2n}} \left| \sum_{x\in\{0,1\}^n} (-1)^{f(x)} \right|^2 = \begin{cases} 1 & \text{if } f \text{ is constant} \\ 0 & \text{if } f \text{ is balanced} \end{cases} . \tag{2.30}$$
The term inside the delimiters gives $2^n(-1)^{f(0\cdots0)} = \pm 2^n$ when f is constant. Thus, a measurement of the first n qubits output determines with a 100% success rate whether f is constant or balanced. As said, this is actually a generalisation of Deutsch's algorithm, which originally gave only a 50% of probability of success when solving this problem [24].

It is remarkable what has been done using this algorithm: its massive quantum parallelism led to the computation of all the 2^n possible values of $f(x)$ in one single run. This arises from the fact that the quantum oracle can perform its task for any linear combination of possible basis states in a single step: this is to be physically identified as an interference pattern. As to the complexity class of this quantised problem, we require only $O(n)$ steps to obtain the final answer. Hence, if we compare this result with that of the classical complexity class, it is found that Deutsch's algorithm leads to an *exponential speedup* of the computations. This is a wonderful property that only a quantum computer can provide.

Deutsch's and Grover's algorithms have been implemented in bulk liquid NMR experiments but only for a few qubit register [39]. More recently, there has been the more demanding implementation of Shor's factoring algorithm, also using NMR quantum computation. This has been done in the simplest scenario: factorisation of the number $N = 15$, by using $n = 7$ qubits [40].

---

[10] The effect of the Hadamard transform over an arbitrary n-QR in a given state $|x\rangle$, $x \in \{0,1\}^n$, is
$$|x\rangle \mapsto \frac{1}{2^{n/2}} \sum_{y\in\{0,1\}^n} (-1)^{x\cdot y} |y\rangle , \tag{2.28}$$
where the product $x \cdot y = (x_{n-1}y_{n-1} + \dots x_1y_1 + x_0y_0)$. Here, $j = (j_{n-1}, \dots, j_0)$, $j = x, y$. For example, if $|x\rangle = |010\rangle$, hence $H(|x\rangle) \equiv \frac{1}{2^{3/2}} \{|000\rangle + |001\rangle - |010\rangle - |011\rangle + |100\rangle + |101\rangle - |110\rangle - |111\rangle\}$.

Next, we examine very briefly the subject of game theory, and discuss the role that quantum computation may play when the players of a given 'game' are allowed to play "quantum strategies."

Quantum games: Game theory is a well established branch of mathematics whose tools and formalism, mainly developed by J. von Neumann [116], aims to solve the conflict between two or more competing parties (players) that hold particular interests. This has a vast range of applications in many different subjects such as social sciences, biology, and economics [117]. By contrast, quantum game theory [16, 17, 18] has been born from motivations regarding QIP, where information has been recognised as a physical quantity. The usefulness of quantum games for 'practical applications' goes back to the idea that many physical, chemical, and biological quantum processes can be thought of as games.

The initial motivation is the recognition of new effects without classical analogue, which are associated with the quantum character of the 'games'. For example, a two-player game [16, 17] can show a vanishing of 'predominant strategies' when the allowed 'moves' are made quantum-mechanically: these strategies should reappear only under the degrading of the quantum coherence [16, 17]. For multi-player quantum games [18], it has been shown that when the resources controlled by competing agents are entangled, they can cooperate to perfectly exploit the 'game' [18]. This has been performed for multi-player quantum games in the cases of the "Minority game," and a game analogous to "Prisoner's Dilemma" [18], with the interesting result that such games can exhibit forms of 'coherent' quantum equilibrium[11] which have no analogue in classical games, or even in two-player quantum games. Thus, quantum players can exploit their moves highly efficiently through the use of collaborative strategies.

Discussion: Because of the computational and physical rewards when performing both quantum algorithms and quantum games, one might be tempted to try to establish a common framework that yields a connection between the two. Many situations in nature, e.g., in biology, can be thought of as games where the competing agents try to establish a strategy that allows them to maximise their pay-off (e.g., their energy efficiency). In this respect, quantum algorithms may play an important role. They could be viewed, for instance, as games played between classical and quantum agents [16]. One can imagine that a deeper understanding of the underlying structure of certain "quantum strategies" for performing quantum games may lead to the possibility of finding a different approach to gain insight into some fundamental physical and chemical processes in the quantum regime. One may think, for example, of the decoherence phenomenon as a *dynamic* multi-agent quantum game where at any given time t, we ask whether or not a given quantum register has been driven by an "environment strategy" to a situation where the QR coherence is lost. From a QIP perspective, we would like to find a way to play this game such that the registers answer is always "no." This example is in contrast with the above proposals [16, 17, 18], where the quantum games are played 'statically,' in the

---

[11] An equilibrium is understood here as a set of strategies, such that neither player can improve his probability of winning by changing his strategy while the others do not.

sense that they are played only once, and hence there is no record of the players history. Dynamical quantum games should be an interesting issue to address in the future, in particular because it could give rise to a new view of addressing *quantum memory effects*, and hence of understanding decoherence. Currently, there is an intense search to find new quantum algorithms. Finding new elements of the repertoire of the advantages of a quantum computer over its classical counterpart would bring, along with the possible development of novel quantum strategies, new insight into the understanding of basic processes in the interdisciplinary field of QIP.

The developments that came after the discovery of efficient quantum algorithms call for the need to solve another outstanding matter: the stabilisation problem. It is clear that environmental influences disturb the quantum computers capability of generating reliable quantum interference and quantum entanglement, hence destroying the possibility of performing arbitrarily complex quantum computations such as quantum algorithms. Fortunately, it was shortly shown afterwards, by Shor [25] and Steane [26], that quantum error-correcting codes exist, thus alleviating this situation. Next, the environmental problem mentioned above, and possible ways to overcome it, including fault-tolerant quantum computation itself, shall be briefly discussed.

2.1.5 Quantum decoherence and quantum error correction

The list of quantum hardware requirements to build a quantum computer presented in Section 2.1.1 possess a common difficulty. This is the problem of stability, which spoils the unitarity of the register evolution, and hence compromises the usefulness of any given computational task. It can be defined by two main ingredients: *noise*, the coupling that may exist between the state of the computer and its surrounding environment, and *imprecision*, the inaccuracy with which elementary quantum gates are performed in an arbitrarily complex computation [129]. As has been discussed, in order to perform quantum computations, a *coherent* evolution of the qubits is required. Noise causes the quantum computer to evolve from a pure quantum state to a statistical mixture of quantum states that exhibit no phase difference between them, the so-called *decoherence* [118]. Thus, decoherence implies that two of the main properties of a quantum computer, say, i) the capability to maintain superpositions of its states, i.e., to perform quantum interference reliably, and ii) the capability to reliably perform entanglement between its qubits, are lost during a given computational process. This can be illustrated by stating that, e.g., if $|S\rangle$ is a superposition of states $|\Phi_i\rangle$ of the quantum computer, say

$$|S\rangle = \tfrac{1}{\sqrt{2}}(|\Phi_1\rangle + e^{i\varphi}\,|\Phi_2\rangle)\ , \tag{2.31}$$

then, a *coherent* evolution of the QC state requires that the $|\Phi_i\rangle$'s *and* the phase φ of the superposition remain unchanged by both noise and imprecision[12]. In practice, these

---

[12] This can be seen in the case of quantum entanglement as follows: suppose that the state $|S\rangle$ is created in an entangled state, say $|\Phi_1\rangle = |01\rangle$, $|\Phi_2\rangle = |10\rangle$, and $\varphi = \pi$ (the singlet state $|01\rangle - |10\rangle$). Hence, its phase bit ("$-$") and its parity bit (spin states are antialigned, "$|\psi\rangle$") should be guaranteed throughout the computational process if the system is to evolve coherently.

criteria are very difficult to match. It is easy to see that an imprecise operation could result in a rotation of the state such that the phase φ becomes undefined. Also, and perhaps more stringent, is the fact that the coupling of $|S\rangle$ to the environment can result in a state of the type $\frac{1}{\sqrt{2}}(|\Phi_1\rangle\,|e_1\rangle + \mathrm{e}^{i\varphi}\,|\Phi_2\rangle\,|e_2\rangle)$, which also affects the phase φ when the states of the environment $|e_i\rangle$ become orthogonal, i.e., when $\langle e_1|e_2\rangle \to 0$. This system-environment coupling—decoherence—results in a leakage of the information such that superpositions of the system's states evolve into entanglements with the environmental degrees of freedom, thus spoiling the unitarity of the evolution.

In the case of a spin half quantum (qubit) system, where $|S\rangle$ can be represented as a general state $\alpha\,|0\rangle + \beta\,|1\rangle$, the qubit-environment interaction leads, in the worst scenario, to a state of the type

$$|e_i\rangle\,(\alpha\,|0\rangle + \beta\,|1\rangle) \;\rightarrow\; \alpha\,(c_{00}\,|e_{00}\rangle\,|0\rangle + c_{01}\,|e_{01}\rangle\,|1\rangle) + \beta\,(c_{10}\,|e_{10}\rangle\,|1\rangle + c_{11}\,|e_{11}\rangle\,|0\rangle)\;, \tag{2.32}$$

where $|e_i\rangle$ is the initial state and $|e_{ij}\rangle$ are the final states of the environment (not necessarily orthogonal), and c_{ij} are noise coefficients. It is interesting that this evolution can be rewritten as

$$|e_i\rangle\,|S\rangle \rightarrow \{|e_{_I}\rangle\,I + |e_x\rangle\,\sigma_x - i\,|e_y\rangle\,\sigma_y + |e_z\rangle\,\sigma_z\}\,|S\rangle \tag{2.33}$$

where $|S\rangle$ is the initial state of the qubit, $e_{_I} = c_{00}\,|e_{00}\rangle + c_{10}\,|e_{10}\rangle$, $|e_x\rangle = c_{01}\,|e_{01}\rangle + c_{11}\,|e_{11}\rangle$, and so on. The Pauli operators σ_i, and the identity I, are written in the computational basis B_1. Recall that $-i\sigma_y = \sigma_x\sigma_z$. It follows from the Pauli matrices in Eq. (2.33) that the errors involved on each qubit are basically of three types: "*bit flip*" (σ_x) errors, "*phase flip*" (σ_z) errors, or "*bit/phase flip*" ($\sigma_x\sigma_z$) errors [26]. Thus, the problem of qubits error correction is reduced to the problem of correcting the above-mentioned errors. In these terms, the physical processes of phase decoherence and spontaneous emission can be stated as:

i. *Phase decoherence*: $(\alpha\,|0\rangle + \beta\,|1\rangle)\,|e\rangle \rightarrow \alpha\,|0\rangle\,|e_0\rangle + \beta\,|1\rangle\,|e_1\rangle$. This is given by $\{\ |e_{_I}\rangle\,, |e_z\rangle \neq 0,\ \ |e_x\rangle = |e_y\rangle = 0,\ \ \langle e_{_I}|e_z\rangle = 0\ \}$.

ii. *Spontaneous emission*: $(\alpha\,|0\rangle + \beta\,|1\rangle)\,|e\rangle \rightarrow \alpha\,|0\rangle\,|e_0\rangle + \beta(|1\rangle\,|e_1\rangle + |0\rangle\,|e_2\rangle)$, $\langle e_{_1}|e_2\rangle = 0$. This is given by $\{\ |e_x\rangle = -\,|e_y\rangle\,,\ \ \langle e_x|e_{_I}\rangle = -\langle e_x|e_z\rangle,\ \ \langle e_{_I}|e_z\rangle = \langle e_x|e_x\rangle\ \}$. If Γ is the spontaneous emission rate, it is found that $\langle e_x|e_x\rangle = \langle e_y|e_y\rangle = \langle e_z|e_z\rangle = \frac{1}{4}(1-\mathrm{e}^{-\Gamma t})$, and $\langle e_{_I}|e_{_I}\rangle = \frac{1}{4}(1+3\mathrm{e}^{-\Gamma t})$.

This latter process is referred to in the NMR literature as the T_1 (relaxation) process, and the former as the T_2 (dephasing) process. In any case, it is clear that the decoherence interaction entangles qubits with the environment. To visualise, e.g., the case of *phase decoherence*, it is useful to write the qubit evolution in terms of its density matrix operator. Thus, tracing out the environments states yields the evolution

$$\begin{pmatrix} |\alpha|^2 & \alpha\beta^* \\ \alpha^*\beta & |\beta|^2 \end{pmatrix} \longrightarrow \begin{pmatrix} |\alpha|^2 & \alpha\beta^*\langle e_0|\,e_1\rangle \\ \alpha^*\beta\langle e_1|\,e_0\rangle & |\beta|^2 \end{pmatrix}\,, \tag{2.34}$$

where the off-diagonal elements "*coherences*," vanish for $\langle e_0|e_1\rangle \to 0$, in agreement with item (i). This is the origin of the term decoherence. Now that the problem has been identified, it is necessary to find a way to avoid or correct decoherence. In so doing, there is a powerful though counter-intuitive method: quantum error correction. By using this technique, a quantum computer is able to compute an arbitrary number of quantum logic gates—a complex quantum interference network—and produce the right answer even though the qubits in the computer relax spontaneously many times during the computational process [26]. To understand why this is so, let's start by noting that the principles of quantum error correction (QEC) are based on two main elements: the quantum states to be processed and the type of noise to be corrected. In order to describe the method, the notations of Ref. [26] are used.

Suppose the coupling between an m-quantum system (Q) and its environment (E) is described by

$$|e\rangle\,|\Phi\rangle \longrightarrow \sum_s |e_s\rangle\, M_s\, |\Phi\rangle \ , \tag{2.35}$$

where $|e\rangle$ ($|\Phi\rangle$) is the initial state of the environment (system). The action of the "error operators" M_s on the system is unitary. These M_s's are a tensor product of operators (one for each qubit of the whole register) that belong to the set $\{I, \sigma_x, -i\sigma_y, \sigma_z\}$. The final states of the environment $|e_s\rangle$ need not be orthogonal nor normalised, and it is clear that the noise process of Eq. (2.35) is irreversible because the environment cannot be controlled. To perform QEC, the system Q has to be coupled to another system "ancilla" (a), which is composed of $n - m$ qubits in the definite state $|0\rangle_a$ (the whole register "$Q + a$" contains n qubits). The interaction A between Q and a, the *syndrome extraction*, is unitary and satisfies

$$A(|0\rangle_a M_s\, |\Phi\rangle) = |s\rangle_a M_s\, |\Phi\rangle \quad \forall\, M_s \in \mathcal{S} \ . \tag{2.36}$$

Here, the ancilla states $|s\rangle_a$ are mutually orthogonal, and the syndrome s gives us information (bits) about the kind of noise the register is experiencing. The set $\mathcal{S}$ is the set of error operators M_s for which syndrome extraction works—the set of correctable errors. This depends on the encoding: a central part of QEC is to find the best syndrome extraction operators [26, 124].

Next, the syndrome extraction A is applied to the composite noisy-ancillary "$Q + E + a$" state. This yields

$$A\left\{\sum_s |e_s\rangle\, |0\rangle_a M_s\, |\Phi\rangle\right\} \longrightarrow \sum_s |e_s\rangle\, |s\rangle_a M_s\, |\Phi\rangle \ . \tag{2.37}$$

The next step is remarkable: by measuring the ancilla state in the $\{|s\rangle_a\}$-basis, the ancilla is projected onto one particular state $|s\rangle_a$, and the outcome value s becomes known to us. Thus, the whole system "$Q+E+a$" is projected onto the state $|e_s\rangle\,|s\rangle_a M_s\,|\Phi\rangle$, where s is known. Furthermore, from the measurement result (value of s), one can identify the operator M_s [13], thus applying M_s^{-1} to "$Q + a$" in order to obtain the final state[14]

$$|e_s\rangle\,|s\rangle_a\,|\Phi\rangle\ . \tag{2.38}$$

This means that our problem has been solved: *the original (noise-free) state $|\Phi\rangle$ has been recovered.* Note: i) After the syndrome extraction operation, the ancilla state $|s\rangle_a$ depends on the noise but not on the quantum state to be corrected (see Eq. (2.36)). ii) After the projective measurement, instead of the general noise of Eq. (2.35), one is left with only one error operator, M_s, which is now known to us. iii) The ancilla a can be again prepared in the state $|0\rangle_a$ for further corrections, thus allowing the quantum computer to overcome decoherence and perform further complex computations. iv) The last step, measure of the ancilla, can be avoided: this can be accomplished by defining another unitary interaction, namely C, that acts between Q and a (after the syndrome extraction) as follows $C(|s\rangle_a\,|\Phi\rangle) = |s\rangle_a\,M_s\,|\Phi\rangle$. Then the final state of the whole register becomes $|\Phi\rangle\sum_s |e_s\rangle\,|s\rangle_a$, thus transferring the "$Q + E$" entanglement onto an "$a + E$" entanglement (this procedure is illustrated in the Example 2, below).

The unitary operation that completes the QEC process, namely *recovery* "$\mathcal{R}$," in general establishes that for any $|\delta\rangle, |\delta_s\rangle \in$ "$E + a$", $\mathcal{R}(|\delta\rangle\,M_s\,|\Phi\rangle) = |\delta_s\rangle\,|\Phi\rangle$. In this sense, the main goal of QEC is to identify the set $\{|\Phi\rangle\}$, and the syndrome extraction A, in order to correct the noise introduced by M_s. In so doing, it suffices to find an orthonormal set of recoverable states (a subspace of Hilbert space) to be able to have a recoverable Hilbert space "$\mathcal{RH}$". Thus, QEC can be viewed as a *projection* of Hilbert system's space onto the recoverable Hilbert space. A *quantum codeword* $\{|j\rangle\}$ is a set of orthonormal quantum states that spans $\mathcal{RH}$. It turns out that A and $\mathcal{R}$ are possible if and only if the codewords satisfy $\langle j|\,M_m^\dagger M_n\,|k\rangle = 0$, and $\langle j|\,M_m^\dagger M_n\,|k\rangle = \langle k|\,M_m^\dagger M_n\,|j\rangle$, $\forall\, M_s \in \mathcal{S}$, and $\langle j|k\rangle = 0$ [124] [15]. For concrete examples of QEC code constructions, see,

---

[13] This is because s is in a one-to-one correspondence with M_s.

[14] The transformation M_s^{-1} is accomplished by means of a sequence of single qubit quantum gates originated from the set $\{\sigma_x,\ \sigma_z$ or $-i\sigma_y\}$.

[15] Example 1 (*Bit-flip σ_x-error-correction*): suppose Q has three qubits, and a has two qubits. Let M_s be the bit-flip error generator σ_x. In this case, there are two orthonormal recoverable states: $|000\rangle$, and $|111\rangle$, thus *dim($\mathcal{RH}$)* = 2. The state $|\Phi\rangle = \alpha\,|000\rangle + \beta\,|111\rangle$ is a general recoverable state of Q. The noisy environment entangles the qubit register as follows:

$$|e_0\rangle\,(\alpha\,|000\rangle + \beta\,|111\rangle) + |e_1\rangle\,(\alpha\,|001\rangle + \beta\,|110\rangle) + |e_2\rangle\,(\alpha\,|010\rangle + \beta\,|101\rangle) + |e_3\rangle\,(\alpha\,|100\rangle + \beta\,|011\rangle)\ . \tag{2.39}$$

In this case, the syndrome extraction A consists of the following four CNOT gates, with "Q" ("a") as the control (target) system: $\mathrm{CNOT}_{14}\mathrm{CNOT}_{24}\mathrm{CNOT}_{15}\mathrm{CNOT}_{35}$. After this A-operation, the whole register "$Q + E + a$" is left in the state

$$|e_0\rangle|00\rangle_a(\alpha|000\rangle{+}\beta|111\rangle){+}|e_1\rangle|01\rangle_a(\alpha|001\rangle{+}\beta|110\rangle){+}|e_2\rangle|10\rangle_a(\alpha|010\rangle{+}\beta|101\rangle){+}|e_3\rangle|11\rangle_a(\alpha|100\rangle{+}\beta|011\rangle). \tag{2.40}$$

Next, a measurement of the ancilla a is performed. Hence, conditional to the measurement result, the following simple operations over the Q-qubits project back the system onto the noise-free state $|\Phi\rangle$: "do nothing," $\sigma_x^{(1)}$, $\sigma_x^{(2)}$, $\sigma_x^{(3)}$, if the ancilla measurement gives 00, 01, 10, or 11, respectively. As said, in the above procedure, the measurement step can be avoided by using Toffoli gates (see below), but in this case, with "a" ("Q") as the control (target) [26].

e.g., Refs. [25, 26, 119, 121] [16]. In Examples 1 and 2, the used codewords only allowed for the correction of either bit-flip (σ_x) or phase-flip (σ_z) errors. A general method that protects against a more general noise, say a combination of σ_x, σ_z, and $\sigma_x\sigma_z$ errors, has been described in Refs. [26, 119, 124], and is based on the 'dual code theorem.' Here, the essential point is to note that [26]

$$\tilde{H}\sum_{i\in C}|i\rangle = \frac{1}{\sqrt{2^k}}\sum_{i\in C^{\perp}}|i\rangle \tag{2.43}$$

where $\tilde{H} \equiv H_1H_2H_3\cdots H_n$ is the Hadamard transform applied to all the members, say n states, of a linear classical error correcting code C. The observation is that the action of $\tilde{H}$ over C produces another linear classical error-correcting code, the superposition of all the members of the dual code $C^{\perp}$. The dual $C^{\perp}$ is defined as the set of all vectors v such that $v \cdot u = 0\ \forall u \in C$. Hence, as long as both C and $C^{\perp}$ have good classical error correction properties, it can be shown that it is possible to correct both σ_x and σ_z errors (and hence errors involving the two of them, i.e., $\sigma_x\sigma_z$) by using states of the type given in Eq. (2.43) [26]. For more details regarding this code construction, the reader is referred to Refs. [26, 119] [17].

---

[16] Example 2 (*Phase-flip σ_z-error-correction*): a single-phase-error-correcting-code that uses three qubits has the following two quantum codewords (encoding)

$$\begin{aligned} H(|000\rangle) &= \tfrac{1}{\sqrt{2}}(|0\rangle+|1\rangle)\otimes\tfrac{1}{\sqrt{2}}(|0\rangle+|1\rangle)\otimes\tfrac{1}{\sqrt{2}}(|0\rangle+|1\rangle) \equiv |\bar{0}\bar{0}\bar{0}\rangle \\ H(|111\rangle) &= \tfrac{1}{\sqrt{2}}(|0\rangle-|1\rangle)\otimes\tfrac{1}{\sqrt{2}}(|0\rangle-|1\rangle)\otimes\tfrac{1}{\sqrt{2}}(|0\rangle-|1\rangle) \equiv |\bar{1}\bar{1}\bar{1}\rangle\ . \end{aligned} \tag{2.41}$$

Next, let's illustrate how to perform QEC without realising the final ancilla measurement operation, i.e., by means of quantum gates only. Suppose one is given the state $|\Phi\rangle = \alpha|0\rangle + \beta|1\rangle$ (system "Q") that needs to be protected against phase decoherence (in this example it is assumed that only single-qubit dephasing errors occur). In so doing, an ancilla "a" of two qubits is introduced. Next, the register "$Q + a$" is encoded following the codeword given before. For illustrative purposes, let's assume that the environment interaction 'dephases' the second qubit only. Then, the decohered state becomes (the normalisation factor $2^{-3/2}$ has been ommitted)

$$\alpha(|0\rangle+|1\rangle)(|0\rangle|e_0\rangle+|1\rangle|e_1\rangle)(|0\rangle+|1\rangle)+\beta(|0\rangle-|1\rangle)(|0\rangle|e_0\rangle-|1\rangle|e_1\rangle)(|0\rangle-|1\rangle)\ . \tag{2.42}$$

The syndrome extraction A (decoding) is then built from two CNOT gates and a Toffoli gate, as shown in the schematic below, thus correcting the phase error and recovering the original state $|\Phi\rangle$. Note that while $|\Phi\rangle$ is a noise-free state, the final ancilla state $|u\rangle_a = |00\rangle(|e_0\rangle+|e_1\rangle)+|10\rangle(|e_0\rangle-|e_1\rangle)$ becomes entangled with the environment.

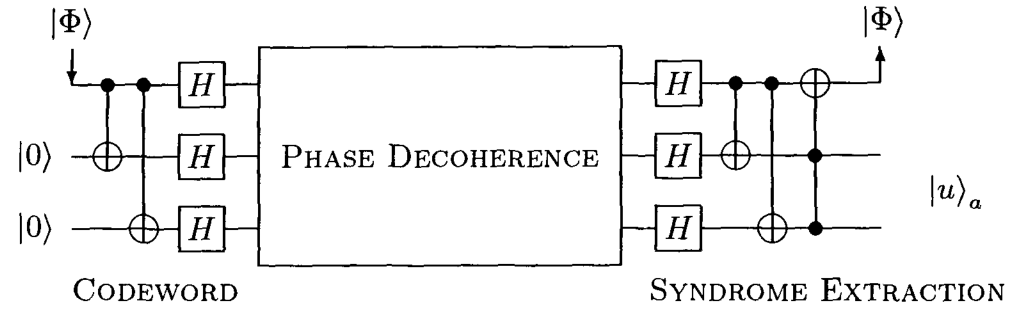

[17] Example 3 (σ_x, σ_z, *&* $\sigma_x\sigma_z$*-error correction*): The construction of codes following the above recipe

In conclusion, the method of QEC is mainly a matter of finding sets of states $|\Phi\rangle$, and the syndrome extraction A that allows one to suppress the influence of noisy environments M_s. Most of this work has been done by revisiting existing classical error-correcting codes. The theory of quantum error-correcting codes has been established within a general framework in Ref. [124]. Quantum error-correction and stabilisation schemes have been built on the work of Shor [25], Steane [26], Calderbank and Shor [119], and the later work reported in Refs. [120, 121, 123, 125]. There is an important issue that has been left out of the discussion presented above: the effect of the proper quantum gates, ancilla, and measurements realised by the QEC method. How perfect must they be in order to do a proper job of error correction instead of introducing further noise and imprecision to the system $Q + a$? Fortunately, the answer to this problem has been dealt with satisfactorily in what has been termed fault-tolerant QEC [126, 127, 128, 129]. It was initially proposed by Shor [126] and Kitaev [127], and the central idea was to perform a convenient design of all the required logic gates where the evolving states are verified wherever possible, and the syndrome extraction repeated. In this way it is guaranteed that the QEC method "corrects more noise than it introduces." These ideas have been conveniently reviewed in Ref. [129], where it has been estimated that a requirement for reliable quantum fault-tolerant computation is that the quantum hardware used in the computations must have a decoherence per qubit per gate below a finite threshold. This has been estimated at 10^{-5} to 10^{-2} [128, 129]. In addition, fault-tolerant computation allows a quantum computer that is built from qubits that undergo spontaneous emission decay with lifetime τ_{rel} to perform a complex quantum computation: the quantum coherence can be preserved for a period of order $10^4\tau_{rel}$ [128]. This counter-intuitive result

---

are referred to in the literature as CSS codes (for Calderbank, Shor, and Steane). This method leads to a single-error-correcting quantum code that has the following parameters: $[[\, n, 2k-n, d \,]] = [[7,1,3]]$. The notation indicates that the length of the codewords is n, there are 2^{2k-n} orthonormal quantum codewords, and d is the 'minimum distance' of the code (the minimum number of places in which each word differs from all others). Hence, the prescribed code requires 7 qubits in order to store and protect a single qubit. The simplest CSS code is obtained from the classical Hamming code, and has the following two orthogonal codewords [26]

$$\begin{aligned} |c_0\rangle &\equiv |0000000\rangle+|1010101\rangle+|0110011\rangle+|1100110\rangle+|0001111\rangle+|1011010\rangle+|0111100\rangle+|1101001\rangle \;, \\ |c_1\rangle &\equiv \sigma_x^{(1111111)}\,|c_0\rangle \;. \end{aligned} \tag{2.44}$$

The superscripts indicate that the bit-flip operation must be performed on each qubit of each single codeword. It is worth pointing out that the above description is not the most general possible theory of QEC. The most general treatment of QEC codes has been developed in Refs. [123, 124, 125]. It turns out that there are more efficient quantum code constructions. In fact, Laflamme *et al.* [121] and Bennett *et al.* [122] have provided a 5-qubit single-error-correcting code that produces the same control as CSS's code, but with the advantage that it requires only 5 qubits to do the job. This $[[5,1,3]]$ code has been referred to as a "perfect quantum code" [121, 122, 125]. Hence, an arbitrary quantum state $|\Phi\rangle = \alpha\,|0\rangle + \beta\,|1\rangle$ that is encoded by using 4 additional ancillary qubits (prepared in the state $|0\rangle$), using a $[[5,1,3]]$ encoding, can evolve in the presence of a general quantum noise (σ_x, σ_y, and $-i\sigma_z$-errors) in such a way that by the end of the computation it can be extracted completely free of noise from the 5-qubit system: that is, if at any stage of the computation, something 'wrong' happened to its coherence, the encoding guarantees that by the end of the computation, $|\Phi\rangle$ is error-free, and completely disentangled from the environment!

means that quantum coherence is preserved even though the qubits may have relaxed (and been re-excited) 10^4 times during the execution of the computations [128].

In this section, only the method of QEC for correcting quantum noise has been presented. However, there have been different, complementary, proposals for suppressing, e.g., dynamical methods, or avoiding decoherence, e.g., decoherence-free subsystems. These alternatives will be reviewed in Chapter 6, where the evolution of decoherence of a quantum register in a noisy environment is studied in detail. In particular, here it is shown that under certain conditions —the collective decoherence coupling— it is possible to find a subspace of Hilbert's system space whose states evolve in a decoherence-free fashion [JHR5]. From this point of view, one can argue that for arbitrarily complex quantum computations to ever be implemented in the laboratory, a combination of stabilisation schemes, such as fault tolerant QEC, decoherence-free subsystems, and dynamical methods to combat decoherence, must be incorporated to the quantum registers dynamical evolution.

Next, the practicalities of QIP are to be introduced, with particular emphasis on quantum dots technology, which, regarding quantum hardware, is one of the main subjects of this thesis.

2.1.6 Physical qubits

A quantum computation demands a coherent quantum evolution, and an active control or manipulations of the qubits, which are to be performed via unitary operations. In this section, a brief discussion of some of the hardware currently available for quantum information processing is given.

Cavity QED: originally proposed by Pellizzari *et al.* [30], this hardware design is based on the idea of trapping neutral atoms inside a small high finesse optical cavity. Here, the quantum information is stored in the internal states of the atoms, which interact with each other via the coupling to the normal modes of the electromagnetic field in the cavity. By means of pulsed lasers, a transition in one atom can be induced as a result of the internal state of another atom, thus performing conditional dynamics. The first experimental attempt at producing these type of quantum gates was realised by Turchete *et al.* [31]. A variant of this scheme is that proposed by Cirac *et al.* [32, 33], allowing a further step: quantum communication. Here, instead of using a photon to couple the atoms, the quantum information is stored in the polarisation of the photon, and the trapped atoms are used as mediators of the interaction amongst the photons via high-Q optical cavities and optical fibres [32, 33]: in this way, quantum information can be transferred between separated atoms (e.g., ion traps, see below), in order to produce photon based logic gates (e.g., phase shift gates, see Ref. [33]). More recently, other proposals involving QED effects for quantum logic have been given in Refs. [34, 35].

Ion traps: proposed by Cirac and Zoller, this scheme has single ions confined in a linear Paul trap as the qubit system [27]. Thus, the qubit states can be represented as $|g\rangle \equiv |0\rangle$, and $|e\rangle \equiv |1\rangle$, the ground state, and a (long-lived metastable) excited state respectively. This ion system is very well shielded from the environment: almost spontaneous decay is the main source of decoherence. The preparation and measurement of corresponding (initial and final) states is easily accomplished by methods of optical pumping and laser cooling, and by means of 'quantum jump' or 'electron shelving' measurement technique, respectively [28].

Single qubit gates are performed via individually addressing the ions with pulsed lasers tuned at the transition frequency ω. This originates Rabi oscillations between the qubit states $|0\rangle$, and $|1\rangle$. Thus, arbitrary single-qubit gates can be performed by an appropriate timing and choosing of the laser phase.

Conditional logic gates rely on a beautiful but rather more complicated effect. The interactions in the ion trap are mainly given by the Coulomb repulsion between the ions. This implies a spectrum of coupled normal modes of vibration for the trapped ions, and the absorption or emission of a laser photon by the ion can be tailored in such a way that a normal mode involving many ions recoils coherently. The lowest frequency vibrational mode (frequency μ) is the centre-of-mass (cm) mode. Via laser cooling, these ions can be kept at an energy $k_B T << \hbar\mu$, hence guaranteeing that each vibrational mode occupies its quantum ground state. The next step, the generation of a "cm phonon," is crucial to this scheme: by shining an ion, say the nth, with a properly timed laser pulse of frequency $\omega - \mu$, the state $|e\rangle_n$ can be made to evolve into $|g\rangle_n$ at a cost of the transition $|0\rangle_{cm} \rightarrow |1\rangle_{cm}$ of the cm oscillator. This operation transforms

$$|g\rangle_n |0\rangle_{cm} \rightarrow |g\rangle_n |0\rangle_{cm} ; \quad |e\rangle_n |0\rangle_{cm} \rightarrow -i\, |g\rangle_n |1\rangle_{cm} \ , \tag{2.45}$$

thus, inducing an interaction between the ions via the collective state of motion of all the ions (the produced cm phonon). Next, the quantum information must be transferred from the cm phonon to the internal state of one of the ions, thus completing the logic gate. This procedure must be tailored in such a way that the cm mode returns to its ground state by the end of the computational process. It has been shown that this hardware design requires 5 appropriately tailored laser pulses in order to produce conditional CNOT gates [27]. The experimental preparation, single gate realisation, and measurement for a single trapped ion was first demonstrated in Ref. [28]. Another ion trap-based scheme for quantum computation has led to the experimental demonstration of up to four qubits (atoms) entanglement [29].

Nuclear magnetic resonance: this hardware design has provided the first few-qubit quantum processors realised in the laboratory, and so far, is in the lead as far as the achievement of a coherent manipulation of qubits is concerned. The most recent experiment has involved 7 qubits, in order to demonstrate the simplest possible case of Shor's factoring algorithm [40]. This hardware scheme uses nuclear magnetic resonance (NMR) technology. The qubits are now represented by the nuclear spins in a particular molecule, where the spin states "up" or "down" serve as qubits. By placing the molecule in a large magnetic field, these nuclei spin states can be manipulated by applying oscillating magnetic fields in pulses of controlled duration. These qubits have very long decoherence and relaxation times. As said, Rabi oscillations of the spin can be induced by applying a pulsed rotating magnetic field of frequency ω (the energy splitting between the spin-up and spin-down states). Arbitrary single-qubit gates can be realised by an appropriate timing of this pulse. This process works in the presence of all of the molecule spins because only the spins on resonance respond to such an excitation. Two-qubit gates can be performed via the dipole-dipole spin interaction. Since the energy splitting between qubit states $|\uparrow\rangle$, and $|\downarrow\rangle$ for one spin depends on the state of neighbouring spins, the application of a resonant pulse that affects one spin is conditioned on the state of another spin. This produces the required conditional dynamics. For experimental demonstrations, see, e.g., Refs. [36, 37, 38, 39, 40].

Major drawbacks of the NMR computers stem from their intrinsic scalability problems (the ratio of the coherent signal to the background declines exponentially with the number of spins per molecule), and from the fact that individual qubits can neither be directly prepared nor measured (only the average state of many processors is detectable).

Optical lattices & Bose-Einstein condensates: the recent experimental observation of a quantum phase transition from a superfluid to a Mott insulator in an ultracold gas has opened the way to a new hardware perspective [42, 43, 44]. By creating an optical lattice, a light-wave interference pattern which gives rise to an energy landscape of mountains and valleys, a gas of rubidium atoms can be reversibly switched from a superfluid to an insulating phase [44], where the rubidium atoms of the condensate have two different behaviours. They can either i) share the same quantum state in the superfluid phase and move freely between valleys, or ii) remain trapped in an individual valley, as a result of an increase in the intensity of the laser beams, which force the gas into an insulating phase.

This phase transition was predicted to occur in an optical lattice by Jaksch *et al.* [43], where conditional dynamics and quantum entanglement has been proposed in moving trap potentials as a result of cold controlled collisions between two atoms. The experimental possibility of switching back and forth between superfluid and insulating behaviour brings an exciting development. In particular, the ideal array of single atoms in the insulating phase could prove useful for quantum computing. Here, the two internal states (magnetic moment) of the rubidium atoms can represent the qubit states $|0\rangle$, and $|1\rangle$. Scalability can be guaranteed due to the large number of rubidium atoms in the optical lattice, which can serve as a quantum memory. Thus, the proposal given in Ref. [43] has the potential for performing quantum computation. This is an emerging hardware perspective that deserves further exploration.

Quantum dots & solid-state systems: the hardware designs corresponding to these technologies will be addressed in the next section.

Time scales: the figure of merit $\mathcal{M} \equiv \tau_{dec}/\tau_{gate}$ for comparing some of the different technologies currently used in quantum information processing is given in Table 2.1. This figure of merit gives the largest number of elementary operations that can, in principle, be performed on the register states before decoherence takes over. The gating time τ_{gate}

is the minimum time required to execute an elementary gate. This has been estimated as $\hbar/\Delta E$, where ΔE is the energy splitting between the qubit states $|0\rangle$, and $|1\rangle$. τ_{dec} is the corresponding qubit phase coherence time (some of the values have been taken from Ref. [86]).

Quantum hardware	τ_{gate} (s)	τ_{dec} (s)	$\mathcal{M}$
Trapped ions [28, 29]	10^{-5}	10^{-1}	10^{4}
Optical cavities	10^{-14}	10^{-5}	10^{9}
Nuclear spin	10^{-3}	10^{4}	10^{7}
Cavity QED [31, 35]	10^{-9}	10^{-3}	10^{6}
Electron spin	10^{-7}	10^{-3}	10^{4}
Excitons [66, 67]	10^{-14}	10^{-10}	10^{4}

Table 2.1: Characteristic 'gating,' and dephasing time scales for comparing different physical systems currently used as qubits. The figure of merit $\mathcal{M}$ gives an estimation of the number of qubit operations that could be realised on a qubit register before it decoheres.

2.2 Quantum dots

Nanostructures are structures (e.g., solid state, biological, chemical, etc.) with dimensions of the order of nanometres (10^{-9} m). Quantum dots [57, 58, 59, 149] are solid state structures on the same nanometre scale which exhibit properties similar to those of 'real atoms' (0.1 nm scale), as a result of a strong spatial confinement in all three dimensions. Thus, these nanostructures are often referred to as "artificial atoms," or "superatoms." The atomlike properties of QDs include an electronic shell structure, Rabi oscillations [65], photon antibunching [75, 79], quantum light emitters [77, 78], and quantum entanglement [JHR1, 53]. What makes quantum dots so interesting arises from the possibility of tailoring their physical properties in the laboratory: shape, dimensions, energy levels structure, and the number of confined electrons can all be controlled experimentally. This offers a wide variety of physical phenomena to be studied at both theoretical and experimental levels. In particular, the possibility of studying few-particle effects in QDs with a small number of electrons (1 to 1000) [149] contrasts with the traditional methods of many-body (10^{23}) effects of condensed matter [180].

Excitons are electronic excitations which play a fundamental role in the optical properties of dielectric solids. They correspond to a bound state of one electron and one hole (*e-h* pair) which can be created by light or can appear as a result of relaxation processes of free electrons and holes. There are two models conventionally used to classify excitons: the small-radius Frenkel exciton model and the large-radius Wannier-Mott exciton model. Frenkel excitons in organic crystals have radii comparable to the lattice constant $a \approx 5$Å. Wannier excitons in semiconductor quantum wells have large Bohr radii: $a_B \approx 100$ Å in III-V materials (e.g., GaAlAs), and $a_B \approx 30$ Å in II-VI ones (e.g., ZnSe).

This thesis proposes a quantum dot model where exciton degrees of freedom are exploited for the processing of quantum information. Currently available exciton dephasing and relaxation times are of the order of 40 ps, and 1 ns, respectively [61, 62]. Although these excitations pose the main disadvantage of having relatively short dephasing times, QDs with stronger confinement where the coupling to phonons is minimised, and an improvement in the experimental techniques required for growth of the samples are expected to *increase* the dephasing time, such that the necessary requirements for information processing are better fulfilled. Indeed, there has been a recent experimental demonstration of 'ultralong' dephasing times in InGaAs QDs [66]: the measured dephasing time is *several hundred picoseconds* (only a few μeV homogeneous broadening). Thus, this remarkable result offers the possibility of having both τ_{dec} and τ_{rel} on the same *nanosecond* time scale, which in turn, should enable a practical demonstration of exciton-based quantum information processing, as proposed in this thesis. Analogous long lived coherence times have also recently been reported in Ref. [67]

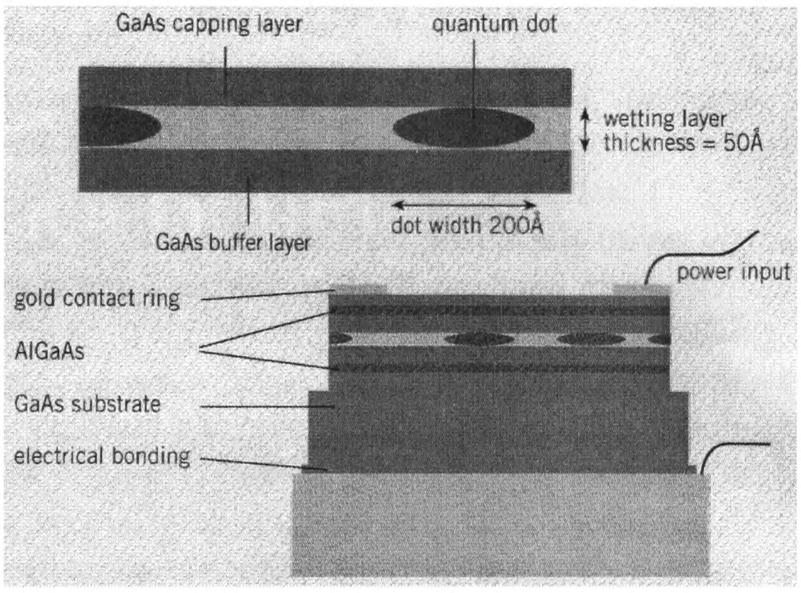

Figure 2.2: Schematic of a quantum dot array. The dots of the figure are formed in a wetting layer, sandwiched between two GaAs layers. Barrier layers of AlGaAs and gold electric contacts complete the structure. The figure is adapted from Ref. [58].

2.2.1 Background to fabrication and involved physical processes

The dimensionality of a given nanostructure system plays a fundamental role in determining its intrinsic properties and associated physical effects. Thus, three-dimensional systems can be reduced to two-, one-, and zero-dimensional structures by means of a strong spatial localisation in which the electrons are free to move on a plane, a line, or completely confined to a quasi-zero dimensional structure. The two-dimensional structure corresponds to the so-called *quantum well* (made by shrinking the third dimension of the confining region, say, the z-direction), which has provided an interesting architecture with which to study the dynamics of the associated two-dimensional electron gas (2DEG). The physical picture of a quantum well is a very thin, flat layer of semiconductor sandwiched between two layers of another semiconductor with a higher conduction-band energy [58]. The most common material used for such a purpose is gallium arsenide, GaAs, where the electrons are confined by the higher energy bandgap (barrier) of surrounding $Al_xGa_{1-x}As$ layers, thus forming very thin epitaxial layers. A structure made with quantum wells 2 nm wide produces light with a wavelength of about 740 nm, as compared to 880 nm for bulk GaAs. Further to this is the *quantum wire*, a nanostructure that confines the electrons in a quasi-one-dimensional structure, which can be produced by etching the sample that contains the quantum well, via accurate lithographic techniques [58].

A logical progression of this dimensionality reduction is the complete quantisation of the electron's motion as a result of its confinement to a quasi-zero-dimensional nanostructure: the so-called *quantum dots*, and one of the main subjects of this thesis. As said, a quantum dot behaves as a superatom in the sense that all the electrons occupy discrete energy levels. Quantum dots can be produced experimentally individually, or in arrays (see fig. 2.2). By tailoring their geometry, a quasi-three, two, or one-dimensional behaviour can be produced.

There are a wide variety of techniques which exploit the recent advances in semiconductor fabrication and processing that can be used for the creation of quantum wires and dots. They can be referred to as two main varieties: i) a "top-down" approach to QD fabrication imposes additional confining potentials on an electron gas in a semiconductor. Starting from a heterostructure with confined quasi 2DEG sandwiched between two semiconductor layers, a quantum dot can be built by *etching* away semiconductor material around a circular mask placed on top of the heterostructure. Another method employs a negatively charged electrode containing a hole: placing this electrode on top of the heterostructure creates a pool of electrons under the hole. Thus, this approach can be realised via a spatially modulated electric field (lithographic techniques), or by interdiffusion between the barrier and the quantum well. In contrast, ii) a "bottom-up" aproach exploits the current capabilities of manipulating single atoms using a Scanning Tunneling Microscope, or even via selective growth, or self-organised growth. This latter approach includes also the formation of QDs in the form of semiconductor microcrystals. Figure 2.2 shows the schematic of dots grown by self-assembly. The above-mentioned techniques allow for a control of the quantum dot shape, size, structure of the energy levels, and the number of confined electrons.

Transport and optical processes: Current QDs experimental studies include transport- and optical-based processes. Optical studies involve a QD excitation spectrum that is explored by purely optical means, such as absorption and emission of light, usually in the visible or far infra-red range because QDs absorb and emit light in a very narrow spectral range, hence the energy separation between the different excited electrons is of the order of a few meV. This is to be contrasted with the case of real atoms, where this energy separation is of the order of eV. In optical based experiments there is no physical connection or tunneling of electrons between neighbouring QDs. In contrast, transport processes involve the physical transfer or tunneling of electrons between dots, as a result of contacts between them and attached electric gates [149]. Thus, transport processes have the disadvantage that the dynamics of the electrons in the dots may be affected by the presence of the electrons in the nearby contacts [152].

The quantum dot proposals for QIP given in this thesis involve *only* optical processes; thus, avoiding the need for electric gates and contacts which certainly introduce additional sources of exciton qubit decoherence.

2.2.2 Experimental state-of-the-art: quantum wave function engineering and quantum light emitters

Quantum control and wave function engineering: a remarkable degree of quantum control in QDs nanostructures is now possible due to the recent advances in coherent nonlinear optical spectroscopy of *single* excitons [60, 61, 62] in *single* quantum dots. This is an outstanding achievement given the size and precision required for such measurements. Previous experiments have typically been forced to measure over an ensemble of dots. Ref. [62] reports the presence of inter-dot energy transfer—this Förster process is a key ingredient in the design of some QIP schemes reported in this thesis. The coherent optical control of the excitation of a single quantum dot on a short time-scale compared to the time-scale for the loss of quantum coherence has also been reported [61]: this allows the realisation of 'wavefunction engineering' developed earlier in atomic and molecular systems, to monitor and control a non-stationary quantum-mechanical state composed of a superposition of eigenstates [61]. Further to this, there has been a recent experimental demonstration of ultralong exciton dephasing times in InGaAs and self-assembled QDs [66, 67]. Phase decoherence of the order of several hundred picoseconds are now currently available for the exciton based scheme for quantum information processing given in this thesis.

In contrast, practical aspects regarding optical NMR from single GaAs quantum dots have also been reported [144]. These dots were formed by interface fluctuations in GaAS/GaAlAs quantum wells. The NMR from constituent Ga and As nuclei was optically detected on excitonic recombination, exploiting the hyperfine coupling between the electronic and nuclear stystems. These experimental results are relevant to the proposal given in Chapter 5.

Thus, reliable control of individual quantum dots can indeed be carried out, toward a level of precision normally associated with atomic systems. The quantum dot excitations, such as a single exciton, on a given dot can be manipulated with minimal loss of coherence using state-of-the-art ultrafast optical techniques. The underlying nuclear spins in the quantum dot can also be controlled with the same optical techniques, via the electron-nucleus coupling. Furthermore, the experimental results of Ashoori *et al.* [148] and others, demonstrate that few electron (i.e., $N \geq 2$) can indeed be prepared, and their ground-state transitions measured as a function of external magnetic field. As will be seen in this thesis, these remarkable experimental achievements are very significant contributions to the goal of realising solid-state based quantum information.

Another important experimental development is that achieved by *near-field* optical spectroscopy. This allows the study of the optical properties of semiconductor nanostructures with spatial resolutions well beyond the diffraction limit of light [64]. This complements the possibilities given by ultrafast optical spectroscopy in the optical study of individual quantum dots, thus enabling, for example, the direct measurement of excitonic and biexcitonic luminiscence from single dots. Figure 2.3 shows a schematic of the set-up used to scan such optical properties of single dots within an entire ensemble of dots.

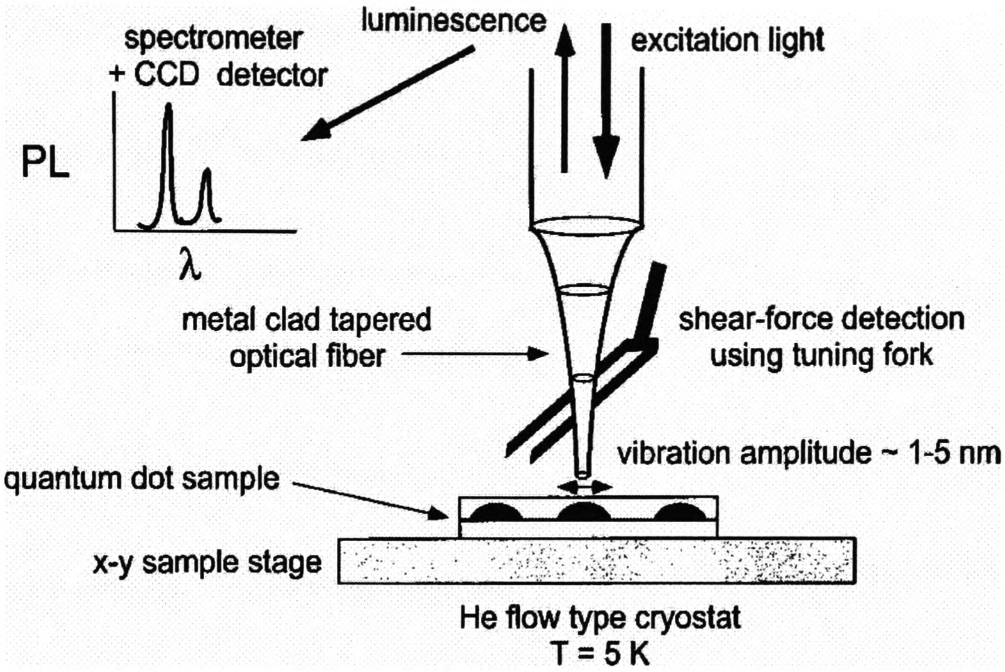

Figure 2.3: Schematic of a nanoprobing (scanning near-field optical probing) system used to measure the near-field luminescence properties of quantum dots at low temperatures. This near-field probe can scan, dot-by-dot, the optical properties of an entire ensemble of dots. The figure is adapted from Ref. [64].

More recently, there has been a further achievement in the control of the optical coherence of quantum dot states. This has been achieved by Guest *et al.* [60] by realising a near-field coherent optical spectroscopy and microscopy of quantum dots. Thus, the above-described techniques have been unified in a single and unique experimental approach. This is a remarkable step in the design and engineering of quantum states in quantum dots, from which the prospects for the physical realisation of quantum computing become more realistic.

Photon emitters: There has recently been an experimental observation of photon antibunching from an artificial atom (a single CdSe/ZnS quantum dot) [75], i.e., the detection of quantum correlations among photons from a single quantum dot. This has also been achieved in optical studies of the fluorescence from single atoms and molecules [76]. Furthermore, it has been demonstrated that under optical pulse excitation, a single QD can emit a single photon per excitation pulse [77, 78]. This has direct implications for quantum cryptography because it means that a single QD can serve as a *quantum light emitter* [77]. Even more recently, measurements of temporal correlations among photons emitted at various wavelengths from a continuous wave (cw) optically excited single-QD have demonstrated that a quantum dot is not only a source of single photon emission, but also a source of *multicolor* photons, such that the correlation among these emitted photons can be manipulated via the cw excitation power, and hence the transition from photon antibunching (low power excitations) to photon bunching (high excitation power) can be observed [79], as illustrated in Fig. 2.4. Here, the results of the measured intensity auto- and cross-correlation functions $g_{ij}^{(2)}(\tau)$ are reported for different excitation powers.

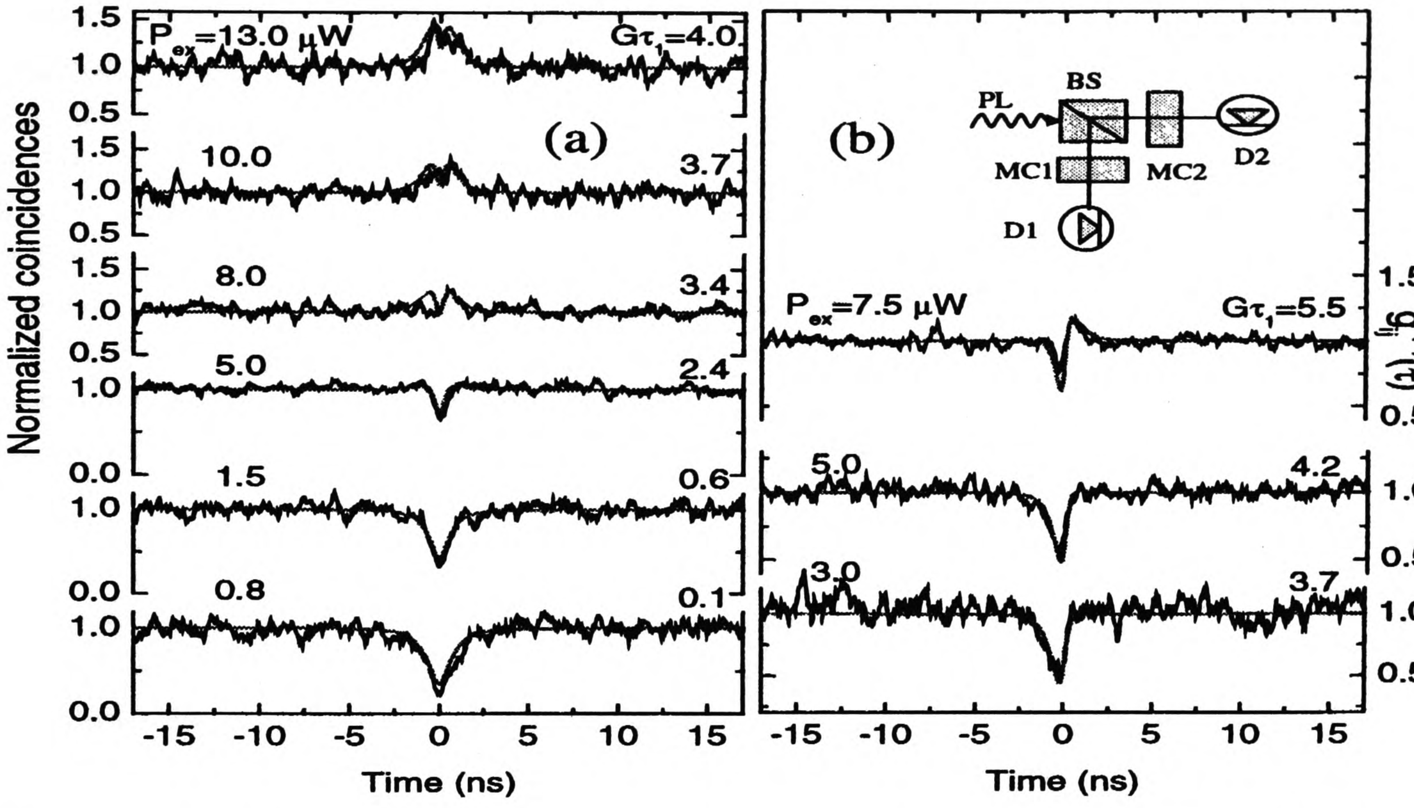

Figure 2.4: Intensity (a) auto- and (b) cross-correlation functions between photons due to the recombination of *e-h* pairs. (a) *Monochromatic* photons: X^0 line auto-correlation function $g_{11}^{(2)}(\tau)$ (as a function of cw excitation power): this gives the probability of finding the QD occupied with a single exciton at time τ after the emission of the previous X^0 photon. (b) *Multicolor* photons: intensity cross-correlation between the emitted photons from the nX^S line and the photons from the X^0 line for increasing cw excitation power. In both plots, thick (thin) solid lines correspond to measured (calculated) values. The figure is adapted from Ref. [79].

Fig. 2.4(a) shows the autocorrelation function $g_{11}^{(2)}(\tau)$ for the X^0 spectral line[18], which is associated with the radiative recombination of the first excited electron-hole (*e-h*) pair (exciton) that is generated after increasing the cw excitation power. It is clear from Fig. 2.4(a) that, for low excitation power, the emitted photons are *antibunched* (the

---

[18] In general, the correlation function $g_{ij}^{(2)}(\tau)$ can be formally expressed as

$$g_{ij}^{(2)}(\tau) = \frac{\langle I_i(t) I_j(t+\tau)\rangle}{\langle I_i(t)\rangle\langle I_j(t)\rangle} \,, \tag{2.46}$$

where $I_k(t)$ is the emission intensity at a wavelength corresponding to the recombination of a kth multiexciton at a given time t. Thus, $g_{ij}^{(2)}(\tau)$ gives the probability that, at time τ, a photon arising from the exciton recombination process that involves j *e-h* pairs is emitted (after the emission that involves the i *e-h* pairs has occurred). The indexes i, j correspond to the spectral lines which are monitored on the two channels of a Hanbury-Brown and Twiss (HBT) set-up that includes a beam splitter which divides the PL emission from the QD into two equal beams [79], as shown in the inset of Fig. 2.4(b). Thus, the set-up allows the measurement of the intensity correlation function among photons emitted at various wavelengths [79]. If $i = j$, the same spectral line is monitored on both channels and hence $g_{ij}^{(2)}(\tau) \equiv g^{(2)}(\tau)$, the second order temporal coherence function.

probability of simultaneous detection of two photons is zero), while for higher excitation power, the X^0 line emission intensity decreases, and the emitted photons are now *bunched.* Thus, a transition from photon antibunching to bunching is observed as the cw excitation power is increased. In contrast, Fig. 2.4(b) shows a measurement of the temporal intensity cross-correlation function between the emitted photons from the X^0 and the nX^S spectral lines for various excitation powers, where nX^S denotes a collective n pair state, the redshifted PL lines (S stands for the analogy with the atomic shells, the first energy level). Here, a more complex behaviour is observed: the cross-correlation function between different wavelength (*multicolor*) photons produces, as a function of the cw excitation power, an asymmetric antibunching-to-bunching behaviour.

The experimental achievements described before may prove useful when looking at the observation of photon correlations arising from entangled QDs and their relevance to exciton-based quantum information processing, as analysed in the next chapter.

2.2.3 Kohn theorem and properties of an interacting system

An important result regarding the properties of an interacting electron system is due to Kohn [68]. Roughly speaking, this establishes that the cyclotron-resonance frequency of an electronic system does not depend on the form of the interaction potential [68]. This result is yielded provided that the separation or decoupling of the centre-of-mass motion from the dynamics of the relative motion in the interacting, say quantum dot, system is possible. It can be shown that a general system of N interacting electrons that is described by the Hamiltonian

$$H = \sum_{i=1}^{N} \left\{ c_0 + c_1 \boldsymbol{r}_i + c_2 \boldsymbol{p}_i + c_3 \boldsymbol{r}_i^2 + c_4 \boldsymbol{p}_i^2 + c_5 \boldsymbol{r}_i \times \boldsymbol{p}_i \right\} + \sum_{i<j}^{N} V_{\rm int}(\boldsymbol{r}_i - \boldsymbol{r}_j) \; , \qquad (2.47)$$

can indeed be split into a sum of two main Hamiltonians, which are expressed in terms of the centre-of-mass and the relative motion variables [58], namely $H_{\rm cm}$ and $H_{\rm rel}$. Hence, $[H_{\rm cm}, H_{\rm rel}] = 0$. Thus, provided that the Hamiltonian (2.47) contains terms that are linear and quadratic in coordinates and momenta, and linear in angular momenta, and provided that the interaction potential is only a function of the distance between particles, the centre-of-mass motion decouples from the relative motion. Then, the following results take place: i) the centre-of-mass (CM) excitation spectrum does not depend on the number of particles, and ii) the particles relative motion is decoupled from far infra-red (FIR) radiation. This means that exciting an N-electrons quantum dot with electromagnetic radiation in the FIR range affects the CM motion but does not produce any effect over the particles relative motion at all [58]. A model for performing qubit control for quantum logic based on a few electron two-dimensional parabolic quantum dots in a magnetic field and FIR radiation is proposed in Chapter 5.

2.2.4 Solid state qubits

There is much current excitement about the possibility of using solid-state based devices for the achievement of quantum computation tasks. In particular, semiconductor nanostructure fabrication technology is well developed and hence offers us a wide and promising arena for the challenging project of building quantum information processors. The quantum mechanical nature, the high degree of engineering and quantum control of individual wavefunctions of solid-state systems, besides intrinsic scalability properties, make quantum dots very promising candidates for the physical implementation of QIP.

The intense research activity in this field makes any attempt of reviewing it become obsolete almost immediately after is written! There are several different proposals that consider different physical degrees of freedom as representative of qubit systems. I shall mention here only the most relevant solid state design schemes for quantum computation proposed to date: Kane [41] has proposed a scheme which encodes information onto the nuclear spins of donor atoms (like P) in doped silicon electronic devices where externally applied electric fields are used to perform logical operations on individual spins. Privman *et al.* [50] suggests controlling the hyperfine electron-nuclear interaction via the excitation of the electron gas in quantum Hall systems. Loss and DiVincenzo [51] have presented a scheme based on electron spin effects, in which coupled quantum dots are used as a quantum gate. This scheme is based on the fact that the electron spins on the dots have an exchange interaction J which changes sign with increasing external magnetic field. Vrijen *et al.* [52] considered electron spin resonance transistors in Silicon-Germanium heterostructures: one and two qubit operations are performed by applying a gate bias.

The above proposals, however, require the attachment of electrodes or gates to the sample in order to manipulate the nuclear spin qubit. Such electrodes are likely to have an invasive effect on the coherent evolution of the qubit, thereby destroying quantum information. In Chapter 5 [JHR2] an NMR solid-state based mechanism for quantum computation free from these shortcomings is proposed.

Possible quantum gate implementations have also been proposed by Barenco *et al.* [49] by considering electronic charge effects in coupled QDs, however this scheme has as the main disadvantage rapid phonon decoherence, as compared with the above proposals. More recently, Imamoglu *et al.* [34] have considered a quantum computer model based on both electron spins and cavity QED which is capable of realising controlled interactions between two distant QD spins. In their model, the effective long-range interaction is mediated by the vacuum field of a high finesse microcavity, and single qubit rotations and CNOT operations are realised using electron-hole Raman transitions induced by classical laser fields and the cavity mode.

A different scheme exploits the exciton degrees of freedom of a QD system in order to generate an entangling network setup by exploiting (Förster) resonant energy transfer processes between coupled QDs [JHR1, 53]. This proposal is analysed in detail in Chapter 3. Similar schemes to this, that also exploit exciton degrees of freedom for quantum computation, have been presented in Refs. [54, 55].

2.3 Discussion

A conciliation of the two main sections of this chapter, theoretical aspects of quantum information and hardware engineering or quantum technology, is the main challenge that has to be faced for a true practical demonstration of QIP, and in particular for large scale quantum computations. Here, an overview of the main hardware implementations available to date has been given. At this stage in the 'race' for the construction of, at least, a 'small quantum computer,' bulk liquid NMR systems have been pushing forward the main experimental demonstrations via a coherent manipulation of up to seven qubits [40] where quantum logic gates have been realised allowing the demonstration of basic quantum algorithms such as those of Deutsch [39], and Shor [40], for a quantum register of size $n = 7$ or less. However, it is rather obscure whether such systems will be scalable to many qubits, neither is there an effective process for individual qubits access and readout, as required by a true quantum computer. Thus, despite the fact that this quantum hardware allows quantum logic gates to be applied at will for a few qubits system, it does not offer the scalability potential, and hence it is very unlikely to succeed in the long term. In contrast, the ion trap proposal of Cirac and Zoller [27] offers both appropriate decoherence time and good scalability prospects. The main drawback of this proposal is that the hardware system is intrinsically very slow. The demonstration of basic quantum logic gates for a few qubits has also been achieved in such systems.

When compared with the above-mentioned QIP systems, quantum dots-based proposals are still in a very embryonic stage. As discussed, only single qubit gates have been achieved so far by means of exciton Rabi oscillations in single dots [65]. However, QDs intrinsic scalability properties, their ultrafast operation, and in particular, the recent demonstration of much longer exciton dephasing times (a few nanoseconds) [66, 67] pave the way for a more solid and stronger prospect for quantum dot-based, and particularly within this hardware, for exciton-based quantum information processing. This thesis provides practical proposals that should allow for the experimental demonstration of such a processing. It is certainly a privilege to be part of the new era of coherent manipulation and quantum engineering of quantum information.

Thus, it is hoped that the proposals given in this thesis will stimulate experimental work in the field of QIP, particularly at the interface between quantum optics and the solid state. Whether the task of building a true quantum computer is ever going to be achieved still remains an open question. In particular, the final goal of building a solid state quantum computer will be extremely challenging. Along this process, many basic physical issues, both theoretical and experimental, will need to be addressed and fully understood, with quantum decoherence being one of the main obstacles to such a purpose.

In the following chapters, this thesis considers several different schemes for the processing of solid-state based quantum information, and a detailed study of the decoherence of quantum registers.

Chapter 3

Quantum entanglement of artificial molecules

As highlighted in the previous chapter, quantum entanglement is of fundamental interest to many quantum information processing protocols. To cite a few examples, quantum teleportation, quantum key distribution, and superdense coding, rely for their entire success on the reliable generation and manipulation of quantum entanglement. In this sense, entanglement has been recognised as an invaluable resource for quantum communication. In particular, Bell and GHZ maximally entangled states are at the heart of fundamental discussions, such as the violation of Bell's inequalities [2, 7], and the "non-locality" problem [3, 4].

This chapter shows how the (Förster) resonant energy transfer process between spatially separated excitons can be exploited to produce maximally entangled states of two (Bell) and three (GHZ) optically-driven QDs, starting from suitably initialised states. Previous experiments have studied entangled states of trapped ions [27, 28, 29], and photons [31, 34, 35], but to our knowledge, there is not such a scheme for producing deterministic entanglement in a semiconductor nanostructures setup. In the proposal given here, the recent experimental results involving *coherent wavefunction control* of excitons in semiconductor quantum dots on the nanometer and femtosecond scales [60, 61, 62, 63, 64] are exploited, i.e., the system requirements can be realised with current experiments employing both ultrafast and near-field optical spectroscopy of quantum dots. These experimental techniques, as well as the recent developments in the task of engineering coherent QDs wavefunctions were discussed in detail in Section 2.2.

In Section 2.1.3, the basic definitions regarding the quantification of the degree of entanglement of a given quantum system were given. Thus, the formal theoretical framework and the motivation for studying entanglement in a concrete physical system have already been introduced. Next, the optically-driven system considered in this chapter is described, and a prescription to generate reliable exciton entanglement using such a setup is given.

3.1 Generation of maximally entangled states in optically-driven quantum dots

Consider a system of N identical and equispaced quantum dots, containing no net charge, which are radiated by long-wavelength classical light (see Figure 3.1). If two of these QDs are sufficiently close, there is a resonant energy transfer process originating from the Coulomb interaction whereby an exciton can hop between dots [130]. Experimental evidence of such energy transfers between quantum dots was reported recently [62]; the resonant process also plays a fundamental role in biological and organic systems, and is commonly called the Förster process [72, 131]. Unlike usual single-particle transport measurements, the Förster process does not require the physical transfer of the electron and the hole, just their energy. Hence it is relatively insensitive to the effects of impurities which lie between the dots. This chapter shows how such a system can be exploited in order to generate highly entangled QD states.

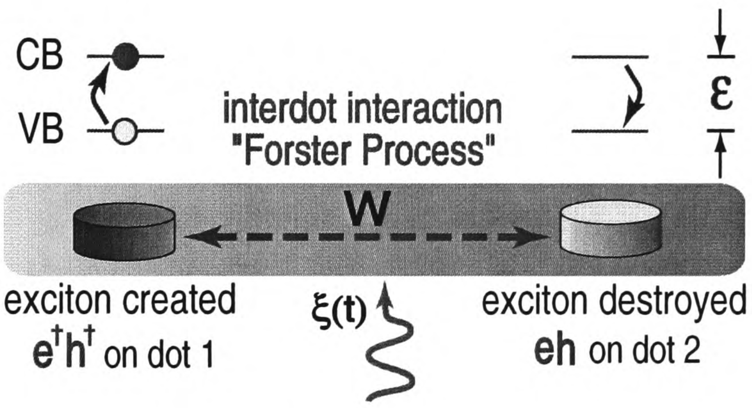

Figure 3.1: Schematic of the optical setup for the $N = 2$ QDs system. The identical QDs, containing no net charge, are radiated with long-wavelength classical light of central frequency ω, $\xi(t) = Ae^{-i\omega t}$. Formation of single excitons within the individual QDs and their inter-dot hopping in the presence of the Förster interaction are illustrated schematically. The bandgap ϵ as well as the conduction band (CB) and the valence band (VB) of the system are also sketched.

3.1.1 Wave function and unitary evolution

This section shows how to generate maximally entangled states of two and three qubits of the form $|\Psi_{\textsc{bell}}(\varphi)\rangle = \frac{1}{\sqrt{2}}(|00\rangle + e^{i\varphi}|11\rangle)$ and $|\Psi_{\textsc{ghz}}(\varphi)\rangle = \frac{1}{\sqrt{2}}(|000\rangle + e^{i\varphi}|111\rangle)$, for arbitrary values of the phase factor φ[1], using a semiconductor nanostructure set-up. Here, 0 (1) denotes a zero-exciton (single exciton) QD. Recall, from what was said in Section 2.1.3, that in order to generate the Bell-basis states, it suffices to generate one of them, say, the state $|\phi^+\rangle \equiv |\Psi_{\textsc{bell}}(0)\rangle$, provided that single qubit transformations such as σ_x, and σ_z are available and can be applied to it. Also, recall that these Bell-basis (GHZ) states can be generated from the "ground state" $|00\rangle$ ($|000\rangle$) via the application of entangling gates, e.g., $\textsc{cnot}_{12}H_1(|00\rangle) \equiv |\phi^+\rangle$ $[\textsc{cnot}_{13}\textsc{cnot}_{12}H_1(|000\rangle) \equiv |\Psi_{\textsc{ghz}}(0)\rangle]$,

---

[1] Throughout this chapter, this phase factor is referred to as the "φ-pulse," to denote the type of entangled state generated in the optical process.

to the input state. Hence, the generation of the entangled states given here can be viewed as the realisation of small entangling gates involving single- and two-qubit unitary transformations.

As previously mentioned, the model presented in this thesis considers a system of N QDs which are radiated by long-wavelength classical light. Hence, formation of single excitons within the individual QDs and their inter-dot transfer can be described, in the frame of the rotating wave approximation (RWA), by the Hamiltonian[2] [JHR1] ($\hbar = 1$ throughout this chapter)

$$H(t) = \tfrac{\epsilon}{2}\sum_{p=1}^{N}\left(c_p^\dagger c_p - h_p h_p^\dagger\right) + \tfrac{W}{2}\sum_{p,p'=1}^{N}\left(c_p^\dagger h_{p'} c_{p'} h_p^\dagger + h_p c_{p'}^\dagger h_{p'}^\dagger c_p\right) + \xi(t)\sum_{p=1}^{N} c_p^\dagger h_p^\dagger + \xi^*(t)\sum_{p=1}^{N} h_p c_p \,, \tag{3.1}$$

where $c_p^\dagger$ ($h_p^\dagger$) is the electron (hole) creation operator in the pth quantum dot, ϵ is the QD band gap, W the interdot interaction, and $\xi(t)$ the laser pulse shape. The operators involved in Eq. (3.1) obey the anticommutation rules $\{c_{p'}, c_p^\dagger\} = \{h_{p'}, h_p^\dagger\} = \delta_{pp'}$. By introducing the pseudo-spin operators

$$J_+ = \sum_{p=1}^{N} c_p^\dagger h_p^\dagger, \quad J_- = \sum_{p=1}^{N} h_p c_p, \quad \text{and} \quad J_z = \tfrac{1}{2}\sum_{p=1}^{N}\left(c_p^\dagger c_p - h_p h_p^\dagger\right) \,, \tag{3.2}$$

Eq. (3.1) adopts the form

$$H(t) = H_0 + H_L(t) \,, \tag{3.3}$$

where

$$\begin{aligned} H_0 &= \epsilon J_z + W(J^2 - J_z^2) \,, \\ H_L(t) &= \xi(t) J_+ + \xi^*(t) J_- \,, \end{aligned} \tag{3.4}$$

with $J^2 \equiv \frac{1}{2}(J_+J_- + J_-J_+) + J_z^2$. The J_i-operators obey the usual angular momentum commutation relations $[J_z, J_\pm] = \pm J_\pm$, $[J_+, J_-] = 2J_z$, and $[J^2, J_+] = [J^2, J_-] = [J^2, J_z] = 0$. Note that, in going from Eq. (3.1) to Eq. (3.3) we have switched from a dot-selective (index p) to a non-selective description. Hence, the quantum dynamical problem associated with the time evolution of any initial state under the action of $H(t)$ is described by:

$$i\partial_t|\Psi(t)\rangle_S = [H_0 + H_L(t)]|\Psi(t)\rangle_S \,, \tag{3.5}$$

where the subscript S indicates Schrödinger picture. In the description given here, a laser pulse shape $\xi(t) = Ae^{-i\omega t}$, where A gives the electron-photon coupling and the incident electric field strength, is considered.

Let us introduce the unitary transformation $\Lambda(t) = e^{-i\omega J_z t}$: this allows one to go from the *laboratory frame* (LF) to the *rotating frame* (RF), by using the rule $|\Psi(t)\rangle_\Lambda = \Lambda^\dagger(t)\,|\Psi(t)\rangle_S$. Hence, Eq. (3.5) can be rewritten as:

$$i\partial_t\,|\Psi(t)\rangle_\Lambda = H'\,|\Psi(t)\rangle_\Lambda \,, \tag{3.6}$$

---

[2] The constant term $\frac{W}{2}\sum_p\{c_p^\dagger c_p + h_p h_p^\dagger\} = \frac{WN}{2}$ has been ommitted.

with

$$H' = \Delta_\omega J_z + W(J^2 - J_z^2) + AJ_+ + A^* J_- \ . \tag{3.7}$$

Here, $\Delta_\omega \equiv \epsilon - \omega$ is the detuning parameter. Let us note the relevance of the Λ transformation: the new Hamiltonian H' is time-independent. From a practical point of view, parameters A and Δ_ω are adjustable in the experiment to give control over the system of QDs (and hence over the qubits). Since J^2 commutes with the operators $J_\pm$, H' may be diagonalised separately in each one of these J-subspaces. Consider the $\{J, q\}$ subspace spanned by $|M\rangle \equiv |J, M; q\rangle$: the only possible values for J are $\frac{N}{2}, \frac{N}{2} - 1, \ldots, \frac{1}{2}$ or 0, and for each $J-$fixed value, we have $2J + 1$ different values for M, which are given by $M = -\frac{N}{2}, -\frac{N}{2} + 1, \ldots, \frac{N}{2} - 1, \frac{N}{2}$. The label q is introduced to further distinguish the states: $q = 1, 2, \ldots, D_J$, where the multiplicity D_J, i.e., the number of states having angular momentum J and $M = J$, is given by

$$D_J = \frac{2J+1}{J + \frac{N}{2} + 1} \begin{pmatrix} N \\ \frac{N}{2} + J \end{pmatrix} \ . \tag{3.8}$$

The product states $\prod_{k=1}^N |m_k\rangle \equiv |m_1, ..., m_N\rangle$, with $J_z = \sum_k m_k$ form a 2^N-dimensional basis which spans the Hilbert space $\mathrm{SU}(2)^{\otimes \mathrm{N}}$. In this basis, the 2^N eigenvalues of H' are obtained by diagonalising the Hamiltonian matrix of elements $\langle J, M, q| H' |J', M', q'\rangle$. The following non-zero elements are then obtained

$$\begin{aligned} \langle M| H' |M'\rangle &= \left(\Delta_\omega M + W\left[J(J+1) - M^2\right]\right) \delta_{M,M'} \\ &\quad + A\sqrt{J(J+1) - M'(M'+1)} \ \ \delta_{M,M'+1} \\ &\quad + A^*\sqrt{J(J+1) - M'(M'-1)} \ \ \delta_{M,M'-1} \ . \end{aligned} \tag{3.9}$$

The matrix elements given in Eq. (3.9) provide us with the general rule for any number of QDs. Since the right side of this equation does not depend on q, one needs only to diagonalise a square matrix of side $2J+1$ for each J. Every eigenvalue so obtained occurs D_J times in the entire spectrum. Next, it is shown that solving the eigenfunction problem associated with Eq. (3.9), under prescribed initial conditions, leads to the generation of maximally N-entangled states of excitons in QDs.

3.1.2 Coupling of $N = 2$ QDs and generation of Bell states

In this section, the procedure for the generation of entangled Bell states $|\Psi_{\text{Bell}}(\varphi)\rangle = \frac{1}{\sqrt{2}}(|00\rangle + e^{i\varphi}|11\rangle)$ is described. Here, 0 (1) denotes a zero-exciton (single exciton) QD, and the direct product of the quantum states $|jk\rangle \equiv |j\rangle \otimes |k\rangle$ form a four-dimensional basis in the Hilbert space $\mathrm{SU}(2) \otimes \mathrm{SU}(2)$. In the $J = 1$ subspace[3], $M \equiv \{-1, 0, 1\}$. Let us define $|M_1\rangle \equiv |J = 1, M = -1\rangle \equiv |0\rangle$, $|M_2\rangle \equiv |J = 1, M = 0\rangle \equiv |1\rangle$, and $|M_3\rangle \equiv |J = 1, M = 1\rangle \equiv |2\rangle$, as the vacuum of excitons, the single-exciton state and the biexciton state, respectively. In the absence of light, the *energy levels* of the system look like

---

[3] In general, for $J = \frac{N}{2}$, the multiplicity $D_J = 1$, hence q is irrelevant. The equivalence between this "excitonic" basis and the computational basis $\mathcal{B}_2$ is given in Appendix B.

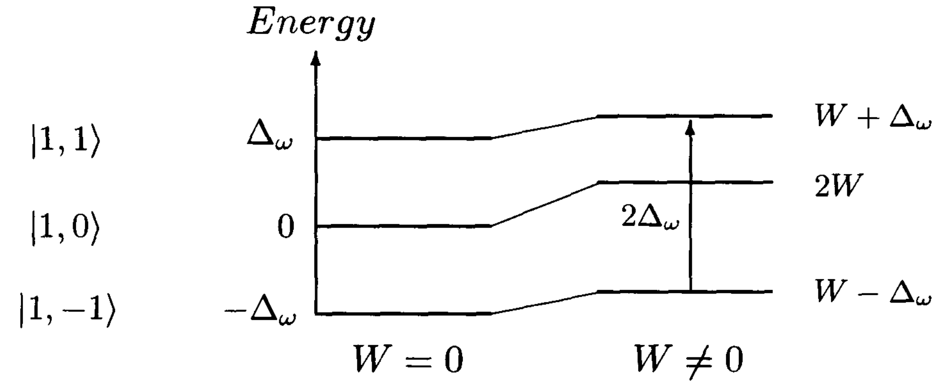

Figure 3.2: Schematic of the energy levels for our 2 QDs system in (a) the absence ($W = 0$), and (b) the presence ($W \neq 0$) of the interdot interaction, when there is no external light applied to the system. If the QDs are sufficiently close to each other, external laser pulses can induce a resonant energy transfer process and hence an exciton can hop between dots. Here, the triplet subspace $J = 1$ is considered as the only one optically active. The states $|J, M_i\rangle$ on the left are the associated kets of the $\{|M_i\rangle\}$ basis.

This is because, in general, for any (J, M)

$$E(J,M) = \Delta_\omega M + W\left[J(J+1) - M^2\right] , \qquad (3.10)$$

hence, the *energy levels* of the system are $E_0 \equiv E(1,-1) = W - \Delta_\omega$, $E_1 \equiv E(1,0) = 2W$, and $E_2 \equiv E(1,1) = W + \Delta_\omega$. Note that $E_{2,0} \equiv E_2 - E_0 = 2\Delta_\omega$ is unaffected by the interdot interaction strength W (see Figure 3.2).

Next, consider the action of the radiation pulse $\xi(t)$ over this pair of QDs. In the $\{|M_i\rangle\}$ basis defined above ($J = 1$ subspace), the Hamiltonian adopts the simple form:

$$\widehat{H'} = \begin{pmatrix} W-\Delta_\omega & \sqrt{2}A^* & 0 \\ \sqrt{2}A & 2W & \sqrt{2}A^* \\ 0 & \sqrt{2}A & W+\Delta_\omega \end{pmatrix} , \qquad (3.11)$$

where $A \equiv |A|\,e^{i\phi}$ defines the real amplitude and the phase of the electron-photon coupling. Diagonalisation gives the eigenenergies and eigenfunctions associated with Eq. (3.11). This yields

$$E^3 - 4WE^2 + \left(5W^2 - 4|A|^2 - \Delta_\omega^2\right)E + 2W\left(\Delta_\omega^2 + 2|A|^2 - W^2\right) = 0 , \qquad (3.12)$$

as the eigenenergy equation. In resonance, $\Delta_\omega \equiv 0$, hence Eq. (3.12) has solutions:

$$E_0 = W, \text{ and } E_{1,2} = \tfrac{1}{2}\left(3W \pm \sqrt{16|A|^2 + W^2}\right) . \qquad (3.13)$$

The eigenenergies for the case of an off-resonance pulse of light can also be found analytically. The result is

$$\begin{aligned} E_0 &= \tfrac{1}{6}\left\{-2\alpha + 2^{2/3} f(\alpha,\beta,\gamma)^{\frac{1}{3}} + 2^{4/3}(\alpha^2 - 3\beta) f(\alpha,\beta,\gamma)^{-\frac{1}{3}}\right\} , & (3.14) \\ E_1 &= \tfrac{1}{12}\left\{-4\alpha - 2^{2/3}(1 - i\sqrt{3}) f(\alpha,\beta,\gamma)^{\frac{1}{3}} - 2^{4/3}(1 + i\sqrt{3})(\alpha^2 - 3\beta) f(\alpha,\beta,\gamma)^{-\frac{1}{3}}\right\} , & \\ E_2 &= \tfrac{1}{12}\left\{-4\alpha - 2^{2/3}(1 + i\sqrt{3}) f(\alpha,\beta,\gamma)^{\frac{1}{3}} - 2^{4/3}(1 - i\sqrt{3})(\alpha^2 - 3\beta) f(\alpha,\beta,\gamma)^{-\frac{1}{3}}\right\} , & \end{aligned}$$

where $f(\alpha,\beta,\gamma) \equiv -2\alpha^3+9\alpha\beta-27\gamma+\sqrt{-4(\alpha^2-3\beta)^3+(2\alpha^3-9\alpha\beta+27\gamma)^2}$, $\alpha \equiv -4W$, $\beta = 5W^2 - 4\left|A\right|^2 - \Delta_\omega^2$, and $\gamma = 2W(2\left|A\right|^2 + \Delta_\omega^2 - W^2)$.

The eigenfunctions for the $N = 2$ problem are given by:

$$\left|E = E_k\right\rangle = \Gamma_k \left(\left|0\right\rangle + \tfrac{E_k+\Delta_\omega - W}{\sqrt{2}|A|} \left|1\right\rangle - \tfrac{2|A|^2+(2W-E_k)(E_k+\Delta_\omega - W)}{2|A|^2} \left|2\right\rangle \right) , \tag{3.15}$$

where $\Gamma_k = \sqrt{2}|A|/\sqrt{4|A|^2+(\Delta_\omega+W)(E_k+\Delta_\omega-W)}$, with E_k given as above ($k = 0, 1, 2$). The procedure described here enables us to find suitable laser pulse lengths required for generating the above-mentioned Bell states.

In general, for any value of N, the total wave function associated with the initial condition $\left|\Psi(t=0)\right\rangle = \left|\Psi_0\right\rangle$ can be expressed as $\left|\Psi(t)\right\rangle_\Lambda = \sum_k C_k \mathrm{e}^{-iE_k t}\left|\psi_k\right\rangle$, where $H'\left|\psi_k\right\rangle = E_k\left|\psi_k\right\rangle$, and $\left|\psi_k\right\rangle = \sum_j A_{kj}\left|M_j\right\rangle$. Here, the normalisation coefficients[4] C_k depend on the chosen initial condition $\left|\Psi_0\right\rangle$. The matrix elements A_{kj} must be determined for each particular value of N, and $\left|M_j\right\rangle \equiv \left|J, M_j; q\right\rangle$, as indicated earlier in this section. Hence, the total wave function $\left|\Psi(t)\right\rangle_\Lambda$ can be written as:

$$\left|\Psi(t)\right\rangle_\Lambda = \sum_k \sum_j C_k A_{kj} \mathrm{e}^{-iE_k t}\left|M_j\right\rangle . \tag{3.16}$$

For the case of $N = 2$ QDs, it is a straightforward exercise to compute the explicit coefficients of Eq. (3.16) for both of the J−subspaces that span the Hilbert space $\mathrm{SU}(2)\otimes\mathrm{SU}(2)$. Next, we centre our attention on the discussion of finding the conditions to produce the maximally entangled Bell states. To achieve this, we project the state $\left|\Psi_{\text{BELL}}\right\rangle$ over the wave function given by Eq. (3.16), thus obtaining the result

$$\left\langle \Psi_{\text{BELL}} \right| \Psi(t)\rangle_\Lambda = \tfrac{1}{\sqrt{2}} \sum_k C_k \left(A_{k1} + \mathrm{e}^{i\varphi}A_{k3}\right)\mathrm{e}^{-iE_k t} . \tag{3.17}$$

Under the unitary evolution of the Hamiltonian H', the density of probability $\wp(\text{BELL})$ for finding the entangled Bell state in this coupled QD system is proportional to $|(\langle 0| + \mathrm{e}^{i\varphi}\langle 2|)|\Psi(t)\rangle_\Lambda|^2$. More explicitly, one has

$$\wp(\text{BELL}) = \tfrac{1}{2}\left|\sum_k C_k \left(A_{k1} + \mathrm{e}^{i\varphi}A_{k3}\right)\mathrm{e}^{-iE_k t}\right|^2 . \tag{3.18}$$

Results and discussion of the time evolution described by Eq. (3.18), for several different combinations of the physical parameters in the model, are given in Section 3.2.

3.1.3 Coupling of $N = 3$ QDs and generation of GHZ states

This section addresses the problem of generating entangled GHZ states of the form $\left|\Psi_{\text{GHZ}}(\varphi)\right\rangle = \frac{1}{\sqrt{2}}(\left|000\right\rangle + \mathrm{e}^{i\varphi}\left|111\right\rangle)$, in the proposed system of 3 coupled QDs. In this

---

[4] Write $\left|\Psi(0)\right\rangle = \sum_k \beta_k \left|M_k\right\rangle$ $(\beta_k = \left\langle M_k \right|\Psi(0)\rangle)$. From the expansion given for $\left|\Psi(t)\right\rangle_\Lambda$, it follows that $\left|\Psi(0)\right\rangle = \sum_k C_k\left|\psi_k\right\rangle$, hence, the general expression for the coefficients C_k becomes $C_k = \left\langle \psi_k \right|\Psi(0)\rangle = \sum_j \beta_j \left\langle \psi_k \right| M_j\rangle = \sum_j \beta_j A^*_{kj}$.

case, the Hilbert space $SU(2)^{\otimes 3}$ is spanned by the eight basis vectors associated with the three different J-subspaces. Without loss of generality, consider the $J = \frac{3}{2}$–subspace as the only one optically active. We introduce the notation $|M_1\rangle \equiv |3/2, -3/2\rangle \equiv |0\rangle$, $|M_2\rangle \equiv |3/2, -1/2\rangle \equiv |1\rangle$, $|M_3\rangle \equiv |3/2, 1/2\rangle \equiv |2\rangle$, and $|M_4\rangle \equiv |3/2, 3/2\rangle \equiv |3\rangle$ to denote the vacuum state, the single-exciton state, the biexciton state, and the triexciton state, respectively.

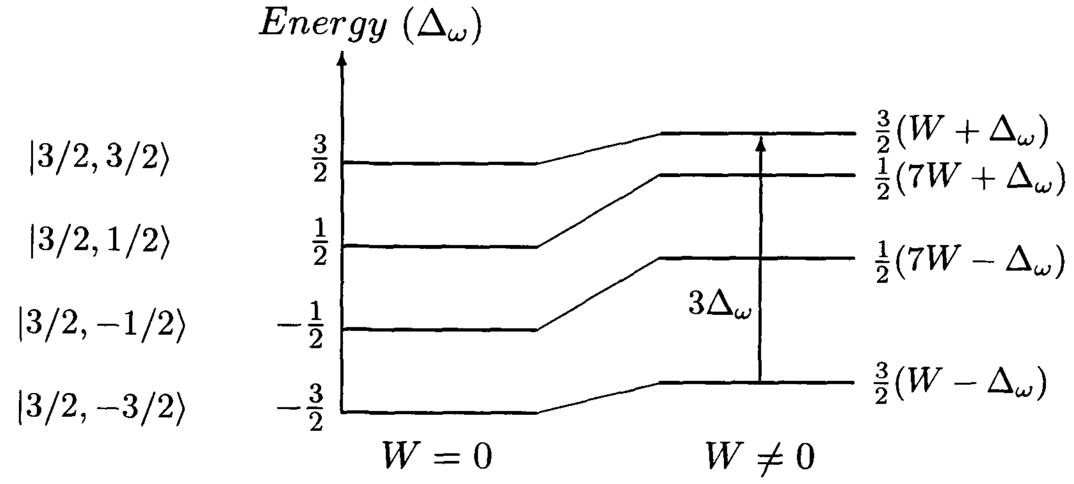

Figure 3.3: Energy diagram for the 3 QD system in the absence of external light, for (a) $W = 0$, and (b) $W \neq 0$ interdot interaction. The depicted energy levels are associated with the $J = 3/2$ subspace states of the $\{|M_i\rangle\}$ basis, whose kets are shown in the left-handside of diagram.

In the absence of light, the energy levels of the system are given by $E_0 \equiv E(3/2, -3/2) = \frac{3}{2}(W - \Delta_\omega)$, $E_1 \equiv E(3/2, -1/2) = \frac{1}{2}(7W - \Delta_\omega)$, $E_2 \equiv E(3/2, 1/2) = \frac{1}{2}(7W + \Delta_\omega)$, and $E_3 \equiv E(3/2, 3/2) = \frac{3}{2}(W + \Delta_\omega)$. Note that, as in the preceding section, the energy separation $E_{3,0} \equiv E_3 - E_0 = 3\Delta_\omega$ is unaffected by the interdot interaction strength W (see Figure 3.3).

Next, consider the effect of the pulse of light $\xi(t)$ over this system of 3 QDs. In the $J = \frac{3}{2}$-subspace of the $\{|M_i\rangle\}$ basis[5], the Hamiltonian reads:

$$\widehat{H'} = \begin{pmatrix} \frac{3W}{2} - \frac{3\Delta_\omega}{2} & \sqrt{3}A^* & 0 & 0 \\ \sqrt{3}A & \frac{7W}{2} - \frac{\Delta_\omega}{2} & 2A^* & 0 \\ 0 & 2A & \frac{7W}{2} + \frac{\Delta_\omega}{2} & \sqrt{3}A^* \\ 0 & 0 & \sqrt{3}A & \frac{3W}{2} + \frac{3\Delta_\omega}{2} \end{pmatrix} . \tag{3.19}$$

Diagonalisation leads us to the quartic order equation

$$\begin{aligned} &\left(\left[\tfrac{3}{2}(W - \Delta_\omega) - E\right]\left[\tfrac{1}{2}(7W - \Delta_\omega) - E\right] - 3|A|^2\right)\left(\left[\tfrac{3}{2}(W + \Delta_\omega) - E\right]\left[\tfrac{1}{2}(7W + \Delta_\omega) - E\right] - 3|A|^2\right) \\ &\quad = 4|A|^2 \left(\tfrac{3}{2}[W - \Delta_\omega] - E\right)\left(\tfrac{3}{2}[W + \Delta_\omega] - E\right) , \end{aligned} \tag{3.20}$$

---

[5] The other subspaces of this 2^3-dimensional Hilbert space are *two-fold* degenerate. The associated "$J = 1/2$ Hamiltonians" are given in Appendix B, where the most general Hamiltonian associated with any number of particles N is presented.

which is non-trivial to solve analytically in the case of a pulse with arbitrary frequency ω. However, if $\xi(t)$ is applied at resonance ($\Delta_\omega = 0$), the following eigenenergies are obtained

$$\begin{aligned} E_{0,1} &= \tfrac{5}{2}W + |A| \pm \sqrt{(W+|A|)^2 + 3\,|A|^2}\,, \\ E_{2,3} &= \tfrac{5}{2}W - |A| \pm \sqrt{(W-|A|)^2 + 3\,|A|^2}\,, \end{aligned} \tag{3.21}$$

with corresponding eigenvectors

$$|E_{0,1}\rangle = \eta_{0,1}\left(|0\rangle + \frac{E_{0,1}-\frac{3W}{2}}{\sqrt{3}|A|}\,|1\rangle + \frac{E_{0,1}-\frac{3W}{2}}{\sqrt{3}|A|}\,|2\rangle + |3\rangle\right)\ , \tag{3.22}$$

$$|E_{2,3}\rangle = \eta_{2,3}\left(|0\rangle + \frac{E_{2,3}-\frac{3W}{2}}{\sqrt{3}|A|}\,|1\rangle - \frac{E_{2,3}-\frac{3W}{2}}{\sqrt{3}|A|}\,|2\rangle - |3\rangle\right)\ , \tag{3.23}$$

where the coefficients $\eta_i = 1/\sqrt{2[1+(E_i-3W/2)^2/3|A|^2]}$ ($i = 0,...,3$) are normalisation constants. The associated total wave function $|\Psi(t)\rangle_\Lambda$ [Eq. (3.16)] depends on the chosen initial condition $|\Psi(t=0)\rangle \equiv |\Psi_0\rangle$, and is a linear combination of the eigenfunctions (3.22) and (3.23). We have computed, in both rotating and laboratory frames, the analytical expressions for $|\Psi(t)\rangle_\Lambda$, for several different initial conditions $|\Psi_0\rangle$. As an example of this procedure, the result for the zero-exciton state as the initial state, i.e., $|\Psi_0\rangle = |M_1\rangle \equiv |0\rangle$, is given. In this case, the wave function $|\Psi(t)\rangle_\Lambda$ is spanned by the following coefficients C_k and A_{kj}

$$C_0 = \frac{E_1 - \frac{3W}{2}}{2\eta_0\,(E_1 - E_0)},\ C_1 = \frac{E_0 - \frac{3W}{2}}{2\eta_1\,(E_0 - E_1)},\ C_2 = \frac{E_3 - \frac{3W}{2}}{2\eta_2\,(E_3 - E_2)},\ C_3 = \frac{E_2 - \frac{3W}{2}}{2\eta_3\,(E_2 - E_3)}\ , \tag{3.24}$$

$$\widehat{A} \equiv \begin{pmatrix} \eta_0 & \frac{(E_0-\frac{3}{2}W)\mathrm{e}^{i\varphi}}{\sqrt{3}|A|}\eta_0 & \frac{(E_0-\frac{3}{2}W)\mathrm{e}^{i2\varphi}}{\sqrt{3}|A|}\eta_0 & \mathrm{e}^{i3\varphi}\eta_0 \\ \eta_1 & \frac{(E_1-\frac{3}{2}W)\mathrm{e}^{i\varphi}}{\sqrt{3}|A|}\eta_1 & \frac{(E_1-\frac{3}{2}W)\mathrm{e}^{i2\varphi}}{\sqrt{3}|A|}\eta_1 & \mathrm{e}^{i3\varphi}\eta_1 \\ \eta_2 & \frac{(E_2-\frac{3}{2}W)\mathrm{e}^{i\varphi}}{\sqrt{3}|A|}\eta_2 & -\frac{(E_2-\frac{3}{2}W)\mathrm{e}^{i2\varphi}}{\sqrt{3}|A|}\eta_2 & -\mathrm{e}^{i3\varphi}\eta_2 \\ \eta_3 & \frac{(E_3-\frac{3}{2}W)\mathrm{e}^{i\varphi}}{\sqrt{3}|A|}\eta_3 & -\frac{(E_3-\frac{3}{2}W)\mathrm{e}^{i2\varphi}}{\sqrt{3}|A|}\eta_3 & -\mathrm{e}^{i3\varphi}\eta_3 \end{pmatrix} . \tag{3.25}$$

Hence, the density of probability $\wp(\mathrm{GHZ})$ of finding the entangled GHZ state between vacuum and triexciton states is given by

$$\wp(\mathrm{GHZ}) = \tfrac{1}{2}\left|\sum_k C_k\left(A_{k1} + \mathrm{e}^{i\varphi}A_{k4}\right)\mathrm{e}^{-iE_k t}\right|^2 . \tag{3.26}$$

Analytical and numerical computations have been performed for several different initial conditions $|\Psi_0\rangle$. These results enable us to obtain specific conditions for the realisation of such maximally entangled GHZ states starting from suitable φ-pulses, and experimental parameters ϵ, W, and A. Details are discussed below.

The quantum dynamical problem given by Eq. (3.5) can be easily expressed in terms of the expansion coefficients $d_M(t)$ of the wave function. As usual, we write $|\Psi(t)\rangle_\Lambda = \sum_{M=-J}^{J} d_M(t)\mathrm{e}^{-iE_M t}\,|M\rangle$, so the time dependent problem is reduced to finding the solutions of the following set of $2J+1$ linear differential equations

$$\begin{aligned} i\partial_t d_M(t) &= A\sqrt{J(J+1)-M(M-1)}\ \exp\Big([E_M - E_{M-1} - \omega]it\Big)d_{M-1}(t) + \\ &\quad A^*\sqrt{J(J+1)-M(M+1)}\ \exp\Big([E_M - E_{M+1} + \omega]it\Big)d_{M+1}(t)\ , \qquad (3.27) \end{aligned}$$

where $E_M = E(J,M) + \omega$. More explicitly, $E_{M,M-1} \equiv E_M - E_{M-1} = \epsilon + W\,[1-2M]$, $E_{M,M+1} = W\,[1+2M] - \epsilon$, hence the problem given by Eq. (3.27) can be expressed in terms of reduced units as follows

$$\begin{aligned} i\partial_\tau f_M(\tau) &= \lambda\sqrt{J(J+1)-M(M-1)}\ \exp\Big([1+\mu(1-2M)-\nu]i\tau\Big)f_{M-1}(\tau) + \\ &\quad \lambda^*\sqrt{J(J+1)-M(M+1)}\ \exp\Big(-[1-\mu(1+2M)-\nu]i\tau\Big)f_{M+1}(\tau), \qquad (3.28) \end{aligned}$$

with the dimensionless parameters $\lambda = \frac{A}{\epsilon}$, $\mu = \frac{W}{\epsilon}$, $\nu = \frac{\omega}{\epsilon}$, $\tau = \epsilon t$, and $d_M(t) \equiv f_M(\tau)$. The set of Eqs. (3.28) gives the dynamics for any number of QDs and (J,M)-values. Numerical solutions were found by varying the parameters λ, μ, and ν. Comparison between these numerical solutions and the analytical ones yields excellent agreement for the generation of both Bell and GHZ states, starting from suitable initial conditions $|\Psi_0\rangle$. Results will be addressed in the next section.

3.2 Results and discussion

This section discusses the main results obtained from the computation of both analytical and numerical solutions for the unitary evolution described in the preceding section. Figure 3.4 shows the probability density for finding the entangled Bell state ($N = 2$) between vacuum and biexciton states given by Eq. (3.18), as a function of time, for the initial condition $|\Psi_0\rangle = |0\rangle$. Here, several different selective pulses of light τ_{Bell} that produce the maximally entangled Bell state $|\Psi_{\text{Bell}}(\varphi = 0)\rangle \equiv |\phi^+\rangle$, in the system of two coupled QDs are shown. In these figures, energies are given in terms of the band gap ϵ: $W = 0.1$, and (a) $A = \frac{1}{25}$, (b) $A = \frac{1}{50}$, (c) $A = 10^{-2}$, and (d) $A = 10^{-3}$. Here, the energy W is kept fixed while the amplitude of the radiation pulse A is varied. As a result of this, the time τ_{Bell} increases with diminishing incident field strength A [JHR1]. Regarding the experimental generation of these Bell states, we suggest a consideration of wide-gap semiconductor QDs, like ZnSe based QDs, for instance. For these materials, the band gap $\epsilon = 2.8$ eV, which implies a resonant optical frequency $\omega = 4.3 \times 10^{15}$ s^{-1}. Femtosecond spectroscopy is currently available for these systems [63]. For a 0 or 2π-pulse, $W = 0.1$, and $A = \frac{1}{25}$, Fig. 3.4(a) shows that the generation of the state $\frac{1}{\sqrt{2}}(|0\rangle + |2\rangle)$ requires a pulse of length $\tau_{\text{Bell}} = 7.7 \times 10^{-15}$ s. By changing the value of the amplitude A [see Figs. 3.4(b), (c) and (d)], the length τ_{Bell} of this Bell pulse can be tailored, i.e., a new A implies a new value for τ_{Bell}: from Fig. 3.4 it can be seen that τ_{Bell} can be tailored

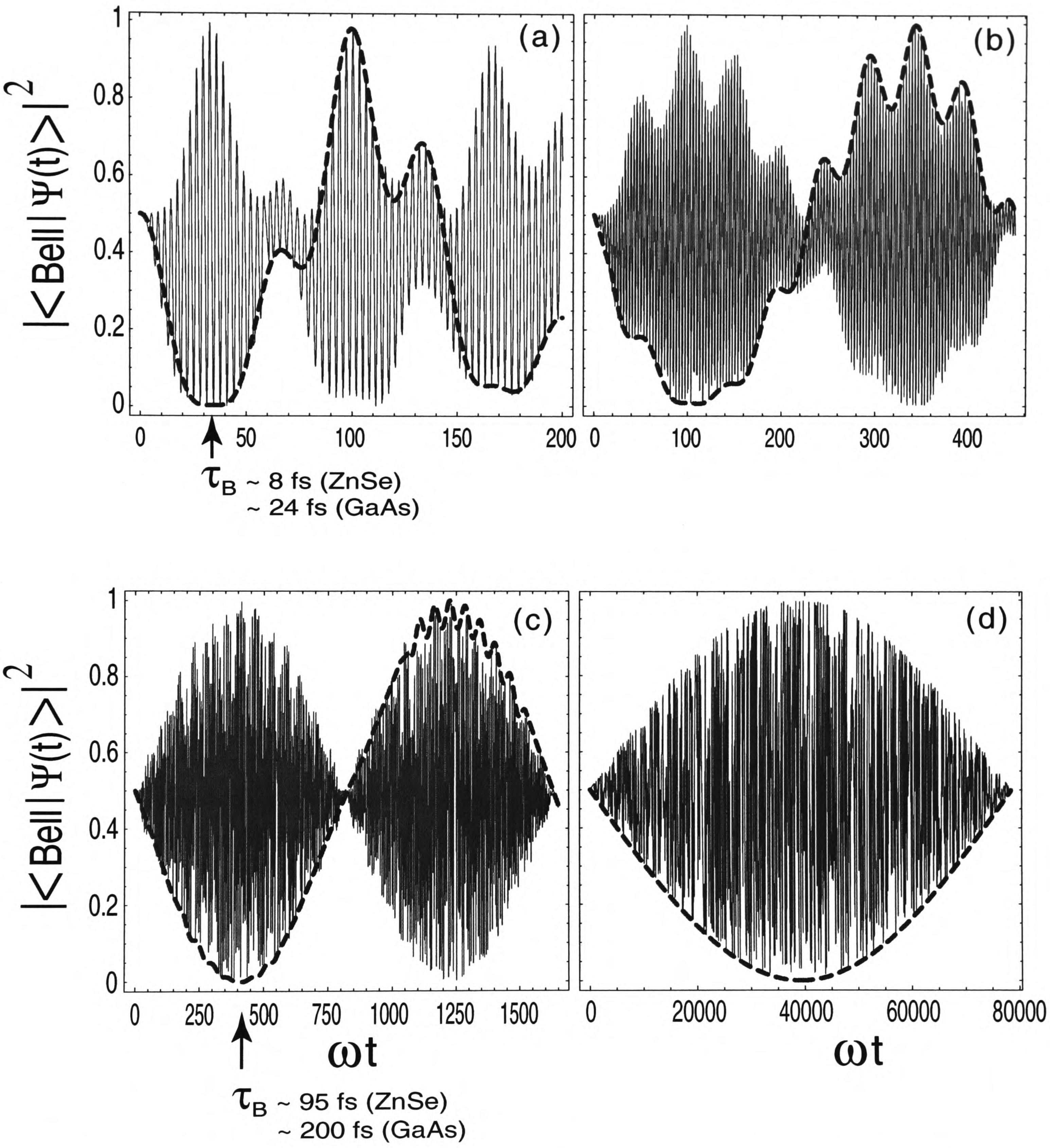

Figure 3.4: Generation of the Bell State $|\phi^+\rangle = \frac{1}{\sqrt{2}}(|00\rangle + |11\rangle)$. The τ_{BELL}-pulses shown here correspond to the implementation of a Hadamard transform followed by a quantum CNOT gate: $\text{CNOT}_{12}H_1$. $W = 0.1$, $\varphi = 0$, and (a) $A = \frac{1}{25}$, (b) $A = \frac{1}{50}$, (c) $A = 10^{-2}$, and (d) $A = 10^{-3}$. $|\Psi(t)\rangle$ denotes the total wavefunction of the system at time t, in both laboratory (solid curves) and rotating frames (dashed curves). The energy is in units of the band gap ϵ, and $|\Psi_0\rangle = |0\rangle$.

in such a way that reliable entangled state preparation can be performed in the time scale 10^{-15} s $< \tau_{\text{BELL}} < 10^{-11}$ s [JHR1], which is in agreement with currently available excitonic dephasing times [61].

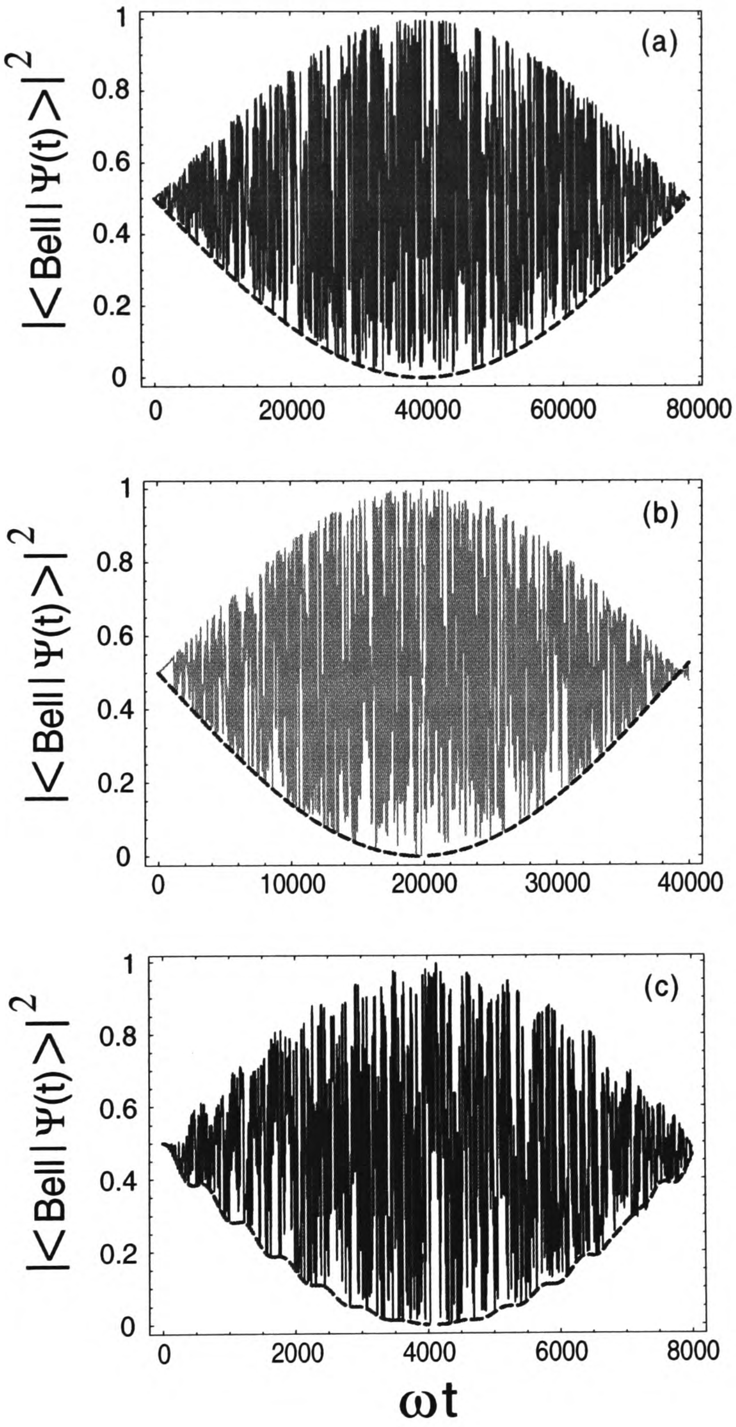

Figure 3.5: Generation of the Bell state $|\phi^+\rangle$. $A = 10^{-3}$, $\varphi = 0$, and (a) $W = 0.1$, (b) $W = 0.05$, and (c) $W = 10^{-2}$.

Figure 3.5 shows another method for manipulating the length τ_{BELL}: keeping the amplitude A fixed while varying W. Here, W is varied for a fixed $A = 10^{-3}$. The analysis shows that for this fixed value of A, the length τ_{BELL} decreases with decreasing interaction strength W [JHR1]. This latter procedure could be experimentally more expensive than the former, since the variation of W has to be tailored by changing the interdot distance and/or the radius of the dots. However, this method should offer an interesting experimental possibility for studying the Förster resonant energy transfer mechanism.

The same investigation of parameter dependence was performed for the case of the entangled GHZ state ($N = 3$) between vacuum and triexciton states. The probability given by Eq. (3.26) is calculated as a function of time, starting with the initial condition $|\Psi_0\rangle = |0\rangle$. Figure 3.6 shows the selective pulses used to create such maximally entangled GHZ states in the system of three coupled QDs. For example, in the case of Fig. 3.6(a), the generation of the GHZ state $\frac{1}{\sqrt{2}}(|0\rangle + |3\rangle)$ requires a time $\tau_{\mathrm{GHZ}} = 2.3 \times 10^{-14}$ s. Figures 3.6(b), (c), and (d) explore several different ranges for the τ_{GHZ}-pulses required in the generation of such GHZ states. For fixed W, the time τ_{GHZ} increases with decreasing incident field strength A. In contrast, for fixed A, the length τ_{GHZ} decreases with decreasing interdot interaction strength. It is worth noting that after the preparation step, which is determined by the length of the pulses τ_{BELL} and τ_{GHZ}, the Förster interaction parameter W, and the field strength A, the system will evolve under the action of the Hamiltonian (3.7) with $\Delta_\omega = A = 0$: each one of the maximally entangled states discussed here are eigenstates of this remaining Hamiltonian.

The above results are not restricted to ZnSe-based QDs: by employing semiconductors of different bandgap ϵ (e.g., GaAs[6], organic-inorganic systems), other regions of parameter space can be explored. We have studied the time evolution of the QD system for several different values of the phase φ. These give similar qualitative results to the ones discussed previously. Here, only the 0 or 2π-pulse results have been included since these are the ones relevant to the discussion presented in Sec. 3.4. The corresponding experimental conditions as well as the required coherent control to realise the above combinations of parameters are compatible with those demonstrated in Refs. [60, 61]. We point out that the procedure described in this chapter is valid for any value of the phase φ, in contrast to Ref. [53] where analytic results were derived for the particular case $\varphi = \frac{\pi}{2}$ (see next section). The generation of maximally entangled states presented in this chapter has considered the experimental situation of *global* excitation pulses, i.e., pulses acting simultaneously on the entire QD system. However, by using near-field optical spectroscopy [60, 64], individual QDs from an ensemble can be addressed by using local pulses, a feature that can be exploited to generate entangled states with different symmetries, such as the singlet (antisymmetric) state $|\psi^-\rangle \equiv \frac{1}{\sqrt{2}}(|01\rangle - |10\rangle)$. From a formal point of view, this can be done via the application of the single qubit transformations σ_x, and σ_z: first, perform the bit-flip of qubit one of $|\phi^+\rangle$, i.e., $\sigma_x^{(1)}(|\phi^+\rangle) \equiv |\psi^+\rangle$, and then perform the phase-flip (σ_z) of qubit 1 of $|\psi^+\rangle$, thus obtaining $|\psi^-\rangle$. Hence, we should be able to generate the so-called Bell basis of four mutually orthogonal states for the 2 qubits, all of which are maximally entangled, i.e., the set of states $\{|\phi^\pm\rangle, |\psi^\pm\rangle\}$. The experimental realisation of such a basis in the proposed solid state set-up given here should be of fundamental relevance to quantum communication protocols (e.g., quantum teleportation), and quantum computation. Currently, there is a lot of motivation to perform such implementations in the solid state, particularly because of the potential scalability of these nanostructure (QD) systems, which makes them promising candidates

---

[6] In the case of GaAs QDs, $\epsilon = 1.4$ eV, which implies a resonance optical frequency $\omega = 2 \times 10^{15}$ s^{-1}.

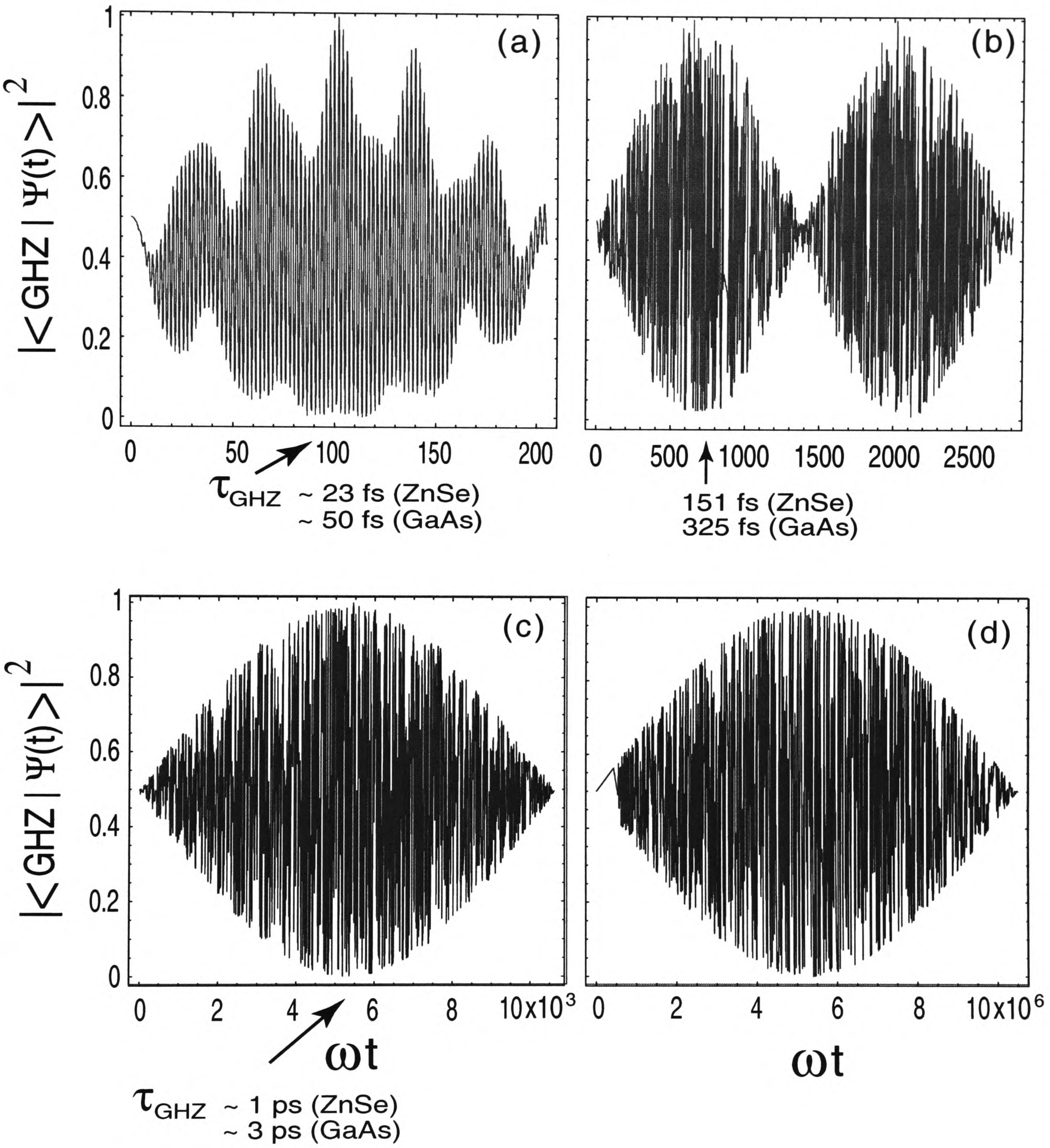

τ_{GHZ} ~ 23 fs (ZnSe) ~ 50 fs (GaAs)

151 fs (ZnSe) 325 fs (GaAs)

τ_{GHZ} ~ 1 ps (ZnSe) ~ 3 ps (GaAs)

Figure 3.6: Generation of the GHZ state $\frac{1}{\sqrt{2}}(|000\rangle + |111\rangle)$. $W = 0.1$, $\varphi = 0$, and (a) $A = \frac{1}{25}$, (b) $A = \frac{1}{50}$, (c) $A = 10^{-2}$, and (d) $A = 10^{-3}$. The τ_{GHZ}-pulses given here are equivalent to the realisation of the entangling network $\text{CNOT}_{13}\text{CNOT}_{12}H_1$.

for quantum computing realisations. However, such solid state experimental demonstrations are still in a very embryonic stage and there are still alot of fundamental issues, e.g., the decoherence phenomenon (see Chap. 6), that need to be properly understood before commencing a new era of solid state devices for the processing of quantum information.

As discussed in Sec. 2.2, there has been a recent experimental demonstration of single qubit rotations in an InGaAs quantum dot: exciton Rabi oscillations have been performed, and hence, coherent population flopping in an excitonic two-level system is now possible [65]. The next step in the process of realising small quantum information processors, the demonstration of controlled two-qubit gates, is therefore within the reach of present technology, as is the demonstration of the proposal given here for the generation of exciton entanglement. Chapter 4 shows how the optical generation of these excitonic entangled states can be exploited in order to perform quantum protocols, such as the teleportation of an excitonic state in a solid state system [JHR3].

Next, it is shown how the density matrix formalism can be used in an equivalent manner to produce entanglement schemes such as the ones described previously [53, JHR4].

3.3 Pseudo-spin operators and the density matrix

Consider a rectangular radiation pulse, starting at time $t = 0$, with central frequency ω, given by $\xi(t) = A\cos(\omega t)$. The time evolution of any initial state under the action of the Hamiltonian (3.7) is easily performed by means of the pseudo $\frac{1}{2}$-spin operator formalism [132, 133]. Single transition operators are defined by

$$\langle i|J_x^{r-s}|j\rangle = \frac{1}{2}(\delta_{ir}\delta_{js} + \delta_{is}\delta_{jr}) \,, \tag{3.29}$$

$$\langle i|J_y^{r-s}|j\rangle = \frac{i}{2}(-\delta_{ir}\delta_{js} + \delta_{is}\delta_{jr}) \,, \tag{3.30}$$

$$\langle i|J_z^{r-s}|j\rangle = \frac{1}{2}(\delta_{ir}\delta_{jr} - \delta_{is}\delta_{js}) \,, \tag{3.31}$$

where r–s denotes the transition between states $|r\rangle$ and $|s\rangle$ within a given J subspace. The three operators belonging to one particular transition r–s obey standard angular momentum commutation relationships $\left[J_\alpha^{r-s}, J_\beta^{r-s}\right] = iJ_\gamma^{r-s}$, where (α, β, γ) represents a cyclic permutation of (x, y, z) (operators belonging to non-connected transitions commute: $\left[J_\alpha^{r-s}, J_\beta^{t-u}\right] = 0$ with $\alpha, \beta = x, y$ or z). In this case, the Hamiltonian in the rotating frame ($\epsilon \gg W$) becomes[7]

$$H_\Lambda = \Delta_\omega J_z - \tfrac{1}{2}A(J_+ + J_-) - W(J^2 - J_z^2) \,. \tag{3.32}$$

Next, the expressions for the density matrix associated with the $N = 2$- and 3-QD systems are given, in order to show that the Hamiltonian (3.32) leads to the generation of the states $|\Psi_{\text{BELL}}(\varphi)\rangle$, and $|\Psi_{\text{GHZ}}(\varphi)\rangle$.

---

[7] The Hamiltonian (3.32) differs from the one given in Eq. (3.7) by a sign because of the choice of the sign for the interdot interaction W.

3.3.1 Bell states

Let us describe the light excitation procedure to obtain the Bell-type states $|\Psi_{\text{Bell}}(\varphi)\rangle$. As in Subs. 3.1.1, the initial condition is represented by the vacuum of excitons: only the $J = 1$ subspace is optically active (the $J = 0$ subspace remains dark). Choosing the basis of eigenstates of J^2 and J_z as in Subs. 3.1.1, the rotating frame Hamiltonian and initial density matrix can be expressed in terms of pseudo-spin operators as follows

$$\begin{aligned} \rho(0) &= \tfrac{1}{3}I + \tfrac{2}{3}\left(J_z^{0-1} + J_z^{0-2}\right) , \\ H_\Lambda &= -2\Delta_\omega J_z^{0-2} + \tfrac{2W}{3}\left(J_z^{0-1} - J_z^{1-2}\right) - \sqrt{2}A\left(J_x^{0-1} + J_x^{1-2}\right) . \end{aligned} \qquad (3.33)$$

Here, I denotes the identity matrix in the subspace $J = 1$. In the absence of light, the energy levels of the system are given as in Subs. 3.1.1 (with accuracy of a sign). Consider the action of a pulse of light at resonance and amplitude $A \ll W$. Assuming that the decoherence processes are negligibly small over the time scale of the evolution (see Chapter 6), the density matrix at time t becomes

$$\rho(t) = \tfrac{1}{3}I + \left[\cos(\omega_2 t) + \tfrac{1}{3}\right] J_z^{0-1} + \left[\cos(\omega_2 t) - \tfrac{1}{3}\right] J_z^{1-2} - \sin(\omega_2 t) J_y^{0-2} \ , \qquad (3.34)$$

which exhibits the generation of coherence between vacuum and biexciton states through the operator J_y^{0-2}, which oscillates at a frequency $\omega_2 = A^2/W$. The state $|\Psi_{\text{Bell}}(\varphi)\rangle$ has a corresponding density matrix

$$\rho_{\text{Bell}} = I/3 + J_z^{0-1}/3 - J_z^{1-2}/3 + \cos(\varphi) J_x^{0-2} - \sin(\varphi) J_y^{0-2} \ . \qquad (3.35)$$

Comparing Eq. (3.35) with Eq. (3.34), it is seen that the system's quantum state at time $\tau_{\text{Bell}} = \pi W/2A^2$ corresponds to the maximally entangled Bell state $|\Psi_{\text{Bell}}(\pi/2)\rangle$. The time evolution of populations and coherences for an initial vacuum state are plotted in Fig. 3.7. The evolution of populations of the vacuum ρ_{00} and the biexciton ρ_{22} states are shown in Fig. 3.7(a). Clearly, the approximate analytic calculation given here describes the system's evolution very well when compared with the exact numerical solution [Fig. 3.7(a)]. Figure 3.7(b) shows the overlap, $O(t) = \mathrm{Tr}\left[\rho_{\text{Bell}}\rho(t)\right]$, between the maximally entangled Bell state and the one obtained by applying a rectangular pulse of light at resonance. The thick solid line [Fig. 3.7(b)] describes $O(t)$ with a maximally entangled Bell state in the rotating frame, while the thin solid line [Fig. 3.7(b)] represents the overlap with a Bell state transformed to the laboratory frame: obviously, the rotating frame case corresponds to the amplitude evolution of the laboratory frame signal. The dashed line illustrates the approximate solution overlap in the rotating frame. The approximate solution works very well, supporting the idea that a selective Bell pulse of length $\tau_{\text{Bell}} = \pi W/2A^2$ can be used to create the Bell state $|\Psi_{\text{Bell}}(\pi/2)\rangle$ in the system of two coupled QDs. The same conclusion can also be drawn from the time evolution of the overlap between the exact Bell-state density matrix and the one obtained directly from the numerical calculation [53]. Therefore, the existence of a selective Bell pulse is numerically confirmed.

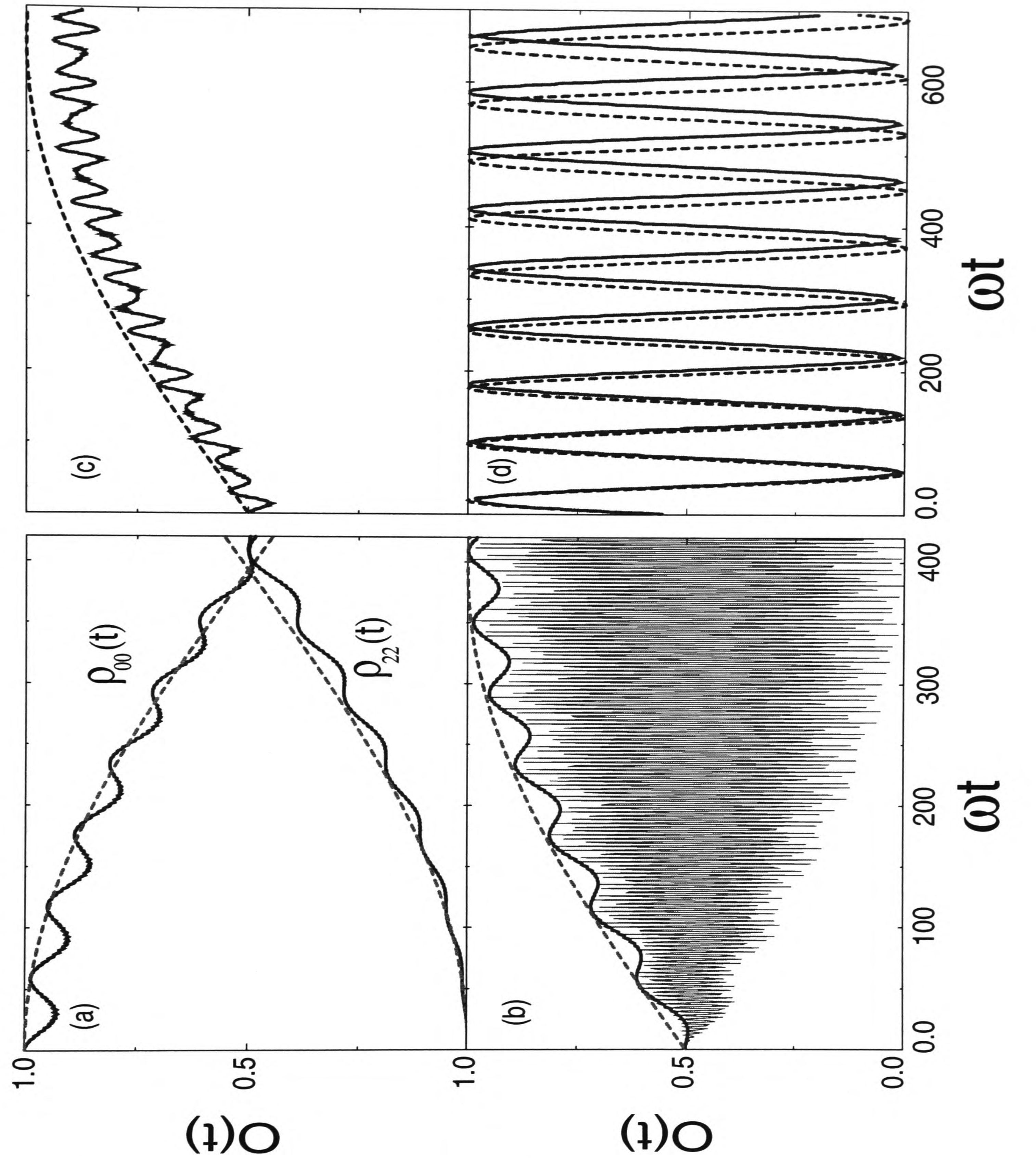

Figure 3.7: (a) Population of the vacuum state ρ_{00} and biexciton state ρ_{22} in two coupled QDs, as a function of time. (b) Time-evolution of overlap with maximally entangled Bell state. $\epsilon = 1$, $W = \epsilon/10$, $A = W/5$, and $\varphi = \pi/2$. Blue (thin solid) line shows exact numerical result in the laboratory frame. Red (thick solid) line in (b) represents the exact numerical solution in the rotating frame. Pink (dashed) line shows approximate analytical result. (c) Time-evolution of overlap with maximally entangled GHZ states $|\Psi_{\mathrm{GHZ}}(\pi/2)\rangle$, and (d) $|\Psi_{\mathrm{GHZ}}(\pi/2)\rangle_2$, under the action of a rectangular pulse of light at resonance. $\epsilon = 1$, $W = \epsilon/10$, and $A = 2W/5$. Red (solid) line represents exact numerical solution. Blue (dashed) line shows approximate analytical result.

3.3.2 GHZ states

Next, consider three quantum dots of equal size, and equidistant from each other (as in Sec. 3.1.1), with the $J = \frac{3}{2}$-subspace being the only one optically active (the basis set being the same of Sec. 3.1.1). In terms of pseudo-spin operators, the rotating frame Hamiltonian, including the radiation term, is now given by

$$H_{\Lambda} = -\Delta_{\omega}\left(3J_z^{0-3} + J_z^{1-2}\right) + 2W\left(J_z^{0-1} - 2J_z^{2-3}\right) - A\left[\sqrt{3}\left(J_x^{0-1} + J_x^{2-3}\right) + 2J_x^{1-2}\right] \; . \tag{3.36}$$

In terms of its associated density matrix, the entangled state $|\Psi_{\text{GHZ}}(\varphi)\rangle$ between vacuum and triexciton states is given by

$$\rho_{\text{GHZ}} = I/4 + J_z^{0-1}/2 - J_z^{2-3}/2 + \cos(\varphi)J_x^{0-3} + \sin(\varphi)J_y^{0-3} \; , \tag{3.37}$$

where I denotes the identity matrix in the $J = \frac{3}{2}$ subspace. This state can be generated after an appropriate $\frac{\pi}{2}$-pulse: starting with a zero-exciton state $|0\rangle$, at resonance, and using the properties of pseudo-spin operators, the evolved state under the action of Hamiltonian Eq. (3.36) can be obtained in a straighforward way in the limit $A/W \ll 1$ [53]:

$$\rho(t) = \tfrac{1}{4}I + \left[\cos(\omega_3 t) + \tfrac{1}{2}\right] J_z^{0-1} + \cos(\omega_3 t)J_z^{1-2} + \left[\cos(\omega_3 t) - \tfrac{1}{2}\right] J_z^{2-3} + \sin(\omega_3 t)J_y^{0-3} \; , \tag{3.38}$$

with $\omega_3 = d_- - d_+ + A$, and $d_\pm = W\sqrt{1 \pm \frac{A}{W} + \frac{A^2}{W^2}}$. Clearly, $|\Psi_{\text{GHZ}}(\pi/2)\rangle$ can be generated with a $\frac{\pi}{2}$-pulse of length $\tau_{\text{GHZ}} = 4\pi W^2/3A^3$. In Fig. 3.7(c), the overlap between the exact density matrix and that corresponding to state $|\Psi_{\text{GHZ}}(\varphi)\rangle$ is shown. The dashed line shows the overlap using the approximate density matrix, Eq. (3.38).

Consider the entangled state between a single exciton $|1\rangle$ and the biexciton $|2\rangle$, $|\Psi_{\text{GHZ}}(\varphi)\rangle_2 = \frac{1}{\sqrt{2}}(|1\rangle + e^{i\varphi}|2\rangle)$. In order to generate $|\Psi_{\text{GHZ}}(\varphi)\rangle_2$, let's take the single exciton state $|1\rangle$ as the initial condition. Evolution of this new initial state under H_{Λ} [Eq. (3.36)], with $\Delta_\omega = 0$, generates a new density matrix $\rho(t)$ which can be used to show that a pulse of duration $\tau'_{\text{GHZ}} = \pi/4A$, generates the state $|\Psi_{\text{GHZ}}(\pi/2)\rangle_2$. Fig. 3.7(d) shows the overlap between $\rho(t)$ and ρ_{GHZ_2} [53]. It is emphasized that the two maximally entangled GHZ states considered above have very different frequencies. This feature should enable each of these maximally entangled GHZ states to be manipulated separately in actual experiments, even if the initial state is mixed.

From the results above, it follows that in order to generate maximally entangled exciton states, $\frac{\pi}{2}$-pulses with sub-picosecond duration should be used. A surprising conclusion of these results is that entangled-state preparation is facilitated by *weak* light fields (i.e., $A \ll W$): strong fields cause excessive oscillatory behavior in the density matrix. As said before, the relevant experimental conditions as well as the required coherent control to realise the above combinations of parameters are compatible with those demonstrated in Refs. [60, 61, 62, 63]: we expect that the experimental generation of the Bell and GHZ states discussed here should be possible with these ultrafast semiconductor optical techniques. Here, it is important to highlight that a corresponding increase in the effective gap will yield a larger exciton binding energy: typical decoherence mechanisms (e.g., acoustic phonon scattering) will hence become less effective [134, JHR5].

To summarise, it has been shown how maximally entangled Bell and GHZ states can be generated using the optically driven resonant transfer of excitons between quantum dots. Selective Bell and GHZ pulses have been identified by an approximate, yet accurate, analytical approach which should prove a useful tool when designing experiments. Exact numerical calculations confirm the existence of such φ-pulses for the generation of maximally entangled states in coupled dot systems.

3.4 Quantum information processing with coupled QDs

The proposal given in this chapter assumes that some experimental techniques, such as ultra-fast, and near-field optical spectroscopy are available and can be used to fit the parameters introduced in our model. Though these techniques have already been discussed in Sec. 2.2.1, a few remarks are necessary, particularly, in the context of realising quantum computation using excitonic degrees of freedom. So far, the dynamics of the exciton operators has assumed a coherent evolution of the qubit states. Thus, our representation of the qubit basis states $|0\rangle$, and $|1\rangle$ as the vacuum, and the single state of excitons, has considered that the states involved in the exciton entanglement generation process are ruled by a unitary evolution. Unfortunately, there is a snag. As we know (see, e.g., Sec. 2.1.5), this is the problem of noise. Quantum dot devices have a strong coupling to the environment, i.e., the substrate that allows for the growing of the samples. This process produces typical dephasing times of the order of a few tens of picoseconds [62], therefore, making the goal of bulding a quantum computer extremely challenging. However, as is demonstrated in Chapter 6, under certain circumstances, these phase decoherence effects (which at low temperatures are mainly due to exciton-acoustic-phonon coupling [183]) can be minimised, such that exciton entanglement generation can still be feasible. Furthermore, the necessary laser pulses to accomplish such an entanglement are in the sub-picosecond time scale (tens of femtoseconds), hence, such a process should take place before decoherence of the exciton states occurs.

As we have seen in Chapter 2, in order to perform universal quantum computation, we need a system that allows us to realise, in a controllable manner, arbitrarily complex computations involving single- and two-qubit quantum gates. Also, there is the delicate matter of reliably storing many qubits of quantum information while performing such computations. This is the challenge that an exciton-based quantum information processor has to face. In this sense, we are "behind" other types of software implementations used for QC, such as ion traps, atomic, and liquid NMR setups, where single- and two-qubit gates have already been achieved for a quantum register of up to seven qubits. However, a quantum dot-based device should offer an advantage that the above-mentioned systems do not possess: scalability, which becomes crucial for any serious attempt at demonstrating the real power of quantum computing. For example, to give an idea of the size of a quantum computer which might lead to the realisation of a complex quantum computational task, say Shor's factorisation algorithm [21], it has been estimated that, in order to factorise a 130-digit number (the achievable limit of a modern classical computer), the quantum computer should require a register of size $n = 2000$ (400 qubits for the storage of the given number, and about 1600 as workspace) [129]. Under these circumstances, QD devices should offer a unique opportunity regarding the number of qubits (scalability) that can be used as quantum memory elements for the processing of QIP. Thus, despite the fact that we do not yet have a physical implementation of a QD-based two-qubit gate controlled at will, this is currently a matter of intense study that involves state-of-the-art technology (see, e.g., Sec. 2.2), and offers potential scalability properties. In this sense, there has not yet been a real demonstration of the computational power that should distinguish a QC from its classical counterpart. Hence, in the near future, regardless of the employed quantum software, we should be able to build small quantum information processors but not "true" quantum computers.

Currently available single-QD exciton dephasing time is of the order of 40 ps [61], hence, the figure of merit $\tau_{gate}/\tau_{dec} \sim 10^{-4}$, which, as discussed in Sec. 2.1.5, should make fault-tolerant exciton QD quantum computation feasible [129]. Thus, we have that the QD model system for quantum entanglement generation presented here should allow for quantum computing realisations. In particular, note that the initialisation and dynamical evolution of the exciton states of our model conveys the realisation of small entangling quantum gates. Thus, starting with the exciton ground state for the two (three) QD system, the state $|00\rangle$ ($|000\rangle$), in order to produce the Bell (GHZ) state $|\phi^+\rangle$ ($|\Psi_{\mathrm{GHZ}}(0)\rangle$), implies the realisation of a single qubit rotation, the Hadamard transform, followed by a two-qubit gate, the CNOT gate, i.e., the entangling network $\mathrm{CNOT}_{12}H_1$ ($\mathrm{CNOT}_{13}\mathrm{CNOT}_{12}H_1$) is realised. Below, it is shown how such single qubit rotations can be experimentally achieved. Note that, in addition to fault-tolerant quantum error correction (see Sec. 2.1.5), there are other possibilities to account for error-correction, which can be applied to our excitonic system, thus allowing for a reliable qubit coherent evolution. These methods shall be discussed in more detail in Chap. 6. Next, some issues regarding exciton QD logic gate operation, and measurement, are discussed.

The capability to reliably perform quantum interference between qubit states, as required in quantum computing, has recently been pushed forward in a QD system, because of the demonstration of exciton Rabi flopping in a single-QD [65]. Here, superpositions such as $|0\rangle + |1\rangle$ have been made to evolve while preserving their phase within a dephasing time $T_2 \sim 40$ ps. The two excitonic levels considered in this experiment had ground state, say $|0\rangle$, with associated energy $E_0 = 1.67243$ eV, and excited excitonic state, namely $|1\rangle$, with $E_1 = 1.6926$ eV: the corresponding energy gap between such a two-state system was $\Delta E = 20.2$ meV. As shown in Fig. 3.8, this InGaAs QD system allows for the observation of Rabi-like oscillations (exciton interference fringes) as a function of the laser power excitation and relative pulse delay [Figs. 3.8(a) to 3.8(d)]. The single-dot photoluminiscence spectrum allows the observation of ultra-fast oscillations associated with the populations of the two states of this exciton two-level system, as shown in Figs. 3.8(e), and 3.8(f). Thus, this important step corresponds to the experimental demonstration of a single-qubit gate, e.g., the Hadamard transform. This qubit gate, in addition to the shift-phase gate allows for the realisation of *all* of the possible single-qubit gates, as demonstrated in Sec. 2.1. We are hopeful that the coupling of QDs, e.g., the ones reported here for the single-qubit rotations experiment [65], should allow, under certain prescribed conditions (e.g., the ones given in our proposal for entanglement generation), the realisation of controlled two-qubit gates, thus completing a set of gates that is universal for quantum computation.

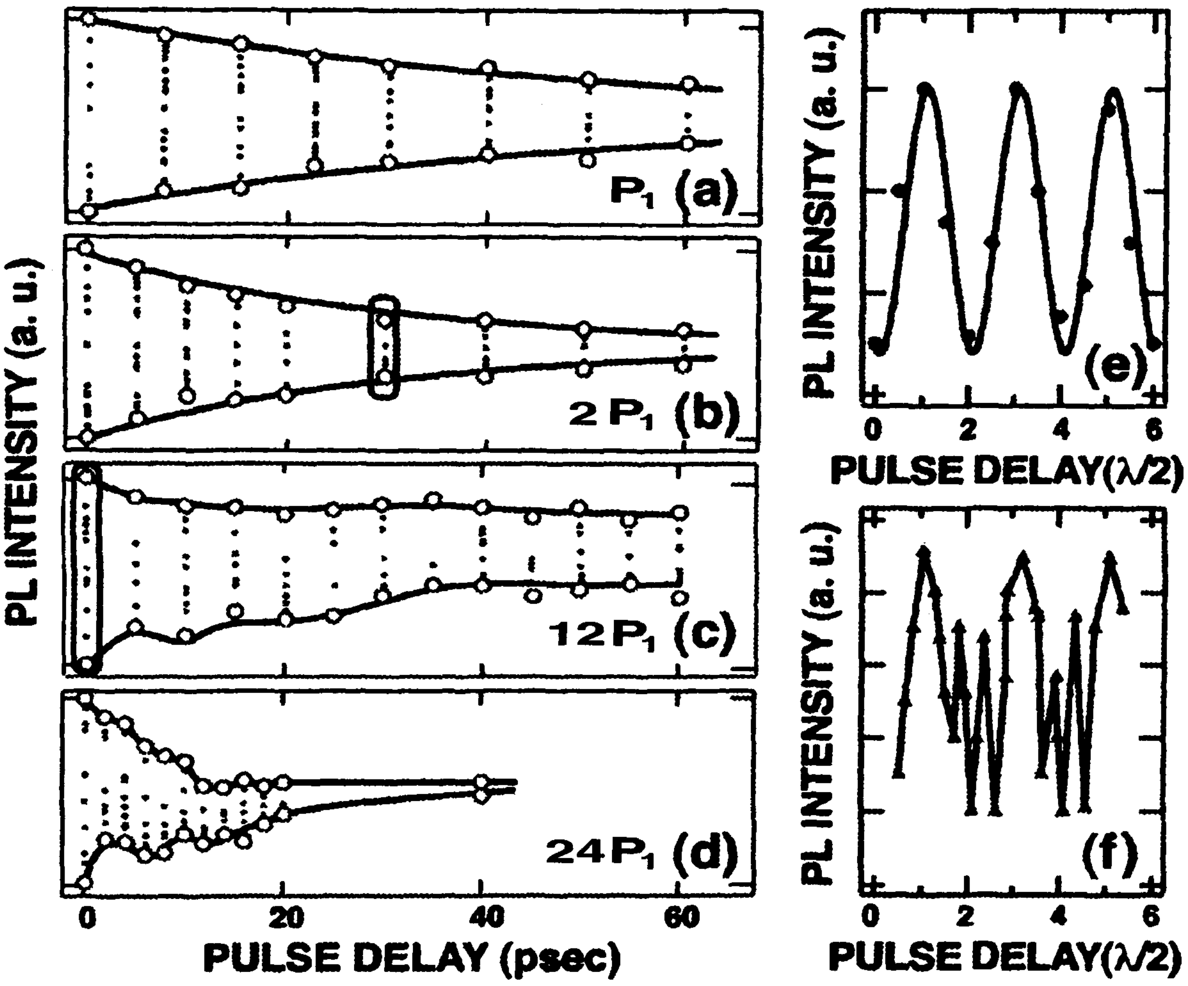

Figure 3.8: Measurement of exciton interference fringes for single-dot photoluminescence emission intensity as a function of relative pulse delay and the power density $P_1 = 0.067\ \mu\text{J cm}^{-2}/\text{pulse}$. Plots (e) and (f) show Rabi-like oscillations due to quantum interference of a two-level (exciton) system for the coarse delay shown in (b) 30 ps, and (c) 0 ps, respectively. The two excitonic levels are the ground state $|0\rangle$, with energy $E_0 = 1.67243$ eV, and the excited excitonic state $|1\rangle$, with $E_1 = 1.6926$ eV ($\Delta E = 20.2$ meV). The figure is adapted from Ref. [65].

Regarding the experimental detection—"measurement"—of the exciton entanglement proposed in this chapter, we note that the statistical properties of resonance fluorescence from the optically-driven QD system given here should likewise give rise to a signature associated with such an excitonic state entanglement. As discussed in Sec. 2.2.2, there has recently been an experimental observation of photon antibunching from an artificial atom (a single CdSe/ZnS quantum dot) [75]. In addition, it has been demonstrated that under optical pulse excitation, a single QD can emit a single photon per excitation pulse [77, 78]. Even more recently, temporal correlations measurements among photons emitted at various wavelengths from a continous wave (cw) optically excited single-QD have demonstrated that a quantum dot is not only a source of single photon emission, but also a source of *multicolor* photons, such that the correlation among these emitted photons can be manipulated via the cw excitation power, and hence the transition from photon antibunching (low power excitations) to photon bunching (high excitation power) can be observed [79], as illustrated in Fig. 2.4 (see Sec. 2.2.2). The above-mentioned experimental possibilities suggest that a measurement of the photon emission arising from our coupled QD systems should allow for the observation of quantum correlations (emitted photon statistics), as a function of the cw excitation power, thus providing us with a signature for the exciton entanglement reported in this chapter. However, it is important to emphasise that our exciton states are not of the same type as the ones analysed in the previously-mentioned experiments: while the *e-h* pairs states of the experiments are just single product QD states, ours is a two-QD *entangled* state, a state that 'shares' the quantum information of each individual QD state in such a way that it cannot be written as a product of states for the two-QD system. Though the difference is clear regarding this point, we believe that an experimental set-up following the same methodology as the one described before (see Sec. 2.2.2) should account for the observation of such statistical correlations arising from entangled quantum dots.

Furthermore, another experimental possibility suggests that a measurement of the two-photon polarisation density matrix of the emitted photons from an exciton Bell-like state decay should be possible. A measurement of such a density matrix has been recently achieved in Ref. [80] for the case of photon emission through biexciton decay in a single InAs QD. Despite the fact that they do not observe photon entanglement, a strong "classical" correlation between them is found [80]. It is conjectured that the realisation of an experiment like theirs for the case of the model QD molecules given in this chapter, should allow for the observation of entanglement transfer between the exciton entangled states reported here and the corresponding emitted photons, via the direct measurement of the off-diagonal elements of the photon polarisation density matrix. Should such an experiment be demonstrated, a mechanism for producing a source of entangled photons is also provided here as a byproduct of the set-up proposed in this chapter.

3.5 Concluding remarks

In summary, the quantum mechanical equation-of-motion for excitons in two and three coupled QD systems driven by classical pulses of light has been solved both analytically and numerically . By doing this, a prescription for preparing maximally entangled Bell and GHZ states of excitons in optically-driven QDs has been given. This exploits current levels of coherent optical control such as the ones demonstrated using ultra-fast spectroscopy [60, 61, 62], and near-field optical spectroscopy [60, 64]. Such ultra-fast coherent optical control should enable us to generate arbitrary single-qubit gates (e.g., Hadamard, and phase-shift gates), and two-qubit controlled-U gates (e.g., the CNOT gate). In particular, the prescription given here should lead to the generation of all of the Bell basis states, a fact that could be exploited for performing quantum communication protocols, such as the quantum teleportation of an excitonic state in a system of coupled QDs (see next chapter [JHR3]). As will be seen later (Chapter 6), by taking into account the main mechanisms that erode the exciton coherence, e.g., dephasing due to exciton-acoustic-phonon coupling, it is found that the optical generation of quantum entanglement given here is preserved over a reasonable parameter window. This leads to the possibility of performing several hundred quantum computation operations before decoherence of these excitonic states takes place.

Chapter 4

Quantum teleportation in a solid state system

Since the original idea of quantum teleportation considered in 1993 by Bennett *et al.* [14], great efforts have been made to realise the physical implementation of teleportation devices [135, 136, 137, 138]. The general scheme of teleportation [14], which is based on Einstein-Podolsky-Rosen (EPR) pairs [2, 4, 7] and Bell measurements [8, 9, 139], using classical and purely nonclassical correlations, enables the transportation of an arbitrary quantum state from one location to another without knowledge or movement of the state itself through space. This process has been explored from various points of view [135, 136, 137, 138]; however none of these experimental set-ups have considered a solid-state approach, despite the recent advances in semiconductor nanostructure fabrication and measurement [60, 61, 62, 64, 140]. Reference [61], for example, demonstrates the remarkable degree of control which is now possible over quantum states of individual quantum dots using ultra-fast spectroscopy. The possibility therefore exists to use optically-driven QDs as "quantum memory" elements in quantum computation operations, via a precise and controlled excitation of the system. In this chapter, we propose a practical scheme capable of demonstrating quantum teleportation which exploits currently available ultrafast spectroscopy techniques in order to prepare and manipulate entangled states of excitons in coupled quantum dots [JHR3]. To our knowledge, this is the first practical proposal for demonstrating quantum teleportation in a solid state system.

4.1 The quantum teleportation protocol

This section shall use the QDs entanglement produced in the preceding chapter as a *resource* for the transmission of quantum information. As is shown below, quantum teleportation allows us to transmit the quantum state of a particle from one point in space to another without the actual physical transportation of such a state. This state can be in principle unknown to us, and its transmission relies on the purely quantum mechanical properties of highly entangled states assisted by the transmission of purely classical information. Since this process has to be consistent with the no-cloning theorem (see Sec. 2.1.1), and as there is not actual physical transportation of the systems state, how does it work? The protocol that performs this process is sketched in Fig. 4.1. In this scenario, the arrow of time indicates how to carry out the protocol:

(t_0) At $t = t_0$ the EPR source prepares *one* of the *entangled* states of the Bell basis $\mathcal{B}_B = \{|\phi^+\rangle, |\phi^-\rangle, |\psi^+\rangle, |\psi^-\rangle\}$ [1] between particles 2 and 3, let's say, the state $|\phi^+\rangle_{2,3}$ [Eq. (4.1)].

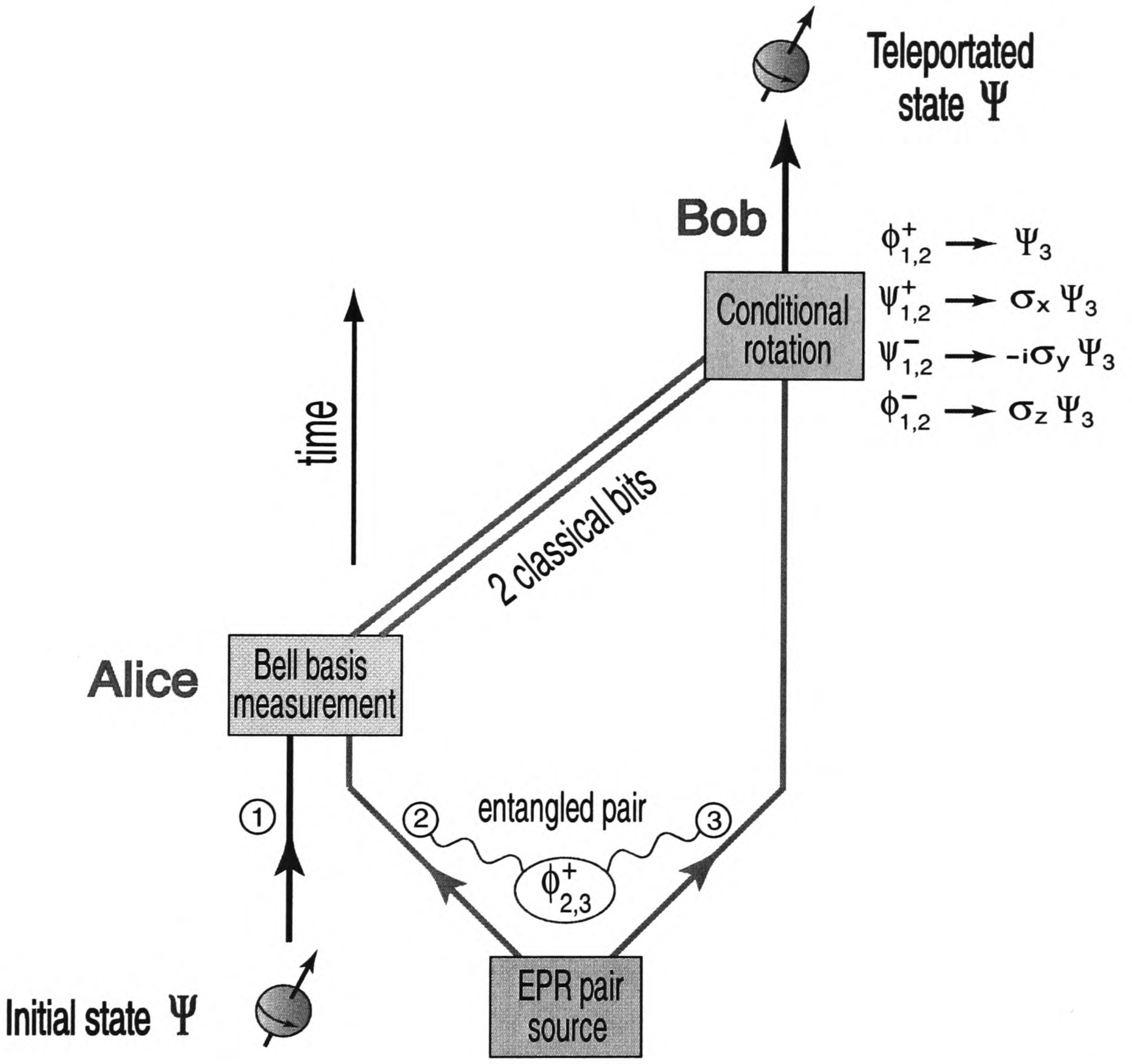

Figure 4.1: Schematics of the quantum teleportation process. For simplicity the kets notation for the quantum states associated with the 3-particle system has been omitted (see text).

(t_1) At $t = t_1$ Alice sends the particle 3 of the EPR-pair to Bob, and unites the other particle of the entangled pair with the unknown qubit state $|\Psi\rangle_1 \equiv \alpha|0\rangle_1 + \beta|1\rangle_1$

---

[1] If we consider spin-$\frac{1}{2}$ particles, with spin states $|\uparrow\rangle \equiv |0\rangle$, and $|\downarrow\rangle \equiv |1\rangle$, recall that the $\mathcal{B}_B$-basis states are given by

$$|\phi^{\pm}\rangle_{1,2} \equiv \tfrac{1}{\sqrt{2}}(|00\rangle_{1,2} \pm |11\rangle_{1,2}) \,, \tag{4.1}$$

$$|\psi^{\pm}\rangle_{1,2} \equiv \tfrac{1}{\sqrt{2}}(|01\rangle_{1,2} \pm |10\rangle_{1,2}) \,. \tag{4.2}$$

($|\alpha|^2 + |\beta|^2 = 1$) that she wants to transmit to Bob. After this, she performs a Bell measurement on the (uncorrelated) particles 1 and 2, which projects onto one of the states of the $\mathcal{B}_{\mathrm{B}}$-basis (see Fig. 4.1). As this stage, the whole system's state can be written as follows:

$$\begin{aligned} |\Psi\rangle_1|\phi^+\rangle_{2,3} &= \tfrac{1}{2}\Big[|\phi^+\rangle_{1,2}(\alpha|0\rangle_3+\beta|1\rangle_3) \;+\; |\psi^+\rangle_{1,2}(\alpha|1\rangle_3+\beta|0\rangle_3) \;+ \\ &\qquad |\psi^-\rangle_{1,2}(\alpha|1\rangle_3-\beta|0\rangle_3) \;+\; |\phi^-\rangle_{1,2}(\alpha|0\rangle_3-\beta|1\rangle_3)\Big] \,. \end{aligned} \tag{4.3}$$

(t_2) Next, Alice sends the result of her measurement, two classical bits of information, to Bob via a classical channel. These classical bits are represented by two straight lines in Fig. 4.1. Eq. (4.3) can then be rewritten as

$$|\Psi\rangle_1|\phi^+\rangle_{2,3} = \tfrac{1}{2}\Big[|\phi^+\rangle_{1,2}|\Psi\rangle_3+|\psi^+\rangle_{1,2}(\sigma_{\mathrm{x}})|\Psi\rangle_3+|\psi^-\rangle_{1,2}(-i\sigma_{\mathrm{y}})|\Psi\rangle_3+|\phi^-\rangle_{1,2}(\sigma_{\mathrm{z}})|\Psi\rangle_3\Big] \,, \tag{4.4}$$

where the σ_i operators are the Pauli matrices in the $\{|0\rangle, |1\rangle\}$ basis[2].

(t_3) After receiving Alice's classical information, Bob performs one of the following unitary operations [see Eq. (4.4)] in order to transform the state of his particle[3] into $|\Psi\rangle$:

$$\begin{aligned} |\phi^+\rangle_{1,2} &\longrightarrow I && \text{(do nothing)} \,, \\ |\psi^+\rangle_{1,2} &\longrightarrow \sigma_{\mathrm{x}} && \text{(do bit flip)} \,, \\ |\psi^-\rangle_{1,2} &\longrightarrow \sigma_{\mathrm{x}}\sigma_{\mathrm{z}} && \text{(do bit- and phase-flip)} \,, \\ |\phi^-\rangle_{1,2} &\longrightarrow \sigma_{\mathrm{z}} && \text{(do phase flip)} \,. \end{aligned} \tag{4.5}$$

Hence, Bob only needs to apply one of the unitary transformations of Eq. (4.5), conditional on the outcome of Alice's measurement, in order to obtain the initial state $|\Psi\rangle$ of particle 1 on his qubit (particle 3). Thus, the process works without actual physical transportation nor previous knowledge of the state $|\Psi\rangle$. A few remarks regarding this teleportation process: i) The Bell measurement establishes a correlation between the two initially uncorrelated particles 1 and 2. The outcome of this measurement is completely random, as can be seen from Eq. (4.4). ii) The protocol is consistent with the no–cloning theorem, since the "copy" of the state $|\Psi\rangle$ obtained by Bob requires the previous Bell basis measurement of particles 1 and 2 which destroys the original state $|\Psi\rangle_1$. iii) Since Bob has to wait for a classical signal to be sent to him in order to perform the quantum state transmission, the process has not been accomplished faster than light.

4.2 Teleportation as a quantum circuit

Next, it is shown that the above quantum teleportation protocol can be described in terms of elementary gates for quantum computation. In order to implement the quan-

---

[2] Recall that these operators are given by $\sigma_x = \begin{pmatrix} 0 & 1 \\ 1 & 0 \end{pmatrix}$, $\sigma_y = \begin{pmatrix} 0 & -i \\ i & 0 \end{pmatrix}$, $\sigma_z = \begin{pmatrix} 1 & 0 \\ 0 & -1 \end{pmatrix}$.

[3] Note that originally ($t = t_0$), Bob's particle 3 was *maximally* entangled with particle 2.

tum operations needed for the description of the practical teleportation scheme proposed here, two elements are employed: i) the Hadamard gate H, and ii) the CNOT (measurement) gate. Recall that these two unitary transformations perform the following operations: i) $\mathrm{H}\left(|i\rangle\right) \equiv \frac{1}{\sqrt{2}}\left\{(-1)^i|i\rangle + |1-i\rangle\right\}$, where $|i\rangle$ is an element of the orthonormal computational basis of single qubits $\mathcal{B}_1$; and ii) $\mathrm{CNOT}_{mn}(|i\rangle_m |j\rangle_n) \equiv |i\rangle_m |i \oplus j\rangle_n$, where $\oplus$ denotes XOR or addition modulo 2, and $|i\rangle, |j\rangle \in \mathcal{B}_2$: this two-qubit gate flips the second "target" qubit (n) if the first "control" qubit (m) is $|1\rangle$, and leaves the target untouched if the control qubit is $|0\rangle$.[4] A pure state $|\Psi\rangle = \alpha|0\rangle + \beta|1\rangle$, where $\alpha, \beta \in \mathbf{C}$, and $|\alpha|^2 + |\beta|^2 = 1$ is also introduced in this Hilbert space. For the purpose of the practical scheme presented in this Chapter, $|0\rangle$ represents the vacuum state for excitons while $|1\rangle$ represents a single exciton, as discussed in Chapter 3. In the present Chapter, the above-mentioned circuit notation will be used in order to provide a description of the quantum teleportation phenomenon in terms of quantum computation.

The *unitarity* of the Hadamard and the CNOT gates has interesting implications: consider the action of the following (Bell) circuit

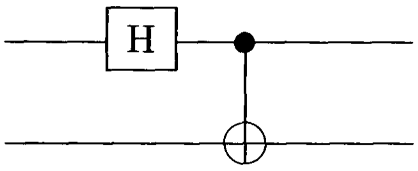

This transforms the states of the (disentangled) computational basis of two qubits $\mathcal{B}_2$ into a set of maximally entangled states. This set is exactly the so-called Bell basis and, as we saw in Section 4.1, is of fundamental relevance to quantum teleportation. As a result of the two-qubit register transformations of the circuit, we are left with the states:

$$|00\rangle \longmapsto \frac{1}{\sqrt{2}}(|00\rangle + |11\rangle) \equiv |\phi^+\rangle \;, \tag{4.7}$$

$$|01\rangle \longmapsto \frac{1}{\sqrt{2}}(|01\rangle + |10\rangle) \equiv |\psi^+\rangle \;, \tag{4.8}$$

$$|10\rangle \longmapsto \frac{1}{\sqrt{2}}(|00\rangle - |11\rangle) \equiv |\phi^-\rangle \;, \tag{4.9}$$

---

[4] As said in Chapter 2, in the language of quantum circuits, qubits are denoted by horizontal lines ("wires"), and the above-mentioned gates are schematically represented as follows

$\mathrm{CNOT}_{mn}\big(|i\rangle_m |j\rangle_n\big) \equiv$

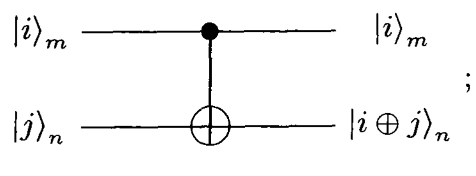

;

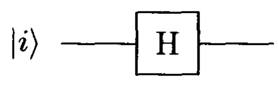

$\frac{1}{\sqrt{2}}\{(-1)^i|i\rangle + |1-i\rangle\}$, (4.6)

where the basis states $i, j = 0$ or 1. In addition, if the above set of gates is to be used for universal quantum computation, another single qubit gate, the *phase shift* $P(\varphi)$ gate must be introduced. This transforms: $|0\rangle \mapsto |0\rangle$, and $|1\rangle \mapsto e^{i\phi}|1\rangle$, and is denoted as $|x\rangle \;\overset{\varphi}{-\!\!\bullet\!\!-}\; e^{ix\varphi}|x\rangle$. The Hadamard and phase gates are sufficient to construct *any* unitary operation on a single qubit. Consequently, the Hadamard transform, all phase gates, together with the CNOT gate form an *universal* set of logic gates, i.e., any given n-qubit unitary transformation required in a certain quantum computation scheme can be exactly simulated with these gates [88].

$$|11\rangle \longmapsto \frac{1}{\sqrt{2}}(|01\rangle - |10\rangle) \equiv |\psi^-\rangle \,. \tag{4.10}$$

Since the Hadamard transform is just a single qubit gate, it is obvious that the CNOT gate is the one responsible for the generation of the *entangled* basis $\mathcal{B}_{\rm B} = \{|\phi^\pm\rangle, |\psi^\pm\rangle\}$. Interestingly, the same CNOT gate can be used to disentangle the Bell basis states: just apply the circuit $\text{CNOT}_{12}\text{H}_1$ to the $\mathcal{B}_{\rm B}$-basis states and you shall end up with the disentangled basis $\mathcal{B}_2$! As discussed in Sec. 2.1.1, this is because of the reversibility of this entangling gate. The above discussion can be easily extended to a qubit register of size n: the Schrödinger's cat state $|\Psi_{\text{N-CAT}}\rangle = \frac{1}{\sqrt{2}}(|00\ldots0\rangle_{1,\ldots,n} + |11\ldots1\rangle_{1,\ldots,n})$ can be produced, for example, starting from the trivial input state $|00\ldots0\rangle_{1,\ldots,n}$, and then applying a sequence of $n+1$ elementary gates. This set of transformations can be equivalently given by either of the following circuits

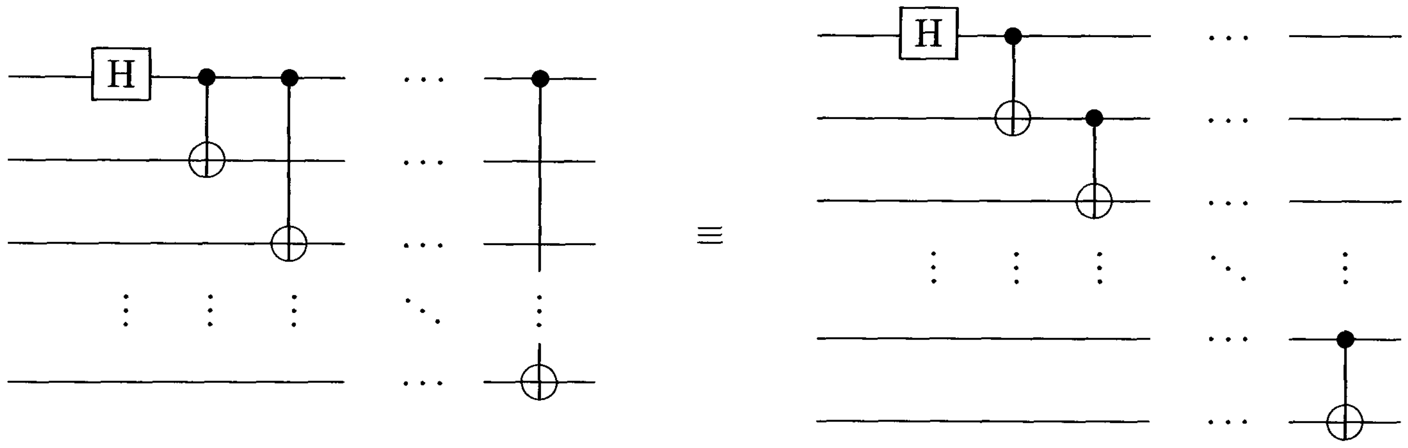

Figure 4.2 shows the general computational approach of this chapter which is based on the work by Brassard *et al.* [141]. As usual, two parties are referred to, Alice and Bob. Alice wants to teleport an arbitrary, unknown qubit state $|\Psi\rangle$ to Bob. Fig. 4.3 shows the specific realisation proposed here, using optically controlled quantum dots with QD a initially containing $|\Psi\rangle$. Alice prepares two qubits (QDs b and c) in the state $|0\rangle$ and then gives the state $|\Psi00\rangle$, as the *input* to the system. By performing the series of transformations shown in Fig. 4.2(a), Bob receives as the *output* of the circuit the state $\frac{1}{\sqrt{2}}(|0\rangle_a + |1\rangle_a)\frac{1}{\sqrt{2}}(|0\rangle_b + |1\rangle_b)|\Psi\rangle_c$, [Fig. 4.3(d)]. This circuit by itself is not a quantum teleportation machine: below is shown how to transform it into a quantum teleportation device.

In Fig. 4.2(b) the analysis of the teleportation process is extended to the case of a four qubit quantum circuit, which can be realised by four coupled QDs. As before, Alice wants to teleport the state $|\Psi\rangle_a$ to Bob. She prepares three qubits in the state $|0\rangle$ (QDs b, c and d) and gives the state $|\Psi000\rangle$ as the input to the system. From Fig. 4.2(b) it is clear that the function of the first three operations performed by Alice is to obtain the maximally entangled GHZ state $|\Psi_{\rm GHZ}(0)\rangle \equiv \frac{1}{\sqrt{2}}(|000\rangle + |111\rangle)$ [56].

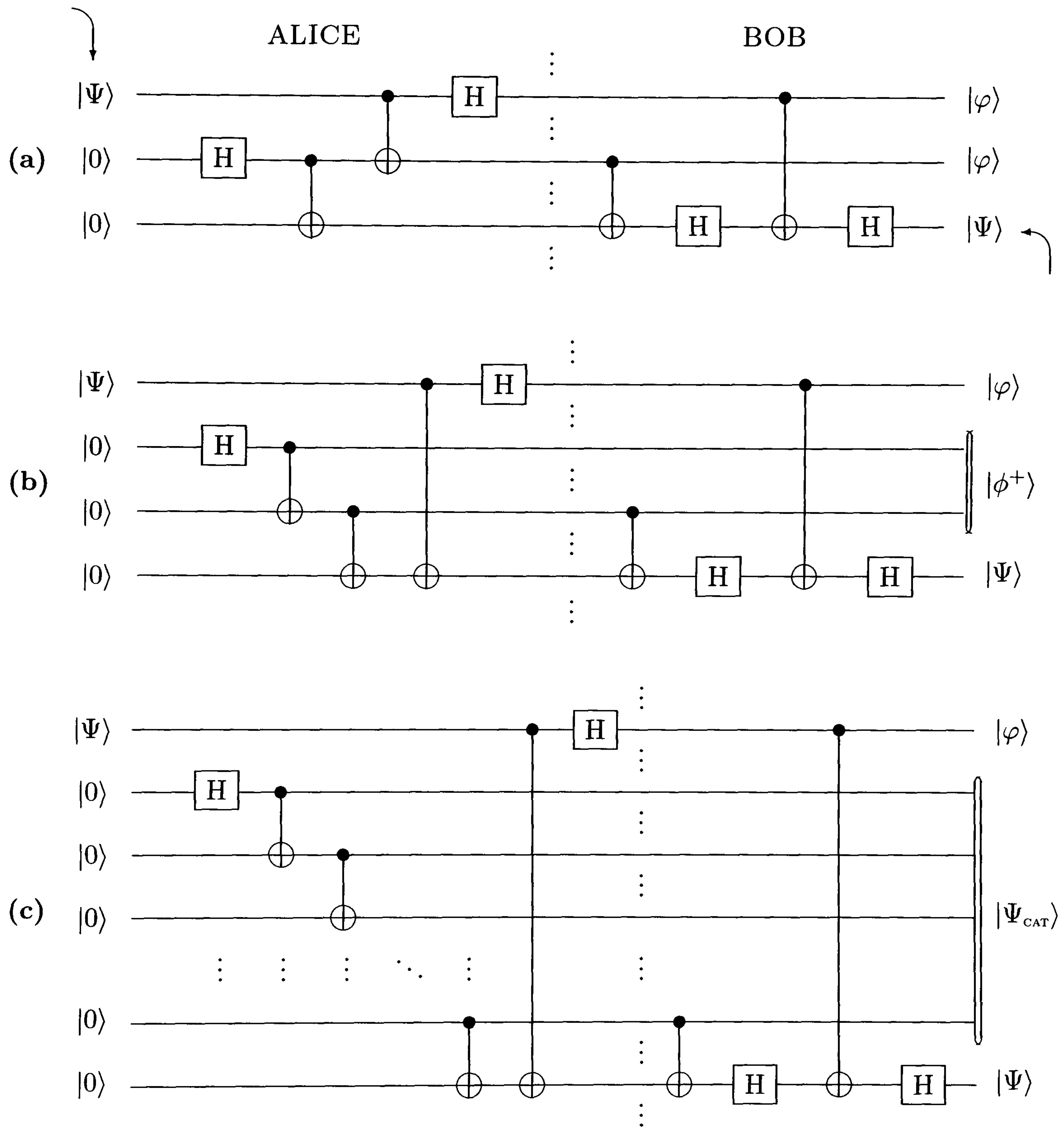

Figure 4.2: Circuit schemes to teleport an unknown quantum state from Alice to Bob using an arrangement of (a) 3, (b) 4 and (c) n qubits (coupled quantum dots). The methods employ (a) Bell, (b) GHZ, and (c) Schrödinger's cat states respectively. In (c) $|\Psi_{\text{CAT}}\rangle \equiv |\Psi_{\text{CAT}}\rangle_{2,n-1}$.

The next two operations realised by Alice (before the dotted line in Fig. 4.2(b)) leave the system in the state

$$\tfrac{1}{2}\Big\{|000\rangle(\alpha|0\rangle+\beta|1\rangle)+|011\rangle(\beta|0\rangle+\alpha|1\rangle)+|100\rangle(\alpha|0\rangle-\beta|1\rangle)+|111\rangle(-\beta|0\rangle+\alpha|1\rangle)\Big\}\,. \quad (4.11)$$

Performing the operations shown after the dotted line in Fig. 4.2(b), Bob gets as the output of the circuit the state $\frac{1}{\sqrt{2}}(|0\rangle_a + |1\rangle_a)|\phi^+\rangle_{b,c}|\Psi\rangle_d$. It is shown below how this result can be viewed in terms of quantum teleportation, where the state $|\Psi\rangle$ is to be teleported from dot a to dot d in the QD system.

In order to describe in detail how this circuit may be implemented as a teleportation circuit, the following steps need to be performed: Alice prepares three qubits in the state $|0\rangle$, and then sends the first two of them through the two first gates between QDs b and c, as shown in Fig. 4.2(b). She keeps this information stored in her quantum memory (QDs b, and c), namely states $\boldsymbol{\beta}$, and $\boldsymbol{\gamma}$, respectively[5]. In the next step she pushes the fourth qubit which is in state $|0\rangle$ together with $\boldsymbol{\gamma}$ to the third gate. Alice then receives from QD a the qubit $|\Psi\rangle$ which she wants to teleport to Bob. To achieve this, she removes the fourth qubit $\boldsymbol{\delta}$ from her quantum memory and sends this, together with qubit $|\Psi\rangle$, to the next two gates of the circuit. After this operation, she sends to Bob the last (fourth) qubit of the register state, namely $\boldsymbol{\delta'}$. She then performs a measurement in the $\mathcal{B}_1$-basis of the output[6] between QDs a and b [at the dotted line in Fig. 4.2(b)] in order to turn the result into two classical bits Λ and Γ respectively. To finish the teleportation process, Alice needs to communicate Λ and Γ to Bob via a classical channel. Hence after the dotted line, Bob receives the classical information and creates the quantum states $|\Lambda\rangle$ and $|\Gamma\rangle$, which belong to the $\mathcal{B}_1$-basis. Next, he removes the qubits $\boldsymbol{\beta'}$ and $\boldsymbol{\delta'}$ from his quantum memory and sends the four qubits to his part of the circuit. At this point, teleportation is complete since Bob receives at his output the state $|\Psi\rangle$ on dot d. It is a straightforward exercise to show that the pair of 'reconstructed' states $|\Lambda\rangle$ and $|\Gamma\rangle$, appear on the QDs a, and b, at the final output of our quantum teleportation circuit (QTC). For example, if the result of the measurement at the dashed line gives $\Lambda \equiv 0$ and $\Gamma \equiv 1$, it follows from Eq. (4.11), and the logic gates shown after the dashed line, that the output of the teleportation device yields $|\Lambda\rangle_a |\Gamma\rangle_b |1\rangle_c |\Psi\rangle_d$. This is the same output state that results if the corresponding measurement result gives $\Lambda \equiv 1$ and $\Gamma \equiv 1$. Otherwise ($\Lambda \equiv 0$ and $\Gamma \equiv 0$, or $\Lambda \equiv 1$ and $\Gamma \equiv 0$), the QD final state is given by $|\Lambda\rangle_a |\Gamma\rangle_b |0\rangle_c |\Psi\rangle_d$.

Interestingly, the above teleportation process can be extended to an n-QTC using the Schrödinger's cat state, as shown in Fig. 4.2(c). Again, the goal is to teleport the state $|\Psi\rangle_a$ from Alice to Bob. She prepares $n-1$ qubits in the state $|0\rangle$ (QDs $b, ..., n$) and hence gives the state $|\Psi 00...0\rangle$ as the input. After the first n elementary gates (Fig. 4.2(c)) she obtains the Schrödinger's cat state $\frac{1}{\sqrt{2}}(|00...0\rangle_{b,...,n} + |11...1\rangle_{b,...,n})$ which, followed by the last two exclusive-or operations before the dotted line, leaves the system in the following state of n qubits

$$\tfrac{1}{2}\Big\{|00...0\rangle(\alpha|0\rangle+\beta|1\rangle)+|011...1\rangle(\beta|0\rangle+\alpha|1\rangle)+|100...0\rangle(\alpha|0\rangle-\beta|1\rangle)+|11...1\rangle(-\beta|0\rangle+\alpha|1\rangle)\Big\}. \tag{4.12}$$

---

[5] These qubits shall be denoted in bold face, but without the ket notation, since they are members of an entangled state that cannot be written as a product state.

[6] Since these qubits are working in Bob's part of the circuit only as the control bit of the CNOT gates, this procedure can be performed without affecting the final outcome of the computation (see also Ref. [142]). The same is true for the n-qubit circuit presented here.

The procedure to realise the circuit of Fig. 4.2(c) as a QTC follows directly from the description given for Fig. 4.2(b). In the case of Fig. 4.2(c), the measurement performed by Alice at the end of her part of the circuit (dashed line) can also be realised between the first and the second qubits in order to turn the result into two classical bits Θ and Υ respectively. Hence Alice communicates these bits to Bob via a classical channel and, after the dotted line, Bob receives the classical information and creates the quantum states $|\Theta\rangle$ and $|\Upsilon\rangle$. Next, he removes from his quantum memory the remaining qubits in order to perform the logic gates shown after the dashed line in Fig. 4.2(c), thereby ultimately obtaining $|\Psi\rangle$ on the n-th dot. It is also noted that the structure of Bob's part of the circuit is the same for all the circuits in Fig. 4.2. This is because Bob's function in the QTC is to realise the "appropriate rotations" over the general state given in Eq. (4.12).

It is interesting to note that if Bob, instead of performing the operations after the dotted line, chooses one of these appropriate unitary transformations [see Eq. (4.14), below] to apply to the n-th qubit after receiving the classical bits from Alice's measurement, then he does not need to perform his part of the circuit. For this reason only two quantum logic gates are needed in order to teleport the state $|\Psi\rangle$. However, from the point of view of our implementation and, more generally, from a quantum algorithms perspective, it is better to undertake the complete process shown in the QTC than to choose such a special rotation. Although our goal is the practical realisation using what is at the limit of current optoelectronics technology, we note that the circuits of Fig. 4.2 *are not restricted* to QD systems: they can be applied to any system where the task of entangled-state preparation has been achieved.

4.3 Physical implementation in a quantum dot system

In order to describe the physical implementation of the quantum circuits using coupled quantum dots, the recent experimental results involving coherent control of excitons in single quantum dots on the nanometer and femtosecond scales [60, 61] are exploited. Consider a system of N identical and equispaced QDs containing no net charge which are radiated by long-wavelength classical light, as illustrated schematically in Fig. 4.3(b) for the case $N = 3$. The formation of single excitons within the individual QDs and their inter-dot hopping can be described by the Hamiltonian Eq. (3.3) [JHR1, 53].

By solving the eigenvalue problem associated with the time-dependent Hamiltonian (3.3), it has been shown for several different values of the phase φ, that Bell and GHZ states $|\Psi_{\text{BELL}}(\varphi)\rangle = \frac{1}{\sqrt{2}}(|00\rangle + e^{i\varphi}|11\rangle)$, $|\Psi_{\text{GHZ}}(\varphi)\rangle = \frac{1}{\sqrt{2}}(|000\rangle + e^{i\varphi}|111\rangle)$ can be prepared in systems comprising two and three coupled quantum dots, respectively [JHR1]. The practical requirements are realisable in present experiments employing both ultrafast [61, 62] and near-field optical spectroscopy [60, 64] of quantum dots. In Fig. 4.4, the generation of φ-pulses which lead to the implementation of our QTC are presented (see also Figs. 3.4 and 3.6). As mentioned previously, $|0\rangle$ represents the vacuum for excitons while $|1\rangle$ denotes a single-exciton state.

For the practical proposal of Fig. 4.2(a), 3 equidistant QDs are required which must initially be prepared in the state $|\Psi\rangle_a|0\rangle_b|0\rangle_c$. As shown in Fig. 4.3(a), one of these (QD a) contains the quantum state $|\Psi\rangle_a$ that we wish to teleport, while the other two (QDs b and c) are initialised in the state $|00\rangle_{bc}$—this latter state is easy to achieve since it is the ground state. Following this initialisation, QDs b and c are illuminated with a radiation pulse of frequency ω given by $\xi(t) = A\exp(-i\omega t)$ [see Fig. 4.3(b)]; here A includes the electron-photon coupling and the electric field strength, and the time-dependence of ξ gives the pulse shape.

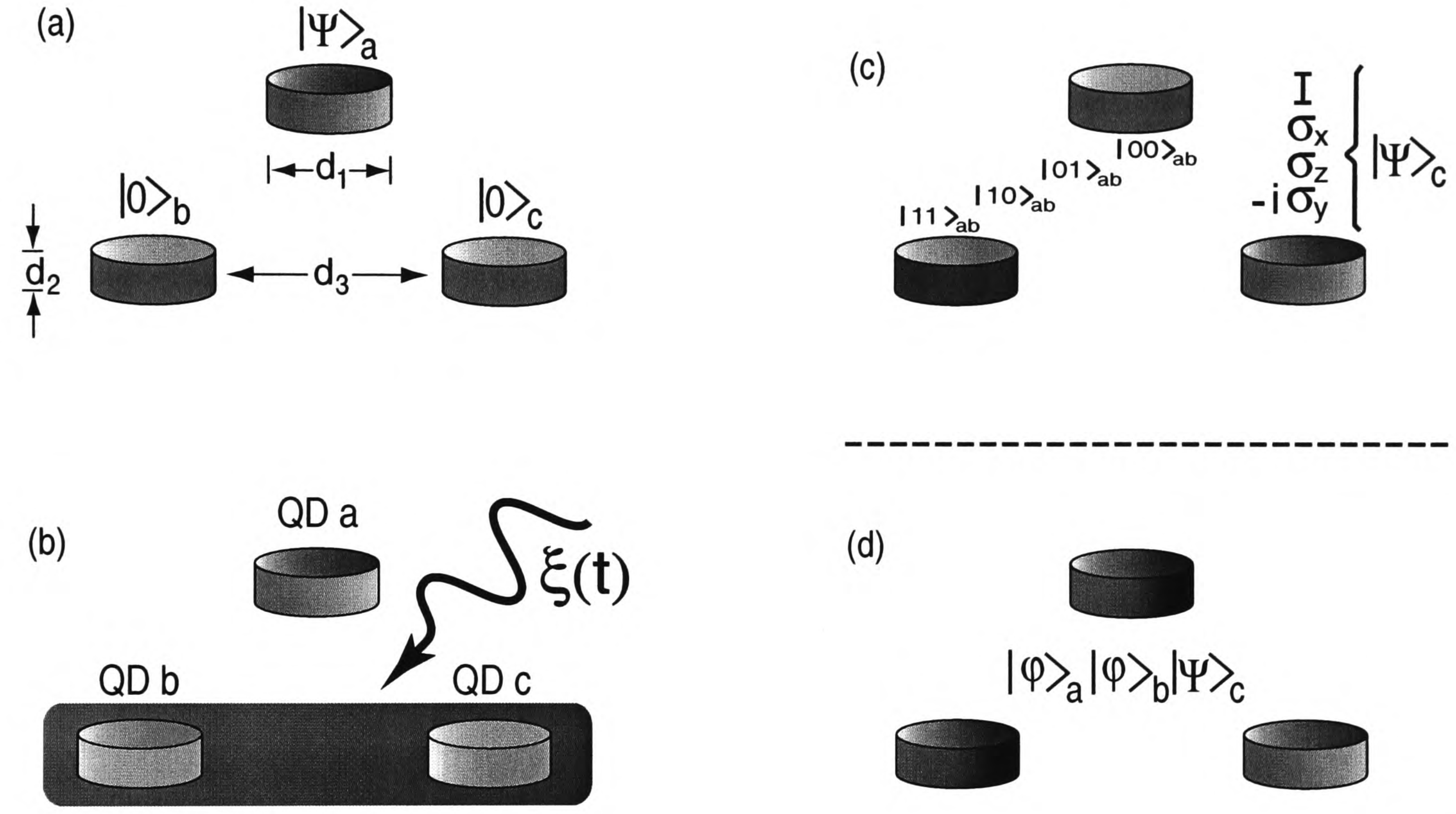

Figure 4.3: Practical implementation of teleportation using optically-driven coupled quantum dots. (a) Initial state of the system. (b) Intermediate step: radiating the system with the pulse $\xi(t)$. (c) Bell basis measurement and the quantum state of the system at the dashed line in Fig. 4.2(a). (d) Final state. Typical values for GaAs-based dots are diameter $d_1 = 20$ nm, thickness $d_2 = 5$ nm and separation $d_3 \leq 20$ nm (these dimensions and separation depend on the kind of materials employed, see text).

As an example, let's consider the case of ZnSe-based QDs. The band gap $\epsilon = 2.8$ eV, hence the resonance optical frequency $\omega = 4.3 \times 10^{15}$ s^{-1}. In units of $\epsilon, W = 0.1$ and $A = \frac{1}{25}$. For a 0 or 2π-pulse, the density of probability for finding the QDs b and c in the Bell state $|\Psi_{\text{BELL}}(0)\rangle$ shows that a time $\tau_{\text{BELL}} = 7.7 \times 10^{-15}$ s is required [see Fig. 4.4(a)]. Hence, this time τ_{BELL} corresponds to the realisation of the first two gates of the circuit in Fig. 4.2(a), i.e., the Hadamard transform over QD b followed by the CNOT gate between QDs b and c. After this, the information in qubit c is sent to Bob, and Alice keeps in her memory the state of QD b (Fig. 4.2(a)). Next, a CNOT gate between QDs a and b, followed by a Hadamard gate over the QD a are performed: this procedure then leaves the system in the state

$$\tfrac{1}{2}\Big\{|00\rangle(\alpha|0\rangle+\beta|1\rangle)+|01\rangle(\beta|0\rangle+\alpha|1\rangle)+|10\rangle(\alpha|0\rangle-\beta|1\rangle)+|11\rangle(-\beta|0\rangle+\alpha|1\rangle)\Big\}\,. \quad (4.13)$$

As can be seen from Eq. (4.13), the realisation of the Bell basis measurement has been proposed in two steps [141]: first, the Bell basis has been mapped into the computational basis of two qubits $\mathcal{B}_2 \equiv \{|00\rangle, |01\rangle, |10\rangle, |11\rangle\}$, by performing the unitary operations shown before the dotted line in Fig. 4.2(a). Hence, the second step is to perform a measurement in this computational basis. At this point, QDs a and b are left in one of the four states $|00\rangle$, $|01\rangle$, $|10\rangle$, $|11\rangle$ [see Fig. 4.3(c)], which are the four possible measurement results. This last step can be experimentally realised by using *near-field optical spectroscopy* [60, 64]. In this way, it is possible to scan, dot-by-dot, the optical properties of the entire dot ensemble, and particularly, to measure directly the excitonic photoluminiscence spectrum of dots a and b, thus completing the Bell basis measurement. The result of this measurement provides us with two classical bits of information, conditional on the nanoprobing measurement of QD states a and b [see Fig. 4.3(c)]. These classical bits are essential for completing the teleportation process: rewriting Eq. (4.13) as

$$\tfrac{1}{2}\Big\{|00\rangle|\Psi\rangle + |01\rangle\sigma_x|\Psi\rangle + |10\rangle\sigma_z|\Psi\rangle + |11\rangle(-i\sigma_y)|\Psi\rangle\Big\}\,, \quad (4.14)$$

we see that, if instead of performing the set of operations shown after the dotted line in Fig. 4.2(a), Bob performs one of the conditional unitary operations I, σ_x, σ_z, or $-i\sigma_y = \sigma_x\sigma_z$ over the QD c [depending on the measurement results or classical signal communicated from Alice to Bob, as shown in Fig. 4.3(c)], the teleportation process is finished since the excitonic state $|\Psi\rangle$ has been teleported from dot a to dot c. This final step can be verified by measuring directly the excitonic luminescence from dot c, which must correspond to the initial state of dot a[7]. For instance, if the state to be teleported is $|\Psi\rangle \equiv |1\rangle$, the final measurement of the near-field luminiscence spectrum of dot c must give an excitonic emission line of the same wavelength and intensity as the initial one for dot a. This measurement process, used for verifying the fidelity of the process, can be used if either the unitary transformations after Alice's measurement are performed [Fig. 4.3(c)] or if the complete teleportation circuit shown in Fig. 4.2(a) is realised, leaving the system in the state $|\Lambda\rangle_a |\Gamma\rangle_b |\Psi\rangle_c$.

Combining spatial and spectral resolutions, it has already been demonstrated that it is possible to excite and probe just one individual QD with the corresponding dephasing time $\tau_{dec} = 4 \times 10^{-11}$ s [61]. Hence, there is the possibility of coherent optical control of the quantum state of a single dot. Furthermore, this mechanism can be extended to include more than one excited state: since $\frac{\tau_{\text{BELL}}}{\tau_{dec}} \sim 10^{-4}$, several hundred unitary operations can in principle be performed in this system before the excited state of the

---

[7] Note that, if instead of performing the above-mentioned unitary transformations, the whole teleportation circuit is to be implemented [see the protocol presented for Fig 4.2(b)], the measurement and reconstruction of the $\mathcal{B}_1$-basis states $|\Lambda\rangle$, and $|\Gamma\rangle$ of QDs a, and b at the dashed line [see Fig. 4.2(a)] imply that the final output state of the teleportation device is given by $|\Lambda\rangle_a |\Gamma\rangle_b |\Psi\rangle_c$, regardless of the measured result for Λ_a and Γ_b at the dashed line.

QD system decoheres. This fact, together with the experimental feasibility of applying the required sequence of laser pulses on the femtosecond time scale [60], leads to the conclusion that it is not necessary to worry unduly about decoherence occurring whilst performing the unitary operations that Bob needs in order to obtain the final states schematically sketched in Figs. 4.3(c) and 4.3(d), thereby completing the teleportation process (the analysis of the decoherence effects on the generation of the QD entangled states is given in Chapter 6). In the case of Fig. 4.4(b), a similar analysis shows that $\tau_{\text{GHZ}} = 2.3 \times 10^{-14}$ s, and hence $\frac{\tau_{\text{GHZ}}}{\tau_{dec}} \sim 10^{-4}$: this also makes the circuit in Fig. 4.2(b) experimentally feasible.

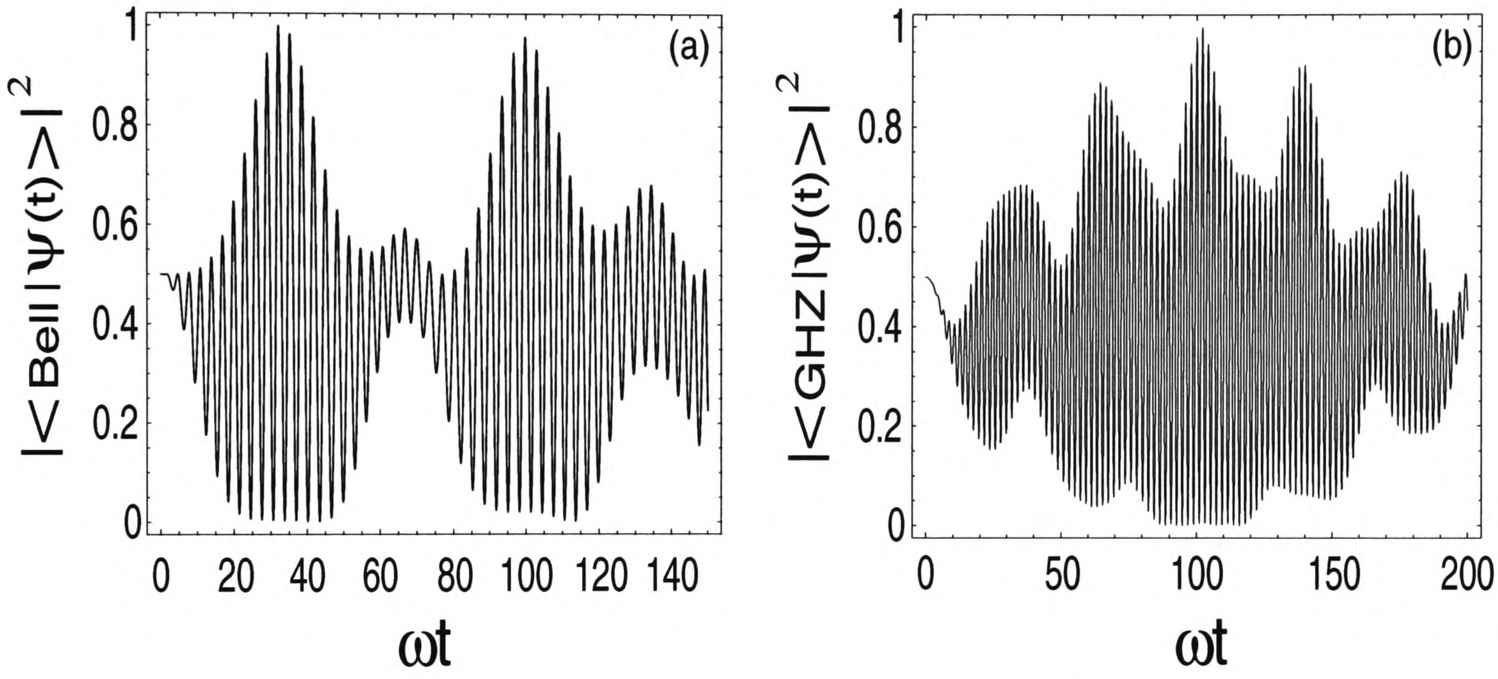

Figure 4.4: Generation of (a) the Bell State $|\Psi_{\text{BELL}}(0)\rangle$ and (b) the GHZ state $|\Psi_{\text{GHZ}}(0)\rangle$. These pulses correspond to the realisation of the Hadamard gate followed by one CNOT gate and two CNOT gates respectively [see Figs. 4.2(a) and 4.2(b)]. In units of the band gap $\epsilon = 2.8$ eV, $W = 0.1$, $A = \frac{1}{25}$. $|\psi(0)\rangle = |0\rangle$. Here $|\psi(t)\rangle$ denotes the total wavefunction of the system in the laboratory frame at time t.

Although this discussion refers to ZnSe-based QDs, other regions of parameter space can be explored by employing semiconductors of different bandgap ϵ. We believe that hybrid organic-inorganic nanostructures [143] are very promising candidates for the setup proposed here. This is because these hybrid structures provide us with large radius (Wannier-Mott) exciton states in the inorganic material and small-radius (Frenkel) exciton states in the organic one. Hence the hybrid material will be characterised by a radius dominated by their Wannier component and by an oscillator strength dominated by their Frenkel component. This means that the desirable properties of both the organic and the inorganic material are brought together to overcome basic limitations which arise if each one acts separately. Following recent results [143], if the three QD setup required in the present proposal is made of an inorganic II-VI material (e.g., the extensively studied ZnSe or ZnCdSe), embedded in bulk-like organic crystalline material (e.g., tetracene, perylene, fullerene, or PTCDA) where their Frenkel and Wannier excitons are in resonance with each other, a strong hybridisation between these excitons would be expected, which means a greater Wannier exciton delocalisation or Förster hopping. To achieve this, the typical distance between QDs should be of the same order as their size: In ZnSe, the Bohr radius of the three dimensional Wannier exciton $a_B \approx 35$ Å, hence QDs with radii of about 50 Å will considerably increase the binding energy of these excitons. If these dots are placed in an organic matrix (as discussed above) separated by a distance of the same order, it should be possible to perform the appropriate quantum operations required in the teleportation process of the excitonic state $|\Psi\rangle$. A more detailed description of the implementation of the quantum entanglement schemes required in the present proposal was presented in the previous chapter [JHR1, 53]. Even though the structures considered here have a dephasing time of order 10^{-11} s, QDs with stronger confinement are expected to have even smaller coupling to phonons giving the possibility for much longer intrinsic coherence times. In addition, and besides quantum error correction, there are some schemes for "noise suppression," where the effects of unwanted system-bath interactions can be dynamically controlled by using a sequence of 'tailored external pulses'; in addition to the existence of "decoherence-free subspaces", a "quiet corner" of the Hilbert's system space where the quantum dynamics of the system can be effectively decoupled from the surrounding environment (see Chapter 6).

In summary, this chapter has proposed the practical implementation of a quantum teleportation device, exploiting current levels of optical control in coupled QDs. Furthermore, the analysis suggests that several hundred quantum computation operations may in principle be performed before decoherence takes over.

The next chapter gives an alternative approach to the ultrafast coherent optical proposal presented here: a setup for the implementation of a solid-state NMR-based quantum switch for quantum logic is given, where typical qubit decoherence times are in the miliseconds time scale [JHR3].

Chapter 5

Spintronics: a solid state NMR-based quantum switch

So far, the schemes presented for the processing of QD-based quantum information have involved "ultrafast" (femtosecond) processes. Given the physical properties of the hardware used as the qubit system—QD excitons—it has been shown that the proposed devices should operate on the sub-picosecond time scale in order to avoid the fast decoherence of the qubits. In this chapter, an alternative mechanism for quantum computation that works on a very different time scale is presented, where typical qubit decoherence times are of the order of miliseconds, with the advantage that typical gating operations can still be accomplished via ultrafast processes.

5.1 Preliminaries

As mentioned in Chapter 2, quantum superposition and entanglement are currently being exploited to create powerful new computational algorithms in the growing field of quantum information processing. A major question for condensed matter physics is whether a solid-state quantum computer can ever be built. As has already been pointed out, there are at least two basic requirements which must be met by any candidate designs: first is the ability to perform single-qubit rotations as well as two-qubit controlled operations. Second, these qubit gates must be performed coherently and accurately in order to guarantee the success of the computation: this implies that the qubits should have a long enough decoherence time, such that at least the criteria $\tau_{gate}/\tau_{dec} < 10^{-4}$ is met [129] (recall that τ_{gate} is the time required to perform an elementary logic gate). Of utmost importance, therefore, is the identification of a solid-state system which can be used to represent the qubits.

Nuclei with spin half are natural qubits for quantum information processing as compared to electrons [51], since they have a far longer decoherence time: indeed they have been used in bulk liquid NMR experiments to perform some basic quantum algorithms like those of Deutsch [39], Grover [39], and Shor [40] for a quantum register of at most, 7 qubits. Their exceptionally low decoherence rates allow implementation of quantum gates by applying a sequence of radio-frequency pulses. Nuclear spins have already been employed in some solid-state proposals, for example that of Kane [41], where a set of donor atoms (like P) is embedded in pure silicon. Here, the qubit is represented by the nuclear spin of the donor atom and single qubit and controlled-NOT operations might then be achieved between neighbour nuclei by attaching electric gates on top and between the donor atoms. Another proposal suggests controlling the hyperfine electron-nuclear interaction via the excitation of the electron gas in quantum Hall systems [50]. Both of these proposals, however, require the attachment of electrodes or gates to the sample in order to manipulate the nuclear spin qubit. Such electrodes are likely to have an invasive effect on the coherent evolution of the qubit, thereby destroying quantum information.

In this chapter a novel solid-state based mechanism for quantum computation is proposed. The essential system is a nuclear spin-$\frac{1}{2}$ impurity placed at the center of a 2 electrons QD in the presence of an external perpendicular magnetic field B, as shown schematically in Fig. 5.1. These electrons undergo abrupt ground-state (so-called "magic number") transitions as the B-field is changed. The different ground states have very different charge distributions and hence different hyperfine interaction with the nucleus. Thus, by changing B we can change the hyperfine coupling and hence tune the nuclear resonance frequency. This allows one to effectively select out one such dot from an array, and the same mechanism may also allow an electron-mediated interaction between nuclei in different dots. The proposal is motivated by recent experimental results which demonstrated the optical detection of an NMR signal in both single QDs [144] and doped bulk semiconductors [145]. The experimental dots were formed by interface fluctuations in GaAs/GaAlAs quantum wells. The NMR signal from constituent Ga and As nuclei was optically detected via excitonic recombination, exploiting the hyperfine coupling between the electronic and nuclear systems. Hence the underlying nuclear spins in the QDs can indeed be controlled with optical techniques, via the electron-nucleus coupling. In addition, the experimental results of Ashoori *et al.* [148] and others, have demonstrated that few electron (i.e. $\mathcal{N} \geq 2$) dots can be prepared, and their magic number transitions measured as a function of the magnetic field. The requirements for the present proposal are therefore compatible with current experimental capabilities and the complications associated with voltage gates or electron transport of other known proposals (e.g., Refs. [41, 50]) are avoided by providing an *all-optical* system.

5.2 The nanostructure switch

Consider a silicon-based $\mathcal{N}$-electron QD in which a ^{13}C impurity atom (nuclear spin $\frac{1}{2}$) is placed at the centre. Ordinary silicon (^{28}Si) has zero nuclear spin, hence it is possible to construct the QD such that no nuclear spins are present other than those carried by the carbon nucleus. Since carbon is an isoelectronic impurity in silicon, no Coulomb field is generated by this impurity. Hence the electronic structure of the bare QD is essentially unperturbed by the presence of the carbon atom. Suppose the quantum dot is quasi two-dimensional (2D) and contains $\mathcal{N} = 2$ electrons. An external perpendicular magnetic field B is applied, as shown in Fig. 5.1. The lateral confining potential in such quasi-2D QDs is typically parabolic to a good approximation: the electrons, with effective mass m^*, are confined to the $z = 0$ plane with lateral confinement $\frac{1}{2}m^*\omega_0^2 r^2$. Repulsion between electrons is modelled by an inverse-square interaction αr^{-2} which leads to the same ground-state physics as a bare Coulomb interaction r^{-1} [59, 151]: moreover, such a non-Coulomb form may actually be more realistic due to the presence of image charges [152]. Any many-valley effects due to the band structure of silicon should be small and will be ignored. In the effective mass approximation, the Hamiltonian is given by $H = H_0 + V$, with

$$\begin{aligned} H_0 &= H_{2e} + H_{\text{ZEEMAN}} \ , \\ V &= \tfrac{8\pi}{3}\gamma_e\gamma_n\hbar^2|\phi(z=0)|^2 \sum_{\nu=1}^{2} \boldsymbol{I}\cdot\boldsymbol{S}_\nu \delta(\boldsymbol{r}_\nu) \ , \end{aligned} \tag{5.1}$$

where H_{2e} includes the orbital degrees of freedom of the two-electron QD in a perpendicular magnetic field and H_{ZEEMAN} corresponds to the individual electron spins and nuclear spin interaction with the magnetic field. The Fermi contact hyperfine coupling of the nuclear spin with the electron spins is expressed by V in Eq. (5.1), where the electron-nucleus hyperfine interaction strength is given by $C \equiv \frac{8\pi}{3}\gamma_e\gamma_n\hbar^2|\phi(z = 0)|^2$, with $\phi(z = 0)$ the single-electron wavefunction evaluated at the QD plane, γ_e (γ_n) is the electronic (nuclear) gyromagnetic ratio, and $\boldsymbol{S}_\nu$ ($\boldsymbol{I}$) is the electron (nuclear) spin. The electron location in the QD plane is denoted by the 2D vector $\boldsymbol{r}_\nu$. Following Ref. [151], H_{2e} splits up into commuting centre-of-mass (CM) motion and relative (rel) motion contributions, for which exact eigenvalues and eigenvectors can be obtained analytically. The electron-electron interaction only affects the relative motion.

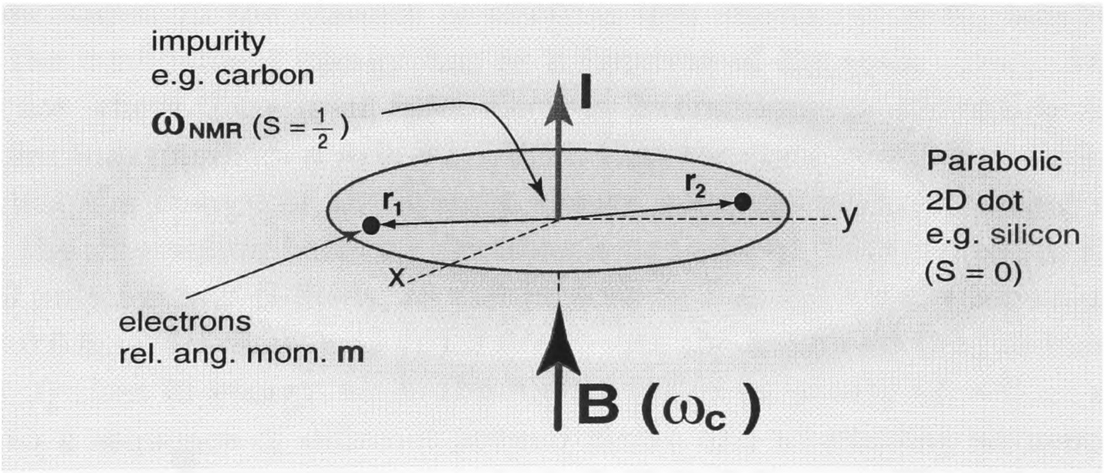

Figure 5.1: Schematics of the model quantum dot. A nuclear impurity of spin-half is placed at the centre of a quasi-2D dot (spin-zero). The dot is in the presence of an external static magnetic field B and laterally confined by the parabolic potential $m^*\omega_0^2 r^2/2$.

The eigenstates of H are linear combinations of states labelled as $|I_z; N, M; n, m; S, S_z\rangle$, where N and M (n and m) are the Landau and angular momentum numbers for the CM (relative motion) coordinates; S and S_z represent the total electron spin and its z-component, while I_z represents the z-component of the carbon nuclear spin. Consider the two-electron system in its ground state, i.e., $N = M = 0$, $n = 0$; m determines the orbital symmetry while $S = 0, 1$ represents the singlet and triplet spin states respectively. Neglecting the off-diagonal orbital coupling terms of the hyperfine interaction V, the corresponding energy spectrum associated with the total Hamiltonian H is

$$E = E_{cm} + E_{rel} + E_{spin} \ , \tag{5.2}$$

where, in general, for any quantum number, the centre-of-mass and relative electron orbital energy contributions are $E_{cm} = \frac{\hbar\omega}{2}[1+2N+|M|]+\frac{\hbar\omega_c}{2}M$, and $E_{rel} = \frac{\hbar\omega}{2}[1+2n+\mu_m] + \frac{\hbar\omega_c}{2}m$; E_{spin} refers to the eigenenergies of the spin Hamiltonian of the electronic-nuclear system (Zeeman spin energy), which we shall consider below. Here m, and M are integer numbers, and $n, N \in [0, \infty]$; $\omega = \sqrt{\omega_c^2 + 4\omega_0^2}$ denotes the effective frequency, and $\omega_c = eB/m^*$ is the cyclotron frequency. The term $\mu_m = \sqrt{\beta + m^2}$ absorbs the effects of the electron-electron interaction through the parameter $\beta \equiv \frac{\alpha/l_0^2}{\hbar\omega_0}$, where $l_0 = \sqrt{\hbar/m^*\omega_0}$ is the oscillator length.

In order to gain insight into the underlying mechanism proposed in this chapter, let's first briefly analyse the dynamics of the bare interacting electron system. Though the unperturbed Hamiltonian H_0 includes the Zeeman (static shift) energy $E_{spin} = g^*\mu_B BS_z - g_N\mu_N BI_z$ (g^* is the associated effective Landé g factor, μ_B and μ_N represent the Bohr and nuclear magnetons), for the sake of an analysis of purely electron correlations, the nuclear Zeeman energy (see below) and the effects of the interaction between nuclear and electron spins shall first be ignored. Thus, Figs. 5.2 and 5.3 show the ground state energy spectrum of the electronic system as a function of the magnetic field for different quantum numbers m. Recall that the ground state of the two-electron system has the quantum numbers $N = M = n = 0$, and $m \leq 0$. In Fig. 5.2, the energy of these states, in the absence of electron spin effects ($g^* = 0$), has been plotted in units of the confinement energy $\hbar\omega_0$ as a function of the ratio ω_c/ω_0. Figure 5.2(a) shows the case where there is no inter-electron interaction: we see clearly from the sequence of quantum numbers $n = 0, -1, -2, \ldots$ that the state $m = 0$ is always the ground state and that the energy of the system always increases with increasing n. By contrast, when the interaction between electrons is considered, they remain in their ground state $m = 0$ only for low B-fields, as can be seen in Fig. 5.2 for the repulsion strengths $\alpha/l_0^2 =$ (b) $0.5\hbar\omega_0$, (c) $\hbar\omega_0$, and (d) $3.0\hbar\omega_0$. As the magnetic field is increased, this state ($m = 0$) rises in energy while the higher states $m = -1, -2, -3, \ldots$ drop, hence giving rise to a sequence of different ground states and alternating sequence of singlet and triplet states $(m, S) = (0, 0), (-1, 1), (-2, 0), (-3, 1), \ldots$. The behaviour of these transitions can be understood by looking at the dynamics of the relative motion: by increasing the magnetic field, the electrons become closer to each other thus increasing their repulsive energy and hence jumping to a higher relative angular momentum because in this way they manage to increase their separation. One can also notice from these figures that the magnetic field strengths at which these transitions occur decrease as the confinement energy increases. The reason for this is found in the stronger confinement due to the harmonic potential which makes the dot size smaller thus requiring much smaller B-field strengths in order to perform the symmetry changes of the ground state. This can be illustrated, for example, by looking at Fig. 5.2(c), where the repulsion strength $\alpha/l_0^2 = \hbar\omega_0$: a confinement energy $\hbar\omega_0 = 1.1$ meV has associated an oscillator length $l_0 = 31.7$ nm, while the higher energy $\hbar\omega_0 = 5.4$ meV has $l_0 = 14.4$ nm.

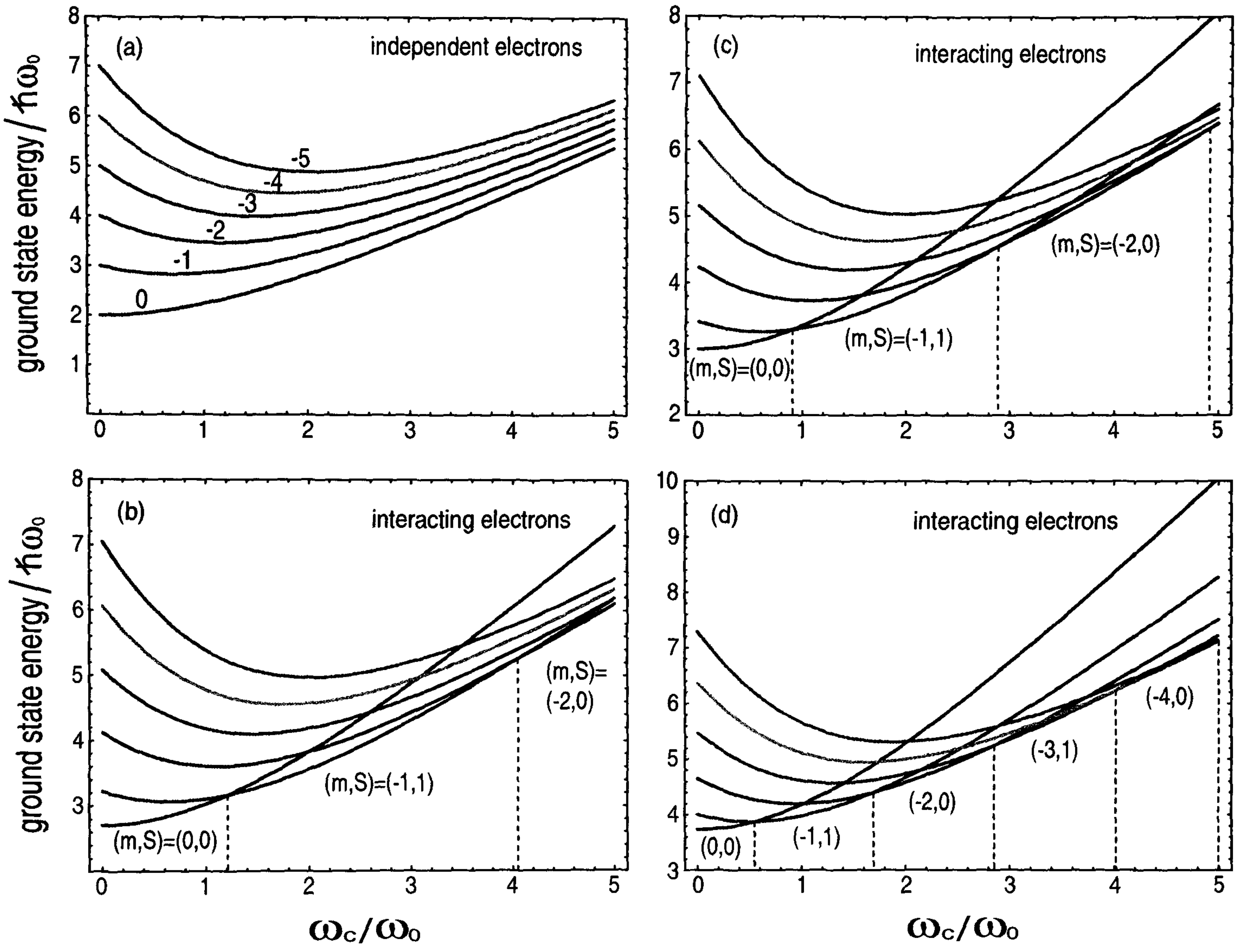

Figure 5.2: Energy of the ground state (in units of the confinement energy $\hbar\omega_0$) of a two-electron QD for vanishing Landé factor $g^* = 0$ (i.e., the Zeeman spin splitting has been ignored) as a function of the ratio of cyclotron and oscillator frequency ω_c/ω_0. (a) without and (b), (c), (d) considering the interaction between electrons. The electron repulsion strength $\beta =$ (b) 0.5, (c) 1.0, (d) 3.0. As the magnetic field increases, the interaction between electrons undergoes a sequence of different ground states, and alternating sequence of singlet and triplet states $(m, S) = (0,0), (-1,1), (-2,0), (-3,1), (-4,0), \ldots$. The magnetic field strengths at which these transitions occur are indicated by the dashed lines.

In Fig. 5.3, the effects of the electron Zeeman energy have been included. The case of an effective Landé factor $g^* = -0.44$, and effective mass $m^* = 0.067m_0$, which are appropriate values for bulk GaAs conduction-band electrons, have been considered. Hence, the additional electron spin energy $E^{e^-}_{spin} = g^*\frac{m^*}{m_0}\frac{\hbar\omega_c}{2}S_z$ means that singlet states remain unchanged ($E^{e^-}_{spin} = 0$) while triplet states split into the three levels $E^{e^-}_{spin} = -g^*\frac{m^*}{m_0}\frac{\hbar\omega_c}{2}$, 0, $g^*\frac{m^*}{m_0}\frac{\hbar\omega_c}{2}$. As a consequence, singlet ground states are totally suppressed and only triplet-triplet transitions are allowed for high magnetic fields, as can be seen from Fig. 5.3 for the $S_z = +1$ component of the triplet states. The sequence of relative angular momentum and total electron spin is given by $(m, S) = (0,0), (-1,1), (-2,0), (-3,1), (-5,1), (-7,1), (-9,1), \ldots$. Here it is worth pointing out that Pauli's exclusion principle requires the total wavefunction of the two electrons to be antisymmetric. Hence, spin singlet states ($S = 0$) must correspond to even m, while triplet ($S = 1$) states must correspond to odd m.

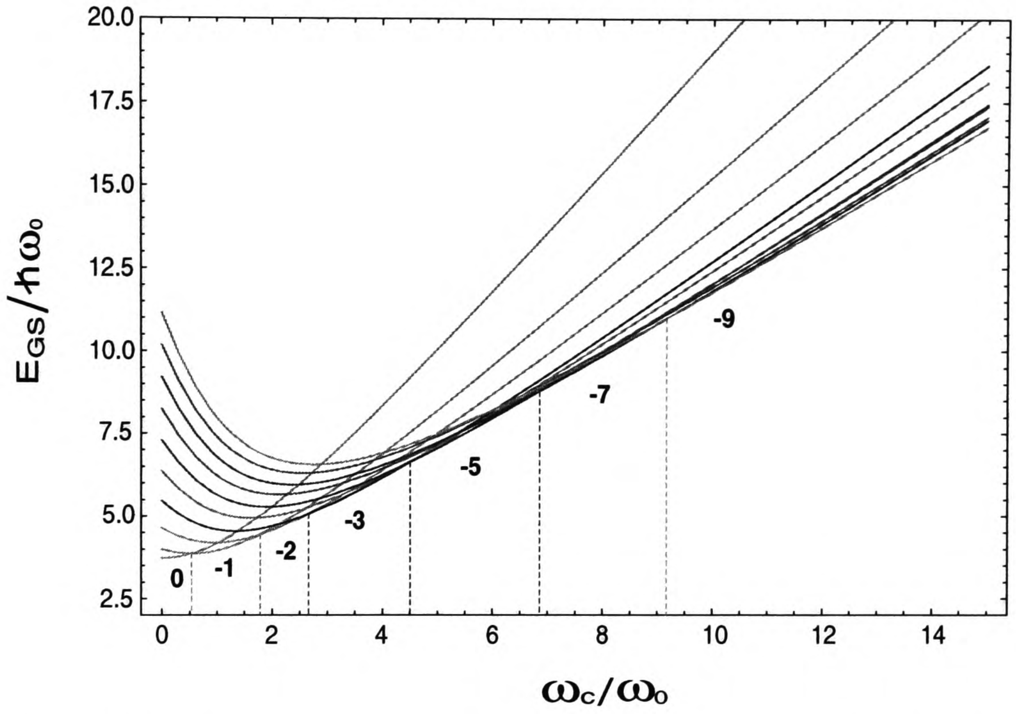

Figure 5.3: Energy of the ground state (in units of the confinement energy $\hbar\omega_0$) of a two-electron system in the presence of Zeeman spin splitting ($g^* = -0.44$) as a function of ω_c/ω_0. The electron repulsion strength $\alpha/l_0^2 = 3.0\,\hbar\omega_0$. As the magnetic field strength increases, the singlet ground states are suppressed and we are left with only triplet-triplet transitions. In this case the (m, S) sequence is given by $(0,0), (-1,1), (-2,0), (-3,1), (-5,1), (-7,1), (-9,1), \ldots$.

The above analysis shows that the physics of the ground-state transitions predicted within our model interaction αr^{-2} remains the same when compared with previous results reported for the bare Coulomb interaction r^{-1} [153]. However, such an inverse-square interaction can actually become more appropriate than the 'true' Coulomb interaction when taking into account the screening effects of the interaction between electrons due to the presence of image charges [148, 152]. Remarkably, the symmetry changes of the two-electron system ground state analysed above have already been experimentally observed [148]. These facts make the solid state NMR-based quantum switch proposal given in this chapter realistically feasible and within the reach of current QD technology.

Next, the dynamics of the whole interacting system, which includes the effects of the electron-nucleus coupling shall be analysed. In so doing, for a given orbital electron state, the spin Hamiltonian matrix elements shall be written in the basis $|I_z; S, S_z\rangle_m$ as

$$\begin{aligned} H_S \;=\; & \tfrac{C}{2}\sum_{\nu=1}^{2} \langle m|\,\delta(\boldsymbol{r}_\nu)\,|m\rangle \Big\{\delta_{I_z,-}\delta_{I_{z'},+}\,\langle S', S_z'|\,\boldsymbol{S}_{\nu,-}\,|S, S_z\rangle + \\ & \delta_{I_z,+}\delta_{I_{z'},-}\,\langle S', S_z'|\,\boldsymbol{S}_{\nu,+}\,|S, S_z\rangle \;+\; I_Z\delta_{I_z I_{Z'}}\,\langle S', S_z'|\,\boldsymbol{S}_{\nu,z}\,|S, S_z\rangle\Big\} + H_{\text{ZEEMAN}}\,. \end{aligned} \tag{5.3}$$

5.3 Nuclear spin-electron spin effective coupling: tuning the resonance frequency ω_{NMR}

As has been shown before, in the presence of the B-field, the low-lying energy levels of the electron system all have $n = 0$ and $m < 0$. The relative angular momentum m of the two-electron ground state jumps in value with increasing B. The particular sequence of m values depends on the electron spin because of the overall antisymmetry of the two-electron wavefunction [153]: only odd values of m arise if the B-field is sufficiently large for the spin wavefunction to be symmetric (the spatial wavefunction is then antisymmetric). These transitions, obtained analytically within our inverse-square model, yield the same sequence of transitions as for the Coulomb interaction. The electron-nucleus coupling depends on the wavefunction value at the nucleus and hence on m. The jumps in m will therefore cause jumps in the amount of hyperfine splitting in the nuclear spin of the carbon atom.

The nuclear spin-electron spin effective coupling affecting the resonance frequency ω_{NMR} of the carbon nucleus is given by $\langle m|\,\delta(\boldsymbol{r}_\nu)\,|m\rangle \equiv \Delta_{m,\nu}$, where

$$\Delta_{m,\nu} = \int d\boldsymbol{R} \int d\boldsymbol{r} \Psi^*_{2e}(\boldsymbol{R},\boldsymbol{r})\delta(\boldsymbol{r}_\nu)\Psi_{2e}(\boldsymbol{R},\boldsymbol{r}) \ . \tag{5.4}$$

Here, $\Psi_{2e}(\mathbf{R},\mathbf{r}) = \xi_{N,M}(\mathbf{R})\zeta_{n,m}(\mathbf{r})$ where $\xi_{N,M}(\mathbf{R})$ $(\zeta_{n,m}(\mathbf{r}))$ is the centre-of-mass (relative) wavefunction[1]. A detailed calculation yields $\Delta_{m,\nu} = \Delta_m$ (see footnote below), where

$$\Delta_m = \frac{1}{\pi l^2 2^{1+\mu_m}} \ , \tag{5.5}$$

and $l = \sqrt{\hbar/m^*\omega}$ is the effective magnetic length. Hence, the effective spin Hamiltonian H_S [Eq. (5.4)] has the form

$$H_S = A_m\left[(I_+S_- + I_-S_+) + 2I_zS_z\right] - \gamma_n BI_z + \gamma_e BS_z \ , \tag{5.6}$$

where $A_m = \frac{1}{2}C\Delta_m$ represents a B-dependent hyperfine coupling. Note that the first term (square brackets) of the hyperfine interaction in Eq. (5.6) corresponds to the dynamic part responsible for nuclear-electron flip-flop spin transitions while the second term describes the static shift of the electronic and nuclear spin energy levels.

---

[1] As an example, consider $\nu = 1$ (the procedure below leads us to show that $\Delta_{m,1} = \Delta_{m,2} \equiv \Delta_m$):

$$\Delta_{m,1} = \int d\boldsymbol{R} \int d\boldsymbol{r}\, \Psi^*_{2e}(\boldsymbol{R},\boldsymbol{r})\delta(\boldsymbol{R} + \tfrac{\boldsymbol{r}}{2})\Psi_{2e}(\boldsymbol{R},\boldsymbol{r}) = \int d\boldsymbol{r}\, \Psi^*_{2e}(-\tfrac{\boldsymbol{r}}{2},\boldsymbol{r})\Psi_{2e}(-\tfrac{\boldsymbol{r}}{2},\boldsymbol{r}) \ .$$

Introducing the wavefunctions $\xi_{N,M}(\mathbf{R}) = \frac{1}{l\sqrt{\pi}}\left[\frac{N^*!}{(N^*+|M|)!}\right]^{\frac{1}{2}}\left(\frac{R}{l}\right)^{|M|} \exp(iM\Phi)\, L^{|M|}_{N^*}\left(\frac{R^2}{l^2}\right)\exp\left(-\frac{R^2}{2l^2}\right)$, and $\zeta_{n,m}(\mathbf{r}) = \frac{1}{2l\sqrt{\pi}}\left[\frac{n^*!}{\Gamma(n^*+\mu_m+1)}\right]^{\frac{1}{2}}\left(\frac{r}{2l}\right)^{\mu_m}\exp(im\theta)\, L^{\mu_m}_{n^*}\left(\frac{r^2}{4l^2}\right)\exp\left(-\frac{r^2}{8l^2}\right)$ [151], we obtain

$$\Delta_{m,1} = \frac{1}{\pi l^2 2^{1+\mu_m}\Gamma(\mu_m+1)}\int_0^\infty x^{\mu_m}e^{-x}dx = \frac{1}{\pi l^2 2^{1+\mu_m}} \ ,$$

where $L^\beta_\alpha(y)$ is the associated Laguerre polynomial, $N^* = N - |M|\Theta(M)$, and $n^* = n - |m|\Theta(m)$. $\Theta(y)$ represents the Heaviside step function, $\Gamma(y)$ is the Gamma function; $x \equiv 2\left(\frac{r}{2l}\right)^2$, and the polar coordinates $\boldsymbol{R} = (R,\Phi)$, and $\boldsymbol{r} = (r,\theta)$ have been used.

Electrons in the singlet state ($S = 0$) are uncoupled from the nucleus. In this case, the nuclear resonance frequency is given by the undoped-QD NMR signal $\hbar\omega_{\text{NMR},0} = \gamma_n B$. For electron triplet states, the nuclear resonance signal corresponds to a transition where the electron spin is unaffected by a radio-frequency excitation pulse whereas the nuclear spin experiences a flip. This occurs for the transition between states $|-;1,-1\rangle$ and $|\Psi\rangle = c_1\,|+;1,-1\rangle + c_2\,|-;1,0\rangle$. The coefficients c_1 and c_2 can be obtained analytically[2] by diagonalising the Hamiltonian given in Eq. (5.6). Hence

$$\hbar\omega_{\text{NMR}} = \tfrac{3}{2}A_m + \tfrac{1}{2}\left(\gamma_n - \gamma_e\right)B + \tfrac{1}{2}\left(\left[A_m + \left(\gamma_n + \gamma_e\right)B\right]^2 + 8A_m^2\right)^{\frac{1}{2}} . \tag{5.13}$$

Since $\gamma_e >> \gamma_n$, the resonance frequency can be approximated as $\hbar\omega_{\text{NMR}} \approx \gamma_n B + 2A_m + \frac{9A_m^2}{4\gamma_e B} \approx \gamma_n B + 2A_m$, which illustrates the dependence of the NMR signal on the effective B-dependent hyperfine interaction.

Figure 5.4 shows the effective coupling Δ_m between the two-electron gas and nucleus as a function of the ratio between the cyclotron frequency and the harmonic oscillator frequency (the CM is in its ground state). For silicon, $C/l_0^2 = 60$ MHz. For B-field values where the electron ground state is a spin singlet (m even) no coupling is present. The strength of the effective coupling decreases as the B–field increases due to the larger spatial extension of the relative wavefunction at higher m values, i.e., the electron den-

---

[2] *Energy levels and eigenstates*: the nuclear spin operators $I_+|+\rangle = |-\rangle$, and $I_-|-\rangle = |+\rangle$. For the electron singlet, nuclear spins are coupled only to the external magnetic field, hence the states $|I_z;S,S_z\rangle$ are given by $|+;0,0\rangle$ and $|-;0,0\rangle$, with corresponding eigenenergies $E_+^S = -\gamma_n B$ and $E_-^S = \gamma_n B$. Next, consider the electron triplet states: the states $|+;1,-1\rangle$ and $|-;1,1\rangle$ are eigenstates of H_S with eigenvalues

$$E_+^{(1,-1)} = -A_m - \tfrac{1}{2}\gamma_n B - \gamma_e B, \quad \text{and} \quad E_-^{(1,1)} = -A_m + \tfrac{1}{2}\gamma_n B + \gamma_e B \ . \tag{5.7}$$

The other 4 eigenstates of this Hilbert space can be obtained by diagonalising the two corresponding 2 × 2 matrices. The eigenvectors are as follows

$$\begin{pmatrix} \Phi_+^{(1)} \\ \Phi_-^{(1)} \end{pmatrix} = \begin{pmatrix} \cos\left(\frac{\varphi}{2}\right) \\ -\sin\left(\frac{\varphi}{2}\right) \end{pmatrix} |-;1,-1\rangle + \begin{pmatrix} \sin\left(\frac{\varphi}{2}\right) \\ \cos\left(\frac{\varphi}{2}\right) \end{pmatrix} |+;1,0\rangle \ . \tag{5.8}$$

By introducing the function $f(A_m, B) \equiv A_m + \left(\gamma_n - \gamma_e\right)B$, the associated eigenenergies look like

$$E_\pm^{(1)} = \tfrac{1}{2}(A_m - \gamma_e B) \pm \tfrac{1}{2}\sqrt{f^2(A_m,B) + 8A^2(m)} \ , \tag{5.9}$$

where

$$\cos\left(\tfrac{\varphi}{2}\right) = \tfrac{1}{\sqrt{2}}\sqrt{1 + \tfrac{f(A_m,B)}{\sqrt{f^2(A_m,B)+8A_m^2}}} \ , \quad \sin\left(\tfrac{\varphi}{2}\right) = \tfrac{1}{\sqrt{2}}\sqrt{1 - \tfrac{f(A_m,B)}{\sqrt{f^2(A_m,B)+8A_m^2}}} \ . \tag{5.10}$$

The other set of eigenstates is given by

$$\begin{pmatrix} \Phi_+^{(2)} \\ \Phi_-^{(2)} \end{pmatrix} = \begin{pmatrix} \cos\left(\frac{\varphi'}{2}\right) \\ -\sin\left(\frac{\varphi'}{2}\right) \end{pmatrix} |-;1,0\rangle + \begin{pmatrix} \sin\left(\frac{\varphi'}{2}\right) \\ \cos\left(\frac{\varphi'}{2}\right) \end{pmatrix} |+;1,1\rangle \ , \tag{5.11}$$

with the following energy levels

$$E_\pm^{(2)} = \tfrac{1}{2}(A_m + \gamma_e B) \pm \tfrac{1}{2}\sqrt{f^2(-A_m,B) + 8A_m^2} \ , \tag{5.12}$$

where $\cos\left(\frac{\varphi'}{2}\right)$ and $\sin\left(\frac{\varphi'}{2}\right)$ are given as in Eq. (5.10) but making the substitution $A_m \mapsto -A_m$.

sity at the centre of the dot becomes smaller. Thus, the B-field provides a very sensitive control parameter for controlling the electron-nucleus effective interaction. In particular, we note the large abrupt variation of Δ_m for $\frac{\omega_c}{\omega_0} \approx 2.1$ where the electron ground state is performing a transition from a spin triplet state ($m = 1$) to a spin triplet state ($m = 3$). This ability to tune the electron-nucleus coupling underlies the present proposal for an NMR-based switch.

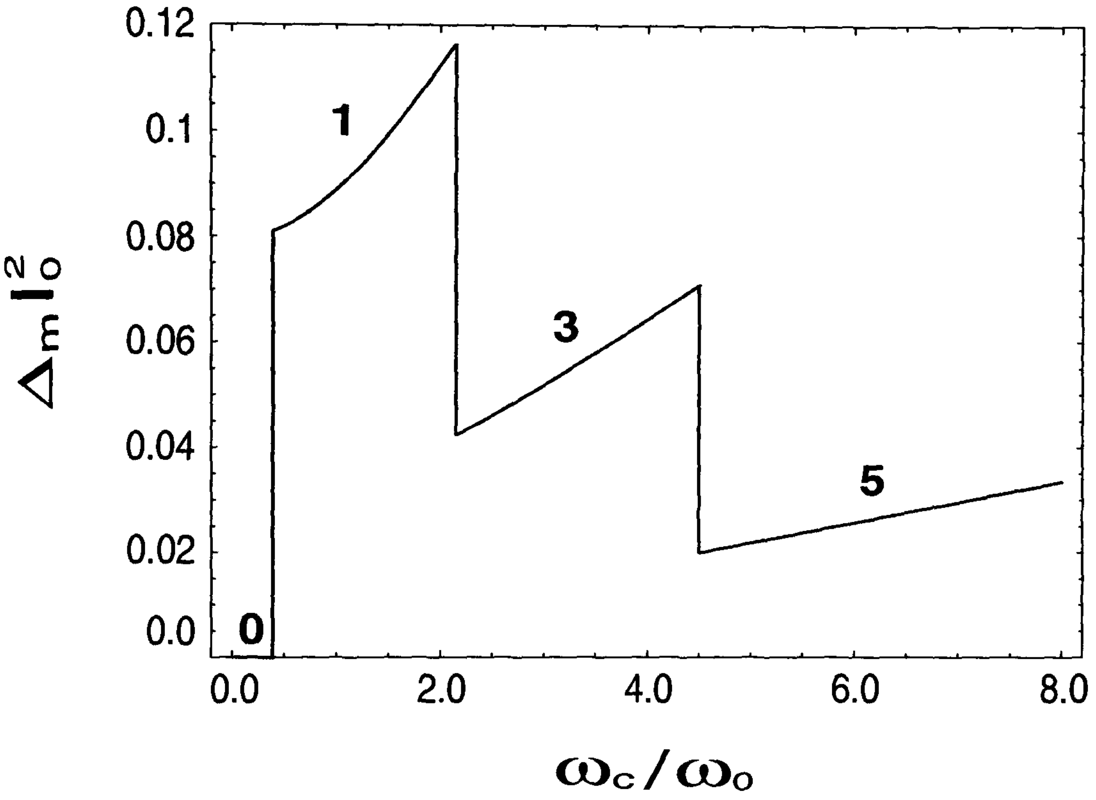

Figure 5.4: Variation of the electron spin-nucleus spin effective coupling Δ_m as a function of ω_c/ω_0. The centre-of-mass motion remains in its ground state. The electron repulsion strength $\beta = 3.0$. The two-electron ground state undergoes transitions in the relative angular momentum m. The sequence, in terms of $|m|$ and the total electron spin S, is given by $(|m|, S) = (0,0), (1,1), (3,1), (5,1), \ldots$. The triplet state component $S_z = -1$.

In order to observe the effects of the confinement potential-intrinsic electron repulsion interplay, in Fig. 5.5, the electron spin-nucleus spin effective coupling as a function of the magnetic field (in units of $m^*\omega_0/e$), for repulsion strengths (a) $\alpha/l_0^2 = \hbar\omega_0$, and (b) $\alpha/l_0^2 = 0.5\ \hbar\omega_0$, has been plotted. As previously noted in Fig. 5.4, the strength of the effective coupling Δ_m decreases as the B-field is increased. In addition, two main features are exhibited: i) for a given quantum number m, the product $\Delta_m l_0^2$ increases with decreasing repulsion strength β, which is also reflected in the large abrupt variation of Δ_m for magnetic field strengths at which the electron ground state performs the triplet-triplet transitions, and ii) the B-field values at which these triplet-triplet transitions occur ($E_m = E_{m-2}$) decrease with increasing β. These features can be understood by looking at the two-electron relative motion dynamics, i.e., the competition between kinetic energy, Zeeman energy, and repulsive electron-electron interaction energy, as the magnetic field is increased.

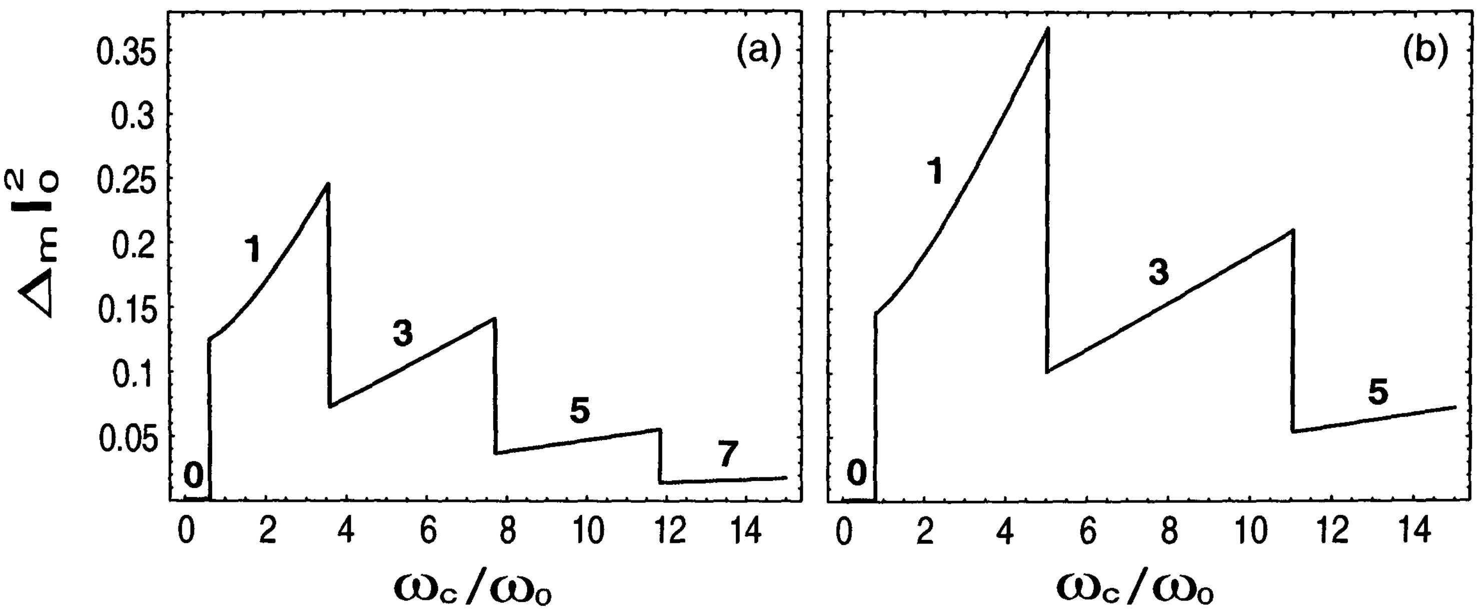

Figure 5.5: Variation of the electron spin-nucleus spin effective coupling Δ_m for electron repulsion strengths (a) $\beta = 1.0$, and (b) $\beta = 0.5$. The $(|m|, S)$ sequence is given by $(0,0), (1,1), (3,1), (5,1), \ldots$. $S_z = -1$. Here, and in Fig. 5.4, the values $m^* = 0.2m_0$, and $g^* = 2.0$, which are appropriate for silicon conduction band electrons, have been used.

The magnetic field strengths at which the two-electron ground state changes its relative angular momentum value are given by $B = 2m^*\omega_0 f_m/e\sqrt{1-f_m^2}$, where $f_m = (\mu_{m-2} - \mu_m)/2$ for triplet-triplet transitions $[\Delta(m) = -2]$, or $f_m = (\mu_{m-1} - \mu_m)/[1 \pm (-1)^{m-1} g^* m^*/m_0]$ for singlet-triplet spin transitions $[\Delta(m) = -1]$, where the ± sign refers to the $S_z = \pm 1$ components of the triplet spin states respectively. Next, a mechanism for a further degree of control of the nuclear spin qubit is introduced.

5.4 Far infrared radiation and nuclear qubit control

In the presence of infra-red (IR) radiation incident on the QD, the CM wavefunction will be altered since the CM motion absorbs IR radiation. The relative motion remains unaffected in accordance with Kohn's theorem. This allows an additional method for externally controlling the nucleus-electron effective coupling, using optics. By considering the CM transition from the ground state $|N = 0, M = 0\rangle$ to the excited state $|N = 1, M = 1\rangle$, which becomes the strongest transition in high B-fields, the new spin-spin coupling term yields

$$\Delta_{\text{CM}}(m) \equiv \langle 1, 1; m|\delta(r_\nu)|1, 1; m\rangle = \left(\frac{1+\mu_m}{2}\right)\Delta_m \,. \tag{5.14}$$

Hence the nuclear spin-electron spin coupling is renormalised by the factor $\frac{1+\mu_m}{2}$ in the presence of IR radiation. By changing the location of the impurity atom in the QD, the discontinuity strengths in Figs. 5.4 and 5.5 shall be modified, since the coupling is affected by the density of probability of the CM wavefunction at the impurity site. However, this fact does not pose any fundamental constraint to the proposal and, even under such a situation, we should still be able to realise the optical control of the nuclear qubit proposed here.

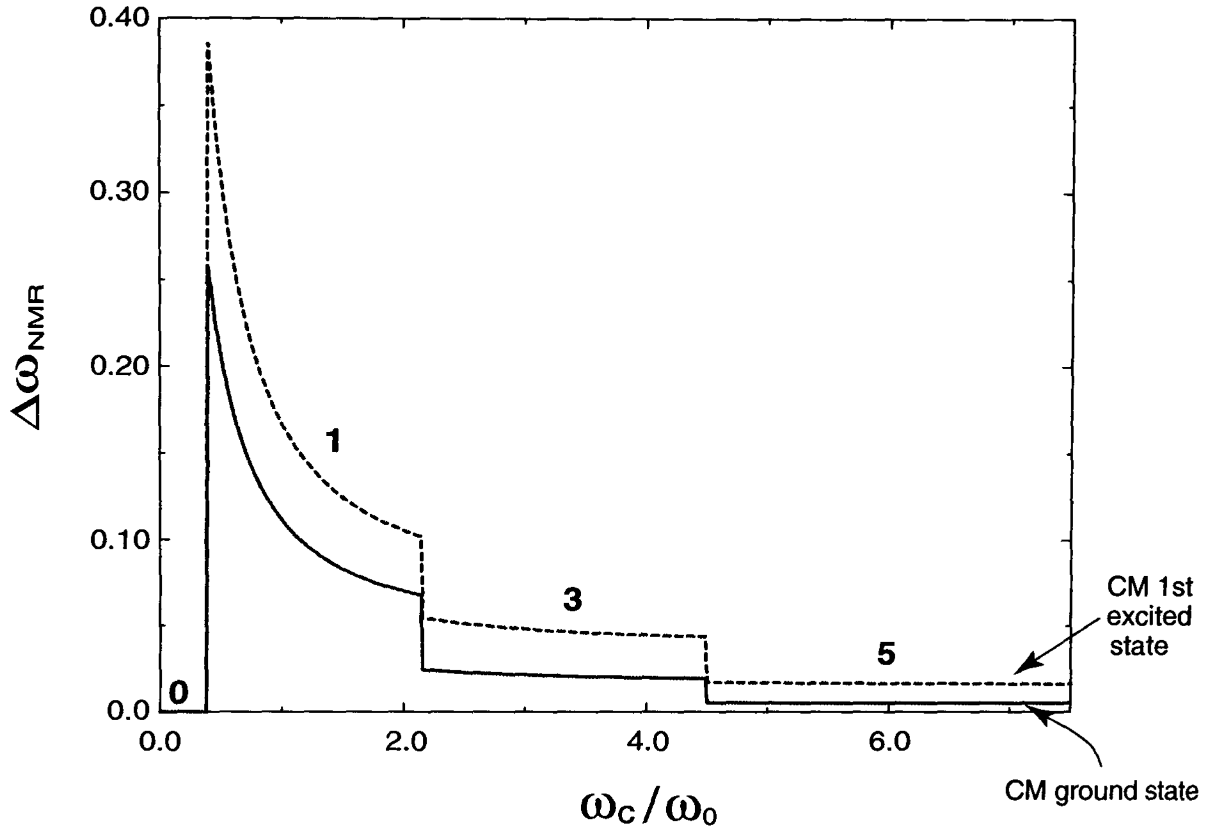

Figure 5.6: Relative variation of the effective nuclear magnetic resonance frequency of the carbon impurity nucleus, $\Delta\omega_{\text{NMR}} = (\omega_{\text{NMR}} - \omega_{\text{NMR},0})/\omega_{\text{NMR},0}$, as a function of ω_c/ω_0. The electron repulsion parameter $\beta = 3.0$. Solid line corresponds to centre-of-mass in the ground state. Dashed line corresponds to centre-of-mass in the first excited state after absorption of IR light. For the nuclear qubit (carbon impurity) we have considered the g-factor $g_N = -0.55477$.

Figure 5.6 shows the relative variation of ω_{NMR} with respect to the undoped QD NMR signal (solid line), i.e., $\Delta\omega_{\text{NMR}} = \frac{\omega_{\text{NMR}} - \omega_{\text{NMR},0}}{\omega_{\text{NMR},0}}$, as a function of the frequency ratio $\frac{\omega_c}{\omega_0}$. The jumps in the carbon nucleus resonance are abrupt, reaching 25% in the absence of IR radiation. This allows a rapid tuning on and off resonance of an incident radio-frequency pulse. The NMR signal in regions of spin-singlet states remains unaltered. The B-fields required to perform these jumps are relatively small. A typical $N = 2$ electrons QD with 30 nm diameter, and lateral confining potential $\omega_0 = 8.2 \times 10^{12}$ s^{-1} ($\hbar\omega_0 = 5.4$ meV) [148], would produce a singlet-triplet jump $(m, S) = (0, 0) \mapsto (-1, 1)$ at $B \approx 1.3$ T, or the triplet-triplet jump $(-1, 1) \mapsto (-3, 1)$ at $B \approx 6.5$ T (see Fig. 5.6). If the harmonic potential is decreased to $\hbar\omega_0 = 1.1$ meV [148], the above transitions would be expected at B-fields of 0.4 T and 1.4 T, respectively. Moreover, the nuclear spin is being controlled by radio-frequency pulses which are externally imposed, thereby offering a significant advantage over schemes which need to fabricate and control electrostatic gates near to the qubits, such as those of Refs. [41, 50]. Illuminating the QD with IR light will shift the frequencies ω_{NMR} (see dashed line in Fig. 5.6), hence providing further all-optical control of the nuclear qubit. A crucial aspect of the present proposal is the capability to manipulate individual nuclear spins. All-optical NMR measurements in semiconductor nanostructures [144, 145, 146] together with local optical probe experiments are quickly approaching such a level of finesse.

Single qubit gates: one-qubit unitary transformations, such as the Hadamard transform, can be performed by rotating the single nuclear qubit of resonant frequency ω_i via the application of RF pulses at the appropriate frequency for a given duration and a given amplitude of the B-field. An estimation of the coherence times T_1 and T_2 of the nuclear spins (nuclear spin-flip relaxation, and the rate of loss of phase coherence, respectively) of our set-up can be estimated as $T_1 \sim 1-10$ hour range ($T < 4$ K) [160], and $T_2 \sim 1$ ms (in isotopically purified ^{28}Si, where Si:P linewidths are < 1 MHz) [41]. In our case, the electrostatically neutral character of the impurity atom ^{13}C (and the fact that the silicon nuclei surrounding it have no nuclear spin) makes the carbon nuclear spin state very effectively shielded from the environment and hence we would expect to have far longer T_2 times than the (charged) donor nuclei mentioned above.

Note that the presence or absence of an IR photon can also represent a qubit: hence the present single QD system in an IR cavity can also be used to perform two qubit gates as a result of the coupling.

Conditional quantum dynamics and two-qubit gates: a controlled-U gate can be performed based on the selective driving of spin resonances for two impurity nuclear qubits I_1, I_2 (spin $\frac{1}{2}$) in a system of two coupled QDs, separated by a distance d, each containing two electrons. The QDs do not need to be identical in size. The orthonormal computation basis of single qubits $\{|0\rangle, |1\rangle\}$ is represented by the spin up and down of the impurity nuclei. The new Hamiltonian corresponding to this coupled quantum dot system must include the effect of the electronic correlations between the two QDs, and also the effects of the electronic-nuclear spin coupling of both QDs. One can imagine two possible configurations for which the electrons in the QDs are confined to the (a) $z = 0$, and d planes [Fig. 5.7(a)], and (b) $z = 0$ plane [Fig. 5.7(b)]. These configurations are considered in such a way that there is no inter-dot tunnelling. As said, in such systems, there are two combined effects which can be exploited to perform conditional quantum logic gates. First, we have the *intra-dot* interaction between electrons in the same QD and their coupling to the nuclear qubits. This interaction produces jumps in the relative angular momentum m of the two-electron ground state with increasing B. It has been shown that these jumps in m cause jumps in the amount of hyperfine splitting in the nuclear spin of the impurity atom, hence providing a switching mechanism for the nuclear-electron spin transitions. Second, there are the correlation between neighbouring dots, i.e., the *inter-dot* interaction between electrons in different QDs [see Figs. 5.7(a) and 5.7(b)]. This is the main mechanism responsible for the two qubit control given here.

The inter-dot interaction potentials associated with each configuration, namely $V^{(1)}_{inter}$ and $V^{(2)}_{inter}$, should produce the necessary nuclear qubit coupling for reliable implementation of two-qubit gates: conditional quantum dynamics can be performed based on the selective driving of spin resonances of the two impurity nuclear qubits I_1, and I_2. The corresponding interaction potentials are given by

$$V_{inter}^{(1)} = \sum_{\nu,\delta=1}^{2} \frac{\alpha}{|\boldsymbol{r}_{2,\nu} - \boldsymbol{r}_{1,\delta}|^2 + d^2} \ , \quad V_{inter}^{(2)} = \sum_{\nu,\delta=1}^{2} \frac{\alpha}{|\boldsymbol{r}_{2,\nu} - \boldsymbol{r}_{1,\delta}|^2} \ . \qquad (5.15)$$

The coupling between QDs gives an additional magic number transition as a function of B-field which can be used for selective switching between dots, i.e., since the ground state switches back and forth between product states and entangled states [155], the resonant frequency for transitions between the states $|0\rangle$, and $|1\rangle$ of one nuclear spin (target qubit) depends on the state of the other one (control qubit). In this way, such coupled QDs can be used to generate e.g., the conditional CNOT gate on arbitrary qubits $|\varphi_1\rangle$, and $|\varphi_2\rangle$.

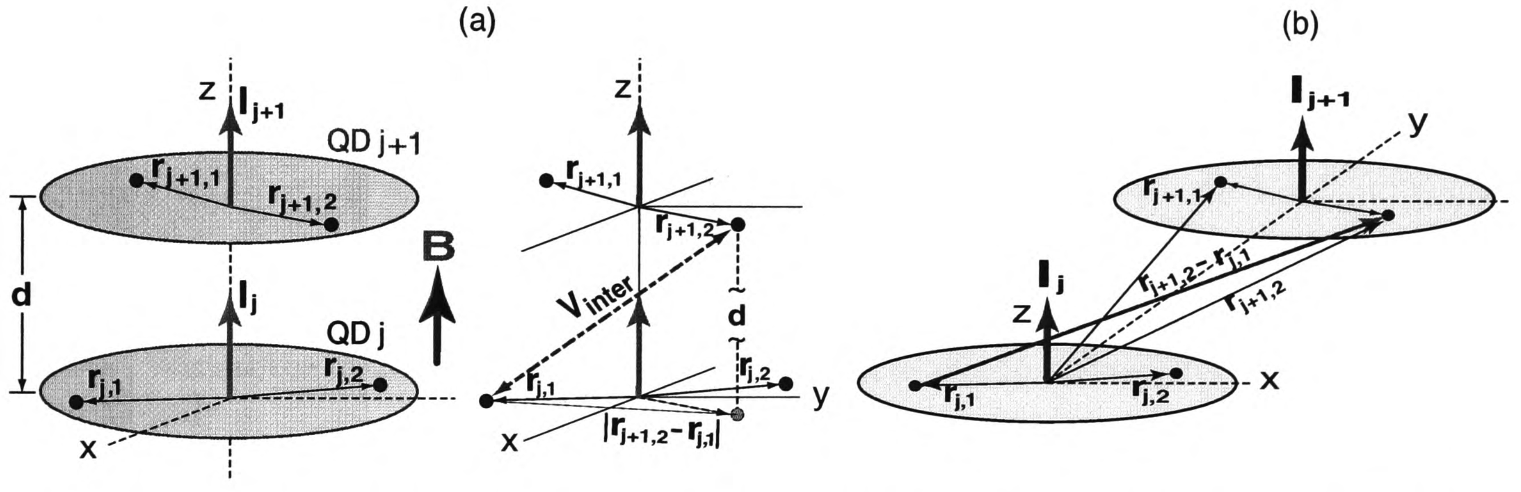

Figure 5.7: Schematic of the double QD system. Each QD contains 2 electrons. (a) Configuration 1, vertically arranged QDs with the nuclear impurity qubits and the electrons in dots j and $j+1$. The *inter-dot* correlation for electrons $(j+1, 2)$, and $(j, 1)$ is illustrated. Note that the separation between electrons in different dots is given in terms of the distances $|\boldsymbol{r}_{i+1,\nu} - \boldsymbol{r}_{i,\delta}|$ and d. The distance d does not correspond with the real scale of the system (see text). (c) Configuration 2, in-plane QDs: schematic of the *inter-dot* correlation for electrons $(j+1, 2)$, and $(j, 1)$. In this case, all of the dots are confined to the $z = 0$ plane.

The schemes proposed here could be, in principle, easily scalable to a quantum register with a large number of qubits[3]: QDs would be individually addressed via the action

---

[3] The case of a K-dots system should have associated a Hamiltonian $H = H_0 + V$, with

$$H_0 = \sum_{i=1}^{K} \left(H_{2e}^{(i)} - \gamma_n B I_i^z + \sum_{\nu=1}^{2} \gamma_e B S_{i,\nu}^z \right), \quad V = C \sum_{i=1}^{K} \sum_{\nu=1}^{2} \boldsymbol{I}_i \cdot \boldsymbol{S}_{i,\nu} \delta(\boldsymbol{r}_{i,\nu}) + V_{inter} \ , \qquad (5.16)$$

where $\boldsymbol{S}_{i,\nu}$ $(\boldsymbol{I}_i)$ is the spin polarization of electron ν (nucleus) in dot i. The location of electron ν in the ith QD is denoted by $\boldsymbol{r}_{i,\nu}$. The first term in Eq. (5.16) represents the ith two-electron QD with a perpendicular B-field, which includes the *intra-dot* interaction (V_{intra}), while the others give the nuclear and the electron-spin Zeeman energies in dot i. $H_{2e}^{(i)} \equiv H_{CM}^{(i)} + H_{rel}^{(i)} + V_{intra}$ is given, within a symmetric gauge, by $H_{2e}^{(i)} = (\boldsymbol{P}_{i,\nu} + 2e\boldsymbol{A}_i(\boldsymbol{R}_{i,\nu}))^2/4m^* + m^*\omega_{i,0}^2|\boldsymbol{R}_{i,\nu}|^2 + \left(\boldsymbol{p}_{i,\nu} + \frac{e}{2}\boldsymbol{A}_i(\boldsymbol{r}_{i,\nu})\right)^2/m^* + \frac{m^*}{4}\omega_{i,0}^2|\boldsymbol{r}_{i,\nu}|^2 + \alpha|\boldsymbol{r}_{i,1} - \boldsymbol{r}_{i,2}|^{-2}$, with $\boldsymbol{R}_{i,\nu} = \frac{1}{2}(\boldsymbol{r}_{i,1} + \boldsymbol{r}_{i,2})$, $\boldsymbol{P}_{i,\nu} = \boldsymbol{p}_{i,1} + \boldsymbol{p}_{i,2}$, $\boldsymbol{r}_{i,\nu} = \boldsymbol{r}_{i,1} - \boldsymbol{r}_{i,2}$, and $\boldsymbol{p}_{i,\nu} = \frac{1}{2}\left(\boldsymbol{p}_{i,1} - \boldsymbol{p}_{i,2}\right)$. The second term of Eq. (5.16) gives the Fermi contact hyperfine coupling of the of an appropriate B-field. This is shown schematically in Fig. 5.8, where a '$B_{j,j+1}$' field is assumed to be locally addressing the qubits j and $j+1$ from the entire ensemble of dots. Even if the QD array is irregular, one may still be able to perform the solid-state equivalent of the bulk/ensemble NMR computing reported in Refs. [36, 37]. The coupling of the qubits to an external reservoir and the task of controlling the quantum coherence can be facilitated due to the exceptionally low decoherence rates of these nuclear qubits: the required RF pulses would allow a sufficiently large number of single qubit rotations and two-qubit gates to be performed, with appropriate gating times, for realising complex quantum computational tasks before the system decoheres.

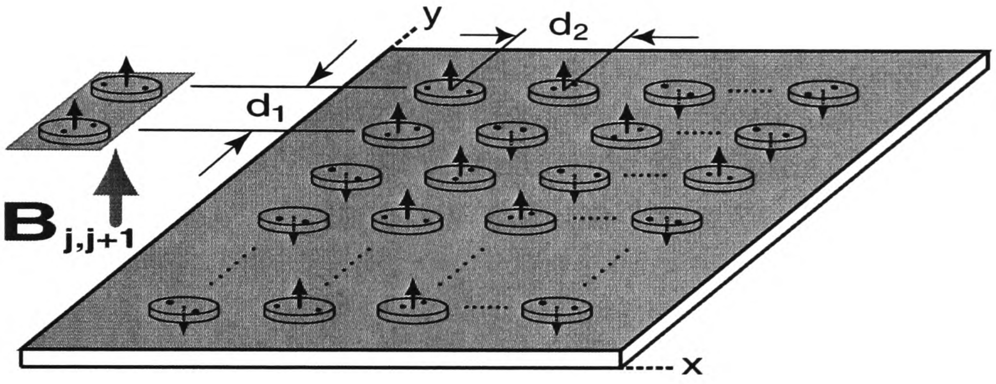

Figure 5.8: Scaling up Configuration 2: The K dots of the system are confined to the $z=0$ plane. Within the entire ensemble of dots, the B-field is able to address the QDs both locally and globally.

5.5 Discussion

Regarding the experimental feasibility of the NMR set-up presented in this chapter, there may be a natural way to make a quantum dot in silicon with a single C atom inside it. C atoms are known to act as nucleation centres for SiGe quantum dots (see e.g., Ref. [150]).

---

nuclear spin of dot i with the electron spin ν in the same dot and V_{inter} represents the *inter-dot* interaction between electrons in neighbouring QDs. The nuclear spin control is performed by this inter-dot coupling V_{inter} due to the interaction between electrons in neighbouring dots. This mechanism (rather than the direct dipole-dipole interaction between the nuclei) is responsible for the qubit control in the present proposal. In the case of configuration 1 [Fig. 5.7(a)], the coupling potential can be written as

$$V^{(1)}_{inter} = \sum_{i=1}^{K} \sum_{\nu,\delta=1}^{2} \frac{\alpha}{|\boldsymbol{r}_{i+1,\nu} - \boldsymbol{r}_{i,\delta}|^2 + d^2} \, , \tag{5.17}$$

where $\boldsymbol{r}_{i+1,\nu} - \boldsymbol{r}_{i,\delta} \equiv \left([r_{i+1,\nu} - r_{i,\delta}]_x, [r_{i+1,\nu} - r_{i,\delta}]_y\right)$. Here, it is assumed that the separation between neighbouring QDs is such that $|\boldsymbol{r}_{i+1,\nu} - \boldsymbol{r}_{i,\delta}|^2 < d^2$. This means that the square of the xy-plane separation between electrons in neighbouring dots [see Fig. 5.7(b)] for the case of electrons $(j+1,2)$, and $(j,1)$) is less than the square of the vertical separation between such dots (d^2), as illustrated in Fig. 5.7(b). Hence, the minimum value for d is determined by the largest xy-projection of electrons in neighbouring dots, which roughly corresponds to the sum of the radii of such dots. The case of configuration 2 (Figs. 5.7(b) and 5.8) has associated a potential $V^{(2)}_{inter}$ given as in Eq. (5.17), but with $d=0$.

Another possibility would be to consider an isolated ^{29}Si (spin 1/2 and natural abundance 4.7%) at the centre of a ^{28}Si based QD. The isoelectronic character of the impurity is reinforced, but possible purification procedures could be harder to implement. The more realistic situation of a non-centred impurity, i.e., when the impurity atom is away from the QD centre, shall modify the discontinuity strengths of the electron-nucleus coupling since this coupling is affected by the density of probability of the CM wavefunction at the impurity site [JHR2]; however the main effects discussed in the present proposal remain the same. It has been shown in Chapter 2 that the ratio between the "gating time" τ_{gate} and the qubit decoherence time τ_{dec} for our qubit system is of the order of 10^{-6} or smaller, i.e., the number of elementary operations that could in principle be performed before decoherence takes over is in agreement with the current criteria for fault-tolerant quantum error correction schemes [129]. Finally, there is the important issue of the spin measurements that have to be implemented for either the input or the readout of single spin qubits. This process must be rapid enough to avoid decoherence of the qubits: optical NMR techniques for reading the input/output of these spin states are currently approaching such a level of finesse [144, 145]. Remarkably, there has been a recent experimental demonstration of ultrafast storage, manipulation, and readout of electron spin coherence [146], which should allow the all-optical proposal for qubit control presented here to be realised on an ultrafast time scale. Other mechanisms for measuring these spin states are also currently under intensive experimental study [41, 147].

The solid state NMR proposal given here is not in principle limited to $\mathcal{N} = 2$ electrons: generalisations [156, 157, 158] of the present angular momentum transitions arise for $\mathcal{N} > 2$. It was pointed out recently [159] that the spin configurations in many-electron QDs could be explained in terms of *just* two-electron singlet and triplet states. Therefore, the present results may occur in QDs with $\mathcal{N} > 2$. In addition, by employing QDs of different sizes, one could switch a subset of a QD array. As said, even if the QD array is irregular, one may still be able to perform the solid-state equivalent of the bulk/ensemble NMR computing reported in Refs. [36, 37]: this again represents a potential advantage of the present scheme. Further advantages stem from the electrostatically neutral character of the impurity atom ^{13}C, and from the fact that the silicon nuclei surrounding it have no nuclear spin: the carbon nuclear spin state will be very effectively shielded from the environment and hence can be expected to have even longer decoherence rates than the (charged) donor nuclei in Ref. [41], thereby offering reliable quantum gate implementation.

It is worth noting that our proposal is not based upon the possibility of applying a localised magnetic field to a single quantum dot. The procedure to switch the NMR frequency of a single nuclear spin is based upon the magic number transitions which can be implemented by an extended magnetic field. It is the local hyperfine electron-nucleus coupling within each quantum dot which can be tuned by such magic number transitions. This is the main point of the current proposal. The control of the local hyperfine coupling by an extended magnetic field may be used to perform single nuclear spin manipulation as well as the solid-state equivalent of the bulk/ensemble liquid NMR computing (see Ref. [36, 37]), for an array of either identical or non-indentical quantum dots. Similar to the liquid NMR experiments, the quantum dot NMR resonance is determined by local effects: in this latter case these are dominated by electron ground-state transitions. Let us note that the magic number transitions considered here require a relaxation process of the electron system to achieve the new ground state, i.e., the changes in the B-field (which change the hyperfine coupling and hence tune the nuclear resonance frequency) must be done adiabatically to be able to perform the jumps in the angular momentum quantum number. However, this electron relaxation is compatible with the requirement of maintaining the quantum coherence due to the fact that the quantum information is stored in the nuclear spin qubit. It is well known that the nuclear spin relaxation times are several orders of magnitude longer than electron relaxation times. Therefore, electrons in the quantum dot can evolve to a new ground state before any environmentally-induced contamination affects the nuclear spin state. In addition to this, it should be pointed out that an ultrafast manipulation of such electron spin states is now experimentally feasible [146].

In summary, a solid-state NMR qubit scheme has been proposed which offers long decoherence times and reliable implementation of quantum gates. The fabrication requirements are compatible with current experimental capabilities. Being all-optical, rather than transport-based, the scheme avoids the need for electrical contacts and gates.

The next chapter studies in detail the impact of decoherence on the dynamical evolution of an arbitrarily large quantum register. Particular emphasis is given to quantum dots based registers.

Chapter 6

The art of noise: decoherence of quantum registers

When any open quantum system, for example, a quantum computer, interacts with an arbitrary surrounding environment, there are two main effects that have to be considered when examining the temporal evolution. First, there is an expected loss of energy of the initial system due to its relaxation, which happens at the rate τ_{rel}^{-1} where τ_{rel} is the relaxation time scale of the system. Second, there is a process that spoils the unitarity of the evolution, the so-called decoherence [118], where the continuous interaction between the quantum computer and the environment leads to unwanted correlations between them in such a way that the computer loses its ability to interfere, giving rise to wrong outcomes when executing conditional quantum dynamics [see, e.g., Section 2.1.5]. This phenomenon is characterised by a time that defines the loss of unitarity (i.e., the departure of coherence from unity), the decoherence time τ_{dec}. Usually, the time scale for this effect to take place is much smaller than the one for relaxation (spontaneous emission) hence quantum computers are more sensitive to decoherence processes than to relaxation ones. For practical applications in quantum computing there are several different systems that might provide a long enough τ_{rel}; however, what really matters for arbitrarily complex quantum information processing tasks (e.g., quantum algorithms) to be performed reliably is the ratio τ_{gate}/τ_{dec}. τ_{gate}, the time required to execute an elementary quantum logic gate, must be much smaller than τ_{dec}. As a rough estimate, fault-tolerant quantum computation has been shown to be possible if the ratio τ_{gate} to τ_{dec} of a single qubit is of the order of 10^{-4} [129].

Decoherence and quantum theory are unavoidably connected. Indeed, the ubiquitous decoherence phenomenon has been ultimately associated with the "frontiers" between the quantum behaviour of microscopic systems and the emergence of the classical behaviour observed in macroscopic objects [118]: roughly speaking, the decoherence time τ_{dec} determines the energy and length scales at which quantum behaviour is observed. It generally depends non-trivially on several different factors such as temperature, dimensionality, quantum vacuum fluctuations, disorder, and others whose origins are less well known (hardware characteristics). The time-scale for decoherence depends on the kind of coupling between the system under consideration and the environment, in a range that can go from *pico*-seconds in excitonic systems [61] up to *minutes* in nuclear-spin systems [162].

In the laboratory, different hardware methodologies for QIP are used, therefore it is important to clarify the underlying physics and limits for each type of physical realisation. In the absence of schemes for protecting the quantum information, these limits are mainly imposed by the decoherence time of each particular system. However theoretical work has shown that, in addition to quantum error correcting codes [25, 26, 124], there are two additional ways that may potentially lead to decoherence-free or decoherence-controlled quantum information processing: one of them is the so-called "error avoiding" approach where, for a given decoherence mechanism (e.g., collective decoherence, discussed below), the existence of "decoherence-free" subspaces within the system's Hilbert space can be exploited in order to obtain a quantum dynamics where the system is effectively decoupled from the environment [163, 165]. This approach requires the system-environment coupling to possess certain symmetry properties. The other approach is based on "noise suppression" schemes, where the effects of unwanted system-bath interactions are dynamically controlled using a sequence of "tailored external pulses" [166, 167]. These strategies have motivated much theoretical and experimental work. In particular, there are some recent experimental results regarding the engineering of decoherence-free quantum memories [168, 169].

This chapter is devoted to the study of decoherence of an arbitrary quantum register of L qubits. In addition to providing a general theoretical framework for studying decoherence, the limits where the qubits are assumed to couple (i) independently and (ii) collectively to an external (bosonic) reservoir are studied in detail. The reservoir is modelled by a continuum of harmonic modes. In Section 6.1, it is shown that the decoherence process is very sensitive to the input states of the register and explicit expressions for the coherence decay functions are given. It is found that these functions possess a novel behaviour which we label "recoherence" (coherence revivals) in the specific case of independent decoherence. This behaviour depends strongly on the temperature and the strength of the qubit-bath coupling. In contrast, for a certain choice of the QR input, the calculation of the reduced density matrix leads to the identification of decoherence-free quantum states [163, 165], when the qubits are coupled "collectively" to the environment, i.e., when the distance between qubits is much smaller than the bath coherence length, and hence, the environment couples in a permutation-invariant way to all qubits. The calculations in this chapter were motivated by the results of Ref. [170, 171]. Here, it is shown that some subtle, but important, details of these earlier results are incomplete. Particularly, the calculation of the $L-$QR density matrix reported here leads both to new qualitative results, when analysing the behaviour of coherence decay, and new quantitative results, when estimating typical decoherence times: these novel results emerge for $L > 1$, as discussed in Section 6.2. Concluding remarks are given in Section 6.3. It is emphasised that the results of this chapter are not restricted to a particular physical system; they are valid for any choice of the qubit system (e.g., photons, atoms, nuclei with spin 1/2, etc.) and any bosonic reservoir.

6.1 Independent versus collective decoherence

Let us consider the general case of a L-QR coupled to a quantised environment modelled as a continuum of field modes with corresponding creation (annihilation) bath operator $b^\dagger$ (b). Throughout this work only phase decoherence (dephasing) mechanisms are analysed. Relaxation mechanisms where the QR exchanges energy with the environment leading to bit-flip errors are not considered. Hence, the n-th qubit operator $J^n \equiv J_z^n$ ($J_x^n = 0$) [1]. As mentioned earlier, this is a reasonable approach since decoherence typically occurs on a much faster time scale than relaxation. The dynamics of the qubits and the environment can be described by a simplified version of the widely studied spin-boson Hamiltonian [172]

$$H = \sum_{n=1}^{L} \epsilon_n J_z^n + \sum_{\boldsymbol{k}} \epsilon_{\boldsymbol{k}} b_{\boldsymbol{k}}^\dagger b_{\boldsymbol{k}} + \sum_{n,\boldsymbol{k}} J_z^n \left(g_{\boldsymbol{k}}^n b_{\boldsymbol{k}}^\dagger + g_{\boldsymbol{k}}^{n*} b_{\boldsymbol{k}} \right) , \tag{6.1}$$

where the first two terms describe the free evolution of the qubits and the environment, and the third term accounts for the interaction between them. Here, $g_{\boldsymbol{k}}^n$ denotes the coupling between the n-th qubit and field modes, which, in general, depends on the physical system under consideration. The initial state of the whole system is assumed to be $\rho^S(0) = \rho^Q(0) \otimes \rho^B(0)$ (the superscripts stand for system, qubits, and bath), i.e., the QR and the bath are initially decoupled[2]. It is also assumed that the environment (E) is initially in thermal equilibrium, a condition that can be expressed as

$$\rho^B(0) = \prod_{\boldsymbol{k}} \rho_{\boldsymbol{k}}(T) = \prod_{\boldsymbol{k}} \frac{\exp(-\beta\hbar\omega_k b_{\boldsymbol{k}}^\dagger b_{\boldsymbol{k}})}{1 + \langle N_{\omega_k} \rangle} , \tag{6.2}$$

where $\langle N_{\omega_k} \rangle = \left[\exp(-\beta\hbar\omega_k) - 1\right]^{-1}$ is the Bose-Einstein mean occupation number, k_B denotes Boltzmann's constant, and $\beta \equiv 1/k_B T$. For the model of decoherence presented here, it is clear that we are in a situation where the qubit operator J_z^n commutes with the total Hamiltonian H and therefore, there is no exchange of energy between qubits and environment, as expected. Here, it is not attempted to perform a group-theoretic description for the study of quantum noise control[3]. Instead, the analysis is devoted to the specific real-time dynamics of the decay in the QR-density-matrix coherences within the model given by the Hamiltonian Eq. (6.1) (i.e., Abelian noise processes, in the language of Refs. [173, 174]).

In the interaction picture, the quantum state of the combined (QR+E) system at time t is given by $|\Psi(t)\rangle_I = U_I(t)|\Psi(0)\rangle$, where $|\Psi(0)\rangle$ is the initial state of the system, $U_I(t)$ is

---

[1] If relaxation mechanisms are also considered, in general $J_x^n \neq 0$. Recall, as seen in Chapter 2, that the noise process can also involve a combination of both types of errors ($\sigma_x\sigma_z$-errors). The presence of distinct error generators along '$x, y,$ and z' make the noise processes non-Abelian and the Hamiltonian can no longer be solved analytically.

[2] This factorisable condition is the one that has been extensively studied so far. However, more general situations have been analysed in connection with the influence functional path-integral method of Feynman and Vernon. See, e.g., Ref. [175].

[3] Formally, noise processes can be characterised in terms of the interaction algebra that they generate, see, e.g., Refs. [173, 174].

the time evolution operator, $U_I(t) = T\exp\left[-i/\hbar \int_o^t H_I(t')dt'\right]$, and T is the time ordering operator. For the Hamiltonian (6.1), we introduce the notation $H = H_0 + V$, where $H_0 = \sum_{n=1}^{L} \epsilon_n J_z^n + \sum_{\boldsymbol{k}} \epsilon_{\boldsymbol{k}} b_{\boldsymbol{k}}^\dagger b_{\boldsymbol{k}}$ denotes the free evolution term, and $V = \sum_{n,\boldsymbol{k}} J_z^n (g_{\boldsymbol{k}}^n b_{\boldsymbol{k}}^\dagger + g_{\boldsymbol{k}}^{n*} b_{\boldsymbol{k}})$ is the interaction term. Hence, the interaction picture Hamiltonian is given by $H_I(t) = U_0^\dagger(t) V U_0(t)$, with $U_0 = \exp(-\frac{i}{\hbar} H_0 t)$. A simple calculation gives the result

$$H_I(t) = \sum_{n,\boldsymbol{k}} J_z^n \left(g_{\boldsymbol{k}}^n \mathrm{e}^{i\omega_k t} b_{\boldsymbol{k}}^\dagger + g_{\boldsymbol{k}}^{*n} \mathrm{e}^{-i\omega_k t} b_{\boldsymbol{k}} \right) , \tag{6.3}$$

which allows us to calculate the time evolution operator $U_I(t)$. The result is (see Appendix D for details)

$$U_I(t) = \exp\left(i\Phi_{\omega_k}(t)\right) \exp\left(\sum_{n,\boldsymbol{k}} J_z^n \left\{ \xi_{\boldsymbol{k}}^n(t) b_{\boldsymbol{k}}^\dagger - \xi_{\boldsymbol{k}}^{*n}(t) b_{\boldsymbol{k}} \right\} \right) , \tag{6.4}$$

with

$$\begin{aligned} \Phi_{\omega_k}(t) &= \sum_{n,\boldsymbol{k}} |J_z^n g_{\boldsymbol{k}}^n|^2 \, \frac{\omega_k t - \sin(\omega_k t)}{(\hbar\omega_k)^2} , \\ \xi_{\boldsymbol{k}}^n(t) &= g_{\boldsymbol{k}}^n \varphi_{\omega_k}(t) \equiv g_{\boldsymbol{k}}^n \, \frac{1 - \mathrm{e}^{i\omega_k t}}{\hbar\omega_k} . \end{aligned} \tag{6.5}$$

This result differs from the one reported in Ref. [170] where the *time-ordering operation for $U_I(t)$ was not performed.* As will become clear later, this correction alters the resulting calculation of Ref. [170], and hence changes the results for the reduced density matrix of an arbitrary L-QR. Based on the time evolution operator of Eq. (6.4), a different result is given here for this density matrix and its implications are discussed with respect to those of Ref. [170].

Unless the contrary is specified, it is assumed that the coupling coefficients $g_{\boldsymbol{k}}^n$ ($n = 1, ..., L$) are *position-dependent*, i.e., that each qubit couples individually to a different heat bath, hence the QR decoheres "*independently*". Implications for the "collective" decoherence case will be discussed later. Let us assume that the n-th qubit experiences a coupling to the reservoir characterised by

$$g_{\boldsymbol{k}}^n = g_{\boldsymbol{k}} \exp(-i\boldsymbol{k}\cdot\boldsymbol{r}_n) , \tag{6.6}$$

where $\boldsymbol{r}_n$ denotes the position of the n-th qubit. It is easy to see that the unitary evolution operator given by Eq. (6.4) produces entanglement between register states and environment states. The degree of the entanglement produced will strongly depend on the qubit input states and also on the separation $||\boldsymbol{r}_m - \boldsymbol{r}_n||$ between qubits because of the position dependent coupling. As is shown later, for some kind of input states, no decoherence occurs at all despite the fact that all of the qubits are interacting with the environment. Also, states with dynamics decoupled from thermal fluctuations are identified; a fact that may be relevant in the design of experiments where the involved quantum states have dephasing times (mainly due to temperature dependent effects) on a very short time scale, as in the solid state, for example. These features are key issues when proposing schemes for maintaining coherence in quantum computers [163].

Due to the Abelian characteristic of the noise model considered here, one can calculate analytically the functional dependence of the decay of the coherences of the QR by taking into account all the field modes of the quantised environment. In what follows, the notations of Ref. [170] are used. Let us consider the reduced density matrix of the L-QR: the matrix elements of this reduced operator can be expressed as

$$\rho^Q_{\{i_n,j_n\}}(t) = \langle i_L, i_{L-1}, \ldots, i_1 |\ \mathrm{Tr}_B\{\rho^S(t)\}\ | j_L, j_{L-1}, \ldots, j_1\rangle \ , \tag{6.7}$$

where $\{i_n, j_n\} \equiv \{i_1, j_1;\ i_2, j_2; \ldots ;\ i_L, j_L\}$ refers to the qubit states of the QR and

$$\rho^S(t) = U_I(t)\rho^Q(0) \otimes \rho^B(0)U_I^\dagger(t) \ . \tag{6.8}$$

From this expression it becomes clear that the dynamics of the register is completely determined by the evolution operator $U_I(t)$. In Eq. (6.8), the initial density matrix of the register can be expressed as $\rho^Q(0) = \rho^Q_{i_1,j_1}(0) \otimes \rho^Q_{i_2,j_2}(0) \otimes \ldots \otimes \rho^Q_{i_L,j_L}(0)$, where $\rho^Q_{i_n,j_n} = |i_n\rangle\langle j_n|$. In this expansion, $|i_n\rangle = |\pm\frac{1}{2}\rangle$ are the possible eigenstates of J_z^n and will be associated with the two level qubit states $|1\rangle$ and $|0\rangle$, respectively. The eigenvalues $i_n = \pm\frac{1}{2}$ and $j_n = \pm\frac{1}{2}$. In what follows, the subscripts of Eq. (6.7) will be renamed with the values one and zero to indicate the actual values $\frac{1}{2}$ and $-\frac{1}{2}$, respectively. Hence, one can rewrite Eq. (6.7) as

$$\rho^Q_{\{i_n,j_n\}}(t) = Tr_B\left\{\rho^B(0)U_I^{\dagger\{j_n\}}(t)U_I^{\{i_n\}}(t)\right\}\rho^Q_{\{i_n,j_n\}}(0) \ , \tag{6.9}$$

$$\begin{aligned} U_I^{\{i_n\}}(t) \equiv\ & \exp\left(i\sum_{\boldsymbol{k}} |g_{\boldsymbol{k}}|^2 s(\omega_k, t) \sum_{m,n} \mathrm{e}^{i\boldsymbol{k}\cdot\boldsymbol{r}_{mn}} i_m i_n\right) \times \\ & \exp\left(\sum_{n,\boldsymbol{k}} \left\{g_{\boldsymbol{k}}\varphi_{\omega_k}(t) i_n \mathrm{e}^{-i\boldsymbol{k}\cdot\boldsymbol{r}_n} b_{\boldsymbol{k}}^\dagger - g_{\boldsymbol{k}}^*\varphi_{\omega_k}^*(t) i_n \mathrm{e}^{i\boldsymbol{k}\cdot\boldsymbol{r}_n} b_{\boldsymbol{k}}\right\}\right) \ , \end{aligned} \tag{6.10}$$

and calculate explicitly the decay of the coherences for the L–QR. The result is (see Appendix D)

$$\begin{aligned} \rho^Q_{\{i_n,j_n\}}(t) =\ & \exp\left(-\sum_{\boldsymbol{k},m,n} |g_{\boldsymbol{k}}|^2 c(\omega_k, t) \coth\left(\frac{\hbar\omega_k}{2k_B T}\right)(i_m - j_m)(i_n - j_n)\cos \boldsymbol{k}\cdot\boldsymbol{r}_{mn}\right) \times \\ & \exp\left(i \sum_{\boldsymbol{k},m,n} |g_{\boldsymbol{k}}|^2 s(\omega_k, t)(i_m i_n - j_m j_n)\cos \boldsymbol{k}\cdot\boldsymbol{r}_{mn}\right) \times \\ & \exp\left(-2i \sum_{\boldsymbol{k},m,n} |g_{\boldsymbol{k}}|^2 c(\omega_k, t) i_m j_n \sin \boldsymbol{k}\cdot\boldsymbol{r}_{mn}\right)\rho^Q_{\{i_n,j_n\}}(0) \ , \end{aligned} \tag{6.11}$$

where $\boldsymbol{r}_{mn} \equiv \boldsymbol{r}_m - \boldsymbol{r}_n$ is the relative distance between the m-th and n-th qubits,

$$\begin{aligned} s(\omega_k, t) &= [\omega_k t - \sin(\omega_k t)]/(\hbar\omega_k)^2 \ , \\ c(\omega_k, t) &= [1 - \cos(\omega_k t)]/(\hbar\omega_k)^2 \ . \end{aligned} \tag{6.12}$$

In the continuum limit, Eq. (6.11) reads

$$\rho^Q_{\{i_n,j_n\}}(t) = \exp\Big(i[\Theta_d(t,t_s) - \Lambda_d(t,t_s)]\Big)\exp\Big(- \Gamma_d(t,t_s;T)\Big)\ \rho^Q_{\{i_n,j_n\}}(0)\ , \qquad (6.13)$$

where

$$\begin{aligned}\Lambda_d(t,t_s) &= 2\int d\omega I_d(\omega)c(\omega,t)\sum_{\substack{m=1\\n=2}}^{L} i_m j_n \sin(\omega t_s)\ , &(6.14)\\ \Theta_d(t,t_s) &= 2\int d\omega I_d(\omega)s(\omega,t)\sum_{\substack{m=1,n=2\\m\neq n}}^{L} (i_m i_n - j_m j_n)\cos(\omega t_s)\ , &(6.15)\end{aligned}$$

$$\Gamma_d(t,t_s;T)=\int d\omega I_d(\omega)c(\omega,t)\coth\left(\frac{\omega}{2\omega_T}\right)\left\{\sum_{m=1}^{L}(i_m-j_m)^2+2\sum_{\substack{m=1,n=2\\m\neq n}}^{L}(i_m-j_m)(i_n-j_n)\cos(\omega t_s)\right\}. \qquad (6.16)$$

Here, $\omega_T \equiv k_B T/\hbar$ is the thermal frequency (see discussion below), $\omega t_s \equiv \boldsymbol{k}\cdot\boldsymbol{r}_{mn}$ sets the *"transit time"* t_s, and $I_d(\omega) \equiv \sum_{\boldsymbol{k}}\delta(\omega-\omega_{\boldsymbol{k}})|g_{\boldsymbol{k}}|^2 \equiv \frac{dk}{d\omega}G(\omega)|g(\omega)|^2$ is the spectral density of the bath. This function is characterised by a cut-off frequency ω_c that depends on the particular physical system under consideration and sets $I_d(\omega) \mapsto 0$ for $\omega >> \omega_c$ [172]. Hence, an explicit calculation for the decay of the coherences requires the knowledge of the spectral density $I_d(\omega)$. Here, it is assumed that $I_d(\omega) = \alpha_d\omega^d e^{-\omega/\omega_c}$ [172], where d is the dimensionality of the field and $\alpha_d > 0$ is a proportionality constant that characterises the strength of the system-bath coupling. Hence, the functional dependence of the spectral density relies on the dimensionality of the frequency dependence of the density of states $G(\omega)$ and of the coupling $g(\omega)$. In Eq. (6.13) the "transit time" t_s has been introduced in order to express the QR-bath coupling in the frequency domain. This transit time is of particular importance when describing the specific "independent" decoherence mechanism, because of the position-dependent coupling between qubits and bath modes. However, in a scenario where the qubits are coupled "collectively" to the same environment, t_s does not play any role at all (see below).

The result of Eq. (6.13) differs in several respects from the one reported in [170]: the decoherence function $\Gamma_d(t,t_s;T)$ contains additional information about the characteristics of the independent decoherence and the way in which the individual qubits couple to the environment through the position-dependent terms which are proportional to $\cos(\boldsymbol{k}\cdot\boldsymbol{r}_{mn})$. In essence, this means that the entanglement of the register with the noise field depends on the qubit separation. Also, the expression for $\rho^Q_{\{i_n,j_n\}}(t)$ reveals the new dynamical factor $\aleph_d(t,t_s) \equiv \Theta_d(t,t_s) - \Lambda_d(t,t_s)$, which must be taken into account when determining typical decoherence times for the L-QR.

It is interesting that the decoherence effects arising from thermal noise can be separated from the ones due purely to vacuum fluctuations. This is simply because the average number of field excitations at temperature T can be rewritten as

$$\langle N_\omega\rangle_T = \frac{1}{2}\exp(-\hbar\omega/2k_B T)\mathrm{cosech}(\hbar\omega/2k_B T)\ , \qquad (6.17)$$

and hence $\coth(\hbar\omega/2k_BT) = 1 + 2\langle N_\omega \rangle_T$ in Eq. (6.16). The other term contributing to the decay of the coherences in Eq. (6.13), $\aleph_d(t, t_s)$, is due purely to quantum vacuum fluctuations. The separation made above allows us an examination of the different time scales present in the (QR + bath) systems dynamics. The fastest time scale of the environment is determined by the cut-off: $\tau_c \sim \omega_c^{-1}$, i.e., τ_c sets the "memory" time of the environment. Hence, the vacuum fluctuations will contribute to the dephasing process only for times $t > \tau_c$. Also note that the characteristic thermal frequency $\omega_T \equiv k_BT/\hbar$ sets another fundamental time scale $\tau_T \sim \omega_T^{-1}$: thermal effects will affect the qubit dynamics only for $t > \tau_T$. Hence, one can see that quantum vacuum fluctuations contribute to the dephasing process only in the regime $\tau_c < t < \tau_T$. From this identification, it becomes clear that the qubit dynamics and hence the decoherence process of our open quantum system will depend on the ratio of the temperature-to-cut-off parameter ω_T/ω_c and the spectral function $I_d(\omega)$. Later follows an exploration of how different qualitative behaviours are obtained for the decoherence depending on the relationship between the cut-off and the thermal frequency. It is worth noting that the analytical separation between the thermal and vacuum contributions to the overall decoherence process is a convenient property of the pure dephasing (Abelian) model considered here. Further generalisations of this model, e.g., by including relaxation mechanisms, should make this separation non-trivial because the problem becomes no longer exactly solvable. Next, the decoherence functions associated with the situation of collective phase decoherence are computed.

Collective decoherence: this situation can be thought of as a bath of "long" coherence length (mean effective wave length λ) if compared with the separation r_{mn} between qubits, in such a way that $\lambda >> r_{mn}$, and hence the product of Eq. (6.6) has $\exp(-i\boldsymbol{k} \cdot \boldsymbol{r}_n) \approx 1$. Roughly speaking, we are in a situation where all the qubits "feel" the same environment, i.e., $g_{\boldsymbol{k}}^n \equiv g_{\boldsymbol{k}}$. A similar calculation to the one followed in Appendix D gives the following result for the decay of the coherences for the case of collective coupling to the reservoir:

$$\begin{aligned} \rho^Q_{\{i_n, j_n\}}(t) &= \exp\left(i\Theta_d(t)\left\{\left[\sum_{m=1}^{L} i_m\right]^2 - \left[\sum_{m=1}^{L} j_m\right]^2\right\}\right) \times \\ & \exp\left(-\Gamma_d(t;T)\left[\sum_{m=1}^{L}(i_m - j_m)\right]^2\right) \rho^Q_{\{i_n, j_n\}}(0) , \end{aligned} \qquad (6.18)$$

where

$$\Theta_d(t) = \int d\omega I_d(\omega) s(\omega, t) , \qquad (6.19)$$

$$\Gamma_d(t;T) = \int d\omega I_d(\omega) c(\omega, t) \coth\left(\frac{\omega}{2\omega_T}\right) . \qquad (6.20)$$

Expressions (6.13) and (6.18) are to be compared with those reported in Refs. [170] and [171]. Clearly, the new result for the evolution operator $U_I(t)$ of Eq. (6.4) induces a

QR-environment dynamics different from the one reported in [170]. This fact has been pointed out in Ref. [171] for the situation of collective decoherence; in this particular case, the results given here coincide with theirs. However, one obtains different results when considering the situation of independent decoherence: the new dynamical factor $\aleph_d(t, t_s)$ includes additional information about individual qubit dynamics that cannot be neglected. Indeed, from the results derived in Ref. [171], the authors argue that the damping of the independent decoherence is insensitive to the type of initial states and hence the sensitivity to the input states is only a property of the collective decoherence. As can be deduced from Eqs. (6.13) and (6.18), one finds that this statement is not generally true and that the sensitivity to the initial states is a property of both collective *and* independent decoherence. This result is illustrated particularly for the case of a 2-QR in the next section. From the expressions (6.19) and (6.20) it can be seen that for $\hbar\omega << k_B T$, the high-temperature environment (high-TE), the phase damping factor $\Gamma_d(t;T)$ is the main agent responsible for the qubits' decoherence, while the other dynamical damping factor $\Theta_d(t)$ plays a minor role. In this case ω_c is actually the only characteristic frequency accessible to the system ($\omega_c << \omega_T$) and thermal fluctuations always dominate over the vacuum ones. However, when we consider the situation $\omega_c >> \omega_T$, the low-temperature environment (low-TE), these damping factors compete with each other over the same time scale, and $\Theta_d(t)$ now plays a major role in eroding the qubits' coherence. Here there is a much more interesting dynamic between thermal and vacuum contributions (see next section). This shows the difference and the importance of the additional terms of the reduced density matrix reported here when compared with those of Refs. [170, 171]. The above statements will be illustrated in the next section.

So far, the dynamics of the qubits and their coupling to the environment has been discussed in the interaction representation. To go back to the Schrödinger representation, recall $\rho_{Sch}(t) = U_0(t)\rho_I(t)U_0^\dagger(t)$, with $\rho_I(t)$ as calculated before for the qubits decoherence (Eqs. (6.13) and (6.18)). Also, note that in the Schrödinger representation (here denoted with subindex *Sch*) $U_0(t)$ introduces mixing but not decoherence. Next, some particular cases which allow an evaluation of the expressions (6.13) and (6.18) and hence give a qualitative picture of the respective decoherence rates for both collective and independent decoherence situations are considered.

6.2 Dimensionality of the field and decoherence rates for few-qubit systems

In this section, the qualitative behaviour of the decay of the coherences given by Eqs. (6.13) and (6.18) for single- and two-qubit systems is analysed.

6.2.1 Single qubit case

Consider the case of only one qubit in contact with a thermal reservoir (Eq. (6.2)). Hence, for both types of coupling (Eqs. (6.13) and (6.18)) one obtains

$$\rho^Q_{i_n,j_n}(t) = \exp(-\Gamma_d(t,T))\rho^Q_{i_n,j_n}(0) \; . \tag{6.21}$$

By using Eq. (6.4), with $d = 1$, it is easy to show that the populations remain unaffected: $\rho^Q_{ii}(t) = \rho^Q_{ii}(0)$, $i = 0, 1$. In general $(i \neq j)$, the decay of coherences is determined by Eq. (6.21). Here one can identify the main time regimes of decoherence for different dimensionalities of the field. In what follows, the case of reservoirs with both one-dimensional density of states ("Ohmic") and three-dimensional density of states ("super-Ohmic") are considered, i.e., $G(\omega) = constant$ and $G(\omega) = \omega^2$, respectively, where the frequency-dependent coupling $g(\omega) \propto \sqrt{\omega}$, as considered in [170]. From Eq. (6.21), it can be seen that a general solution for the case $d = 1$ requires numerical integration (see Appendix C). However, the case where the interplay between thermal and vacuum effects is more complex, i.e., the low-TE ($\omega_T << \omega_c$), yields

$$\Gamma_1(t,T) \approx c_1 \left[2\omega_T t \arctan(2\omega_T t) + \frac{1}{2} \ln \left(\frac{1+\omega_c^2 t^2}{1+4\omega_T^2 t^2} \right) \right], \tag{6.22}$$

where $c_1 \equiv \alpha_1/\hbar^2$. On the other hand, an exact solution for the super-Ohmic case $d = 3$ [Eq. (6.21)] can be found for any temperature T. The result is

$$\Gamma_3(t,T) = c_3 \left\{ \theta^2 \Big[\zeta(2,\theta) + \zeta(2,1+\theta) - \zeta(2,\theta+i\omega_T t) - \zeta(2,\theta-i\omega_T t) \Big] + \frac{1-\omega_c^2 t^2}{[1+\omega_c^2 t^2]^2} \right\}, \tag{6.23}$$

where $\zeta(z,q) = [1/\Gamma(z)] \int_o^\infty dt\, [t^{z-1} \mathrm{e}^{-qt}/(1-\mathrm{e}^{-t})]$ is the generalised Riemann zeta function, $\Gamma(z) = \int_o^\infty dt\, t^{z-1}\mathrm{e}^{-t}$ is the Gamma function, and $c_3 = \alpha_3 \omega_c^2/\hbar^2$.

For the purpose of this chapter, the case $L > 1$ is concentrated on, for which we have several novel results. The analysis of the $L = 1$ case is left to Appendix C, where the process of identifying typical decoherence times for a single qubit, and the interplay between the different decoherence regimes as a function of the temperature are discussed.

6.2.2 $L = 2$ qubit register

Let us analyse the case of two qubits in the presence of the bosonic reservoir discussed in the present chapter. Using the same expressions for the density of states $G(\omega)$ and for the frequency-dependent coupling $g(\omega)$ as above, the coherence decay for several different input states shall be analysed. Let's set the qubits at positions r_a and r_b with coupling factors given by $g^n_{\boldsymbol{k}} = g_{\boldsymbol{k}} \mathrm{e}^{-i\boldsymbol{k}\cdot\boldsymbol{r}_n}$, $n = a, b$. It is easy to see that the unitary evolution operator induces entanglement between qubit states and field states: $U_I(t)$ acts as a conditional displacement operator for the field with a displacement amplitude depending on both qubits of the QR [170]. As pointed out previously, it is this entanglement that is responsible for the phase decoherence processes studied here. In particular, the case of two qubits has $\rho^Q_{i_a j_a, i_b j_b}(t) = \langle i_a, i_b |\, \mathrm{Tr}_B\{\rho^S(t)\}\, | j_a, j_b \rangle$. Next, the register dynamics for the independent and collective decoherence situations is analysed.

1. Independent decoherence

a. $i_a = j_a$, $i_b \neq j_b$: $\rho^Q_{i_a i_a, i_b j_b}(t) = \exp[i\Theta_d(t) f_{i_a i_a, i_b j_b} - \Gamma_d(t;T)] \rho^Q_{i_a i_a, i_b j_b}(0)$, where $f_{i_a i_a, i_b j_b} = 2 i_a (i_b - j_b) \cos(\boldsymbol{k} \cdot \boldsymbol{r}_{ab})$. Hence, $f_{00,01} = f_{11,10} = \cos(\boldsymbol{k} \cdot \boldsymbol{r}_{ab})$, and

$f_{00,10} = f_{11,01} = -\cos(\boldsymbol{k} \cdot \boldsymbol{r}_{ab})$: $\rho^{Q}_{i_a i_a, i_b j_b}(t)$ shows collective decay. This result is contrary to the one reported in Ref. [170].

b. $i_a = j_a$, $i_b = j_b$: $\rho^{Q}_{i_a i_a, i_b i_b}(t) = \rho^{Q}_{i_a i_a, i_b i_b}(0)$; as expected, the populations remain unaffected.

c. $i_a \neq j_a$, $i_b \neq j_b$: $\rho^{Q}_{i_a j_a, i_b j_b}(t) = \exp\left[-\Gamma_d(t;T) h_{i_a j_a, i_b j_b}\right] \rho^{Q}_{i_a j_a, i_b j_b}(0)$, where $h_{i_a j_a, i_b j_b} = 2[1 + (i_a - j_a)(i_b - j_b)\cos(\boldsymbol{k} \cdot \boldsymbol{r}_{ab})]$. Clearly, $h_{10,10} = h_{01,01} = 2[1 + \cos(\boldsymbol{k} \cdot \boldsymbol{r}_{ab})]$, and $h_{10,01} = h_{01,10} = 2[1 - \cos(\boldsymbol{k} \cdot \boldsymbol{r}_{ab})]$. Hence, $\rho^{Q}_{i_a j_a, i_b j_b}(t)$ also shows collective decay.

In the above cases, analytic expressions for the corresponding decoherence functions can be found. As in Subsection 6.2.1, two different surrounding environments are considered. In the low-TE regime, the 'Ohmic environment' ($d = 1$) induces the following coherence decay (the high-TE requires numerical integration):

$$\rho^{\pm}_{d=1}(t) \approx \exp\left(-\Gamma_1(t,T) \pm i c_1 \left[\frac{1}{2}\arctan(\omega_c t_-) - \frac{1}{2}\arctan(\omega_c t_+) + \frac{\omega_c t}{1 + \omega_c^2 t_s^2} \right] \right) \rho^{\pm}_{d=1}(0) \ , \tag{6.24}$$

for $i_a = j_a$, and $i_b \neq j_b$. For brevity, the subindices of the reduced density matrix have been dropped; $t_+ = t_s + t$, and $t_- = t_s - t$. For $i_a \neq j_a$, and $i_b \neq j_b$ one obtains the result

$$\begin{aligned} \rho^{\pm}_{d=1}(t) \ \approx \ \exp\Bigg(& -2\Gamma_1(t,T) \mp 2c_1 \times \\ & \left[\frac{1}{4}\left\{ 2\ln\left(\frac{1 + 4\omega_T^2 t_s^2}{1 + \omega_c^2 t_s^2}\right) + \ln\left(\frac{1 + \omega_c^2 t_-^2}{1 + 4\omega_T^2 t_-^2}\right) + \ln\left(\frac{1 + \omega_c^2 t_+^2}{1 + 4\omega_T^2 t_+^2}\right) \right\} - \right. \\ & \left. \omega_T \left\{ 2t_s \arctan(2\omega_T t_s) - t_- \arctan(2\omega_T t_-) - t_+ \arctan(2\omega_T t_+) \right\} \right] \Bigg) \rho^{\pm}_{d=1}(0) \ . \end{aligned} \tag{6.25}$$

In Figs. (6.1) and (6.2), the decay of two qubit coherence due to the coupling to an environment of the Ohmic type [Eqs. (6.25)] has been plotted. Here, $\Gamma_1^{\mp}(t,T)$ are defined from Eqs. (6.25) as $\rho^{\pm}_{d=1}(t) = \exp[-\Gamma_1^{\mp}(t,T)]\rho^{+}_{d=1}(0)$. From these figures one can see the variations of the onset of decay when increasing the temperature. Figure 6.1 shows how the departure of coherence from unity changes with t_s [plot 6.1 (i)], while for high temperature [plot 6.1 (iii)], there is no variation with t_s at all. In the limit of large t_s (see Table 6.1), one recovers the onset of decay of Fig. 6.6 (Appendix C). Note the difference between the time scales of plots 6.1 (i) and (iii), and how an estimation of typical decoherence times strongly relies on the temperature of the environment. Figure 6.2 shows how the coherence decay shown in Fig. 6.1 disappears for small t_s values, i.e., for a given temperature, it is possible to find a t_s from which there is no decoherence of the two-qubit system. This interesting behaviour occurs only for the density-matrix elements $\langle 10|\, \mathrm{Tr}_B\{\rho^S(t)\}\, |01\rangle = \langle 01|\, \mathrm{Tr}_B\{\rho^S(t)\}\, |10\rangle$.

In Table 6.1, some typical two-qubit decoherence times τ_{dec} for an Ohmic environment in terms of the temperature, coupling constants c_1, and t_s are given. In all of the tables in this chapter, the beginning of the decoherence process is assumed to occur when the reduced density matrix of the whole system exhibits a 2% deviation from the initial condition, i.e., when $\exp[-\Gamma_i(t \equiv \tau_{dec}, T)] = 0.98$.

c_1	$k_B T/\hbar\omega_c$	$\omega_c t_s$	$\omega_c \tau^-_{dec}$	$\omega_c t^-_f$	$\omega_c \tau^+_{dec}$	$\omega_c t^+_f$
0.25	10^{-3}	0.5	0.436919	saturates	0.235446	103.507
0.25	10^{0}	0.5	0.183755	saturates	0.104119	2.05958
0.25	10^{-3}	10^4	0.290113	1279.63	0.290113	1279.64
0.25	10^{0}	10^4	0.127778	3.45901	0.127778	3.45901
0.1	10^{-3}	0.5	0.913573	saturates	0.37654	2025.75
0.1	10^{0}	0.5	0.303135	saturates	0.16504	4.28334
0.1	10^{-3}	10^4	0.47316	5669.66	0.473159	5670.15
0.1	10^{0}	10^4	0.203549	7.86596	0.203549	7.86596
0.01	10^{-3}	0.5	saturates	saturates	1.45274	35004.7
0.01	10^{0}	0.5	saturates	saturates	0.538502	37.2732
0.01	10^{-3}	10^4	2.55738	saturates	2.55738	40816.8
0.01	10^{0}	10^4	0.709492	73.8325	0.709492	73.8325

Table 6.1: Characteristic times for two-qubit independent decoherence $\tau^{\pm}_{dec}$ for ($d = 1$)- dimensional density of states of the field. Different temperature, transit time, and coupling strength values are considered. $i_a \neq j_a$, $i_b \neq j_b$ (see text).

The tables have been generated from the corresponding decoherence functions reported in this chapter. Here, t_f is defined from $\exp[-\Gamma_i(t = t_f, T)] = 0.01$, i.e., the difference between t_f and τ_{dec} gives an estimate for the duration of the decoherence process, namely t_{decay}; and $\tau^{\pm}_{dec}$, and $t^{\pm}_f$ are evaluated from the respective decoherence functions $\Gamma^{\pm}_i(t, T)$, with $i = 1, 3$. In order to gain insight into some characteristic time scales, consider, for example, the case of the solid state, where in many situations the noise field can be identified with the phonon field. Here, the cut-off ω_c can be immediately associated with the Debye frequency ω_D. A typical Debye temperature $\Theta_D = 100$ K has $\omega_D \equiv \omega_c \approx 10^{13}$ s^{-1}, so $\theta \equiv \omega_T/\omega_c \approx 10^{-2}\ T$. Hence, one can see from Table 6.1 (Figs. 6.1 and 6.2) that for $c_1 = 0.25$, $\omega_c t_s = 0.5$, and $T = 0.1$ K, the decoherence process starts at $\tau^+_{dec} \approx 23.5$ fs and $\tau^-_{dec} \approx 43.7$ fs, and it lasts for $t^+_{decay} \approx 10.3$ ps (for t^-_{decay}, $\exp[-\Gamma^-_1(t \mapsto \infty, 0.1\text{ K})]$ saturates above 0.01). If the strength of the coupling goes down to $c_1 = 0.01$, then $\tau^+_{dec} \approx 0.2$ ps, and $t^+_{decay} \approx 3.5$ ns. In this latter case, τ^-_{dec}, and t^-_{decay} are not reported, since the coherence saturates to a value above 0.98. From the data reported in Table 6.1 it is clear that the weaker the coupling between the qubits and the environment, the longer the decoherence times and the slower the decoherence process. In addition, the higher the temperature, the faster the qubits decohere, as expected intuitively.

The effect of the transit time becomes more evident from Table 6.1: for large t_s values, there is no difference between τ^+_{dec} and τ^-_{dec} (also, $t^+_{decay} \approx t^-_{decay}$). This is because for large t_s, the contribution due to terms involving t_s in Eq. (6.25) is negligible, hence the reduced

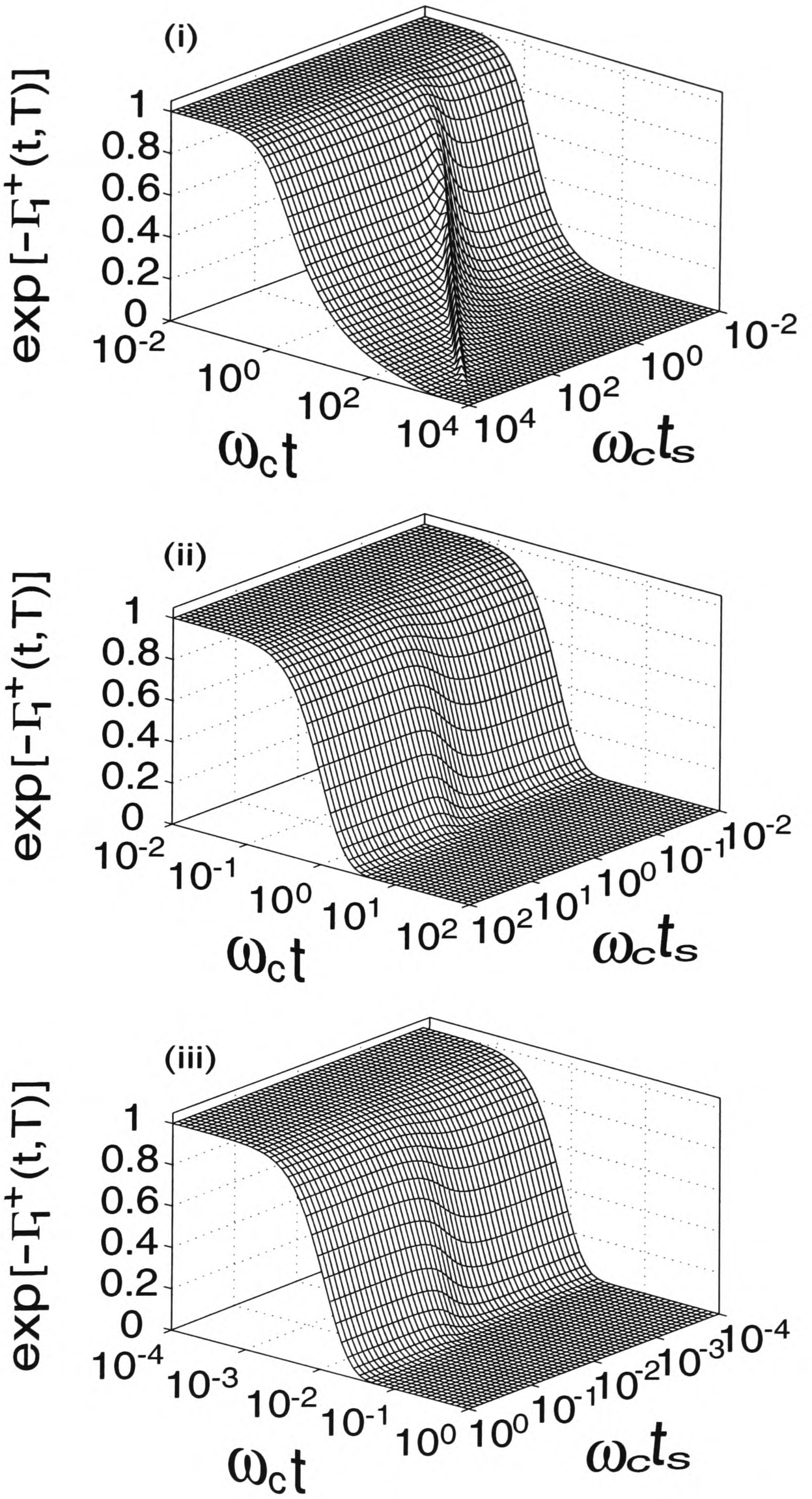

Figure 6.1: Two-qubit "independent decoherence" due to the coupling to a reservoir of the Ohmic type ($d = 1$) as a function of time t and the transit time t_s, for the input states associated with $\Gamma_1^+(t,T)$ ($i_a \neq j_a$, $i_b \neq j_b$). Here, $c_1 = 0.25$, and (i) $\theta = 10^{-3}$, (ii) 10^0, and (iii) 10^2. $\Gamma_i^{\pm}(t,T)$, with $i = 1,3$ are defined in the text.

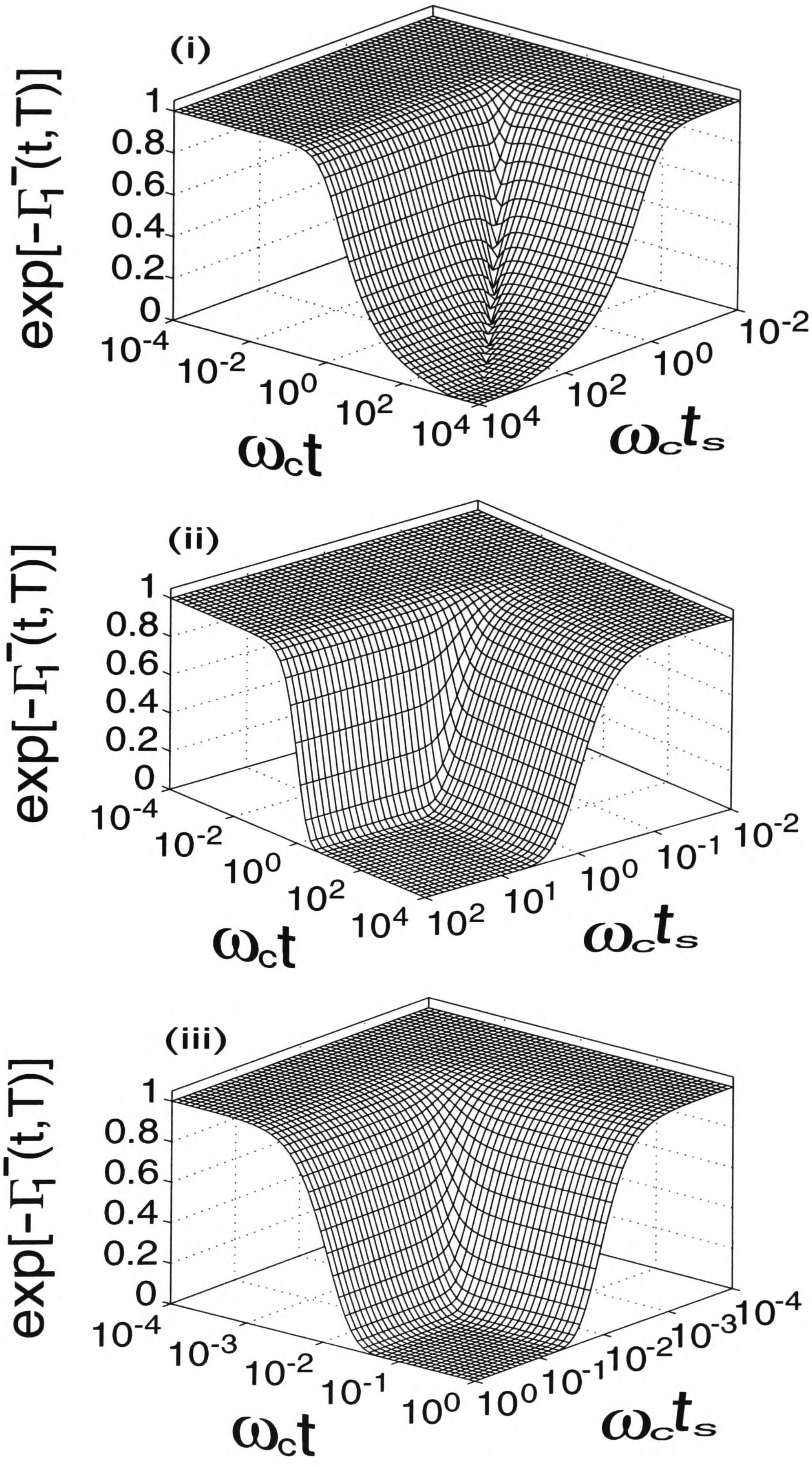

Figure 6.2: Two-qubit "independent decoherence" caused by the coupling to an 'Ohmic environment' as a function of times t and t_s, for the input states associated with $\Gamma_1^-(t,T)$ $(i_a \neq j_a$, $i_b \neq j_b)$. $c_1 = 0.25$, and (i) $\theta = 10^{-3}$, (ii) 10^0, and (iii) 10^2.

density-matrix $\rho^{\pm}_{d=1}(t) \equiv \rho_{d=1}(t) \approx \exp[-2\Gamma_1(t,T)]$ and hence, has a similar behaviour to the single-qubit case (Eq. (6.21)). Hence, for large t_s (e.g., $t_s = 10^4$), Figs. 6.1 and 6.2 resemble the onset of decay of the single-qubit case (see later Fig. 6.6) where there is no dependence on t_s. Note that $\exp[-\Gamma_1^{+}(t,T)]$ ($\exp[-\Gamma_1^{-}(t,T)]$) is the corresponding decay of the coherences $\rho_{10,10} = \rho_{01,01}$ ($\rho_{10,01} = \rho_{01,10}$), hence, $\rho^{Q}_{10,10}(t) = \rho^{Q}_{10,01}(t)$ for large t_s.

By contrast, the super-Ohmic $d = 3$ field leads to the following coherence decay:

$$\begin{aligned}\rho^{\pm}_{d=3}(t) \;&=\; \exp\Bigg(- \Gamma_3(t,T) \pm ic_3 \Bigg[\frac{\sin[2\arctan(\omega_c t_-)]}{2(1+\omega_c^2 t_-^2)} - \frac{\sin[2\arctan(\omega_c t_+)]}{2(1+\omega_c^2 t_+^2)} + \\ &\quad \frac{2\omega_c t\cos[3\arctan(\omega_c t_s)]}{(1+\omega_c^2 t_s^2)^{3/2}}\Bigg]\Bigg)\rho^{\pm}_{d=3}(0) \quad , \end{aligned} \tag{6.26}$$

for $i_a = j_a$, and $i_b \neq j_b$, and

$$\begin{aligned}\rho^{\pm}_{d=3}(t) \;&=\; \exp\Bigg(- 2\Gamma_3(t,T) \mp 2c_3 \Bigg[- \frac{1-\omega_c^2 t_s^2}{[1+\omega_c^2 t_s^2]^2} + \frac{1-\omega_c^2 t_+^2}{2[1+\omega_c^2 t_+^2]^2} + \frac{1-\omega_c^2 t_-^2}{2[1+\omega_c^2 t_-^2]^2} + \\ &\quad \frac{\theta^2}{2}\Bigg\{ 2\zeta(2,\theta - i\omega_T t_s) + 2\zeta(2,\theta + i\omega_T t_s) - \zeta(2,\theta + i\omega_T t_+) - \zeta(2,\theta - i\omega_T t_+) - \\ &\quad \zeta(2,\theta + i\omega_T t_-) - \zeta(2,\theta - i\omega_T t_-)\Bigg\}\Bigg]\Bigg)\rho^{\pm}_{d=3}(0) \quad , \end{aligned} \tag{6.27}$$

for $i_a \neq j_a$, and $i_b \neq j_b$. The results of Eqs. (6.26) and (6.27) are exact: no approximations have been made in obtaining them. Therefore, they are valid for any temperature of the environment.

In Figs. 6.3 and 6.4, the decay of two-qubit coherence due to the coupling to a reservoir with three-dimensional density of states [Eqs. (6.27)] has been plotted. Some estimates for τ_c and t_{decay} have been given in Table 6.2. The decoherence functions $\Gamma_3^{\pm}(t,T)$ are defined as $\rho^{\pm}_{d=3}(t) = \exp[-\Gamma_3^{\pm}(t,T)]\rho^{\pm}_{d=3}(0)$.

As can be seen, there is a *non-monotonic* behaviour for the decay of coherence for low-temperature values, as can be seen from Figs. 6.3(i), and 6.3(ii). The decay given by the functions $\Gamma_3^{+}(t,T)$ (Fig. 6.3) and $\Gamma_3^{-}(t,T)$ (Fig. 6.4) saturates to a particular value, which is fixed by the strength of the coupling and the temperature of the reservoir: the lower the temperature, the slower the decay, and the higher the residual coherence. Some estimates for these saturation values $e^{-\Gamma_3^{\pm}(t_f^{\pm},T)}$ are shown in Table 6.2. From Fig. 6.4, it is possible to find small t_s values for which the onset of decay does not change in time and coherence remains unaffected. This result is very different from the case of Fig. 6.3, where coherence either vanishes (at high temperatures) or saturates to a residual coherence value (at low temperatures). Also note that while nothing happens to the onset of decay of Fig. 6.4, the coherence decay is amplified in the case of Fig. 6.3, for small t_s values. From Figs. 6.3[(i), and (ii)] and 6.4[(i), and (ii)], it is seen that there is saturation of the decay in the presence of a *non-trivial* coherence process. However,

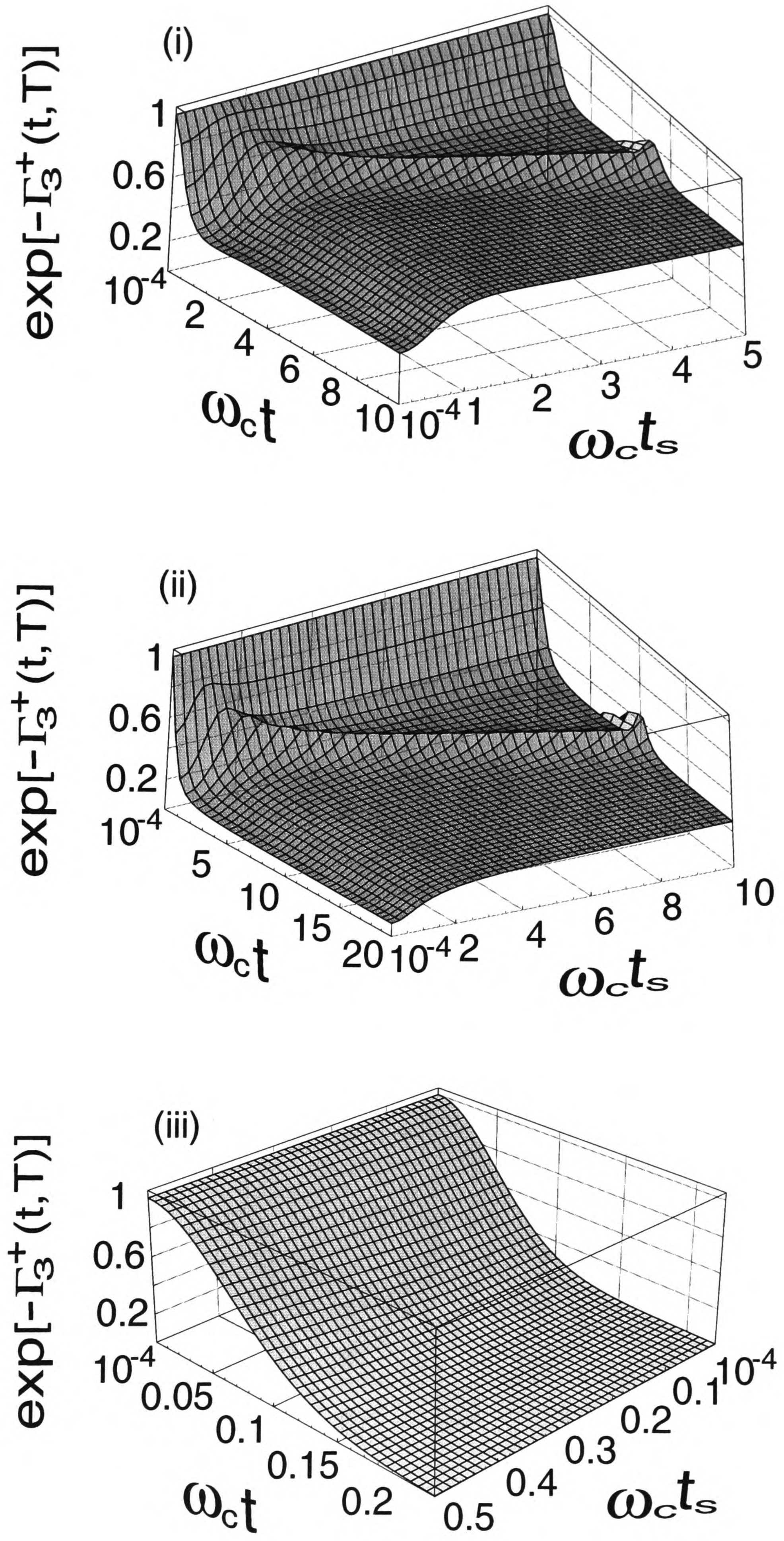

Figure 6.3: Two qubit "independent decoherence" due to the super-Ohmic environment $d=3$ [Eq. (6.27)], as a function of times t and t_s, for the input states associated with $\Gamma_3^+(t,T)$. $c_3=0.25$, and (i) $\theta=10^{-3}$, (ii) 10^0, and (iii) 10^2.

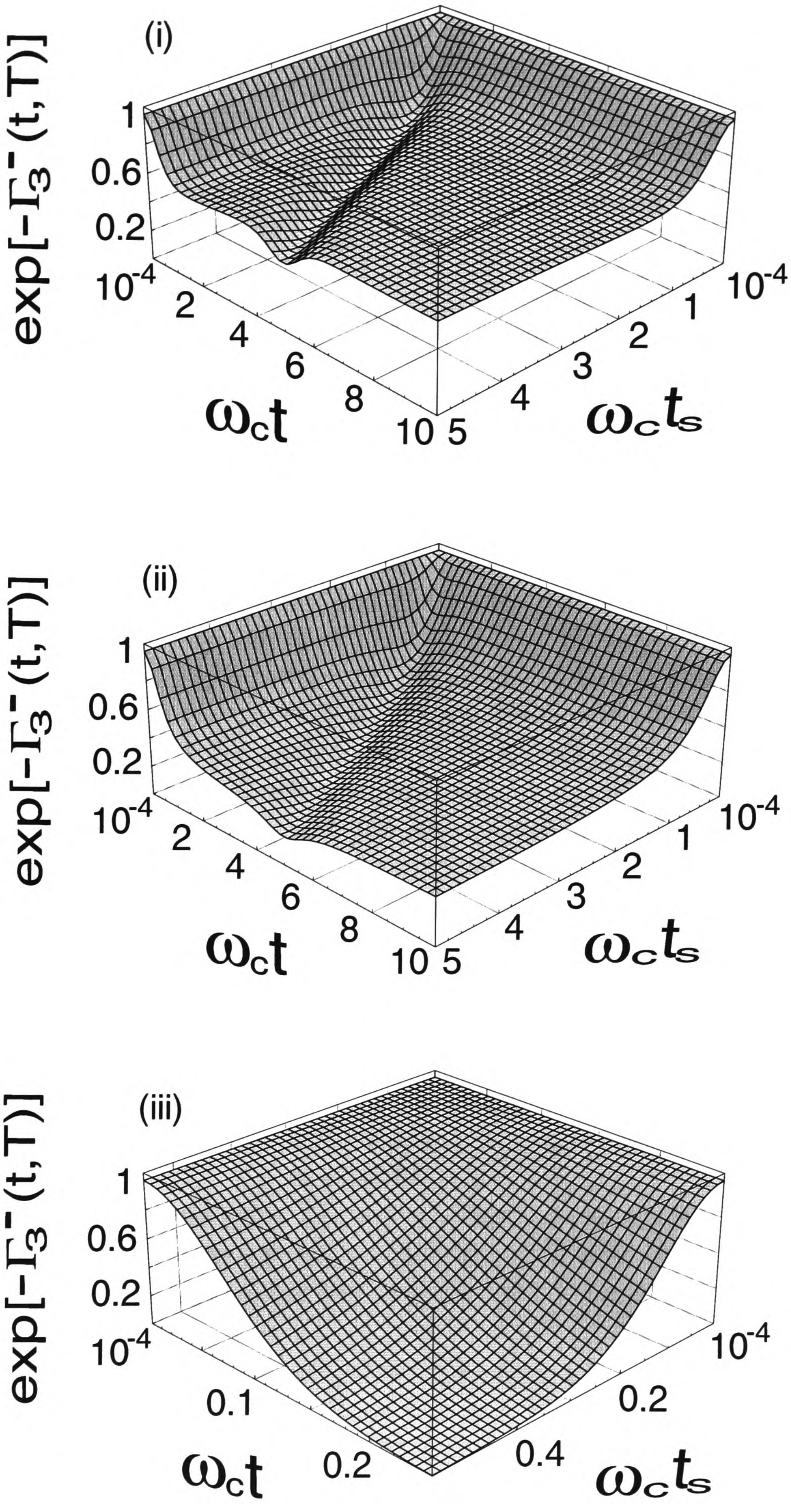

Figure 6.4: Two-qubit "independent decoherence" due to the super-Ohmic environment $d = 3$ as a function of times t and t_s for the input states associated with $\Gamma_3^-(t,T)$. $c_3 = 0.25$, and (i) $\theta = 10^{-3}$, (ii) 10^0, and (iii) 10^2.

c_3	ω_T/ω_c	$\omega_c t_s$	$\omega_c\tau^+_{dec}$	$\omega_c t^+_f$	$e^{-\Gamma^+_3(t^+_f)}$	$\omega_c\tau^-_{dec}$	$\omega_c t^-_f$	$e^{-\Gamma^-_3(t^-_f)}$
0.25	10^{-3}	0.5	0.1292	sat.	0.477	0.10818	sat.	0.771
0.25	10^2	0.5	0.01338	0.20	0.01	0.01522	0.24	0.01
0.25	10^{-3}	10^2	0.11738	sat.	0.6065	0.11738	sat.	0.6065
0.25	10^2	10^2	0.01421	0.22	0.01	0.01421	0.22	0.01
0.01	10^{-3}	0.5	0.79957	sat.	0.971	sat.	sat.	0.989
0.01	10^2	0.5	0.066994	1.51	0.01	0.07645	sat.	0.449
0.01	10^{-3}	10^2	9.7767	sat.	0.9802	9.7767	sat.	0.9802
0.01	10^2	10^2	0.07124	sat.	0.01831	0.07124	sat.	0.01832

Table 6.2: Characteristic times for two qubit independent decoherence $\tau^{\pm}_{dec}$ for ($d = 3$)-dimensional density of states of field. $i_a \neq j_a$, $i_b \neq j_b$.

for high temperatures [Figs. 6.3(iii) and 6.4(iii)] there is a monotonic behaviour where no saturation occurs at all and the residual coherence vanishes.

Note that the non-monotonic behaviour reported here for the low-temperature regime is not just a characteristic of high-dimensionality fields: it also occurs for the $d = 1$ field, as can be seen from Figs. 6.1(i) and 6.2(i). One believes that this purely quantum-mechanical phenomenon must be associated with an interplay between the quantum vacuum and thermal fluctuations of the system and the quantum character of the field. The system undergoes a dynamics where the environment manages to 'hit back' at the qubits in such a way that the coherences then exhibit an effective revival before vanishing (at high temperatures) or saturating to a residual value (at low temperatures). An essential feature of the model studied here is the fact that the QR and bath are assumed to be initially uncorrelated. In future work, the behaviour of these 'recoherences' with more general initial conditions, where the initial state of the combined system is allowed to contain some correlations between the bath and the QR (see also Ref. [175]) will be addressed. Such studies will help to clarify the origins of this 'recoherence effect' and also the effectiveness of decoherence as a function of the initial conditions. It is noted that there is a previous work by Hu *et al.* [177] where the study of quantum Brownian motion in a general environment gives rise to a similar behaviour (although in a different context) to the one reported here for the 'recoherences'. A more detailed analysis of the physical implications of this interesting behaviour of the coherence decay is intended to be addressed elsewhere [178].

It is interesting that the dynamics of coherences depends so strongly on the strength of the coupling. It can be seen from Table 6.2 and Fig. 6.5 that (i) the coherences saturate (sat.) to a very high 'residual value' and show less than a 2% decay for weak coupling (e.g., $c_3 = 0.01$) and low temperatures ($T = 0.1$ K). This result is to be compared with the $d = 1$ case where the coherences always vanish for long t_s; (ii) even at high temperatures ($T = 10^4$ K), where the coherences vanish, and weak coupling, there is an appearence of the 'recoherence effect' discussed above. This makes more evident the role of the QR-bath coupling: recoherences should appear only under certain conditions imposed by the strength c_3 (hence by the spectral density) and the temperature.

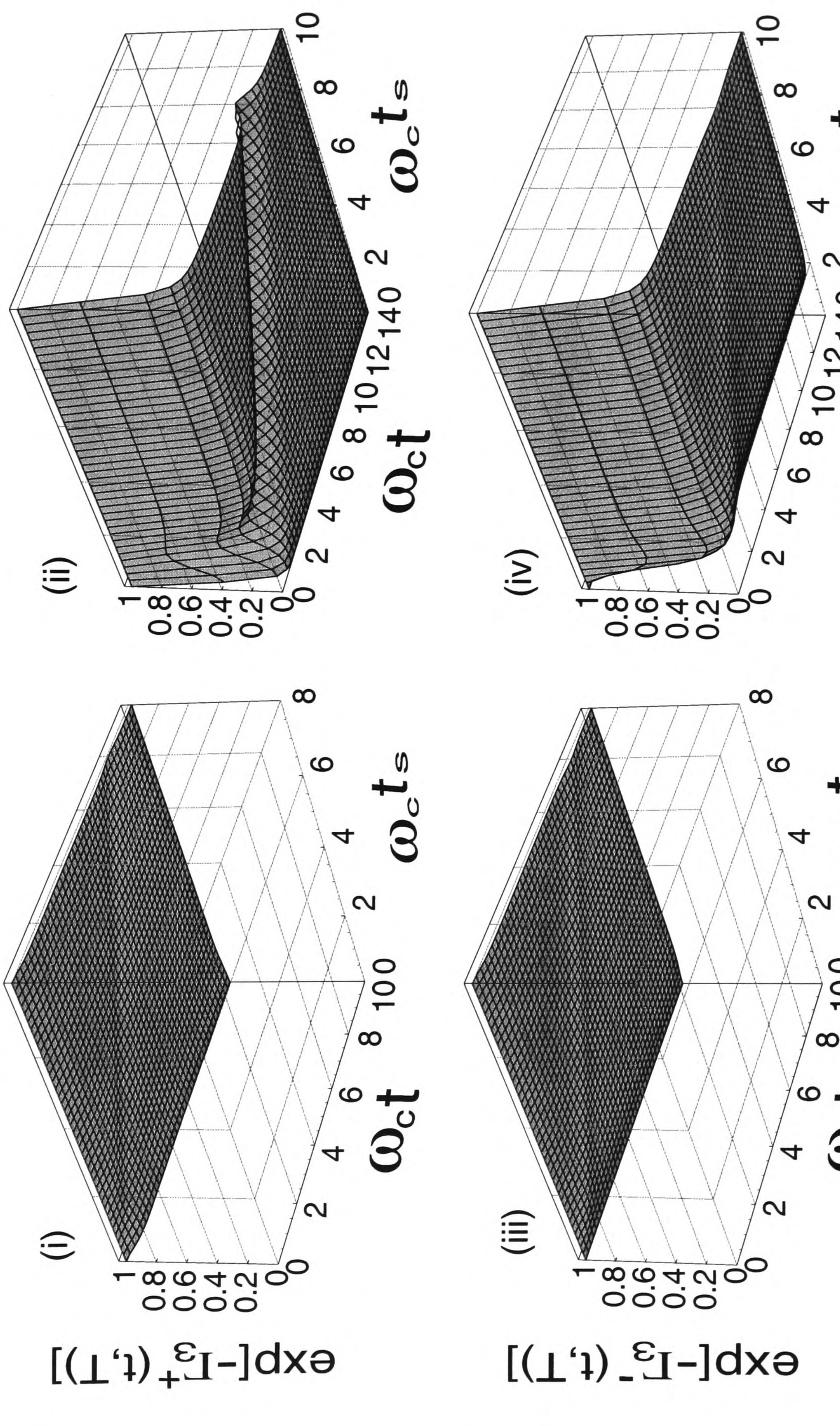

Figure 6.5: Two-qubit "independent decoherence". $d = 3$, coupling strength $c_3 = 0.01$, and (i), (iii) $\theta = 10^{-3}$, and (ii), (iv) $\theta = 10^{2}$.

These conditions can be directly obtained from the decoherence functions reported in this chapter. Typical $\tau_{dec}^{\pm}$ times for this ($d = 3$)-dimensional environment are given in Table 6.2. From these one can conclude that the 2-QR decoherence time scales are shorter, and the decoherence process occurs faster, than in the single-qubit case.

2. Collective decoherence

The reduced density matrix for the two-qubit system now reads: $\rho^Q_{i_a j_a, i_b j_b}(t) = \exp\left(i\Theta_d(t)[(\sum_{m=a}^{b} i_m)^2 - (\sum_{m=a}^{b} j_m)^2]\right) \exp\left(-\Gamma_d(t;T)[\sum_{m=a}^{b}(i_m - j_m)]^2\right)\rho^Q_{i_a j_a, i_b j_b}(0)$. In particular, one finds:

a. $i_a = j_a$, $i_b \neq j_b$: $\rho^Q_{i_a i_a, i_b j_b}(t) = \exp[i\Theta_d(t) f'_{i_a i_a, i_b j_b} - \Gamma_d(t;T)]\rho^Q_{i_a i_a, i_b j_b}(0)$, where $f'_{i_a i_a, i_b j_b} = 2i_a(i_b - j_b)$. Hence, $f'_{00,01} = f'_{11,10} = 1$, and $f'_{00,10} = f'_{11,01} = -1$. The corresponding decoherence rates are

$$\rho^{\pm}_{d=1}(t) \approx \exp\Big(- \Gamma_1(t,T) \pm ic_1[\omega_c t + \arctan(\omega_c t)]\Big)\rho^{\pm}_{d=1}(0) \quad , \tag{6.28}$$

$$\rho^{\pm}_{d=3}(t) = \exp\left(- \Gamma_3(t,T) \pm ic_3\left[2\omega_c t - \frac{\sin(2\arctan(\omega_c t))}{1+\omega_c^2 t^2}\right]\right)\rho^{\pm}_{d=3}(0) \quad , \tag{6.29}$$

for the Ohmic environment and the ($d = 3$)-dimensional density of states, respectively.

b. $i_a = j_a$, $i_b = j_b$: $\rho^Q_{i_a i_a, i_b i_b}(t) = \rho^Q_{i_a i_a, i_b i_b}(0)$; as expected, the populations remain unaffected.

c. $i_a \neq j_a$, $i_b \neq j_b$: $\rho^Q_{i_a j_a, i_b j_b}(t) = \exp\left(-\Gamma_d(t;T) h'_{i_a j_a, i_b j_b}\right)\rho^Q_{i_a j_a, i_b j_b}(0)$, where $h'_{i_a j_a, i_b j_b} = (i_a + i_b - j_a - j_b)^2$. Then, $h'_{10,10} = h'_{01,01} = 4$, and $h'_{10,01} = h'_{01,10} = 0$. Obviously, the corresponding decoherence rates are:

$$\begin{aligned} \rho^{-}_{d=1}(t) &= \rho^{-}_{d=1}(0) \ , & (6.30) \\ \rho^{+}_{d=1}(t) &\approx \exp\Big(- 4\Gamma_1(t,T)\Big)\rho^{+}_{d=1}(0) \ , & (6.31) \end{aligned}$$

for the ($d = 1$)-dimensional field, and

$$\begin{aligned} \rho^{-}_{d=3}(t) &= \rho^{-}_{d=3}(0) \ , & (6.32) \\ \rho^{+}_{d=3}(t) &\approx \exp\Big(- 4\Gamma_3(t,T)\Big)\rho^{+}_{d=3}(0) \ , & (6.33) \end{aligned}$$

for the ($d = 3$)-dimensional field. Hence, regarding the input states, the case of *collective decoherence* shows two very well defined situations:

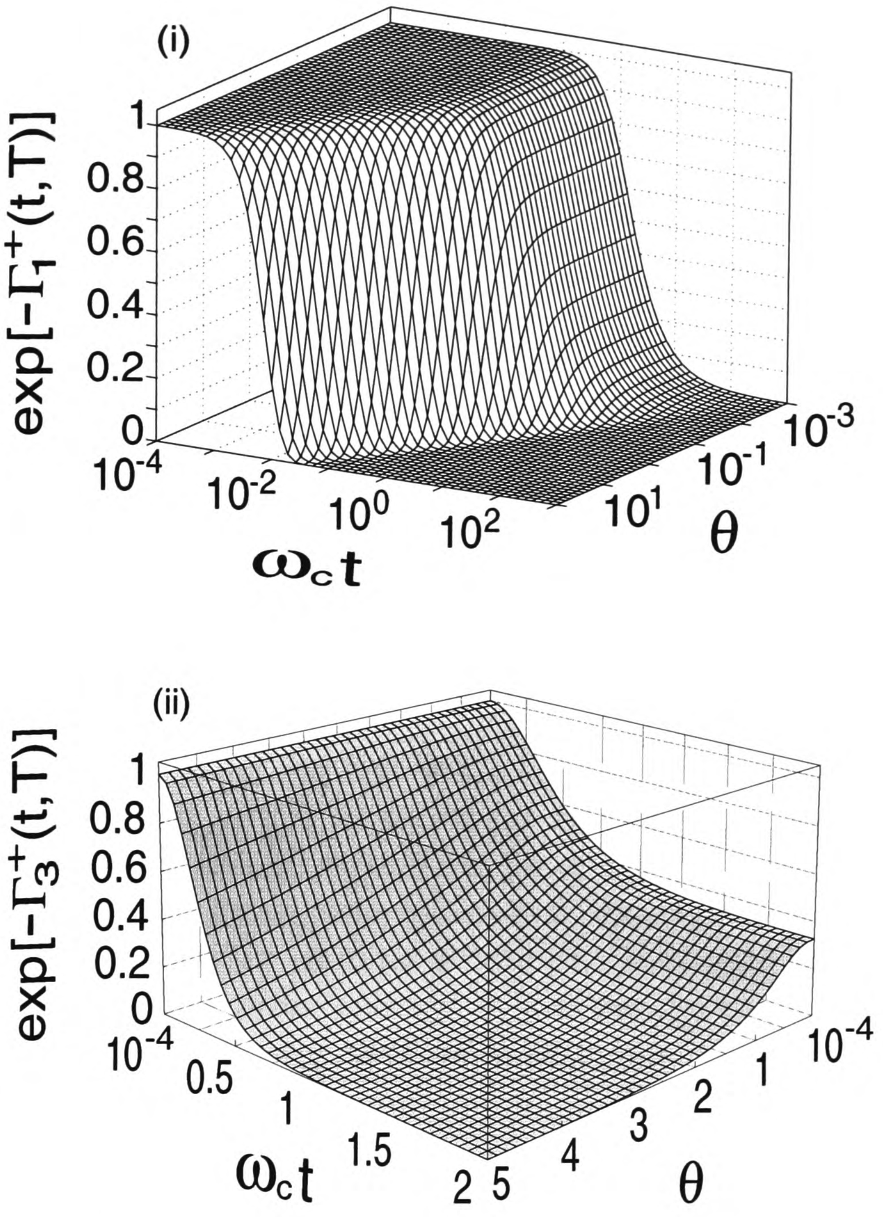

Figure 6.6: Two-qubit "collective decoherence" for (i) $d = 1$ 'Ohmic environment' [Eq. (6.31)], and (ii) $d = 3$ 'super-Ohmic environment' [Eq. (6.33)], as a function of time and the temperature $\theta \equiv \omega_T/\omega_c$. $c_1 = c_3 = 0.25$, and $i_a \neq j_a$, and $i_b \neq j_b$. $\Gamma_d^+(t,T)$ $(d = 1,3)$ is defined using Eqs. (27) and (28).

i. A set of input states that shows no decoherence at all, despite the fact that the qubits are interacting with the environment [see Eqs. (6.30) and (6.32)]. This is because under the specific situation of collective coupling there is a set of initial qubit states that does not entangle with the bosonic field and hence the states preserve their coherence. These states are the so-called "coherence-preserving" states and, for the case of a 2-QR, the corresponding reduced-density matrix elements are $\langle 10|\,\mathrm{Tr}_B\{\rho^S(t)\}\,|01\rangle$, and $\langle 01|\,\mathrm{Tr}_B\{\rho^S(t)\}\,|10\rangle$. This result can be used as an encoding strategy, where an arbitrary L-QR can be decoupled from its environment provided that every single qubit of the register can be encoded using two qubits: e.g., using the simple encoding (though not the most efficient one) $|0\rangle \mapsto |01\rangle$, and $|1\rangle \mapsto |10\rangle$ [163]. It turns out that this procedure is ensured even if relaxation effects are included in the Hamiltonian (6.1) [163]. Hence in the specific situation of collective decoherence one can find, for arbitrary L, a decoherence-free subspace (DFS) $C_L \in \mathcal{H}^{\otimes L}$ (the Hilbert space $\mathcal{H} = \mathcal{H}_{QR} \otimes \mathcal{H}_B$) that does not get entangled with the environment, and hence, the QR should evolve without decoherence. Besides quantum error correction codes, this is currently one of the most outstanding results in the battle against decoherence [163], particularly because of its relevance to maintaining a coherent qubit memory in quantum information processing.

ii. The other two input states have associated the decay of coherences given by $\langle 11|\mathrm{Tr}_B\{\rho^S(t)\}|00\rangle$ and $\langle 00|\,\mathrm{Tr}_B\{\rho^S(t)\}\,|11\rangle$: these give a situation of 'superdecoherence' [170], where the qubits are collectively entangled, and hence these matrix elements give the fastest decay for the coherences. This means that while there is a subspace which is robust against decoherence as discussed above, the remaining part of the Hilbert space gets strongly entangled with the environment. This superdecoherence situation is illustrated in Fig. 6.6, for the case of reservoirs with one- and three-dimensional density of states.

The above process of calculating explicit results for the decay of any coherence associated with the coupling of a L-QR to a bosonic reservoir, for both types of coupling (independent and collective), can be carried out for any $L > 2$ using the general formulas Eqs. (6.13) and (6.18). In so doing, one can obtain an estimate of typical decoherence times for a QR with an arbitrary number of qubits. It should be pointed out that if no schemes for controlling the errors induced by the decoherence phenomenon are used [25, 124, 163, 164, 165, 166, 167], τ_{dec} establishes an upper bound to the duration of any reliable quantum computing process.

6.3 Discussion

A model of decoherence based upon the one previously studied by Leggett *et al.* [172] in connection with the tunneling problem in the presence of dissipation, and used later by Palma *et al.* and Unruh [170, 179] for describing the decoherence process of a quantum register has been revisited. A more complete description of this latter problem has been presented here, which provides the following new results. The decoherence rates of the density-matrix elements are correctly derived, leading to new quantitative results for both independent and collective decoherence situations. As discussed here, if no error correcting/preventing strategies are used, this has implications for an estimation of decoherence time scales for which the quantum memory of a QR can be maintained in any reliable computation (note, however, that there has been a recent proposal by Beige *et al.* regarding the use of dissipation to remain and manipulate states within a DFS [164]). The results reported in this chapter agree with those given in [171] for the case of collective decoherence but they are different to the ones reported there for the case of independent decoherence: in Ref. [171] it is argued that independent decoherence, as opposed to collective decoherence, is insensitive to the qubit input states. Here, it has been shown instead that both cases are very sensitive to the input states and that both of them show collective decay.

In the specific situation of independent decoherence, one has found a non-trivial behaviour in the decay of the off-diagonal elements of the reduced density matrix. Here, the coherences experience an effective revival before they either vanish or saturate to a residual value. This behaviour depends on the temperature of the environment and also depends strongly on the strength of the coupling: the coherence dynamics are different in the weak and strong coupling regime. Also, there are important qualitative differences between the Ohmic $d = 1$ and the super-Ohmic environment $d = 3$, which is ultimately linked to the spectral density of the bath. In the former case the coherence is always lost, while in the latter, the coherence generally saturates to a residual value which is fixed by the temperature and strength of the coupling and *only* vanishes in the high-TE regime. By contrast, in the case of collective decoherence, QR input states that allow the system to evolve in a decoherence-free fashion (coherence-preserving states) have been identified. Note that DFS's are not found in the specific situation of independent qubit decoherence[4].

From the point of view of complexity analysis (and without including any strategy for the stabilising of quantum information), we should ask how the results reported in the present chapter affect those of Ref. [170]. We must identify the coherences that are destroyed more rapidly: from Eqs. (6.13) and (6.18) it is easy to see that the coherences with the fastest decay are given by the matrix elements $\rho_{\{0_n,1_n\}}$ and $\rho_{\{1_n,0_n\}}$. These off-diagonal elements decay as $\exp[-\Gamma_d(t;T)f(L)]$, with

$$f(L) = L + 2 \sum_{\substack{m=1,n=2 \\ m\neq n}}^{L} (i_m - j_m)(i_n - j_n)\cos(\omega t_s) \ , \tag{6.34}$$

for the limit of independent qubit decoherence, and as $\exp[-L^2\Gamma_d(t;T)]$ for the collective decoherence case. Hence, it is clear that for both cases, the longer the QR coherence length, the faster the coherence decay. Despite the fact that the results of Palma *et al.* [170] are not the same as ours, it turns out that both sets of results lead to the same unwelcome exponential increase of the error rate. One notes that the result of Eq. (6.34) is in general different from the one reported in [170]. Also, note that the coherence decay for the case of collective decoherence coincides with that of [170] only for the fastest off-diagonal element decay: if one considers different density-matrix elements, the results of Ref. [170] no longer coincide with those presented here. If the calculations reported in this chapter are used for an estimation of the actual decoherence time associated with any given off-diagonal density-matrix element (coherence), the results are in general quite different from the ones reported in [170].

It has been shown how a bosonic environment destroys the coherences of an arbitrary quantum register. In doing so, one has identified DFS states that are invariant under the coupling to such an environment. This result could be of crucial importance for improving

---

[4] Recently, our attention has been drawn to a dynamical-algebraic description that unifies the currently known quantum errors stabilization procedures [174] (see also Refs. [166](a), [173]). Within the framework of a system formed by a collection of L uncorrelated clusters of subsystems where each cluster fulfills the requirements of collective decoherence, Zanardi has shown that noiseless subsystems can be built [174].

the efficiency of quantum algorithms, for example. The author believes that, if arbitrarily complex computations are ever going to be realised in the laboratory, the engineering of DFSs, together with fault-tolerant QEC, must become intrinsic to the designs of future quantum computation architectures. Indeed, there was a recent experimental demonstration of decoherence-free quantum memories [168, 169]. This has been achieved for *one* qubit only, by encoding it into the DFS of a pair of trapped $^9\mathrm{Be}^+$ ions: in this way, Kielpinski *et al.* have demonstrated the immunity of a DFS of two atoms to collective dephasing [168]. Prior to this experiment with trapped ions, Kwiat *et al.* demonstrated the robustness of a DFS for two photons to collective noise [169]. Robust quantum memories seem therefore to be well on their way, both theoretically and experimentally, to overcoming the main obstacle to quantum information processing — namely, decoherence.

In the next section, the model of phase decoherence analysed here will be applied to a concrete physical system: an optically-driven QD system, the setup proposed in Chapter 3 for the generation of exciton quantum entanglement.

6.4 Relevance to a model quantum dot Hamiltonian

Consider the optically-driven setup of Chapter 3. In terms of the discussion given in the present chapter, the relevant Hamiltonians, H_0, and V, can be identified as

$$\begin{aligned} H_0 &= \epsilon_0 J_z + W(J^2 - J_z^2) + \sum_{\boldsymbol{k}} \epsilon_{\boldsymbol{k}} b_{\boldsymbol{k}}^\dagger b_{\boldsymbol{k}} \,, \qquad (6.35) \\ V &= J_z \sum_{\boldsymbol{k}} g_{\boldsymbol{k}} \left(b_{\boldsymbol{k}}^\dagger + b_{\boldsymbol{k}} \right) \,, \qquad (6.36) \end{aligned}$$

where, in the first instance, the external light source term $H_L = AJ_+ + A^*J_-$ of Hamiltonian Eq. (3.7) has been dropped. The third term of Eq. (6.35) represents a 'phonon field bath,' and V gives the interaction between the field and the dot system (see discussion in next section). Hence, it can be seen that H_0 commutes with the J_z part of V. However, this is not the case when the H_L contribution is included in H_0. In this latter case, $[H_0, J_z] = A^*J_- - AJ_+$, i.e., now H_0 does not commute with the J_z part of V. For illustrative purposes, consider the case of the 3-QD system described in Chapter 3, in the absence of incident radiation light. Note that the interaction term [Eq. (6.36] between exciton operators and phonon bath corresponds to a situation of collective decoherence. In this case, the exciton phase coherence decay obtained for a GHZ state of the type $\frac{1}{\sqrt{2}}(|0\rangle + \mathrm{e}^{i\phi}|3\rangle)$ yields

$$\begin{aligned} \hat{\rho}(t) &= \frac{1}{2}\Bigg\{ \left|\tfrac{3}{2}, -\tfrac{3}{2}\right\rangle \left\langle \tfrac{3}{2}, -\tfrac{3}{2}\right| + \left|\tfrac{3}{2}, \tfrac{3}{2}\right\rangle \left\langle \tfrac{3}{2}, \tfrac{3}{2}\right| + \\ &\quad \mathrm{e}^{i\phi} \exp\left[- 9 \sum_{\boldsymbol{k}} |g_{\boldsymbol{k}}|^2 c(\omega_k, t) \coth\left(\frac{\omega_k}{2\omega_T}\right)\right] \left|\tfrac{3}{2}, \tfrac{3}{2}\right\rangle \left\langle \tfrac{3}{2}, -\tfrac{3}{2}\right| + \\ &\quad \mathrm{e}^{-i\phi} \exp\left[- 9 \sum_{\boldsymbol{k}} |g_{\boldsymbol{k}}|^2 c(\omega_k, t) \coth\left(\frac{\omega_k}{2\omega_T}\right)\right] \left|\tfrac{3}{2}, -\tfrac{3}{2}\right\rangle \left\langle \tfrac{3}{2}, \tfrac{3}{2}\right| \Bigg\} \hat{\rho}(0) \,, \qquad (6.37) \end{aligned}$$

where $\rho(0) = \frac{1}{2}\left\{ \left|\frac{3}{2},-\frac{3}{2}\right\rangle\left\langle\frac{3}{2},-\frac{3}{2}\right| + \mathrm{e}^{i\phi}\left|\frac{3}{2},\frac{3}{2}\right\rangle\left\langle\frac{3}{2},-\frac{3}{2}\right| + \mathrm{e}^{-i\phi}\left|\frac{3}{2},-\frac{3}{2}\right\rangle\left\langle\frac{3}{2},\frac{3}{2}\right| + \left|\frac{3}{2},\frac{3}{2}\right\rangle\left\langle\frac{3}{2},\frac{3}{2}\right| \right\}$ is the associated initial GHZ state density-matrix. Note that the Abelian character of the noise process introduced in Eqs. (6.35) and (6.36), allows one to find analytical solutions for the coherences decay. However, the inclusion of an external source of light that irradiates the QD system makes the problem analytically unsolvable, and hence, one has to find an alternative approach to calculate the influence of decoherence in such an optically-driven system.

6.5 Decoherence effects on the generation of QD exciton entangled states

Here, the reliability of the exciton entanglement generation presented in Chapter 3, in the presence of phase decoherence effects, is analysed. By recognising that exciton decoherence in semiconductor QDs is dominated by acoustic phonon scattering at low temperatures [182, 183], one can use the model introduced in Section 6.1 in order to study decoherence effects on the entanglement generation. Hence, the quantum unitary evolution of the exciton states [Eq. (3.7)] must include the acoustic phonon dephasing mechanism

$$H_d = \sum_{\boldsymbol{k}} \epsilon_{\boldsymbol{k}} b^\dagger_{\boldsymbol{k}} b_{\boldsymbol{k}} + \sum_{\boldsymbol{k}} J_z\left(g_{\boldsymbol{k}} b^\dagger_{\boldsymbol{k}} + g^*_{\boldsymbol{k}} b_{\boldsymbol{k}}\right) , \tag{6.38}$$

where $J_z \equiv \sum_i J^i_z$, $b^\dagger_{\boldsymbol{k}}$ $(b_{\boldsymbol{k}})$ is the creation (annihilation) operator of the acoustic phonon with wavevector $\boldsymbol{k}$. Let us note that Eq. (6.38) corresponds to the Hamiltonian (6.1) without the term that accounts for the free evolution of the qubits, which has to be replaced by a term that models the dynamics of the QD system, i.e., Hamiltonian (3.7). The first term of the Hamiltonian (6.38) corresponds to the phononic environment, and the second term accounts for the interaction between exciton states (represented by the operators J_z) and the environment. Here, $g_{\boldsymbol{k}}$ denotes the coupling between QD states and field modes, and, in the collective decoherence situation analysed here, $g_{\boldsymbol{k}} = g^*_{\boldsymbol{k}}$. It is worth pointing out that there is experimental evidence [183] in support of the fact that at low temperatures, H_d can be considered as the main factor responsible for the decoherence effects on the generation of the maximally entangled exciton states analysed in Chapter 3.

The QD system's time evolution, in the presence of acoustic phonon dephasing mechanisms, is now ruled by the Hamiltonian $H' = H_\Lambda + H_d$, with H_Λ as given in Eq. (3.7). Here, only phase decoherence effects are considered. This was physically justified in Section 6.1. The exact kinetic equations for the system of QDs can be obtained by applying the method of operator-equation hierarchy developed for Dicke systems in Ref. [184]. Following Ref. [134], by assuming a very short correlation time for exciton operators, the exact hierarchy of equations transforms into a Markovian master equation. The initial condition is represented by the density matrix $\rho(0) = |0\rangle\langle 0|\rho_{ph}(T)$, the product state of the exciton vacuum and the equilibrium phonon reservoir at temperature T. At resonance $(\Delta_\omega = 0)$ the dynamical equation for the expectation value of exciton operators is given by [134]

$$\frac{\partial\langle J_\alpha^{r-s}\rangle}{\partial t} = -iW\langle[J_\alpha^{r-s}, J_z^2]\rangle - iA\langle[J_\alpha^{r-s}, J^+ + J^-]\rangle - \Gamma_d(T)(2\langle[J_\alpha^{r-s}, J_z]J_z\rangle - \langle[J_\alpha^{r-s}, J_z^2]\rangle)\,, \tag{6.39}$$

where $\Gamma_d(T) = \int d\omega' \omega'^n e^{-\omega'/\omega_c}[1 + 2N(\omega', T)]$ is the decoherence rate, with n depending on the dimensionality of the phonon field, ω_c is the cut-off frequency (typically the Debye frequency), and $N(\omega', T)$ denotes the phonon Bose-Einstein occupation factor. It is a well known fact that very narrow linewidth of the photoluminescence signal of a *single* QD does exist due to the elimination of inhomogeneous broadening effects. Consequently, the decoherence rate $\Gamma_d(T)$ in this analysis should be associated with just homogeneous broadening effects. At low temperature, the main decoherence mechanisms are indeed acoustic phonon scattering processes. The decoherence parameter $\Gamma_d(T)$ is temperature dependent and it amounts to 20-50 μeV for typical III-V semiconductor QDs in a temperature range from 10 K to 30 K [182]. Typical values for $\Gamma_d(T) \equiv \Gamma$ which can represent real situations for QDs at low temperatures, together with the experimental conditions $\epsilon = \omega = 1$, and the Förster term $W = 0.1\,\epsilon$ are considered below. Laser strengths and decoherence rates are expressed in units of W. The coupled differential linear equations for the time dependent pseudo-spin expectation values are solved and the results are given in terms of the time dependent overlaps $O_{\text{BELL}} = \text{Tr}\{\rho_{\text{BELL}}\rho(t)\}$ and $O_{\text{GHZ}}(t) = \text{Tr}\{\rho_{\text{GHZ}}\rho(t)\}$ [134].

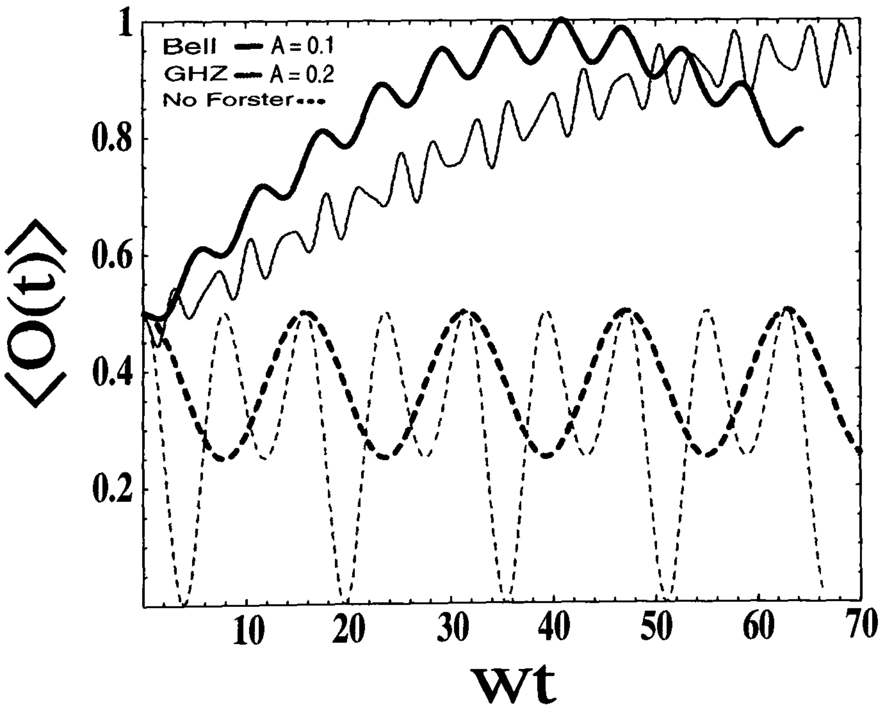

Figure 6.7: Relevance of the Förster interaction in the entanglement generation process (zero decoherence limit). Thick (red) lines represent the Bell-state overlap, $A = 0.1$: solid, Forster term included; dotted, Forster term not included. Thin (blue) lines represent the GHZ-state overlap, $A = 0.2$; same meaning as for solid and dotted lines.

Figure 6.7 shows the evolution of the overlaps $O_{\text{BELL}}(t)$ and $O_{\text{GHZ}}(t)$ in the limit of very weak light excitation and zero decoherence. It can be seen that no maximally entangled exciton states generation is possible if the Förster interaction is turned off. This implies that efficient exciton entangled states generation should be helped by compact QD systems where the Förster term can take a significant value, as discussed in Chapter 3.

Figures 6.8(a) and 6.8(c) show the case of Bell-state generation ($N = 2$ QDs) in the presence of noise. In Fig. 6.8 (a) the decoherence rate $\Gamma = 0.001$, and the laser intensities are $A = 0.1$, and $A = 0.4$. It is shown that τ_{BELL} is significantly shortened by applying stronger laser pulses. Therefore, decoherence effects can be minimised by using higher excitation levels. However, a higher laser intensity also implies a sharper evolution which therefore requires a very precise pulse length. Figure 6.8(c) shows temperature-dependent results for $\Gamma = 0.001$, 0.01 and 0.1, when $A = 0.4$ is kept fixed. One can see that at high temperatures ($\Gamma = 0.1$) no maximally entangled states generation is possible. However, it can be estimated that Γ values between 0.001 and 0.01 are typical in the temperature range from 10 K to 50 K: in this parameter window successful generation of Bell states can be produced [134], as shown in Fig. 6.8(c).

Figures 6.8(b) and 6.8(d) show the case of GHZ states generation ($N = 3$ QDs). As above, τ_{GHZ} is shortened by using higher laser excitation levels, as can be seen from Fig. 6.8(b) for $\Gamma = 0.001$. Figure 6.8(d) shows the temperature effects through the variation of Γ for $A = 0.4$. It is seen that similar decoherence rates yield a more dramatic reduction of the coherence in the GHZ case than in the Bell case. However, as for Bell generation, a parameter window does exist where the generation of such entangled states is feasible [134]. It is worth noting the different scaling behaviour of the generation frequency of these entangled states at very low temperature, i.e., vanishing Γ and very low laser excitation. While selective $\frac{\pi}{2}$ laser pulse length for the Bell case scales like W/A^2, selective $\frac{\pi}{2}$ pulse length for the GHZ case scales like W^2/A^3. This property of $\frac{\pi}{2}$ pulses to generate maximally entangled exciton states was demonstrated analytically in Subsection 3.5 and is verified in the present section by looking at the numerical results presented in Figure 6.8.

In summary, decoherence effects can be minimised when generating maximally entangled states by applying stronger laser pulses and working at low temperatures where acoustic phonon scattering is the main decoherence mechanism. Since it has been shown that the generation of maximally entangled exciton states is preserved over a reasonable parameter window, even in the presence of decoherence mechanisms, we stress that this optical generation could be reliably exploited in solid state devices to perform quantum communication protocols, such as the teleportation of an excitonic state in a coupled QD system [JHR3], as shown in Chapter 4.

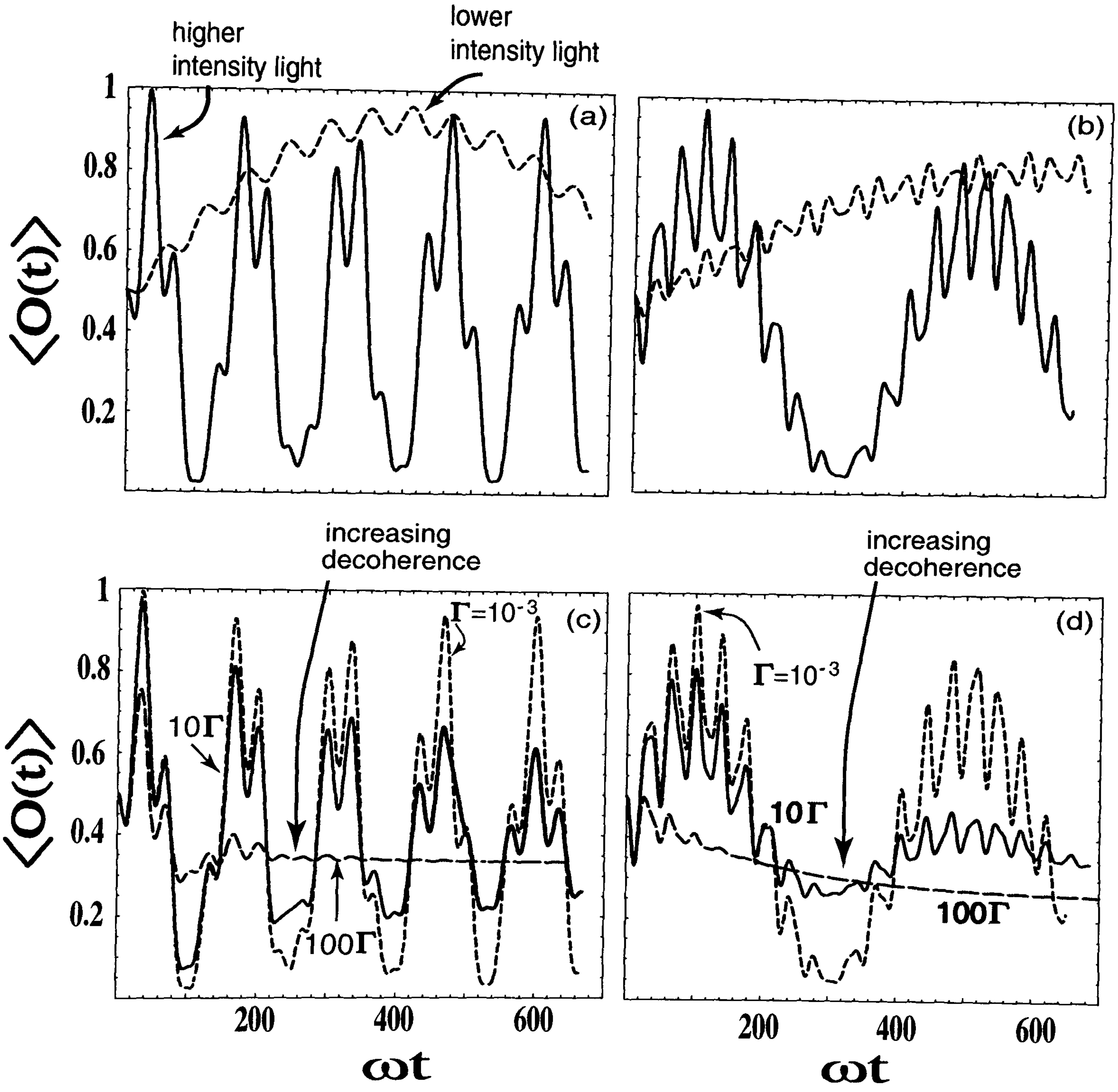

Figure 6.8: Maximally entangled exciton states generation in the presence of phase decoherence: (a) $\langle O_{\text{Bell}}(t)\rangle$ for $A = 0.1$, red (dashed) line and $A = 0.4$, blue (solid) line. (b) $\langle O_{\text{GHZ}}(t)\rangle$ for $A = 0.2$, red (dotted) line and $A = 0.4$, blue (solid) line. In plots (a) and (b) Γ is kept fixed: $\Gamma = 0.001$. In figures (c) and (d) $A = 0.4$ is kept fixed whereas Γ is varied: $\Gamma = 0.001$, red (short dashed) line, $\Gamma = 0.01$, blue (solid) line and $\Gamma = 0.1$, green (long dashed) line. These curves correspond to (c) $\langle O_{\text{Bell}}(t)\rangle$ and (d) $\langle O_{\text{GHZ}}(t)\rangle$.

Chapter 7

Conclusions and perspectives

7.1 Summary

This thesis has provided practical schemes for the processing of solid state-based quantum information. Within this framework, a detailed analysis of the way in which decoherence due to a bosonic reservoir may affect such a processing is given. Although the bulk of this work is devoted to the study of QD nanostructures and the way they can be exploited for QIP, this thesis is aimed at providing a more general framework in the understanding of fundamental physical processes. In so doing, Chapter 2 presents the main developments and breakthroughs of the multidisciplinary field of quantum information at both theoretical and experimental levels. Given the intense research activity in this field, it is evident that a review will become out of date almost immediately after is written. However, it is the author's hope that the basic physics required to allow an adequate introduction to the field has been provided. Thus, Chapter 2 should help (and hopefully motivate) the reader to understand the place and relevance of the subsequent work presented in this thesis. A summary of this work is outlined below.

Chapter 2 is divided into two main parts. The first one reviews the field of quantum information and quantum computation. Quantum registers, through to the universal gate for building quantum circuits that are universal for quantum computation, are first introduced. It is shown how two-qubit gates suffice for quantum computation, and the power of the quantum circuit representation for entangling and disentangling quantum states is emphasised. This led to the no-cloning theorem and its interesting implications. The basic ideas of holonomic or geometric computation—an alternative approach for quantum computation—are also introduced. Following this, the power of quantum entanglement as a communication resource is highlighted in order to describe some of its most celebrated practical applications to date: quantum teleportation, quantum cryptography, dense coding, and quantum data compression. Deutsch's concept of quantum parallelism is introduced in order to gain insight into the potential for efficiently solving certain classically intractable algorithms. After this, two processes fundamental to QIP, decoherence and 'recoherence' (e.g., quantum error correction), are discussed. This first part of Chapter 2 ends by briefly describing the main qubit systems currently employed for the processing of quantum information.

The second part of this chapter, Section 2.2, deals with the practical side of QIP, in particular, with the experimental techniques and state-of-the-art of quantum dot engineering, thus providing an overview of the practicalities required for the work presented in this thesis. In so doing, far- and near-field optical spectroscopy, in addition to coherent optical ultrafast spectroscopy techniques are described. Following this, the properties of an interacting (QD) system and Kohn's theorem are presented. The most representative solid-state qubit proposals for quantum computing to date are summarised. Finally, a discussion of the role of quantum information theory and quantum technology, and their implications for the new era of quantum-mechanically assisted processing of information is highlighted.

Chapter 3 gives a detailed prescription for producing an all-optical generation and control of exciton maximally entangled states in coupled QDs [JHR1]. Starting from suitably initialised states, it is shown that this optically-driven coupled QD system leads to reliable generation of highly entangled states of two and three exciton qubits. The set-up exploits currently available coherent optical control of excitons in single quantum dots on the nanometer and femtosecond scales.

Chapter 4 shows that exciton maximally-entangled states can be used as a quantum resource for performing a true solid-state teleportation protocol [JHR2]. The set-up allows the teleportation of an excitonic state from one dot to another. It is shown that only two unitary transformations are needed to perform this process: a quantum CNOT gate and a Hadamard gate. The explicit laser pulses necessary to generate the source of entangled states are given, along with the corresponding quantum logic gates employed in the process [JHR2].

In contrast to the above ultrafast coherent optical proposals for quantum entanglement generation and quantum teleportation, Chapter 5 gives a setup for the implementation of a solid-state NMR-based quantum switch for quantum logic [JHR3]. Here, the so-called magic-number transitions in few-electron QDs containing a nuclear spin impurity can be used to implement single and two-qubit gates. Since the hyperfine coupling between the electrons and the nucleus can be changed as a function of an externally applied magnetic field, the nuclear magnetic resonance is controlled by the corresponding electron ground state transitions. This nuclear qubit control is also shown to be accomplished by means of exciting the QDs with infra-red (IR) radiation. Decoherence effects in systems of spin half nuclei are expected to be minimal as nuclear spins are weakly coupled to their environment. Therefore, such spin systems are natural qubits for quantum information processing since they offer both long decoherence and long relaxation times.

In Chapter 6, the dynamical evolution of a quantum register of arbitrary length coupled to an environment of arbitrary coherence length is predicted within a general model of decoherence [JHR5]. The situations of qubits coupling individually to different environments ("independent decoherence") and qubits interacting collectively with the same reservoir ("collective decoherence") have been studied. In both cases, explicit decoherence functions are derived for any number of qubits. It is found that the decay of the coherences of the register strongly depend on the input states: it is shown that this sensitivity is a characteristic of both types of coupling (collective and independent) and not only of the collective coupling, as has been reported previously. A non-trivial behaviour—"recoherence"—is found in the decay of the off-diagonal elements of the reduced density matrix in the specific situation of independent decoherence. The results of the collective decoherence limit led to the identification of decoherence-free states. These states belong to subspaces of the system's Hilbert space that do not get entangled with the environment, making them ideal elements for the engineering of "noiseless" quantum codes. The relations between decoherence of the quantum register and computational complexity are also discussed, based on the dynamical results obtained for the register density matrix. The formalism developed in this chapter is applied to the analysis of decoherence effects on the optical generation of the exciton maximally entangled states reported in Chapter 3 [JHR4]. In so doing, it is shown that there is a reasonable parameter window in which the role of phonons, at low temperatures, does not necessarily amount to the loss of control over the exciton system due to coherences destruction.

Appendix A gives preliminary results on the exciton coherent dynamics of an optically driven coupled quantum dot system confined within a semiconductor microcavity [JHR6]. It is shown that the coupling of the QD system to a single mode microcavity enables the control of exciton entanglement by varying the coupling strength between the dot system and the microcavity. The exciton entanglement shows collapses and revivals for suitable amplitudes of incident radiation field and dot-cavity coupling strengths. The results given here can be viewed as an alternative approach for the control of decoherence mechanisms arising from entangled artificial molecules.

Future directions and perspectives derived from the results provided by this thesis are discussed below.

7.2 Future directions

There are several aspects of the topics developed in this thesis that pave the way to further investigations at both theoretical and experimental levels. There are two fundamental issues that arise from the contents of this thesis. One of them is related to the experimental exploration of appropriate materials and appropriate experimental conditions—hardware engineering—that may lead to the experimental demonstration of most of the theoretical predictions reported in this thesis. For example, materials where Förster's resonant energy transfer (FRET) rates are enhanced, as a result of the exciton coupling, are of particular relevance for the quantum entanglement generation proposed in this thesis. As has already been pointed out, different regions of parameter space can be explored by employing semiconductors of different bandgap ϵ. An interesting possibility is that provided by hybrid organic-inorganic nanostructures [143], where the effects due to the large radius (Wannier-Mott) exciton states in the inorganic material and small-radius (Frenkel) exciton states in the organic one are combined. The desirable QD molecule could be built of an inorganic II-VI material (e.g., ZnSe or ZnCdSe), embedded in bulk-like organic crystalline material (e.g., tetracene, perylene, fullerene, or PTCDA) where their Frenkel and Wannier excitons are in resonance with each other, therefore obtaining a strong hybridisation between these excitons, which means a greater Wannier exciton delocalisation or Förster hopping. The choice of any solid-state set-up to be used as a hardware for exciton-based QIP would need a careful analysis of FRET rates as a function of the given geometry and confinement effects of the dot molecule. Most important is the issue related to the characteristic dephasing effects that might affect the coherent evolution of the qubits. Therefore, before commencing any attempt at an experimental demonstration of exciton entanglement, or even simpler, of single qubit gates, the model hardware should provide good enough coherence properties. Another aspect that deserves further exploration is related to the quantum dot photon emission and the possibility of entangling photons at will as a result of tailoring the QDs exciton coupling.

The second issue is related to more theoretical aspects regarding the decoherence phenomenon. It has been shown that decoherence is the main obstacle to any solid-state based prospectus for QIP. In fact, one can argue that large scale quantum information processing will be a reality only when optimal control of quantum coherence in noisy environments can be achieved. Thus, at a more fundamental level, this phenomenon needs to be better understood, and in particular in the solid-state. It is a hope that in the not-too-distant future, further experimental designs in the battle against decoherence will increase the currently available QDs dephasing times[1], and that the complex interplay existing amongst several different factors that affect the coherences evolution, such as vacuum and thermal fluctuations, dimensionality, and disorder, becomes also better understood. In this respect, detailed theoretical studies of the non-markovian dynamical evolution that accomplishes this usually ultrafast quantum dynamical processes will be needed.

Next, the possibility of exploiting highly efficient and ultrafast processes exhibited by some biological molecules due to FRET [69, 70, 71, 72] and Dexter [73] processes in order to perform a coherent quantum evolution is discussed. In so doing, let us first briefly review the main characteristics and relevance of such a 'biological' experimental set-up. The primary process of photosynthesis in bacteria, algae, and plants, is based on the absorption of photons by light-harvesting complexes (LHs) and the transfer of this excitation energy from the LHs to the photosynthetic reaction centre (RC), the place where the necessary photochemical reactions are performed [70, 71]. The LHs are molecular aggregates of pigments, such as the chlorophylls, that act as light-harvesting antennas in order to capture the sunlight and to funnel the resulting electronic excitation to the RC[2].

Figure 7.1 shows an example of a biological system—the purple bacteria—where

---

[1] This might be helped via a better engineering and control of quantum noise: error avoiding decoherence schemes (decoherence free subspaces), methods for dynamical suppression of decoherence, and of course, quantum error correction are available techniques which will be essential for maintaining a qubit coherent evolution.

[2] This process takes place in the so-called photosynthetic unit (PSU), which is built of an RC and associated pigments, the LHs and associated clorophylls, chromophores, and caretonoids (accessories). See fig. 7.1(a).

the above-mentioned process takes place (all light-harvesting complexes are built in a remarkably similar fashion, so that what is said here for the case of the purple bacteria can be applied to other biological complexes). The purple bacteria contains two types of light-harvesting complexes[3]: The LH-I that surrounds the RCs, and the LH-IIs that capture and transfer the energy to the RCs via the LH-I complex [see Fig. 7.1(a)].

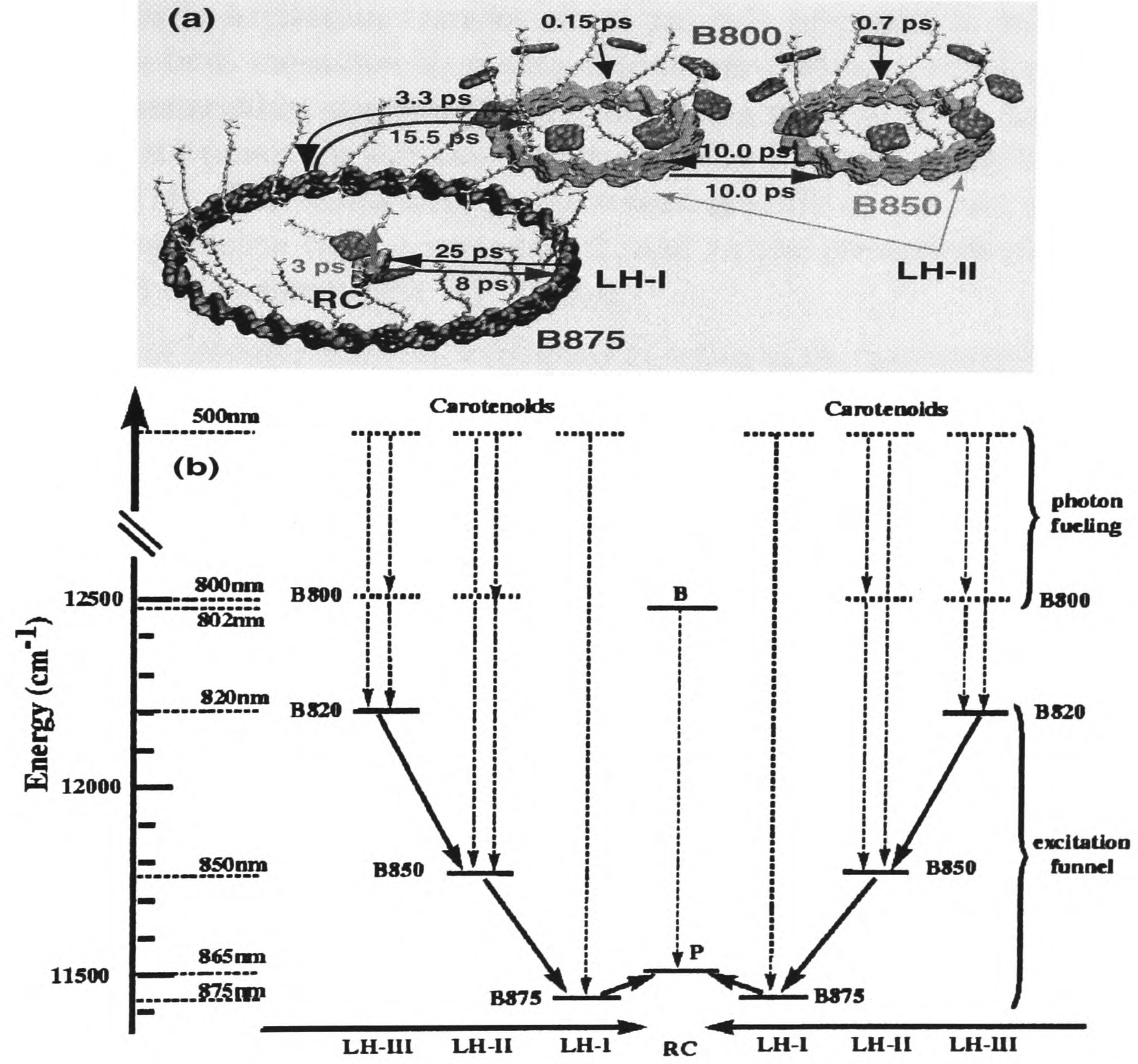

Figure 7.1: (a) Measured excitation transfer times in the photosynthetic unit (PSU) of purple bacteria. The pigments of the LH1 (32 BChls in a ring of radius $r \sim 59$ Å) complex absorb at 875 nm, while the LH2 complexes contain two types of BChls which absorb at 850 nm (16 BChls, $r \sim 23$ Å) and 800 nm (8 BChls, $r \sim 28$ Å), which are labelled B850 and B800. Carotenoids are shown as 'curled strings.' Typical distances between B800 and B850 are of the order of 20 Å. (b) Schematic of the energy levels of the electronic excitations in the PSU of BChl-a containing purple bacteria. The funneling of the excitation energy towards the photosynthetic reaction centre (RC) is shown. Dashed (solid) lines represent intracomplex (intercomplex) energy transfer. LH-I is found in all purple bacteria; LH-II exists in most species. The additional complex LH-III appears in certain species only. P, and B stand for RC accessory pigments. The figure is adapted from Refs. [70, 71].

---

[3] The LH-II contains three bacteriochlorophylls (BChls): two of them absorb at 850 nm (B850) and the other one, B800, absorbs at 800 nm. In contrast, the LH-I has only one pair of BChls that absorbs at 875 nm.

As can be seen, there is an important energetic hierarchy in this process: the further the LHs are from the reaction centre, the higher the energy at which they absorb, as shown in Fig. 7.1(b). Thus, two types of excitation transfer cascading towards the RC can be identified: i) excitation transfer *within* each BChl (LH-II, LH-I, RC) complex ('intracomplex transfer'), and ii) excitation transfer *between* pigment protein complexes: LH-II → LH-II, LH-II → LH-I, and LH-I → RC ('intercomplex transfer'). Figure 7.1(a) shows characteristic excitation transfer times for this processes to take place in the PSU, which have been measured by means of time-resolved picosecond and femtosecond spectroscopy. Remarkably, the overall light-harvesting process in the purple bacteria is highly efficient: it funnels the light energy towards the RC with about 95% efficiency in less than 100 ps [71]. This excitation transfer within the PSU occurs on the subpicosecond time scale for the photon fueling components, and on the picosecond time scale for the excitation funnel components [see Fig. 7.1(b)].

The excitation transfer has been explained in terms of two processes which are rather different in range and in dependence on the donor-acceptor separation [70, 71]: i) the Förster mechanism [69], that involves induced dipole-dipole coupling is based on the coupling of the optically allowed transitions and operates over 'long' distances (20-50 Å), while ii) the Dexter mechanism [73] involves electron exchange between donor and acceptor and is based on the significant overlap of the wave functions of acceptor and donor, therefore requiring a closer contact between them (distances of a few Å). Thus, intercomplex processes such that LH-II → LH-I occur via 'exciton transport' between these near-resonant molecules. This has been observed via single molecule spectroscopy experiments, where the fluorescence excitation spectrum of a single LH-II complex has been measured [74]. As a remarkable result, evidence for coherent exciton transport in the LH-II (at low temperature) has been reported [74]. Hence, single-molecule spectroscopy, in addition to x-ray diffraction, are available techniques that provide crucial information regarding the optical spectra and structural characterisation of the PSU elements, thus paving the way to time-resolved investigation of single molecules, such as the LHs complexes.

The motivation for studying these biological molecules lies within a QIP perspective, particularly to explore whether these molecules may serve as basic units for performing a coherent quantum evolution, which in turn should lead to gaining insight into the way decoherence affects such biophysical processes. An experimental set-up in which to test the possibility of performing such a coherent evolution is next highlighted. Consider the B850 complex of the LH-II molecule, which is built of 16 BChls distributed on a ring of radius $r \sim 23$ Å. The associated intracomplex energy transfer occurs on the subpicosecond time scale. The B850 complex absorbs light at 850 nm. Suppose one is able to prepare a source of single photons whose states have a definite phase relation, e.g., the state $|H\rangle + |V\rangle$ (H and V stand for horizontal and vertical polarisation states), with appropriate matching energy, and give them periodically (e.g., at a MHz frequency rate) as the input states of the BChls. The question one wants to answer is whether the phase coherence of such a state is preserved towards the final outcome, and to what extent this task might be facilitated by an exciton coherent energy transfer, as a function of different excitation frequencies and photon configurations. This set-up could also be extended to include intercomplex energy transfer processes between the LHs. It should also be interesting to consider the possibility of engineering the energy structure of one (or several) of the BChls, thus breaking the ring's symmetry, to further analyse the energy transfer and 'photon transmission' processes.

Perhaps nature herself offers us the necessary built-in nanostructures where the processing of information at a quantum level is feasible. It may be that 'biological qubits' could provide a novel framework with which to study "naturally efficient" ultrafast optical processes that may prove useful for quantum information processing tasks. Future work is intended to explore these thoughts in more detail.

Appendix A

Collapsing and reviving QD entanglement in a microcavity

As discussed throughout this thesis, one major challenge to all solid-state QIP schemes is the battle against high decoherence rates. This appendix gives some preliminary results regarding a set-up that includes an additional degree of freedom in order to further control the system studied in Chapter 3.

A.1 Model and results

The set-up consists of a QD-molecule confined within a semiconductor microcavity: it will be shown that such a system can be used to control the generation of exciton entangled states in artificial molecules, and hence, provides an indirect mechanism to fight the battle against environmental decoherence effects. Recent experiments on microcavities containing dye molecules have demonstrated the enhancement of Förster transfer rates [72]. As has been shown in Chapter 3, experimental results on optically-generated electron-hole pairs in *single* semiconductor QDs have shown coherent wavefunction control on the nanometer and femtosecond scales [60, 62, 61]. The fabrication of QDs in photonic dots has also recently been experimentally achieved [189], in addition to the recent advances in the fabrication of semiconductor (GaAlAs- and CdTe-based) microcavities for ultrafast polariton (exciton-cavity photons excitations) parametric amplification [186], and also the demonstration of strong exciton-photon coupling in organic semiconductor microcavities [187, 188]. Hence, the possibility of controlling exciton coherences in coupled QDs embedded in a microcavity is compatible with state of the art of nanofabrication technology.

Consider the $N = 2, 3$ QD system[1] studied in Chapter 3, but now confined within a

---

[1] In real experimental conditions it is difficult to have identical QDs. However, it can be shown that as far as the difference in dots size is such that the energy difference between the dots bandgap is less than $\delta = 1$ meV, generation of exciton entanglement in these dot-molecules is still possible (even in the presence of phase decoherence effects). For instance, if the case $N = 2$ shows a "slight" difference in dot sizes such that the detuning parameter $\Delta_1 \equiv \epsilon_1 - \omega \neq \Delta_2 \equiv \epsilon_2 - \omega$, the rotating wave Hamiltonian

semiconductor lossless microcavity, and radiated by long-wavelength classical light. The Hamiltonian describing the formation of single excitons within the individual QDs and their inter-dot coupling can be expressed in terms of the quasi-spin operators J and J_i $(i = x, y, z)$, as shown in Refs. [JHR1, 53]. Taking into account the microcavity terms, the full Hamiltonian now reads

$$H(t) = \hbar\omega_{\mathrm{x}} J_{\mathrm{z}} - V(J^2 - J_{\mathrm{z}}^2) + \hbar\omega_c a^\dagger a + E(t)J_+ + E^*(t)J_- + \hbar g_c(a^\dagger J_- + aJ_+) \ , \quad \text{(A.1)}$$

where ω_{x} denotes the exciton energy, ω_c stands for the microcavity photon energy associated with the creation operator $a^\dagger$, and g_c is the QD-cavity coupling strength. The time dependence of $E(t)$ describes the laser pulse shape, while its magnitude includes the electron-photon coupling and the incident electric field strength. As discussed in Chapter 3, $H(t)$ contains a non-linear term in J and J_{z} (strength V), which takes into account the exciton-exciton interdot coupling, that can be exploited to generate exciton entangled states [JHR1, 53]. There are two main effects associated with the dynamics of the QD-cavity system: the first one is the coupling between the cavity and the QD system, and the second one is the coupling between the QD and the external source of light, a process that under certain prescribed conditions may lead to the generation of exciton entanglement in the QD molecule. Here, it is shown that the former coupling leads to a dynamical control of the latter one in such a way that the QD exciton entanglement exhibits collapses and revivals that can be tailored according to the exciton-photon coupling. Let us consider a rectangular radiation pulse, starting at time $t = 0$, with central frequency ω: $E(t) = g_l e^{i\omega t}$.

Time evolution: The system's time evolution is ruled by the action of $H(t)$ [Eq. (A.1)], and can be obtained by means of suitable unitary transformations [190, 191] (details are given below, in Sec. A.2). The state of the QD-cavity system at time t is exactly given by the state vector $(\hbar = 1)$

$$|\Psi(t)\rangle = \exp\left[i\Big(\omega_{\mathrm{x}} J_{\mathrm{z}} + \omega_c a^\dagger a\Big)t\right] D^\dagger(\eta) \exp\left[i\Big(g_c[a^\dagger J_- + aJ_+] - V[J^2 - J_{\mathrm{z}}^2]\Big)t\right] D(\eta)|\Psi(0)\rangle \ , \quad \text{(A.2)}$$

where $\eta = g_l/g_c$ is a parameter that measures the QD-cavity coupling, and $D(\alpha) = \exp(\alpha a^\dagger - \alpha^* a)$ denotes the photon displacement operator: this creates the coherent state $|\alpha\rangle$ from the vacuum state $|0\rangle$, i.e., $|\alpha\rangle = e^{-|\alpha|^2/2} \sum_{n=0}^{\infty} \frac{\alpha^n a^{\dagger n}}{n!} |0\rangle = D(\alpha)|0\rangle$ [recall that $D^\dagger(\alpha) = D(-\alpha)$]. The system's initial state to be considered here is given by the product state of the vacuum of excitons for the QD system and the coherent state $|\alpha\rangle$ for the cavity: $|\Psi(0)\rangle = |J = N/2, M = -N/2\rangle \otimes |\alpha\rangle$. Let us concentrate on the results for the two QD-molecule embedded in a semiconductor microcavity. From the initial QD state considered above, it follows that the system's evolution occurs within the subspace $J = 1$, for any time t. The subspace $J = 0$ remains dark and will be ignored. The generation of Bell states in an unconfined QD system has been previously reported [JHR1, 53].

---

representing the QD-molecule dynamics will have $\Delta_\omega J_Z \mapsto \Delta_1 J_{1z} + \Delta_2 J_{2z} \equiv \Delta J_Z + \frac{\delta}{2}(J_{1z} - J_{2z})$, where $\delta \equiv \Delta_1 - \Delta_2$, and $\Delta \equiv \frac{1}{2}(\Delta_1 + \Delta_2)$, instead of $\Delta_\omega J_Z = (\epsilon - \omega)J_Z$ which arises when all of the dots are identical in size.

Effects due to decoherence mechanisms affecting the generation of such Bell states were reported in Chapter 6. Here, the overlap $O(t) = \mathrm{Tr}\{\rho(t)\rho_{\mathrm{BELL}}\}$ between the QD-cavity density matrix at time t and the Bell density matrix is calculated. The former is given by $\rho(t) = |\Psi(t)\rangle\langle\Psi(t)|$ while the latter is given by $\rho_{\mathrm{BELL}} = |\Psi_{\mathrm{BELL}}\rangle\langle\Psi_{\mathrm{BELL}}|$, where $|\Psi_{\mathrm{BELL}}\rangle = \frac{1}{\sqrt{2}}(|00\rangle + i|11\rangle) \otimes |\beta\rangle$, and $|\beta\rangle$ denotes a coherent photon state. This overlap is easily calculated in the representation of eigenvectors of the reduced Hamiltonian $g_c(a^\dagger J_- + aJ_+) - V(J^2 - J_z^2)$. In what follows, the system's dynamics is given with energies measured in units of the interdot coupling constant $V = 1$, and resonance condition $\omega_x = \omega_c = \omega = 10$. The choice of these parameters follows the recent experimental situation reported in Ref. [189], where a QD-cavity system based on a hybrid inorganic-semiconductor and an organic-material has been studied.

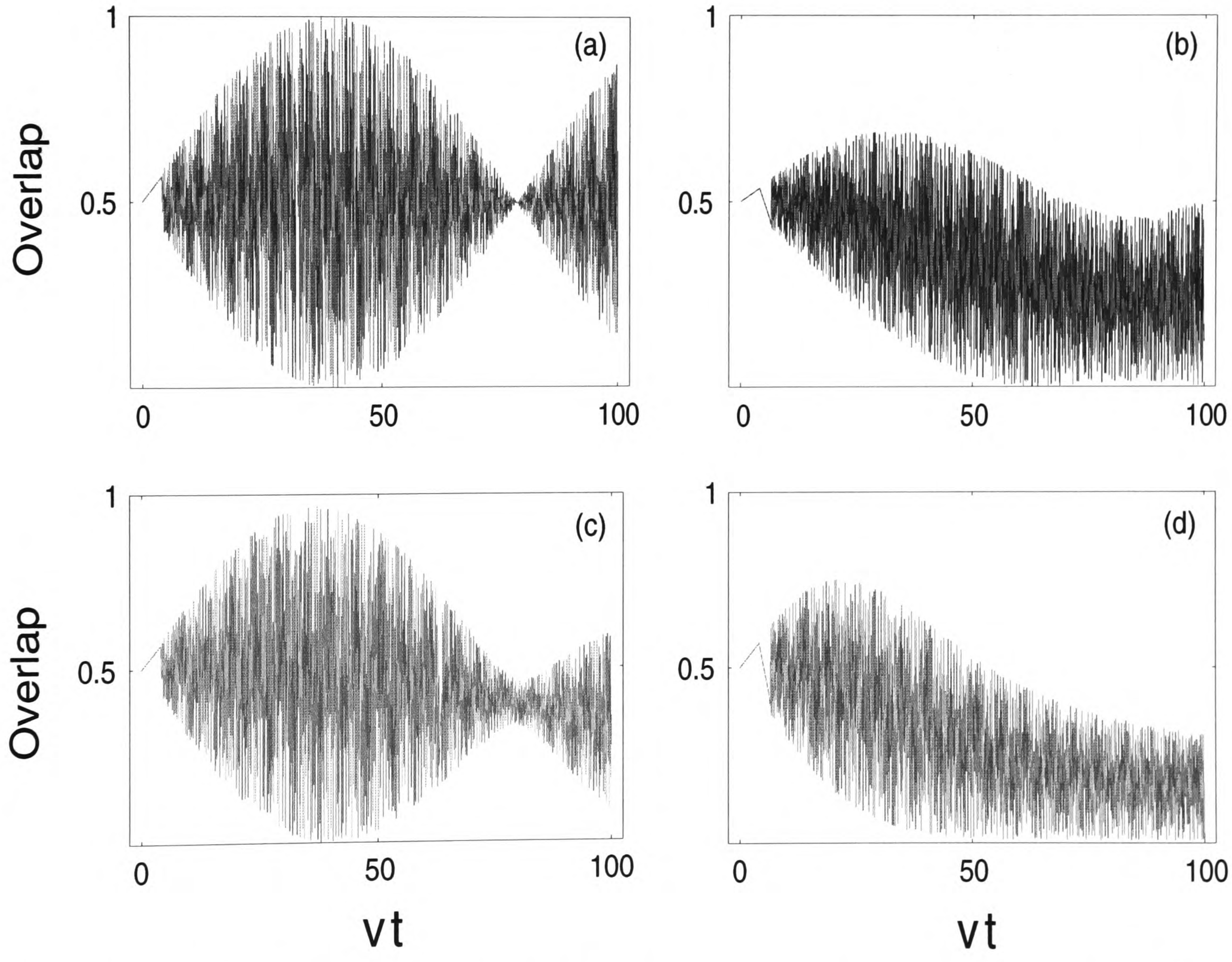

Figure A.1: Overlap $O(t) = \mathrm{Tr}\{\rho(t)\rho_{\mathrm{BELL}}\}$ of Bell state as a function of time. The driving classical field coupling factor is kept fixed at $g_l = 0.1$, while $g_c =$ (a) 0.001, (b) 0.01, (c) 0.02, and (d) 0.08. In all of the plots, energies are measured in units of $V = 1$. The given results correspond to the resonance condition $\omega_x = \omega_c = \omega = 10$.

Fig. A.1 shows the Bell overlap for different QD-cavity coupling strengths g_c (the initial and final photon states are both taken as the vacuum state). The amplitude of the driving light is kept constant, $g_l = 0.1$. For low values of g_c, the results reported in Refs. [JHR1, 53] are recovered, as expected. By increasing g_c, a non-monotonic behaviour for the Bell overlap arises. Clearly, there are some QD-cavity coupling strengths for which the generation of Bell states is favored. Fig. A.2 shows the results for different amplitudes g_l of the driving field while $g_c = 0.02$ is kept fixed. Clearly, the interplay between the driving light and the microcavity confined photons generates a non trivial behaviour for Bell states generation.

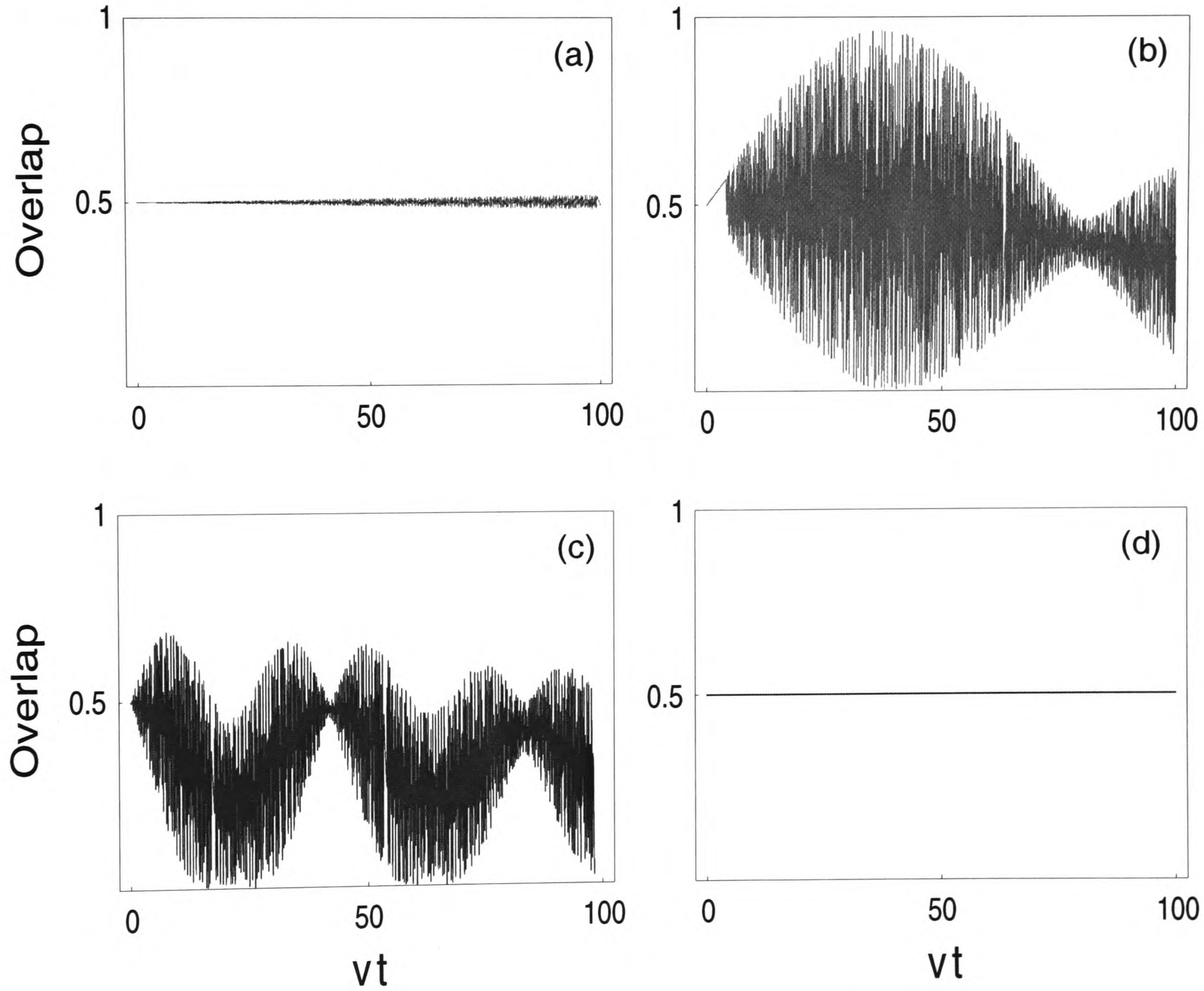

Figure A.2: Overlap $O(t)$ of the Bell state as a function of time for driving field amplitudes $g_l =$ (a) 0.01, (b) 0.1, (c) 0.2, (d) 0.5. The QD-cavity coupling is kept fixed at $g_c = 0.02$.

It has been shown previously [JHR1, 134], in the absence of cavity confinement, that the higher the driving field, the shorter the pulse τ_{Bell} required for generating such Bell states. In contrast, when the photon environment of the QD-molecule is modified by the presence of the cavity, a rather different behaviour emerges, as can be seen from Fig. A.2: for certain values of the amplitude g_l, no generation of maximally entangled states is possible, and again, the entanglement generation is favored for certain values of the amplitude of the driving field.

As a more dramatic effect induced by the microcavity confinement, Fig. A.3 shows collapses and revivals of the Bell state on a larger time scale. This phenomenon is a clear manifestation of the quantum nature of the light confined in the cavity. Collapses and revivals of population inversion in atomic systems have been considered previously [192]. However, similar phenomena in coherence related features have not been fully explored. The results presented in this thesis show that a coherent evolution of excitons, and in particular, of entangled excitons in semiconductor QDs in microcavities could bring an exciting opportunity to closely consider these effects for the processing of quantum information.

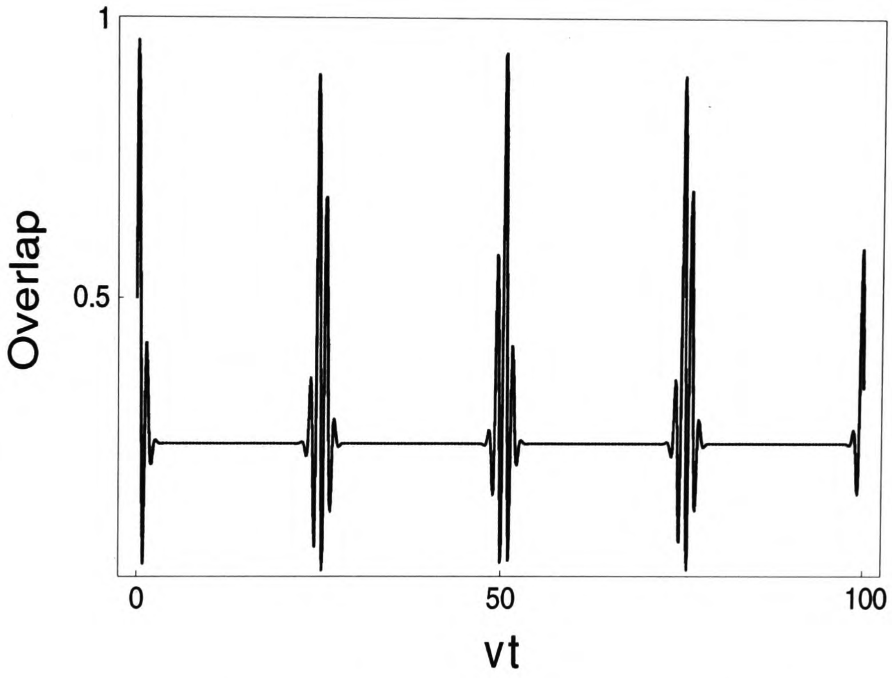

Figure A.3: Collapses and revivals of the Bell state as a function of time in the rotating frame. The driving field amplitude $g_l = 1.2$, and the QD-cavity coupling $g_c = 0.25$.

Within the framework of a dynamical suppression of decoherence, one can imagine that the additional photonic degree of freedom introduced in our model mediates in the control of the coherent evolution of the excitonic system: the single mode microcavity can be thought of as an external controllable interaction which leads to "exciton recoherence". This is because of the occurrence of revivals of the exciton entangled states on a long time scale, which have a well determined period $T_{rev} = T_{rev}(\eta)$: the QD-microcavity system undergoes a dynamics that, despite the fact that it does not prevent the collapse of its entangled state, disturbs the decoherence process in such a way that at a later time $\tau_{\text{BELL}} + nT_{rev}$ $(n = 1, 2, \ldots)$, such a 2 QD-microcavity entangled state is recovered. Interestingly, the system's Hamiltonian [Eq. (A.1)] resembles the character of the system-bath interaction analysed in Chapter 6: the bosonic "bath" is given in this case by the single-mode cavity field $\hbar\omega_c a^\dagger a$, and the interaction between the exciton system and the bath is given by $\hbar g_c(a^\dagger J_- + aJ_+)$. The other terms in Eq. (A.1) stand for the QD exciton dynamics. Thus, one can suggest that, since the frequencies ω_x, ω_c, and ω, the driving field amplitude g_l, and the QD-cavity coupling g_c can be experimentally tailored, the set-up given here offers a feasible approach for engineering the quantum noise affecting the exciton coherent evolution. Similar results have also been derived for the 3 QD-molecule.

In summary, this appendix has shown that by modifying the photon environment of a QD-molecule with the extra degree of freedom provided by a single-mode cavity field, a further level of exciton entanglement coherent control is accomplished. A remarkable effect, a long time evolution of this entanglement, showing collapses and revivals, is predicted. These results can be easily extended to include non-resonance conditions, and different photon field configurations. A study including losses in the cavity, in addition to the analysis of the strong coupling regime $g_c >> V$, is intended to be published elsewhere [JHR6].

A.2 The QD-microcavity wave function & Bell state generation

Here, the procedure to obtain the wave function (A.2) is outlined. By setting $\omega_x = \omega_c = \omega$; $\hbar = 1$, the system's Hamiltonian yields

$$H(t) = \omega\left(a^\dagger a + J_z\right) + V J_z^2 + g_l\left(\epsilon e^{-i\omega t} J_+ + \epsilon^* e^{i\omega t} J_-\right) + g_c\left(a^\dagger J_- + a J_+\right) \ . \tag{A.3}$$

QD-microcavity wave function: in order to describe the system's time evolution, it will be convenient to move to the interaction picture. Let us first write down

$$H(t) = H_0 + H_0' + H_1(t) \ , \tag{A.4}$$

with

$$\begin{aligned} H_0 &= \omega\left(a^\dagger a + J_z\right) \ , & \text{(A.5)}\\ H_0' &= g_c\left(a^\dagger J_- + a J_+\right) + V J_z^2 \ , & \text{(A.6)}\\ H_1(t) &= g_l\left(\epsilon e^{-i\omega t} J_+ + \epsilon^* e^{i\omega t} J_-\right) \ , & \text{(A.7)} \end{aligned}$$

hence, $H(t)$ can be written in the interaction picture as

$$H_I = e^{iH_0 t}\left[H_0' + H_1(t)\right] e^{-iH_0 t} \ . \tag{A.8}$$

By using the following relations for the quasi-spin and the photon operators

$$\begin{aligned} e^{i\omega J_z t} J_\pm e^{-i\omega J_z t} &= e^{\pm i\omega t} J_\pm \ , & \text{(A.9)}\\ e^{i\omega a^\dagger a t} a e^{-i\omega a^\dagger a t} &= e^{-i\omega t} a \ , & \text{(A.10)}\\ e^{i\omega a^\dagger a t} a^\dagger e^{-i\omega a^\dagger a t} &= e^{i\omega t} a^\dagger \ , & \text{(A.11)} \end{aligned}$$

the following expression for the interaction Hamiltonian H_I arises

$$H_I = g_c\left(a^\dagger J_- + a J_+\right) + V J_z^2 + g_l\left(\epsilon J_+ + \epsilon^* J_-\right) \ . \tag{A.12}$$

Hence, a general state of the QD-cavity system can be written as

$$|\Psi(t)\rangle = \mathrm{e}^{-i\omega t(a^\dagger a + J_z)} U_I(t)\,|\Psi(0)\rangle \ , \tag{A.13}$$

where the operator $U_I(t)$ satisfies

$$i\frac{\partial U_I(t)}{\partial t} = H_I U_I(t) \ . \tag{A.14}$$

Following standard methods of quantum optics [192], the displacement operator $D(\alpha) = \mathrm{e}^{\alpha a^\dagger - \alpha^* a}$ is introduced. This has the following properties:

$$\begin{aligned} D^\dagger(\alpha)\, a D(\alpha) &= a + \alpha \ , && \text{(A.15)}\\ D^\dagger(\alpha)\, a^\dagger D(\alpha) &= a^\dagger + \alpha^* \ , && \text{(A.16)}\\ D(\alpha) D(\beta) &= \mathrm{e}^{(\alpha\beta^* - \alpha^*\beta)/2} D(\alpha+\beta) \ . && \text{(A.17)} \end{aligned}$$

From Eq. (A.17), it follows that the effect of $D(\alpha)$ acting over any coherent state $|\beta\rangle$ is to "displace" such a state to $|\beta+\alpha\rangle$, i.e., $D(\alpha)\,|\beta\rangle = \mathrm{e}^{(\alpha\beta^*-\alpha^*\beta)/2}|\alpha+\beta\rangle$. Let's define

$$U_I(t) = D^\dagger(g_l\epsilon/g_c)\, U_{\text{QD-C}} D(g_l\epsilon/g_c) \ , \tag{A.18}$$

$$H_{\text{QD-C}} = D(g_l\epsilon/g_c)\, H_I D^\dagger(g_l\epsilon/g_c) = g_c(J_+ a + a^\dagger J_-) + V J_z^2 \ . \tag{A.19}$$

It's easy to see that $U_{\text{QD-C}}$ satisfies the differential equation

$$i\frac{\partial U_{\text{QD-C}}}{\partial t} = H_{\text{QD-C}} U_{\text{QD-C}} \ , \tag{A.20}$$

and given that $H_{\text{QD-C}}$ is time-independent, $U_{\text{QD-C}}$ has the following form

$$U_{\text{QD-C}} = \mathrm{e}^{-i\,[g_c(a^\dagger J_- + a J_+) + V J_z^2]\,t} \ . \tag{A.21}$$

Therefore, the general state of the system can be rewritten as:

$$|\Psi(t)\rangle = \mathrm{e}^{-i\omega t(a^\dagger a + J_z)} D^\dagger(g_l\epsilon/g_c)\, \mathrm{e}^{-i\,[g_c(a^\dagger J_- + a J_+) + V J_z^2]\,t} D(g_l\epsilon/g_c)\,|\Psi(0)\rangle \ . \tag{A.22}$$

Collapsing and reviving Bell states: let's outline the procedure to obtain the density of probability of generating Bell states in the driven Jaynes-Cummings system (DJCS) proposed above and give the subsequent characterization of the collapses and revivals experienced by such states. Starting with Eq. (A.22), the energy spectrum and eigenvectors of Eq. (A.19) can be found. There are an infinite number of energies allowed for the system. However, three of them are not dependent on the number of photons in the cavity. The eigenvectors of Eq. (A.19) shall be expanded in the base of the proper functions of J (the angular momentum) and a ($a^\dagger$) (the Fock states). The convention for these energies, and associated proper functions is to be taken as

$$\begin{aligned} e_i &\longrightarrow |e_i\rangle \ , && \text{(A.23)}\\ e_{i,n} &\longrightarrow |e_{i,n}\rangle \ , \end{aligned}$$

with $i = -1, 0, 1$ and $n = 0, 1, \ldots$. The eigenvalues and eigenvectors of Eq. (A.19) must have the following characteristics:

$$\begin{aligned} H_{C-QD}|e_i\rangle &= \mathrm{e}^{ie_it}|e_i\rangle \,, & \text{(A.24)} \\ H_{C-QD}|e_{i,n}\rangle &= \mathrm{e}^{ie_{i,n}t}|e_{i,n}\rangle \,, & \text{(A.25)} \\ \langle e_i|e_j\rangle &= \delta^i_j \,, & \text{(A.26)} \\ \langle e_{i,n}|e_{j,m}\rangle &= \delta^i_j\delta^n_m \,, & \text{(A.27)} \end{aligned}$$

$$\hat{1} = \sum_{i=-1}^{1}\Big(|e_i\rangle\langle e_i| + \sum_{n=0}^{\infty}|e_{i,n}\rangle\langle e_{i,n}|\Big) \,, \tag{A.28}$$

where $\hat{1}$ is the unity matrix. The initial state of the system will be the lowest energy state with α mean number of photons inside the cavity, i.e.,

$$|\Psi\,(t=0)\rangle = |-1, \alpha\rangle \,. \tag{A.29}$$

Next, multiply Eq. (A.22) and Eq. (A.28) to obtain

$$|\Psi\,(t)\rangle = \mathrm{e}^{-i\omega t(a^\dagger a+J_z)}D^\dagger\,(g_l\epsilon/g_c)\,\mathrm{e}^{-i\,[g_c(J_+a+a^\dagger J_-)+VJ_z^2]\,t}\,|-1, g_l\epsilon/g_c+\alpha\rangle \,. \tag{A.30}$$

In order to compute the density of probability of finding the excitonic Bell state $|\Psi_{\text{BELL}}\rangle$ in the coupled QD-microcavity system, we project the general state of the QD on the target state

$$|\Psi_{\text{BELL}}\rangle = \frac{1}{\sqrt{2}}\Big(|-1\rangle + \mathrm{e}^{i\phi}|1\rangle\Big)\otimes|\beta\rangle \,, \tag{A.31}$$

where $|-1\rangle$ is the lowest excitonic energy state, $|1\rangle$ the highest, $|\beta\rangle$ the coherent state of the cavity in which one is trying to find $|\Psi_{\text{BELL}}\rangle$, and ϕ is a phase that defines the particular type of Bell state we are looking for. Let's compute $|\langle\Psi_{\text{BELL}}|\Psi\,(t)\rangle|^2$. In so doing, let's first find $\langle\Psi_{\text{BELL}}|\Psi\,(t)\rangle$. The result is

$$\begin{aligned} \langle\Psi_{\text{BELL}}|\Psi\,(t)\rangle \;&=\; \tfrac{1}{\sqrt{2}}\Big[\Big(\langle -1| + \mathrm{e}^{-i\phi}\langle 1|\Big)\otimes\langle\beta|\Big]\,\mathrm{e}^{-i\omega t(a^\dagger a+J_z)}\,\times \\ &\quad D^\dagger\,(g_l\epsilon/g_c)\,\mathrm{e}^{-i\,[g_c(J_+a+a^\dagger J_-)+VJ_z^2]\,t}\,|-1, g_l\epsilon/g_c+\alpha\rangle \,. \end{aligned} \tag{A.32}$$

It is easy to see that

$$\mathrm{e}^{i\omega t(a^\dagger a+J_z)}\tfrac{1}{\sqrt{2}}\Big(|-1\rangle + \mathrm{e}^{i\phi}|1\rangle\Big)\otimes|\beta\rangle = \Big(\mathrm{e}^{-i\omega t}|-1\rangle + \mathrm{e}^{i\phi}\mathrm{e}^{i\omega t}|1\rangle\Big)\otimes|\mathrm{e}^{i\omega t}\beta\rangle \,, \tag{A.33}$$

and that

$$D\,(g_l\epsilon/g_c)\,|\mathrm{e}^{i\omega t}\beta\rangle = \mathrm{e}^{g_l/g_c\left(\epsilon\beta^*\mathrm{e}^{-i\omega t}-\epsilon^*\beta\mathrm{e}^{i\omega t}\right)}|g_l\epsilon/g_c+\mathrm{e}^{i\omega t}\beta\rangle \,, \tag{A.34}$$

hence, by inserting the two previous equations in Eq. (A.32), and multiplying it by Eq. (A.28), one finds that

$$\begin{aligned} \langle\Psi_{\text{BELL}}|\Psi\,(t)\rangle \;&=\; \tfrac{1}{\sqrt{2}}\mathrm{e}^{g_l/g_c(\epsilon^*\beta\mathrm{e}^{i\omega t}-\epsilon\beta^*\mathrm{e}^{-i\omega t})}\Big(\mathrm{e}^{i\omega t}\langle -1| + \mathrm{e}^{-i\phi}\mathrm{e}^{-i\omega t}\langle 1|\Big)\otimes\langle g_l\epsilon/g_c+\mathrm{e}^{i\omega t}\beta|\otimes \\ &\quad \sum_{i=-1}^{1}\Big(\mathrm{e}^{-ie_it}\langle e_i|-1, g_l\epsilon/g_c+\alpha\rangle|e_i\rangle + \sum_{n=0}^{\infty}\mathrm{e}^{-ie_{i,n}t}\langle e_{i,n}|-1, g_l\epsilon/g_c+\alpha\rangle|e_{i,n}\rangle\Big) \,. \end{aligned} \tag{A.35}$$

Recall some useful relations for inner products between Fock ($|\alpha\rangle$) and number ($|m\rangle$) states:

$$\begin{aligned} \langle\alpha|\alpha'\rangle &= \mathrm{e}^{-\frac{1}{2}|\alpha|^2+\alpha'\alpha^*-\frac{1}{2}|\alpha'|^2} , && \text{(A.36)} \\ \langle\alpha|m\rangle &= \frac{(\alpha^*)^m}{\sqrt{m!}}\mathrm{e}^{-\frac{|\alpha|^2}{2}} . && \text{(A.37)} \end{aligned}$$

The eigenfunctions of Eq. (A.19) are given in terms of the angular momentum and the Fock states basis as

$$\begin{aligned} |e_{-1}\rangle &= |-1,0\rangle , && \text{(A.38)} \\ |e_0\rangle &= d_2|-1,1\rangle + d_0|0,0\rangle , && \text{(A.39)} \\ |e_1\rangle &= d_1|-1,1\rangle + d_4|0,0\rangle , && \text{(A.40)} \\ |e_{i,n}\rangle &= C^i_{1,n}|1,n\rangle + C^i_{2,n}|0,n+1\rangle + C^i_{3,n}|0,n+2\rangle . && \text{(A.41)} \end{aligned}$$

Let's now evaluate the following products:

$$\left(\mathrm{e}^{i\omega t}\langle -1| + \mathrm{e}^{-i\phi}\mathrm{e}^{-i\omega t}\langle 1|\right) \otimes \langle \tfrac{g_l}{g_c}\epsilon + \beta\mathrm{e}^{i\omega t}|e_{-1}\rangle = \mathrm{e}^{i\omega t}\mathrm{e}^{-\frac{1}{2}\left|\frac{g_l}{g_c}\epsilon + \beta\mathrm{e}^{i\omega t}\right|^2} , \qquad \text{(A.42)}$$

$$\left(\mathrm{e}^{i\omega t}\langle -1| + \mathrm{e}^{-i\phi}\mathrm{e}^{-i\omega t}\langle 1|\right) \otimes \langle \tfrac{g_l}{g_c}\epsilon + \beta\mathrm{e}^{i\omega t}|e_0\rangle = d_2\mathrm{e}^{i\omega t}\left(\tfrac{g_l}{g_c}\epsilon^* + \beta^*\mathrm{e}^{-i\omega t}\right)\mathrm{e}^{-\frac{1}{2}\left|\frac{g_l}{g_c}\epsilon + \beta\mathrm{e}^{i\omega t}\right|^2} , \qquad \text{(A.43)}$$

$$\left(\mathrm{e}^{i\omega t}\langle -1| + \mathrm{e}^{-i\phi}\mathrm{e}^{-i\omega t}\langle 1|\right) \otimes \langle \tfrac{g_l}{g_c}\epsilon + \beta\mathrm{e}^{i\omega t}|e_1\rangle = d_1\mathrm{e}^{i\omega t}\left(\tfrac{g_l}{g_c}\epsilon^* + \beta^*\mathrm{e}^{-i\omega t}\right)\mathrm{e}^{-\frac{1}{2}\left|\frac{g_l}{g_c}\epsilon + \beta\mathrm{e}^{i\omega t}\right|^2} , \qquad \text{(A.44)}$$

$$\begin{aligned} &\left(\mathrm{e}^{i\omega t}\langle -1| + \mathrm{e}^{-i\phi}\mathrm{e}^{-i\omega t}\langle 1|\right) \otimes \langle \tfrac{g_l}{g_c}\epsilon + \beta\mathrm{e}^{i\omega t}|e_{i,n}\rangle = \mathrm{e}^{-\frac{1}{2}\left|\frac{g_l}{g_c}\epsilon + \beta\mathrm{e}^{i\omega t}\right|^2} \times \\ &\left[\frac{C^i_{3,n}\mathrm{e}^{i\omega t}}{\sqrt{(n+2)!}}\left(\tfrac{g_l}{g_c}\epsilon^* + \beta^*\mathrm{e}^{-i\omega t}\right)^{n+2} + \frac{C^i_{1,n}\mathrm{e}^{-i\phi}\mathrm{e}^{-i\omega t}}{\sqrt{n!}}\left(\tfrac{g_l}{g_c}\epsilon^* + \beta^*\mathrm{e}^{-i\omega t}\right)^{n}\right] , \qquad \text{(A.45)} \end{aligned}$$

another set of products that must be calculated is

$$\begin{aligned} \langle e_{-1}|-1, g_l\epsilon/g_c + \alpha\rangle &= \mathrm{e}^{-\frac{1}{2}\left|\frac{g_l}{g_c}\epsilon + \alpha\right|^2} && \text{(A.46)} \\ \langle e_0|-1, g_l\epsilon/g_c + \alpha\rangle &= d_2^*\left(g_l\epsilon/g_c + \alpha\right)\mathrm{e}^{-\frac{1}{2}\left|\frac{g_l}{g_c}\epsilon + \alpha\right|^2} && \text{(A.47)} \\ \langle e_1|-1, g_l\epsilon/g_c + \alpha\rangle &= d_1^*\left(g_l\epsilon/g_c + \alpha\right)\mathrm{e}^{-\frac{1}{2}\left|\frac{g_l}{g_c}\epsilon + \alpha\right|^2} && \text{(A.48)} \\ \langle e_{i,n}|-1, g_l\epsilon/g_c + \alpha\rangle &= \frac{\left(C^i_{3,n}\right)^*}{\sqrt{(n+2)!}}\left(g_l\epsilon/g_c + \alpha\right)^{n+2}\mathrm{e}^{-\frac{1}{2}|g_l\epsilon/g_c+\alpha|^2} . && \text{(A.49)} \end{aligned}$$

Putting all the previous equations [Eqs. (A.42) - (A.49)] into Eq. (A.35) and multiplying by its hermitian conjugate, the density of probability of finding the QD in the Bell state

$|\Psi_{\text{BELL}}\rangle$ yields:

$$\begin{aligned}
|\langle\Psi_{\text{BELL}}|\Psi\,(t)\rangle|^2 = {} & \tfrac{1}{2}\mathrm{e}^{-\left|\frac{g_l}{g_c}\epsilon+\alpha\right|^2}\mathrm{e}^{-\left|\frac{g_l}{g_c}\epsilon+\beta\mathrm{e}^{i\omega t}\right|^2}\Bigg|\mathrm{e}^{i\omega t}\Bigg[\mathrm{e}^{-ie_1 t}+\left(\tfrac{g_l}{g_c}\epsilon+\alpha\right)\times \\
& \left(\tfrac{g_l}{g_c}\epsilon^*+\beta^*\mathrm{e}^{-i\omega t}\right)\left(|d_2|^2\mathrm{e}^{-ie_0 t}+|d_1|^2\mathrm{e}^{-ie_1 t}\right)\Bigg]+ \\
& \sum_{i=-1}^{1}\sum_{n=0}^{\infty}\left(\frac{[C^i_{1,n}]^*\mathrm{e}^{-ie_{i,n}t}}{\sqrt{(n+2)!}}\left(\tfrac{g_l}{g_c}\epsilon+\alpha\right)^{n+2}\times\right. \\
& \left.\left[\frac{\mathrm{e}^{i\omega t}C^i_{1,n}}{\sqrt{(n+2)!}}\left(\tfrac{g_l}{g_c}\epsilon^*+\beta^*\mathrm{e}^{-i\omega t}\right)^{n+2}+\frac{\mathrm{e}^{-i\phi}\mathrm{e}^{-i\omega t}C^i_{-1,n}}{\sqrt{n!}}\left(\tfrac{g_l}{g_c}\epsilon^*+\beta^*\mathrm{e}^{-i\omega t}\right)^{n}\right]\right)\Bigg|^2 .
\end{aligned} \tag{A.50}$$

Appendix B

n-dimensional Hilbert space of exciton entanglement

The whole Hilbert space for the $N = 3$ dot problem should include the other two-fold degenerate $J = 1/2$ subspaces. In general, the problem is to be treated in the "λ basis" $\{|J, M; q\rangle\}$. The $N = 3$ QDs case has $|\lambda_i\rangle$ defined as $|\lambda_1\rangle = |3/2, -3/2\rangle$, $|\lambda_2\rangle = |3/2, -1/2\rangle$, $|\lambda_3\rangle = |3/2, 1/2\rangle$, $|\lambda_4\rangle = |3/2, 3/2\rangle$, $|\lambda_5\rangle = |1/2, -1/2; 1\rangle$, $|\lambda_6\rangle = |1/2, 1/2; 1\rangle$, $|\lambda_7\rangle = |1/2, -1/2; 2\rangle$, and $|\lambda_8\rangle = |1/2, 1/2; 2\rangle$. In this basis, the Hamiltonian $\widehat{H}'$ must be written as

$$\begin{pmatrix} \frac{3W}{2} - \frac{3\Delta_\omega}{2} & \sqrt{3}A^* & 0 & 0 & 0 & 0 & 0 & 0 \\ \sqrt{3}A & \frac{7W}{2} - \frac{\Delta_\omega}{2} & 2A^* & 0 & 0 & 0 & 0 & 0 \\ 0 & 2A & \frac{7W}{2} + \frac{\Delta_\omega}{2} & \sqrt{3}A^* & 0 & 0 & 0 & 0 \\ 0 & 0 & \sqrt{3}A & \frac{3W}{2} + \frac{3\Delta_\omega}{2} & 0 & 0 & 0 & 0 \\ 0 & 0 & 0 & 0 & \frac{W}{2} - \frac{\Delta_\omega}{2} & A^* & 0 & 0 \\ 0 & 0 & 0 & 0 & A & \frac{W}{2} + \frac{\Delta_\omega}{2} & 0 & 0 \\ 0 & 0 & 0 & 0 & 0 & 0 & \frac{W}{2} - \frac{\Delta_\omega}{2} & A^* \\ 0 & 0 & 0 & 0 & 0 & 0 & A & \frac{W}{2} + \frac{\Delta_\omega}{2} \end{pmatrix} . \tag{B.1}$$

It is desirable that a given initial condition of the quantum system used as a "hardware" can be expressed in terms of the $\{|m_1, m_2, ..., m_N\rangle\}$ basis, where m_i stands for one of the two Boolean states (e.g., $+$, $-$, or $\uparrow, \downarrow$, etc.) of the ith qubit. For the $N = 3$ QD system[1], let us define the "θ basis" $|m_1, m_2, m_3\rangle$ such that $|\theta_1\rangle = |---\rangle$, $|\theta_2\rangle = |--+\rangle$,

---

[1] For the $N = 2$ QD system, the λ basis $\{|\lambda_i\rangle\} = \{|\lambda_1\rangle = |1, -1\rangle, |\lambda_2\rangle = |1, 0\rangle, |\lambda_3\rangle = |1, 1\rangle, |\lambda_4\rangle = |0, 0\rangle\}$ is related to the $|m_1, m_2\rangle$ ("computational") basis $\{|\theta_1\rangle = |\downarrow\downarrow\rangle, |\theta_2\rangle = |\downarrow\uparrow\rangle, |\theta_3\rangle = |\uparrow\downarrow\rangle, |\theta_4\rangle = |\uparrow\uparrow\rangle\}$ by $|\lambda_1\rangle = |\theta_1\rangle, |\lambda_2\rangle = \frac{1}{\sqrt{2}}(|\theta_2\rangle + |\theta_3\rangle), |\lambda_3\rangle = |\theta_4\rangle, |\lambda_4\rangle = \frac{1}{\sqrt{2}}(|\theta_3\rangle - |\theta_2\rangle)$. Hence, $|\lambda_i\rangle = \sum_j T_{ij}^{(2)} |\theta_j\rangle$, where the matrix elements $T_{ij}^{(2)} = \langle\theta_j|\lambda_i\rangle$ are given by

$$\widehat{T}^{(2)} = \begin{pmatrix} 1 & 0 & 0 & 0 \\ 0 & \frac{1}{\sqrt{2}} & \frac{1}{\sqrt{2}} & 0 \\ 0 & 0 & 0 & 1 \\ 0 & -\frac{1}{\sqrt{2}} & \frac{1}{\sqrt{2}} & 0 \end{pmatrix} . \tag{B.2}$$

$|\theta_3\rangle = |-+-\rangle$, $|\theta_4\rangle = |+--\rangle$, $|\theta_5\rangle = |-++\rangle$, $|\theta_6\rangle = |+-+\rangle$, $|\theta_7\rangle = |++-\rangle$, $|\theta_8\rangle = |+++\rangle$. One can show that the two sets of base kets are related by

$$\begin{aligned}
|\lambda_1\rangle &= |\theta_1\rangle \\
|\lambda_2\rangle &= \tfrac{1}{\sqrt{3}}(|\theta_2\rangle + |\theta_3\rangle + |\theta_4\rangle) \\
|\lambda_3\rangle &= \tfrac{1}{\sqrt{3}}(|\theta_5\rangle + |\theta_6\rangle + |\theta_7\rangle) \\
|\lambda_4\rangle &= |\theta_8\rangle \\
|\lambda_5\rangle &= \tfrac{1}{\sqrt{2}}(|\theta_2\rangle - |\theta_4\rangle) \\
|\lambda_6\rangle &= \tfrac{1}{\sqrt{2}}(|\theta_7\rangle - |\theta_5\rangle) \\
|\lambda_7\rangle &= \tfrac{1}{\sqrt{6}}(|\theta_2\rangle - 2|\theta_3\rangle + |\theta_4\rangle) \\
|\lambda_8\rangle &= \tfrac{1}{\sqrt{6}}(|\theta_5\rangle - 2|\theta_6\rangle + |\theta_7\rangle)\ .
\end{aligned} \tag{B.3}$$

Hence, $|\lambda_i\rangle = \sum_j T_{ij}^{(3)}\,|\theta_j\rangle$, where the elements $T_{ij}^{(3)} = \langle\theta_j|\lambda_i\rangle$ are explicitly given by

$$\widehat{T}^{(3)} = \begin{pmatrix}
1 & 0 & 0 & 0 & 0 & 0 & 0 & 0 \\
0 & \frac{1}{\sqrt{3}} & \frac{1}{\sqrt{3}} & \frac{1}{\sqrt{3}} & 0 & 0 & 0 & 0 \\
0 & 0 & 0 & 0 & \frac{1}{\sqrt{3}} & \frac{1}{\sqrt{3}} & \frac{1}{\sqrt{3}} & 0 \\
0 & 0 & 0 & 0 & 0 & 0 & 0 & 1 \\
0 & \frac{1}{\sqrt{2}} & 0 & -\frac{1}{\sqrt{2}} & 0 & 0 & 0 & 0 \\
0 & 0 & 0 & 0 & -\frac{1}{\sqrt{2}} & 0 & \frac{1}{\sqrt{2}} & 0 \\
0 & \frac{1}{\sqrt{6}} & -\frac{2}{\sqrt{6}} & \frac{1}{\sqrt{6}} & 0 & 0 & 0 & 0 \\
0 & 0 & 0 & 0 & \frac{1}{\sqrt{6}} & -\frac{2}{\sqrt{6}} & \frac{1}{\sqrt{6}} & 0
\end{pmatrix} . \tag{B.4}$$

Thus, if the quantum register input state is given in terms of the θ basis, one can use the transformation matrix $\widehat{T}$ (hereafter the superscript of $\widehat{T}$ shall be omitted) in order to calculate the density of probability for finding exciton entangled states of 3 QDs. The procedure indicated next for the $N = 3$ case applies for any number of quantum dots and any given initial condition. In so doing, let states $|\chi_i\rangle$ be the eigenstates of the Hamiltonian (3.7), with associated eigenenergies E_i. The solution to the quantum dynamical problem can be written as[2]

$$|\Psi(t)\rangle_\Lambda = \sum_i \exp(-iE_it)A_i\,|\chi_i\rangle \equiv \sum_j B_j(t)\,|\lambda_j\rangle\ , \tag{B.5}$$

where $|\chi_i\rangle = \sum_j |\lambda_j\rangle\,\langle\lambda_j|\chi_i\rangle$, i.e., $|\chi_i\rangle = U_{ij}^*\,|\lambda_j\rangle$, with $U_{ij} \equiv \langle\chi_i|\lambda_j\rangle$, and $B_j(t) = \exp(-iE_it)A_iU_{ij}^*$. Hence, it follows that $A_i = \exp(iE_it)\sum_j U_{ij}B_j(t)$. Note that the states $|\chi_i\rangle$ are all in the $|3/2, M\rangle$ subspace for $i = 1, \ldots, 4$, or in the $|1/2, M; 1\rangle$ subspace for $i = 5, 6$, or in $|1/2, M; 2\rangle$ for $i = 7, 8$. Thus, if at $t = 0$ the system is in the initial state $\widehat{B}(0)$, one has $\widehat{A} = \widehat{U}\widehat{B}$.

---

[2] Recall that in the Schrödinger picture, $|\Psi(t)\rangle_S = \Lambda(t)\,|\Psi(t)\rangle_\Lambda$, where $\Lambda(t) = \exp(-i\omega tJ_z)$.

If the initial state is given in terms of the θ basis, the T matrix allows one to express $|\lambda_i\rangle$ in terms of $|\theta_j\rangle$. Suppose that in the θ basis

$$|\Psi(t)\rangle_\Lambda = \sum_i C_i(t)\,|\theta_i\rangle \ , \tag{B.6}$$

and, since in the λ basis one has $|\Psi(t)\rangle_\Lambda = \sum_i B_i(t)\,|\lambda_i\rangle$, it follows that $B_i(t) = \sum_j C_j(t)\langle\lambda_i|\theta_j\rangle = \sum_j C_j(t)T^*_{ij}$. Hence

$$A_i = \exp(iE_it)\sum_k C_k(t)\sum_j U_{ij}T^*_{jk} \equiv \exp(iE_it)\sum_k L_{ik}C_k(t) \ , \tag{B.7}$$

where $L_{ik} = \langle\chi_i|\theta_k\rangle = \sum_j\langle\chi_i|\lambda_j\rangle\langle\lambda_j|\theta_k\rangle$. Thus, given the input state coefficients $C_k(0)$ in the λ basis, one obtains, at $t = 0$, $A_i = \sum_k L_{ik}C_k(0)$. Since the matrix $\widehat{T}$ is to be real, $\langle\lambda_i|\theta_k\rangle = \langle\theta_k|\lambda_i\rangle$, and the only remaining part of the procedure is to determine $\widehat{U}$. It is easy to see that $\widehat{U} = \widehat{V}^\dagger$, where V is the matrix of overlaps $V_{ij} = \langle\lambda_i|\chi_j\rangle$. Thus, $L_{ik} = \sum_j\langle\theta_k|\lambda_j\rangle\langle\lambda_j|\chi_i\rangle^* = \sum_j T_{kj}V^*_{ji}$. For illustrative purposes, let's consider an example. Suppose one wishes the system to be in the maximally entangled GHZ state $|\Psi_{\text{GHZ}}\rangle = \frac{1}{\sqrt{2}}(|\downarrow\rangle\,|\downarrow\rangle\,|\downarrow\rangle - |\uparrow\rangle\,|\uparrow\rangle\,|\uparrow\rangle) \equiv \frac{1}{\sqrt{2}}(|\theta_1\rangle - |\theta_8\rangle)$. Then, the density of probability $|\langle\Psi_{\text{GHZ}}|\Psi(t)\rangle_\Lambda|^2$ must be calculated. In so doing, let's first calculate the overlap $O_{\text{GHZ}}(t) = \langle\Psi_{\text{GHZ}}|\Psi(t)\rangle_\Lambda$. One finds that

$$\begin{aligned} O_{\text{GHZ}}(t) \ &= \ \frac{1}{\sqrt{2}}\sum_{ij}\sum_{mn}\exp(-iE_it)V^*_{mi}T^*_{mn}C_n(0)V_{ji}[\delta_{j1} - \delta_{j4}] = \\ &\quad \frac{1}{\sqrt{2}}\sum_n\sum_{i,m=1}^{4}\exp(-iE_it)V^*_{mi}T^*_{mn}C_n(0)[V_{1i} - V_{4i}] \ . \end{aligned} \tag{B.8}$$

Let's suppose, for example, that $C_n(0) = \delta_{n1}$. Hence

$$O_{\text{GHZ}}(t) = \frac{1}{\sqrt{2}}\sum_{i=1}^{4}\exp(-iE_it)[V^*_{1i}V_{1i} - V^*_{1i}V_{4i}] \ , \tag{B.9}$$

thus, in the rotating frame

$$\left|\langle\Psi_{\text{GHZ}}|\Psi(t)\rangle_\Lambda\right|^2 = \tfrac{1}{2}\sum_{ij}\exp[i(E_j - E_i)t]V^*_{1i}V_{1j}\left\{V_{4i}V^*_{4j} + V_{1i}V^*_{1j} - V_{1i}V^*_{4j} - V_{4i}V^*_{1j}\right\} \ , \tag{B.10}$$

while in the laboratory frame, the above result yields

$$\left|\langle\Psi_{\text{GHZ}}|\Psi(t)\rangle_{\text{S}}\right|^2 = \tfrac{1}{2}\sum_{ij}\exp[i(E_j - E_i)t]V^*_{1i}V_{1j}\left\{V_{4i}V^*_{4j} + V_{1i}V^*_{1j} - \mathrm{e}^{-i3\omega t}V_{1i}V^*_{4j} - \mathrm{e}^{i3\omega t}V_{4i}V^*_{1j}\right\} . \tag{B.11}$$

Next, the Hamiltonian (B.1) is generalised to the case of an N-QD system. Let us concentrate on the non-degenerate $J = N/2$ subspace, whose basis states are $|J = N/2, M\rangle$.

One can show that in this case, the system Hamiltonian adopts the form

$$\begin{pmatrix} -\frac{N\Delta_\omega}{2}+\frac{NW}{2} & \sqrt{N}A^* & 0 & 0 & \cdots \\ \sqrt{N}A & (-\frac{N}{2}+1)\Delta_\omega+(\frac{3N}{2}-1)W & \sqrt{2(N-1)}A^* & 0 & \cdots \\ 0 & \sqrt{2(N-1)}A & (-\frac{N}{2}+2)\Delta_\omega+(\frac{5N}{2}-4)W & \sqrt{3(N-2)}A^* & \cdots \\ 0 & 0 & \sqrt{3(N-2)}A & (-\frac{N}{2}+3)\Delta_\omega+(\frac{7N}{2}-9)W & \cdots \\ 0 & 0 & 0 & \sqrt{4(N-3)}A & \cdots \\ \vdots & \vdots & \vdots & \vdots & \ddots \end{pmatrix}, \tag{B.12}$$

from where the corresponding eigenenergies and eigenfunctions for the N-QD problem can be found.

Appendix C

Single-qubit decoherence

The decoherence rates for a single qubit coupled to a reservoir with $d = 1$, and $d = 3$ density of states are [Eq. (6.21)]

$$\Gamma_1(t,T) = \frac{\alpha_1}{\hbar^2}\int d\omega\, \mathrm{e}^{-\omega/\omega_c}\frac{1-\cos(\omega t)}{\omega}\coth\left(\frac{\omega}{2\omega_T}\right) \tag{C.1}$$

$$\Gamma_3(t,T) = \frac{\alpha_3}{\hbar^2}\int d\omega\, \omega\, \mathrm{e}^{-\omega/\omega_c}[1-\cos(\omega t)]\coth\left(\frac{\omega}{2\omega_T}\right). \tag{C.2}$$

In Subs. 6.2.1 the analytic solutions to these integrals were given. However, a full analysis of those results was not performed. Let us start here by recalling that the solution found for the integral (C.1) was an approximate one, valid only for the low-TE ($\omega_T << \omega_c$): a general solution to this integral requires numerical integration. The second integral was solved analytically for any temperature value T (without making any approximation). In these calculations, note that the constant coupling α_d changes its units with the dimensionality of the field: $[\alpha_1] = [(\mathrm{eV})^2\mathrm{s}^2]$, $[\alpha_3] = [(\mathrm{eV})^2\mathrm{s}^4]$, etc.

Let us first analyse the case $d = 1$. In the low-TE, Eq. (6.22) leads to the identification of three main regimes for the decay of the coherences: (a) a "quiet" regime, for which $t < \tau_c$, and $\Gamma_1(t,T) \approx c_1\omega_c^2 t^2/2$; (b) a "quantum" regime, where $\tau_c < t < \tau_T$, and $\Gamma_1(t,T) \approx c_1\ln(\omega_c t)$; and (c) a "thermal" regime, for which $t >> \tau_T$, and $\Gamma_1(t,T) \approx 2c_1\omega_T t$. These regimes have also been discussed in Refs. [170, 179] and can be easily identified in Fig. C.1 for several different temperatures. Fig. C.1(i) plots Eq. (6.21) as a function of $\omega_c t$ for several different temperatures and for $d = 1$. Since the decoherence effects arising from thermal noise can be separated from the ones due to quantum vacuum fluctuations, we have also plotted these partial contributions in order to see their effects over the time scales involved in the decoherence of the single qubit [Eq. (C.1)]. It can be seen that for a given value of the temperature parameter θ, a characteristic time for which we start observing deviation of coherence from unity is determined by the shortest of the two time scales τ_c and τ_T, and that this value is increased when the temperature T is decreased, as expected.

From Fig. C.1(i.c), it can clearly be seen that at low temperatures, the quantum vacuum fluctuations play the major role in eroding the qubit coherence, while the contribution due to thermal fluctuations plays a minor role. From this plot, we can see the three main regimes indicated above: a quiet ($t < \tau_c$), a quantum ($\tau_c < t < \tau_T$), and a thermal ($t > \tau_T$) regime. In this limit of low-TE, τ_c is the characteristic time that signals the departure of coherence from unity. Here, the qubit dynamics shows a competition between contributions arising from vacuum and thermal fluctuations: even at thermal time scales, the contribution to the decoherence due to vacuum fluctuations remains important.

In the case of the high-TE, the decay due to thermal noise [see dashed line in Fig. C.1(i.a)] becomes more important than the vacuum fluctuation contribution[1] and the start of the decoherence process is ruled by τ_T. Similar conclusions can be obtained from Fig. C.1(ii), where the decay of coherence has been plotted as a function of time, but in units of the thermal frequency ω_T for several different temperatures.

d	c_i	ω_T/ω_c	$\omega_c\tau_{dec}$	$e^{-\Gamma_i(\tau_{dec})}$	$\omega_c t_f$	$e^{-\Gamma_i(t_f)}$
$d=1$	0.25	10^{-5}	0.418831	0.98	273950.34	0.01
	0.25	1.0	0.181611	0.98	6.39891	0.01
	0.1	10^{-5}	0.705612	0.98	1153307.91	0.01
	0.1	1.0	0.291365	0.98	15.19703	0.01
	0.01	10^{-5}	7.47367	0.98	14346140.39	0.01
	0.01	1.0	1.09604	0.98	147.12606	0.01
$d=3$	0.25	10^{-5}	0.167969	0.98	saturates	0.778801
	0.25	1.0	0.154762	0.98	saturates	0.564132
	0.25	10^2	0.020104	0.98	0.318417	0.01
	0.1	10^{-5}	0.275766	0.98	saturates	0.904837
	0.1	1.0	0.251550	0.98	saturates	0.795339
	0.1	10^2	0.031791	0.98	0.546769	0.01
	0.01	10^2	0.101012	0.98	saturates	0.135331

Table C.1: Single-qubit decoherence times for different temperatures, and coupling strength c_i ($i = 1, 3$); for $d = 1$ (Ohmic), and $d = 3$ (super-Ohmic) dimensional density of states of the field.

It can be seen from Table C.1, and Fig. C.1 that t_{decay} is comparable to τ_c for the high-TE, and to τ_T for the low-TE. Indeed, if ω_c is assumed to be the Debye cut-off ($\omega_c \sim 10^{13}$ s^{-1}), we obtain from Table C.1 that for $c_1 = 0.25$, and $T = 1$ mK, the decoherence process starts at $\tau_{dec} \approx 41.9$ fs and lasts for $t_{decay} \approx 27.4$ ns (for $d = 1$). Here, $\omega_T = 1.3 \times 10^{11}\, T \approx 1.3 \times 10^8$ s^{-1}, hence $\tau_T \sim 8$ ns is of the same order of magnitude as t_{decay}. For the super-Ohmic environment $d = 3$ (c_3 and T as before) one obtains $\tau_{dec} \approx 16.8$ fs. In this case, the coherences saturate to a residual value, as discussed below [see Table C.1 and Fig. C.2(ii)]. From Table C.1, the effects of the high-TE can also be seen: the qubit decoheres several orders of magnitude faster than in the low-TE case. For example, for $T = 100$ K, $k_B T > \hbar\omega_c$ ($\hbar\omega_c = 6.58$ meV), hence

---

[1] Over the time scale considered for curve (a) in Fig. C.1(i), the vacuum fluctuation plot overlaps with curve (b), obscuring it from view. The same happens with the vacuum fluctuation contribution associated with curve (b): this gets superposed with curve (c) and neither can be directly observed in Fig. C.1(i).

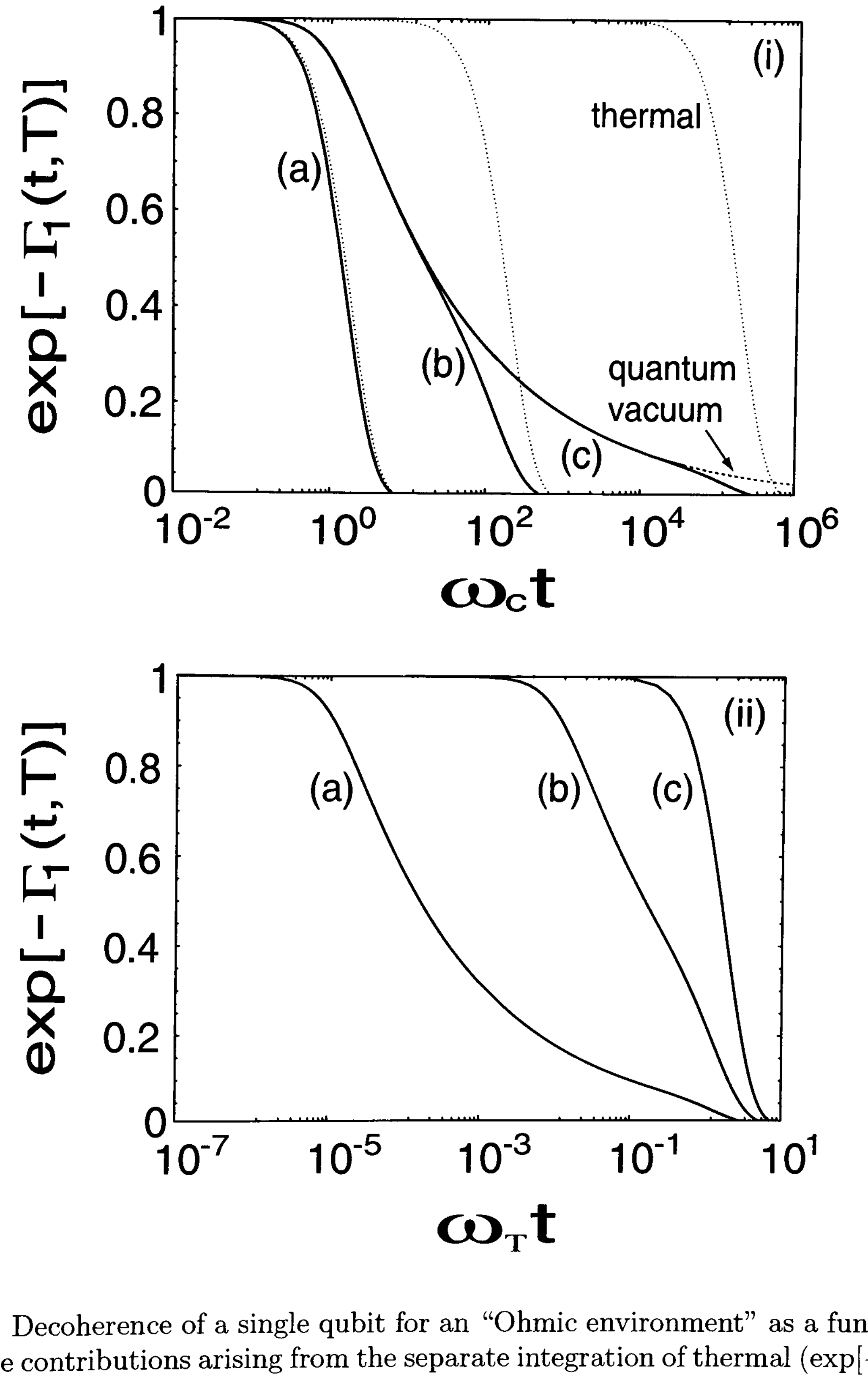

Figure C.1: (i) Decoherence of a single qubit for an "Ohmic environment" as a function of t (in units of ω_c). The contributions arising from the separate integration of thermal ($\exp[-\Gamma_T(t)]$) and vacuum ($\exp[-\Gamma_V(t)]$) fluctuations are shown as dotted curves. $c_1 = 0.25$, (a) $\theta \equiv \omega_T/\omega_c = 1$, (b) 10^{-2}, (c) 10^{-5}. If ω_c is the Debye cutoff, $\theta \approx 10^{-2}\ T$ (see text): the decoherence shown corresponds to $T = 100$ K, $T = 1$ K, and $T = 1$ mK, respectively. (ii) Coherence decay for (a) $\theta = 10^{-5}$, (b) 10^{-2}, (c) 10^{2}. $c_1 = 0.25$. Here, time is given in units of the thermal frequency $\omega_T \equiv k_B T/\hbar$.

$\tau_{dec} \approx 18.1$ fs, and $t_{decay} \approx 0.6$ ps ($c_1 = 0.25$, $d = 1$). A similar behaviour is also observed in the $d = 3$ case.

Table C.1 shows the effect of the coupling strength on the decoherence time scales. Let $c_1 = 0.01$ ($d = 1$), hence, for i) $T = 1$ mK, $\tau_{dec} \approx 0.75$ ps, and $t_{decay} \approx 1.4$ μs; for ii) $T = 100$ K, $\tau_{dec} \approx 0.11$ ps, and $t_{decay} \approx 14.6$ ps. Hence the weaker the coupling between the qubit and the environment, the longer the decoherence times and the slower the duration of the decoherence process. This result also holds for the case $d = 3$, as can be seen from Table C.1. All of the above analysis concerning the different regimes for the decay of the coherences presented here is explicitly illustrated in the three-dimensional plots of Fig. C.2.

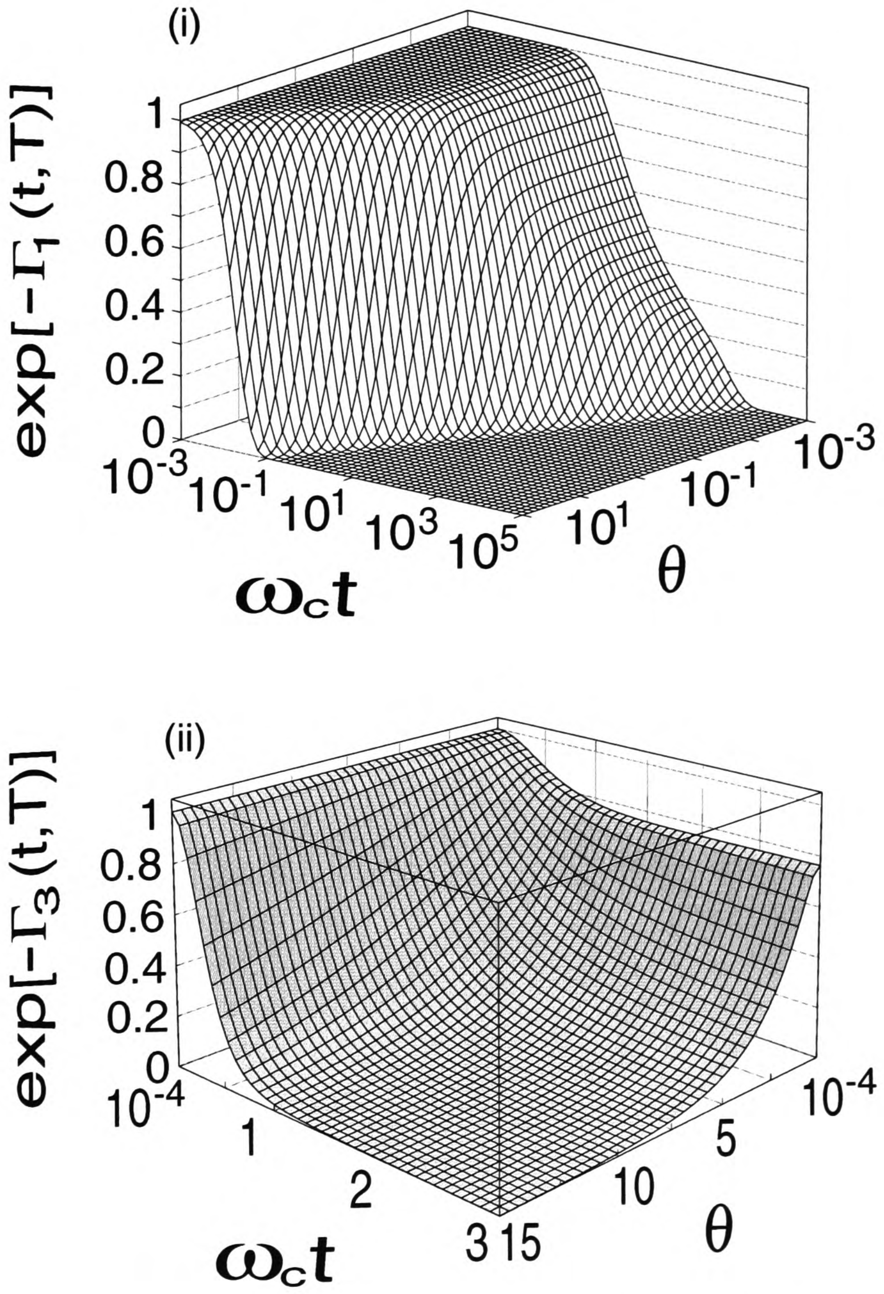

Figure C.2: Decoherence of a single qubit for (i) $d = 1$, and (ii) $d = 3$, as a function of time (in units of the cut-off ω_c) and the temperature parameter $\theta \equiv \omega_T/\omega_c$. $c_1 = c_3 = 0.25$. If ω_c is the Debye cut-off, the range of coherence decay goes from a few mK up to (a) 10^4 K [plot (i)] and (b) 1.5×10^3 K [plot (ii)].

Next, the decoherence behaviour of the single qubit when coupling to the super-Ohmic $d = 3$ reservoir is analysed. The corresponding decoherence function is given by Eq. (6.23). As can be seen from Fig. C.2(ii) and Table C.1, this case shows an interesting behaviour for the coherence decay: once the end of the 'quiet' regime has been reached, the coherences decay to either zero, as in the case of Fig. C.2(i), or saturate to a particular value determined by the temperature parameter ω_T/ω_c. Here, the particular temperature value for which no saturation occurs at all and the expected decoherence takes place can be identified. Table C.1 gives some saturation values for different temperatures and coupling strengths c_3. For $c_3 = 0.1$, and 0.25, the temperature value for which any residual coherence vanishes falls in the interval $10 < \theta < 100$ (high-TE). Apparently, these residual values shown in Fig. C.2(ii) and Table C.1 vanish when additional frequency modes associated with the three-dimensionality of the field are taken into account [170]. Even if this is not the case, the effects of relaxation mechanisms would mark the extent of these residual values.

Appendix D

Time evolution and the reduced density matrix

This Appendix gives details of the main steps followed in the calculation of the reduced density matrix given by Eq. (6.11).

D.1 The time evolution operator $U_I(t)$

Since Eq. (6.3) gives $H_I(t) = \sum_{n,\boldsymbol{k}} J_z^n (g_{\boldsymbol{k}}^n \,\mathrm{e}^{i\omega_k t}\, b_{\boldsymbol{k}}^\dagger + g_{\boldsymbol{k}}^{*n}\, \mathrm{e}^{-i\omega_k t}\, b_{\boldsymbol{k}})$, the time evolution operator can be written as

$$U_I(t) = T \exp\left(-\frac{i}{\hbar} \int_o^t \sum_{\boldsymbol{k}} g_{\boldsymbol{k}} \Big[\mathrm{e}^{i\omega_k t'} J_z^{\boldsymbol{k}}\, b_{\boldsymbol{k}}^\dagger + \mathrm{e}^{-i\omega_k t'} J_z^{\dagger\boldsymbol{k}}\, b_{\boldsymbol{k}} \Big] dt' \right) , \tag{D.1}$$

where the shorthand notation $J_z^{\boldsymbol{k}} = \sum_n \mathrm{e}^{-i\boldsymbol{k}\cdot\boldsymbol{r}_n} J_z^n$ has been introduced. Hence, one can rewrite Eq. (D.1) as [180]

$$\begin{aligned} U_I(t) \;=\;& \exp\left(\sum_{\boldsymbol{k}} g_{\boldsymbol{k}} \varphi_{\omega_k}(t) J_z^{\boldsymbol{k}}\, b_{\boldsymbol{k}}^\dagger \right) T \exp\left[-\frac{i}{\hbar} \int_o^{t'} dt' \sum_{\boldsymbol{k}} \mathrm{e}^{-i\omega_k t'} \times \right. \\ & \left. \exp\left(-\sum_{\boldsymbol{k'}} g_{\boldsymbol{k'}} \varphi_{\omega_{k'}}(t') J_z^{\boldsymbol{k'}}\, b_{\boldsymbol{k'}}^\dagger \right) g_{\boldsymbol{k}} J_z^{\dagger\boldsymbol{k}}\, b_{\boldsymbol{k}} \exp\left(\sum_{\boldsymbol{k'}} g_{\boldsymbol{k'}} \varphi_{\omega_{k'}}(t') J_z^{\boldsymbol{k'}}\, b_{\boldsymbol{k'}}^\dagger \right) \right] . \end{aligned} \tag{D.2}$$

It is easy to show that the calculation of the product given by the second line of Eq. (D.2) gives the result

$$g_{\boldsymbol{k}} J_z^{\dagger\boldsymbol{k}} \Big[\, b_{\boldsymbol{k}} + g_{\boldsymbol{k}} \varphi_{\omega_k}(t) J_z^{\boldsymbol{k}} \Big] . \tag{D.3}$$

Hence, the following expression for $U_I(t)$ arises

$$\begin{aligned} U_I(t) \;=\;& \exp\left(\sum_{\boldsymbol{k}} g_{\boldsymbol{k}} \varphi_{\omega_k}(t) J_z^{\boldsymbol{k}}\, b_{\boldsymbol{k}}^\dagger \right) \exp\left(-\sum_{\boldsymbol{k}} g_{\boldsymbol{k}} \varphi_{\omega_k}^*(t) J_z^{\dagger\boldsymbol{k}}\, b_{\boldsymbol{k}} \right) \times \\ & \exp\left(-\frac{i}{\hbar} \sum_{\boldsymbol{k}} \left| g_{\boldsymbol{k}} J_z^{\boldsymbol{k}} \right|^2 \int_o^t dt' \varphi_{\omega_k}(t') \mathrm{e}^{-i\omega_k t'} \right) = \end{aligned}$$

$$\exp\left(\sum_{\boldsymbol{k}} g_{\boldsymbol{k}}\Big[\varphi_{\omega_k}(t) J_z^{\boldsymbol{k}}\, b_{\boldsymbol{k}}^{\dagger} - \varphi_{\omega_k}^{*}(t) J_z^{\dagger \boldsymbol{k}}\, b_{\boldsymbol{k}}\Big]\right) \times$$
$$\exp\left(\sum_{\boldsymbol{k}} \left|g_{\boldsymbol{k}} J_z^{\boldsymbol{k}}\right|^2 \left[\frac{it}{\hbar^2\omega_k} - \frac{\varphi_{\omega_k}^{*}(t)}{\hbar\omega_k} + \frac{|\varphi_{\omega_k}(t)|^2}{2}\right]\right), \tag{D.4}$$

where the result $\mathrm{e}^{A+B} = \mathrm{e}^{A}\mathrm{e}^{B}\mathrm{e}^{-[A,B]/2}$, which holds for any pair of operators A, B that satisfy $[A,[A,B]] = 0 = [B,[A,B]]$ has been used. It is straightforward to see that Eq. (D.4) gives the final result

$$U_I(t) = \exp\left(i\sum_{\boldsymbol{k}} |g_{\boldsymbol{k}}|^2 \frac{\omega_k t - \sin(\omega_k t)}{(\hbar\omega_k)^2} J_z^{\dagger\boldsymbol{k}} J_z^{\boldsymbol{k}}\right) \exp\left(\sum_{\boldsymbol{k}} \left\{A_{\boldsymbol{k}}^{\dagger}(t) - A_{\boldsymbol{k}}(t)\right\}\right), \tag{D.5}$$

where $A_{\boldsymbol{k}}(t) = g_{\boldsymbol{k}}^{*}\varphi_{\omega_k}^{*}(t) J_z^{\dagger\boldsymbol{k}} b_{\boldsymbol{k}}$.

D.2 The reduced density matrix of a L-qubit register

Next, the result for $U_I(t)$ is used in order to calculate the decay of coherences, i.e., $\mathrm{Tr}_B[\rho^B(0) U_I^{\dagger\{j_n\}}(t) U_I^{\{i_n\}}(t)]$, with $U_I^{\{i_n\}}(t)$ as defined in Eq. (6.10). In so doing, we first compute the operator algebra for the product $U_I^{\dagger\{j_n\}}(t) U_I^{\{i_n\}}(t)$ by taking into account the expression (D.5). The result gives

$$U_I^{\dagger\{j_n\}}(t) U_I^{\{i_n\}}(t) = \exp\left[i\sum_{\boldsymbol{k}} |g_{\boldsymbol{k}}|^2 \frac{\omega_k t - \sin(\omega_k t)}{(\hbar\omega_k)^2} \sum_{m,n} (i_m i_n - j_m j_n)\cos(\boldsymbol{k}\cdot\boldsymbol{r}_{mn})\right] \times$$
$$\exp\left[i\sum_{\boldsymbol{k}} |g_{\boldsymbol{k}}\varphi_{\omega_k}(t)|^2 \sum_{m,n} i_m j_n \sin(\boldsymbol{k}\cdot\boldsymbol{r}_{mn})\right] \exp\left[\sum_{\boldsymbol{k}} \left\{\sigma_{\boldsymbol{k}} b_{\boldsymbol{k}}^{\dagger} - \sigma_{\boldsymbol{k}}^{*} b_{\boldsymbol{k}}\right\}\right], \tag{D.6}$$

where $\sigma_{\boldsymbol{k}} \equiv g_{\boldsymbol{k}}\varphi_{\omega_k}(t)\sum_m (i_m - j_m)\mathrm{e}^{-i\boldsymbol{k}\cdot\boldsymbol{r}_m}$. From the above equation, note that the first two exponential terms commute, hence one only needs to take the trace over the third term. By doing this (see e.g., Ref. [176]), the following result is obtained

$$\mathrm{Tr}_B\left[\rho^B(0)\exp\left(\sum_{\boldsymbol{k}} \left\{\sigma_{\boldsymbol{k}} b_{\boldsymbol{k}}^{\dagger} - \sigma_{\boldsymbol{k}}^{*} b_{\boldsymbol{k}}\right\}\right)\right] = \prod_{\boldsymbol{k}} \exp\left(-|g_{\boldsymbol{k}}|^2 \frac{1-\cos(\omega_k t)}{(\hbar\omega_k)^2} \coth\left(\frac{\hbar\omega_k}{2k_B T}\right) \times \right.$$
$$\left.\sum_{m,n} (i_m - j_m)(i_n - j_n)\cos(\boldsymbol{k}\cdot\boldsymbol{r}_{mn})\right), \tag{D.7}$$

from where Eq. (6.11) immediately arises.

Bibliography

[1] B. d'Espagnat, *Conceptual Foundations of Quantum Mechanics*, Benjamin, Reading, Massachusetts (1976).

[2] A. Peres, *Quantum Mechanics: Concepts and Methods*, Kluwer, Dordrecht (1993).

[3] N.D. Mermin, Physics Today **38** (4), 38 (1985).

[4] A. Einstein, B. Podolsky, and N. Rosen, Phys. Rev. **47**, 777 (1935).

[5] E. Schrödinger: Natürwissenschaften **23**, 807 (1935).

[6] Useful reviews of the subject of quantum information and quantum computation can be found in C.H. Bennett, and D.P. DiVincenzo, Nature **404**, 247 (2000); A. Ekert, P. Hayden, and H. Inamori preprint at quant-ph/0011013; A. Steane, Rep. Prog. Phys. **61**, 117 (1998); C.H. Bennett, Physics Today **48** (10), 24 (1995). See also the special issue of Physics World, March (1998). Note that most of the literature in the field can be found at the Los Alamos National Laboratory e-print archive, http://xxx.lanl.gov/archive/quant-ph.

[7] J.S. Bell, Physics **1**, 195 (1964); J.S. Bell, *Speakable and Unspeakable in Quantum Mechanics*, Cambridge University Press (1987).

[8] A. Aspect, J. Dalibard, and G. Roger, Phys. Rev. Lett. **49**, 1804 (1982).

[9] F. Selleri, *Quantum Paradoxes and Physical Reality*, Kluwer, Dordretch (1989); W. Tittel *et al.*, Phys. Rev. Lett. **81**, 3563 (1998); G. Weihs *et al.*, Phys. Rev. Lett. **81**, 5039 (1998).

[10] R.P. Feynman, Int. J. Theor. Phys. **21**, 467 (1982); Opt. News **11**, 11 (1985).

[11] P. Benioff, Phys. Rev. Lett. **48**, 1581 (1982); J. Stat. Phys. **29**, 515 (1982).

[12] D. Deutsch, Proc. R. Soc. London A **400**, 97 (1985).

[13] A.K. Ekert, Phys. Rev. Lett. **67**, 661 (1991); C.H. Bennett, G. Brassard, and N.D. Mermin, *ibid.* **68**, 557 (1992); C.H. Bennett, G. Brassard, and A. Ekert, Scientific American **267** 4, 26 (1992).

[14] C.H. Bennett, G. Brassard, C. Crépeau, R. Jozsa, A. Peres, and W.K. Wooters, Phys. Rev. Lett. **70**, 1895 (1993).

[15] C.H. Bennett and S.J. Wiesner, Phys. Rev. Lett. **69**, 2881 (1992); A. Barenco and A. Ekert, J. Mod. Opt. **42**, 1253 (1995).

[16] D.A. Meyer, Phys. Rev. Lett. **82**, 1052 (1999); quant-ph/0004092 and references therein.

[17] J. Eisert, M. Wilkens, and M. Lewenstein, Phys. Rev. Lett. **83**, 3077 (1999). See also quant-ph/0004076.

[18] S. Benjamin and P. Hayden quant-ph/0007038; quant-ph/0003036.

[19] D. Deutsch and R. Josza, Proc. R. Soc. London A **439**, 553 (1992).

[20] D.R. Simon, in *Proceedings of the 35th Annual Symposium on the Foundations of Computer Science*, ed. by S. Goldwasser (IEEE Computer Society, Santa Fe, Los Alamitos, CA), pp. 116 (1994).

[21] P.W. Shor, in *Proceedings of the 35th Annual Symposium on the Foundations of Computer Science*, ed. by S. Goldwasser (IEEE Computer Society, Santa Fe, Los Alamitos, CA), pp. 124 (1994). A revised version can be found at http://xxx.lanl.gov/archive/quant-ph/9508027.

[22] L.K. Grover, Phys. Rev. Lett. **79**, 325 (1997).

[23] A. Ekert and R. Jozsa, Rev. Mod. Phys. **68**, 733 (1996).

[24] R. Cleve, A. Ekert, C. Macchiavello and M. Mosca, Proc. R. Soc. Lond. A **454** 339 (1998).

[25] P.W. Shor, Phys. Rev. A **52**, R2493 (1995).

[26] A.M. Steane, Phys. Rev. Lett. **77**, 793 (1996); Proc. R. Soc. Lond. A **452**, 2551 (1996); Phys. Rev. A **54**, 4741 (1996).

[27] J.I. Cirac and P. Zoller, Phys. Rev. Lett. **74**, 4091 (1995); J.I. Cirac and P. Zoller, Nature **404**, 579 (2000).

[28] C. Monroe, D.M. Meekhof, B.E. King, W.M. Itano, and D.J. Wineland, Phys. Rev. Lett. **75**, 4714 (1995).

[29] K. Molmer and A. Sorensen, Phys. Rev. Lett. **82**, 1835 (1999); C.A. Sackett *et al.*, Nature **393**, 133 (2000).

[30] T. Pellizzari, S.A. Gardiner, J.I. Cirac, and P. Zoller, Phys. Rev. Lett. **75**, 3788 (1995).

[31] Q.A. Turchete, C.J. Hood, W. Lange, H. Mabuchi, and H.J. Kimble, Phys. Rev. Lett. **75**, 4710 (1995).

[32] J.I. Cirac, T. Pellizari, and P. Zoller, Science **273**, 1207 (1996).

[33] J.I. Cirac, P. Zoller, H.J. Kimble, and H. Mabuchi, Phys. Rev. Lett. **78**, 3221 (1997).

[34] A. Imamoglu *et al.*, Phys. Rev. Lett. **83**, 4204 (1999).

[35] A. Rauschenbeutel *et al.*, Phys. Rev. Lett. **83**, 5166 (1999); Phys. Rev. A **64**, 050301(R) (2001).

[36] N.A. Gershenfeld and I.L. Chuang, Science **275**, 350 (1997); I.L. Chuang, N. Gershenfeld, and M. Kubinec, Phys. Rev. Lett. **80**, 3408 (1998); I.L. Chuang *et al.*, Nature **393**, 143 (1998).

[37] D.G. Cory, A.F. Fahmy, and T.F. Havel, Proc. Natn. Acad. Sci. USA **94**, 1634 (1997).

[38] E. Knill, I.L. Chuang, and R. Laflamme, Phys. Rev. A **57**, 3348 (1998).

[39] J.A. Jones, M. Mosca, and R.H. Hansen, Nature **393** , 344 (1998); J.A. Jones and M. Mosca, J. Chem. Phys. **109**, 1648 (1998).

[40] L.M.K. Vandersypen *et al.*, Nature **414**, 883 (2001).

[41] B.E. Kane, Nature **393**, 133 (1998).

[42] G.K. Brennen *et al.*, Phys. Rev. Lett. **82**, 1060 (1999).

[43] D. Jacksch *et al.*, Phys. Rev. Lett. **82**, 1975 (1999).

[44] M. Greiner *et al.*, Nature **415**, 39 (2002).

[45] A. Shnirman, G. Schön, and Z. Hermon, Phys. Rev. Lett. **79**, 2371 (1997); Y. Makhlin, G. Schön, and A. Shnirman, Nature **398**, 305 (1999).

[46] D.V. Averin, Solid State Commun. **105** , 659 (1998).

[47] Y. Nakamura, Yu.A. Pashkin, and J.S. Tsai, Nature **398**, 786 (1999).

[48] C.H. van der Wal *et al.*, Science **290**, 773 (2000).

[49] A. Barenco, D. Deutsch, A. Ekert, and R. Jozsa, Phys. Rev. Lett. **74**, 4083 (1995).

[50] V. Privman, L.D. Vagner, and G. Kventsel, Phys. Lett. A **239**, 141 (1998).

[51] D. Loss, and D.P. DiVincenzo, Phys. Rev. A **57**, 120 (1998); G. Burkard, D. Loss, and D.P. DiVincenzo, Phys. Rev. B **59**, 2070 (1999).

[52] R. Vrijen *et al.*, Phys. Rev. A **62**, 012306 (2000).

[JHR1] J.H. Reina, L. Quiroga, and N.F. Johnson, Phys. Rev. A **62**, 12305 (2000).

[53] L. Quiroga and N.F. Johnson, Phys. Rev. Lett. **83**, 2270 (1999).

[JHR2] J.H. Reina, L. Quiroga, and N.F. Johnson, Phys. Rev. B **62**, 2267(R) (2000).

[54] E. Biolatti *et al.*, Phys. Rev. Lett. **85**, 5647 (2000).

[55] F. Troiani *et al.*, Phys. Rev. B **62**, 2263(R) (2000).

[56] D.M. Greenberger, M.A. Horne, and A. Zeilinger, in *Bell's theorem, Quantum Theory and Conceptions of the Universe*, ed. M. Kafatos, pp. 73, Kluwer, Dordrecht, The Netherlands (1989); D.M. Greenberger, M.A. Horne, A. Shimony, and A. Zeilinger, Am. J. Phys. **58**, 1131 (1990).

[57] M.A. Kastner, Physics Today, January, pp. 24 (1993); M.A. Reed, Scientific American, January, pp. 98 (1993).

[58] C. Weisbuch and B. Vinter, *Quantum Semiconductor Structures: Fundamentals and Applications*, Academic Press (1991); L. Jacak, P. Hawrylak, and W. Jójs, *Quantum Dots*, Springer-Verlag, Berlin Heidelberg (1998).

[59] For a review see, e.g., N.F. Johnson, J. Phys: Condens. Matter **7**, 965 (1995), and references therein.

[60] J.R. Guest *et al.*, Science **293**, 2224 (2001).

[61] N.H. Bonadeo, J. Erland, D. Gammon, D.S. Katzer, D. Park, and D.G. Steel, Science **282**, 1473 (1998).

[62] N.H. Bonadeo, G. Chen, D. Gammon, D.S. Katzer, D. Park, and D.G. Steel, Phys. Rev. Lett. **81**, 2759 (1998).

[63] G. Bartels *et al.*, Phys. Rev. Lett. **81**, 5880 (1998).

[64] A. Chavez-Pirson, J. Temmyo, H. Kamada, H. Gotoh, and H. Ando, Appl. Phys. Lett. **72**, 3494 (1998).

[65] H. Kamada *et al.*, Phys. Rev. Lett. **87**, 246401 (2001).

[66] P. Borri *et al.*, Phys. Rev. Lett. **87**, 157401 (2001).

[67] D. Birkedal, K. Leosson, and J.M. Hvam, Phys. Rev. Lett. **87**, 227401 (2001).

[68] W. Kohn, Phys. Rev. **123**, 1242 (1961).

[69] T. Förster, Ann. Phys. (Leipzig) **2**, 55 (1948).

[70] X. Hu and K. Schulten, Physics Today, pp. 28, August (1997); Biophys. J. **75**, 683 (1998); X. Hu *et al.*, Proc. Natl. Acad. Sci. USA **95**, 5935 (1998).

[71] H. Sumi, J. Phys. Chem. B **103**, 252 (1999); T. Ritz *et al.*, Journal of Luminescence **76**, 310 (1998); X. Hu *et al.*, J. Phys. Chem. B **101**, 3854 (1997).

[72] P. Andrew and W.L. Barnes, Science **290**, 785 (2000).

[73] D. Dexter, J. Chem. Phys. **21**, 836 (1953).

[74] A.M. van Oijen *et al.*, Science **285**, 400 (1999).

[75] P. Michler *et al.*, Nature **406**, 968 (2000).

[76] B. Lounis and W.E. Moerner, Nature **407**, 491 (2000); C. Brunel *et al.*, Phys. Rev. Lett. **83**, 2722 (1999).

[77] P. Michler *et al.*, Science **290**, 2282 (2000).

[78] C. Santori *et al.*, Phys. Rev. Lett. **86**, 1502 (2001).

[79] D.V. Regelman *et al.*, Phys. Rev. Lett. **87**, 257401 (2001).

[80] C. Santori *et al.*, preprint at cond-mat/0111242.

[81] B.W. Schumacher, Phys. Rev. A **51** 2738 (1995).

[82] B.W. Schumacher and M.A. Nielsen, Phys. Rev. A **54**, 2629 (1996).

[83] D. Deutsch, Proc. R. Soc. Lond. A **425**, 73 (1989).

[84] D. Deutsch, A. Barenco and A. Ekert, Proc. R. Soc. Lond. A **449**, 669 (1995).

[85] A. Barenco, Proc. R. Soc. Lond. A **449**, 679 (1995).

[86] D.P. DiVincenzo, Phys. Rev. A **51**, 1015 (1995).

[87] S. Lloyd, Phys. Rev. Lett. **75**, 346 (1995).

[88] A. Barenco *et al.*, Phys. Rev. A **52**, 3457 (1995).

[89] V. Vedral, A. Barenco and A. Ekert, Phys. Rev. A **54**, 147 (1995).

[90] W. K. Wootters and W. H. Zurek, Nature **299**, 802 (1982).

[91] T. Toffoli, *Automata, Languages, and Programming, 7th Colloqium*, Lecture Notes in Computer Science 84, pp 632, eds. J.W. de Bakker and J van Leeuwen, Springer (Berlin) (1980).

[92] M.V. Berry, Proc. Roy. Soc. A **392**, 45 (1984).

[93] F. Wilczek and A. Zee, Phys. Rev. Lett. **52**, 2111 (1984).

[94] A. Shapere and F. Wilczek, *Geometric Phases in Physics*, World Scientific, Singapore (1989).

[95] P. Zanardi, M. Rasetti, Phys. Lett. A **264**, 94 (1999).

[96] J. Pachos, P. Zanardi, and M. Rasetti, Phys. Rev. A **61**, 010305(R) (2000); J. Pachos, S. Chountasis, Phys. Rev. A **62**, 052318 (2000).

[97] A. Ekert *et al.*, J. Mod. Opt. **47**, 2501 (2000).

[98] A. Galindo and P. Pascual, *Quantum Mechanics II*, Springer-Verlag (1990).

[99] J. A. Jones, V. Vedral, A. Ekert, and G. Castagnoli, Nature **403**, 869 (2000).

[100] G. Falci *et al.*, Nature **407**, 355 (2000).

[101] L.-M. Duan, J.I. Cirac, and P. Zoller, Science **292**, 1695 (2001).

[102] W. Xiang-Bin and M. Keiji, Phys. Rev. Lett. **87**, 097901 (2001). See also quant-ph/0112071.

[103] M. Horodecki, P. Horodecki, and R. Horodecki, in *Quantum Information: An Introduction to Basic Theoretical Concepts and Experiments*, Springer Tracts in Modern Physics, July (2001).

[104] A. Ekert and R. Josza, Phil. Trans. R. Soc. Lond. A **356**, 1769 (1998).

[105] R. F. Werner, Phys. Rev. A **40**, 4277 (1989).

[106] S. Popescu, Phys. Rev. Lett. **72**, 797 (1994).

[107] S. Popescu, Phys. Rev. Lett. **74**, 2619 (1995).

[108] M. Żukowski, R. Horodecki, M. Horodecki and P. Horodecki: Phys. Rev. A **58**, 1964 (1998).

[109] A. Peres, Phys. Rev. Lett. **77**, 1413 (1996); Found. Phys. **29**, 589 (1999).

[110] C. H. Bennett and G. Brassard, *Proc. IEEE Int. Conference on Computers, Systems and Signal Processing*, IEEE, New York, (1984).

[111] D. Mayers, preprint at quant-ph/9802025.

[112] H.-K. Lo and H.F. Chau, Science **283**, 2050 (1999).

[113] C. H. Bennett and G. Brassard, SIGACT news, **20**, 78 (1989); R.J. Hughes *et al.*, Contemp. Phys. **36**, 149 (1995); S.J.D. Phoenix and P.D. Townsend, *et al.*, Contemp. Phys. **36**, 165 (1995); H. Zbinden *et al.*, Electron. Lett. **33**, 586 (1997).

[114] R. Jozsa and B. Schumacher, J. Mod. Optics **41**, 2343 (1994).

[115] R. L. Rivest, A. Shamir and L. M. Adleman, *Communication of the ACM* **21**, 120 (1978); C. Cocks, *Tech. report* Communications-Electronics Security Group, United Kingdom (1973).

[116] J. von Neumann and O. Morgenstern, *Theory of Games and Economic Behavior*, third edition, Princeton University Press (1953).

[117] See, e.g., http://www.unifr.ch/econophysics/minority/.

[118] W.H. Zurek, Physics Today **44**(10), 36 (1991).

[119] R. Calderbank and P. W. Shor, *Phys. Rev. A* **54**, 1098 (1996).

[120] A. Ekert and C. Macchiavello, Phys. Rev. Lett. **77**, 2585 (1996).

[121] R. Laflamme, C. Miquel, J.P. Paz and W.H. Zurek, Phys. Rev. Lett. **77**, 198 (1996).

[122] C.H. Bennett *et al.*, Phys. Rev. A **54**, 3825 (1996).

[123] D. Gottesman, Phys. Rev. A **54**, 1862 (1996).

[124] E. Knill and R. Laflamme, Phys. Rev. A **55**, 900 (1997).

[125] A.R. Calderbank, E.M. Rains, P.W. Shor and N.J.A. Sloane, Phys. Rev. Lett. **78**, 405 (1997).

[126] P.W. Shor, Preprint at quant-ph/9605011.

[127] A. Yu Kitaev, Preprint at quant-ph/9707021.

[128] A.M. Steane, Phys. Rev. Lett. **78**, 2252 (1997).

[129] J. Preskill, Proc. R. Soc. Lond. A **452**, 567 (1998); Proc. R. Soc. Lond. A, **454**, 385 (1998).

[130] K. Obermayer, W.G. Teich and G. Mahler, Phys. Rev. B **37**, 8111 (1988).

[131] X. Hu and K. Schulten, Physics Today, pp. 28, August (1997).

[JHR3] J.H. Reina and N.F. Johnson, Phys. Rev. A **63**, 012303 (2000).

[JHR4] J.H. Reina, L. Quiroga, and N.F. Johnson, invited chapter, *Proceedings of the ISI-Accademia dei Lincei Conference* on "Conventional and Non Conventional Computing (Quantum and DNA)," Springer Verlag.

[JHR5] J.H. Reina, L. Quiroga, and N.F. Johnson, Phys. Rev. A **65**, 0323xx (2002), in press.

[132] A. Wokaun and R.R. Ernst, J. Chem. Phys. **67**, 1752 (1977).

[133] S. Vega, J. Chem. Phys. **68**, 5518 (1978).

[134] F.J. Rodríguez, L. Quiroga, and N.F. Johnson, Phys. Stat. Sol.(a) **178**, 403 (2000).

[135] D. Bowmeester, J.W. Pan, K. Mattle, M. Eibl, H. Weinfurter and A. Zeilinger, Nature **390,** 575 (1997).

[136] D. Boschi, S. Branca, F. De Martini, L. Hardy and S. Popescu, Phys. Rev. Lett., **80**, 1121 (1998).

[137] A. Furusawa, J.L. Sorensen, S.L. Braunstein, C.A. Fuchs, H.J. Kimble and E.S. Polzik, Science **282**, 706 (1998).

[138] M.A. Nielsen, E. Knill and R. Laflamme, Nature **396**, 52 (1998).

[139] S.L. Braunstein, A. Mann and M. Revzen, Phys. Rev. Lett. **68**, 3259 (1992).

[140] N.F. Johnson, J. Phys.: Cond. Matt. **7**, 965 (1995).

[141] G. Brassard, S.L. Braunstein and R. Cleve, Physica D **120**, 43 (1998).

[142] R.B. Griffiths and C.-S. Niu, Phys. Rev. Lett. **76**, 17 (1996).

[143] See e.g., V.M. Agranovich, D.M. Basko, G.C. La Rocca, and F. Bassani, J.Phys.: Condens. Matter **10**, 9369 (1998); Phys. Stat. Sol. (a) **178**, 69 (2000).

[144] S.W. Brown, T.A. Kennedy, and D. Gammon, Solid State Nuclear Mag. Res. **11**, 49 (1998).

[145] J.M. Kikkawa and D.D. Awschalom, Science **287**, 473 (2000).

[146] J.A. Gupta *et al.*, Science **292**, 2458 (2001).

[147] J.H. Smet *et al.*, Nature **415**, 281 (2002).

[148] R.C. Ashoori, H.L. Stormer, J.S. Weiner, L.N. Pfeiffer, K.W. Baldwin, and K.W. West, Phys. Rev. Lett. **71**, 613 (1993).

[149] For a review see e.g., R.C. Ashoori, Nature **379**, 413 (1996), and references therein.

[150] O.G. Schmidt, S. Schieker, K. Eberl, O. Kienzle, and S. Ernst, App. Phys. Lett. **73**, 659 (1998).

[151] L. Quiroga, D.R. Ardila, and N.F. Johnson, Solid State Commun. **86**, 775 (1993).

[152] L.D. Hallam, J. Weis, and P.A. Maksym, Phys. Rev. B **53**, 1452 (1996).

[153] M. Wagner, U. Merkt and A.V. Chaplik, Phys. Rev. B **45**, 1951 (1992).

[154] J.H. Reina, unpublished.

[155] S.C. Benjamin and N.F. Johnson, Phys. Rev. B **51**, 14733 (1995).

[156] P.A. Maksym and T. Chakraborty, Phys. Rev. Lett. **65**, 108 (1990).

[157] N.F. Johnson and L. Quiroga, Phys. Rev. Lett. **74**, 4277 (1995).

[158] N.F. Johnson and L. Quiroga, J. Phys.: Condens. Matt. **9**, 5889 (1997).

[159] S. Tarucha, D.G. Austing, Y. Tokura, W.G. van der Wiel and L.P. Kouwenhoven, Phys. Rev. Lett. **84**, 2485 (2000).

[160] G. Feher, Phys. Rev. **114**, 1219 (1959); D.K. Wilson and G. Feher, Phys. Rev. **124**, 1068 (1961).

[161] B. Kane, e-print quant-ph/0003031. See also Ref. [52].

[162] C. P. Slichter, *Principles of Magnetic Resonance*, Springer Verlag, Berlin (1996).

[163] P. Zanardi and M. Rasetti, Phys. Rev. Lett. **79**, 3306 (1997); L.-M. Duan and G.-C. Guo, *ibid.* **79**, 1953 (1997); D.A. Lidar *et al.*, *ibid.* **81**, 2594 (1998).

[164] A. Beige *et al.*, Phys. Rev. Lett. **85**, 1762 (2000).

[165] J. Kempe *et al.*, Phys. Rev. A **63**, 042307 (2001), and references therein.

[166] L. Viola, E. Knill and S. Lloyd, Phys. Rev. Lett. **85**, 3520 (2000); *ibid.* **82**, 2417 (1999); L. Viola and S. Lloyd, Phys. Rev. A **58**, 2733 (1998).

[167] G. S. Agarwal *et al.*, Phys. Rev. Lett. **86**, 4271 (2001), and references therein; G. S. Agarwal, Phys. Rev. A **61**, 013809 (2000); C. Search and P.R. Berman, Phys. Rev. Lett. **85**, 2272 (2000).

[168] D. Kielpinski *et al.*, Science **291**, 1013 (2001).

[169] P.G. Kwiat *et al.*, Science **290**, 498 (2000).

[170] G.M. Palma, K.-A. Suominen, and A.K. Ekert, Proc. R. Soc. London A **452**, 567 (1996).

[171] L.-M. Duan and G.-C. Guo, Phys. Rev. A **57**, 737 (1998).

[172] A. J. Leggett *et al.*, Rev. Mod. Phys. **59**, 1 (1987).

[173] E. Knill, R. Laflamme, and L. Viola, Phys. Rev. Lett. **84**, 2525 (2000).

[174] P. Zanardi, Phys. Rev. A **63**, 012301 (2001), and references therein.

[175] C. Morais Smith and A.O. Caldeira, Phys. Rev. A **41**, 3103 (1990) and references therein; *ibid.* **36**, 3509 (1987); V. Hakim and V. Ambegaokar, *ibid.* **32**, 423 (1985).

[176] C.W. Gardiner and P. Zoller, *Quantum Noise*, Springer Verlag, Berlin (2000).

[177] B.L. Hu, J.P. Paz, and Y. Zhang, Phys. Rev. D **45**, 2843 (1992).

[178] J.H. Reina, in preparation.

[179] W.G. Unruh, Phys. Rev. A **51**, 992 (1995).

[180] G.D. Mahan, *Many-Particle Physics*, pp. 314 (2nd edition), Plenum press, New York (1990).

[181] M. Hillery, R.F. O'Connell, M.O. Scully, and E.P. Wigner, Phys. Rep. **106**, 121 (1984).

[182] T. Takagahara, Phys. Rev. B **60**, 2638 (1999).

[183] X. Fan *et al.*, Solid State Commun. **108**, 857 (1998).

[184] N. Bogolubov Jr. *et al.*, Physica A **151**, 293 (1988).

[JHR6] J. Villalobos, L. Quiroga, J.H. Reina, and N.F. Johnson, to be published.

[185] For a QIP scheme based on electron spin transitions in QDs inside a microdisk cavity see Ref. [34].

[186] M. Saba *et al.*, Nature **414**, 731 (2001), and references therein.

[187] D.G. Lydzey *et al.*, Science **288**, 1620 (2000).

[188] D.G. Lydzey *et al.*, Nature **395**, 53 (1998).

[189] M.V. Artemyev and U. Woggon, Appl. Phys. Lett. **76**, 1353 (2000).

[190] S.M. Dutra, P.L. Knight, and H. Moya-Cessa, Phys. Rev. A **49**, 1993 (1994).

[191] F.-L. Li and S.-Y. Gao, Phys. Rev. A **62**, 43809 (2000).

[192] M.O. Scully and M.S. Zubairy, *Quantum Optics*, Cambridge University Press, UK, (1997).